UNIVERSIDAD AUTÓNOMA DE SAN LUIS POTOSÍ

FACULTAD DE CIENCIAS QUÍMICAS

Centro de Investigación y Estudios de Posgrado

Posgrado en Ciencias en Ingeniería Química

UNIVERSIDAD DE GRANADA
FACULTAD DE CIENCIAS

Departamento de Química Inorgánica

Programa de Doctorado en Química

Desarrollo de monolitos de carbono, con geometría, textura porosa y química superficial adaptada mediante el uso de tecnología de impresión 3D, para la valorización de CO_2

Tesis en cotutela para obtener el título de:

Doctor en Ciencias en Ingeniería Química por
la Universidad Autónoma de San Luis Potosí

Doctor en Química
por la Universidad de Granada

Presenta:

PARRA MARFIL ADRIANA

Directores de Tesis:

Dr. Raúl Ocampo Pérez
Dra. Esther Bailón García

SAN LUIS POTOSÍ, S. L. P.   JULIO 2024

Esta Tesis está enmarcada en el Convenio de Cotutela de Tesis Doctoral Suscrito entre la Universidad de Granada, España (UGR) y la Universidad Autónoma de San Luis Potosí, México (UASLP), de fecha 19 de noviembre de 2021.

Los datos del trabajo titulado "Desarrollo de monolitos de carbono, con geometría, textura porosa y química superficial adaptada mediante el uso de tecnología de impresión 3D para la valoración de CO_2" se encuentran bajo el resguardo de la Universidad Autónoma de San Luis Potosí y de la Universidad de Granada.

UNIVERSIDAD AUTÓNOMA DE SAN LUIS POTOSÍ

FACULTAD DE CIENCIAS QUÍMICAS

Centro de Investigación y Estudios de Posgrado
Posgrado en Ciencias en Ingeniería Química

UNIVERSIDAD DE GRANADA

FACULTAD DE CIENCIAS

Departamento de Química Inorgánica
Programa de Doctorado en Química

Desarrollo de monolitos de carbono, con geometría, textura porosa y química superficial adaptada mediante el uso de tecnología de impresión 3D, para la valorización de CO_2

Tesis en cotutela para obtener el título de:
Doctor
por la Universidad Autónoma de San Luis Potosí
y por la Universidad de Granada

Presenta:

PARRA MARFIL ADRIANA

SINODALES:

Presidente: _____

Secretario: _____

Secretario: _____

Vocal: _____

Vocal: _____

SAN LUIS POTOSÍ, S. L. P.   JULIO 2024

"La recompensa de nuestro

trabajo no es lo que obtenemos,

sino en lo que nos convertimos."

-Paulo Coelho

A mi familia

AGRADECIMIENTO A LAS INSTITUCIONES

Agradecimientos

Al concluir esta etapa de mi vida quiero expresar mi más profundo agradecimiento a quiénes hicieron posible que llegara a esta meta, aquellos que me acompañaron durante el proceso, ya sea física o espiritualmente, y que han sido mi inspiración, motivación, apoyo y fortaleza.

En especial a Dios, que me acompaña siempre, que guía mi camino y me ha permitido vivir esta experiencia; y a mi familia, mis padres, mis hermanos, y mis hermosos sobrinos, sin duda alguna, la parte más difícil ha sido estar lejos de ustedes. Gracias por creer en mí, por su amor y su apoyo incondicional, por alentarme y por estar para mí siempre a pesar de la distancia. Ustedes son mi motor y mi más grande orgullo, los amo.

A mi querido novio Emilio, gracias por tu amor y tu paciencia. Este camino ha sido especial con tu compañía y apoyo, gracias por aguantarme y estar ahí en los momentos buenos y los no tan buenos. Espero seguir compartiendo muchos sueños y metas a tu lado.

A mi familia Granaína, gracias por su recibimiento y su calidez. Ha sido una fortuna encontrarlos en mi camino.

Mi más sincero agradecimiento a mis directores de tesis, el Dr. Raúl Ocampo Pérez y la Dra. Esther Bailón García, por darme la oportunidad de realizar este proyecto, por sus enseñanzas, consejos y apoyo durante la realización de mi doctorado, tanto en San Luis como en Granada. Sin sus conocimientos y soporte no habría sido posible. Gracias Esther por tu orientación y dedicación. Gracias Dr. Raúl, por creer en mí, una vez más.

Mi gratitud también a cada uno de los profesores, tanto de la UASLP como de la UGR, quienes me brindaron su apoyo a lo largo de mi doctorado, Dr. Paco, Dr. Agustín, Dra. María, Dr. Hakim, Dra. Erika, y Dr. Nahúm. Gracias también al Dr. Carlos, y al Dr. Agustín Bueno.

Al Dr. Cristian Chaparro, por toda la ayuda y el tiempo dedicado, por tu paciencia y consejos.

A todos mis compañeros y a los chicos de estancia que han estado presentes durante el doctorado, muchas gracias por los buenos momentos compartidos.

A mis amigos, que están siempre en las buenas y en las malas, gracias por su paciencia y comprensión, por aguantarme y por sacarme una sonrisa cuando lo necesitaba, y hacer esta etapa más amena, aunque es difícil mencionarlos a todos, quisiera agradecer en especial a Elías, y mis parceritos Edgar y Cris.

¡Muchas gracias!

Resumen

En esta Tesis Doctoral se desarrolla una metodología innovadora para sintetizar monolitos de carbono, combinando la impresión 3D con el proceso sol-gel. Esta técnica supera las limitaciones de las técnicas convencionales de fabricación, permitiendo obtener estructuras más complejas y eficientes para su aplicación como soportes de catalizadores.

Mediante el diseño de plantillas poliméricas impresas en 3D, usadas como moldes para los canales monolíticos, se prepararon estructuras con canales entrecruzados, canales tipo válvula Tesla con diferentes ángulos, y canales rectos con varias densidades de celda. Estos últimos se utilizaron como referencia en el análisis del efecto del diseño. Los moldes impresos se llenaron con solución precursora de gel de carbono, compuesta por resorcinol, formaldehído y agua, que se polimerizó de forma controlada para obtener monolitos orgánicos. Finalmente, los monolitos orgánicos se carbonizaron donde el polímero termofusible de las plantillas se funde, dejando libres los canales.

Estos monolitos se emplearon como soportes de la fase activa Ni/CeO_2, evaluando su desempeño catalítico y el efecto de las geometrías propuestas en una reacción de gran interés socioeconómico y ambiental: la metanación de CO_2. La caracterización de la fase activa y los catalizadores confirmó que las características de la Ni/CeO_2 no se vieron afectadas al estar soportadas en el monolito de carbono, demostrando así que los efectos observados en catálisis corresponden al diseño de los monolitos.

Inicialmente, se analizó el efecto de los canales rectos en un monolito de cordierita comercial, empleado a nivel industrial, comparando la influencia del incremento de densidad de celda. El estudio mostró que los materiales presentan control difusional, y que, aunque el incremento de densidad de celda puede mejorar la dispersión de fase activa, promueven el flujo laminar y reduce su eficiencia. En cuanto a los monolitos de carbono diseñados, se observó que la creación de caminos tortuosos favorece un flujo más caótico. Este, a su vez, promueve la interacción del

fluido con la fase activa, dispuesta tanto en los canales como en la matriz carbonosa, lo que resulta en un mejor aprovechamiento de esta y mayor actividad catalítica. En el caso del diseño Tesla, la generación de puntos de sobrepresión por la convergencia y obstrucción de flujos, favorece aún más la reacción de acuerdo con el principio de Le Châtelier.

Por otra parte, se realizó un estudio adicional enfocado a la remediación de agua mediante procesos avanzados de oxidación. Se utilizó un sistema $UV/S_2O_8^{2-}$ y, siguiendo un diseño de superficie de respuesta tipo Box-Behnken, se analizó el efecto de las variables de operación en la fotodegradación de metformina en solución acuosa. Mediante el análisis de varianza se determinó que la concentración inicial de metformina, la concentración de oxidante y la temperatura son los factores más significativos en la degradación y mineralización de la metformina. Asimismo, se identificaron seis subproductos principales con los cuales se sugirieron tres vías de degradación.

Palabras clave:

Catalizadores monolíticos, impresión 3D; mejoramiento fluídico; xerogel de carbono; valorización de CO_2.

Abstract

In this Doctoral Thesis, an innovative methodology is developed to synthesize carbon monoliths by combining 3D printing with the sol-gel process. This technique overcomes the limitations of conventional manufacturing techniques, allowing for the creation of more complex and efficient structures for their application as catalyst supports.

Polymeric templates were designed using 3D printing and used as molds for the monolithic channels. Structures with crisscrossed channels, Tesla valve-type channels with different angles, and straight channels with various cell densities were prepared. The latter served as a reference in analyzing the design effect. The printed molds were filled with a carbon gel precursor solution composed of resorcinol, formaldehyde, and water, which was polymerized in a controlled manner to obtain organic monoliths. Finally, the organic monoliths were carbonized, during which the thermofusible polymer of the templates melted, leaving the channels free.

These monoliths were utilized as supports for the active phase Ni/CeO_2, and their catalytic performance was evaluated, along with the effect of the proposed geometries, in a reaction of significant socioeconomic and environmental interest: the methanation of CO_2. Characterization of the active phase and the catalysts confirmed that the characteristics of the Ni/CeO_2 were unaffected when supported in the carbon monolith, demonstrating that the observed effects in catalysis corresponded to the monolith design.

Initially, the effect of straight channels in a commercial cordierite monolith, used at an industrial level, was analyzed, comparing the influence of the increase in cell density. The study revealed diffusion control in the materials, and while increasing cell density could improve active phase dispersion, it also increased laminar flow, thereby reducing efficiency. Regarding the designed carbon monoliths, the creation of tortuous paths was observed to favor a more chaotic flow, promoting greater interaction of the fluid with the active phase arranged in both the channels and the carbonaceous matrix, resulting in enhanced utilization and catalytic activity. In the case of the Tesla design, the generation of overpressure points due to the convergence and obstruction of flows

further facilitated the reaction, in accordance with Le Châtelier's principle.

On the other hand, an additional study was carried out focused on water remediation through advanced oxidation processes. A UV/$S_2O_8^{2-}$ system was used and, following a Box-Behnken response surface design, the effect of operating variables on the photodegradation of metformin in aqueous solution was analyzed. Through the analysis of variance, it was determined that the initial concentration of metformin, the oxidant concentration and temperature are the most significant factors in the degradation and mineralization of metformin. Likewise, six main byproducts were identified with which three degradation pathways were suggested.

Keywords:

Monolithic catalysts; 3D printing; fluidic enhancement; carbon xerogel; CO_2 valorization.

Table of Contents

List of Figures

velocity profiles inside of NCM, adapted from; b) General structure and cross sectional view of 3D printed ceramic substrates utilizing different offset angles between meshed layers from; and c) Four geometry designs used for FDM of polymeric monoliths: straight channels (I), orthogonal mesh layers (II), shifted orthogonal mesh layers (III), and diamond structure in which each channel connects to three other channels in a tetrahedral node (IV).

List of Tables

1

INTRODUCTION

1.1. Introduction

One of the main environmental problems that society currently faces is global warming and the consequent climate change. The burning of fossil fuels has caused an increase in the amount of atmospheric CO_2, boosting the greenhouse effect since it represents close to 80 % of total greenhouse gas emissions and contributes to global warming [1]. Due to this, political, industrial, and scientific interest has increased in promoting alternative and sustainable energy sources that contribute to mitigating global warming caused by the emissions of these gases, as well as reducing dependence on fossil fuels. In this sense, the production of biogas from the anaerobic digestion of organic waste results in a great opportunity from the point of view of waste treatment, energy supply, and environmental protection. Biogas is a gas mixture consisting mainly of CH_4 (50-70%) and CO_2 (30-50%), which can be used as a renewable fuel [2]. However, the calorific value of biogas is low due to its high CO_2 content, so enrichment or "upgrading" is done, in which the CO_2 is separated to obtain biomethane with specifications similar to natural gas. This enrichment allows a versatile application, whether its direct injection into the gas pipeline network, its use in the generation of heat or power, or as fuel for vehicles. After the biogas purification, the separated CO_2 cannot be released into the environment as it would reintroduce pollution and exacerbate the initial issue of greenhouse gas emissions. Therefore, effective management and valorization of residual CO_2 obtained in large quantities in biogas generating facilities is crucial to maintain the benefits of biogas as a renewable fuel without compromising the environment.

In this regard, the transformation of CO_2 through the methanation reaction provides a solution to this economic, industrial, and environmental problem. Moreover, the development of CO_2 methanation will lead to the generation of more methane that can be added to the previously purified biomethane. However, the main drawback in the transformation of CO_2 is the high stability of the C=O bond, and, hence, a large amount of energy is required for its dissociation [3-5]. Consequently, the conversion of CO_2 has kinetic limitations and requires suitable catalysts to improve the speed at which

the chemical reactions occur for its transformation [6]. Most industrial catalytic processes today are "heterogeneous catalysis", where the catalysts usually consist of an inert support on which the phases with catalytic activity are deposited. The supports can be particles of different sizes, meshes, pellets, monoliths with a cellular structure (honeycomb), etc. At the same time, the active phases can be noble and non-noble metals, metal oxides, and crystalline solids with defined porous and acidic properties.

Additionally, industrial processes entail the treatment of large volumes of gases, thus requiring systems with minimal pressure drops. Honeycomb monoliths are gaining importance at an industrial scale due to their kinetic, fluid-dynamic, and diffusional properties. Their structure, composed of parallel axial channels through which the fluid circulates, reduces total pressure drop compared to particle or pellet systems [7]; this allows for the use of higher flow rates while simultaneously decreasing equipment dimensions and costs. Further, the use of monolithic structures offers several advantages over packed-bed reactors: greater external surface area of material exposed; reduction of external and internal matter transfer limitations; better heat transfer properties; reduction of incrustations and obstructions, leading to a longer useful life of the material; and ease of handling for cleaning and maintenance [8]. Generally, monoliths are manufactured by extrusion, limiting their geometry and design to straight and parallel channels. Straight channels impose a laminar circulation flow due to friction forces, thus resulting in non-uniform flow and velocities up to 5 times greater at the centerline compared to the channel wall. In consequence, this leads to less efficient utilization of the specific surface area and/or active phases supported in the monolith.

On the other hand, due to the characteristics and generally non-porous properties of typical ceramic or metallic materials used for manufacturing monolithic structures, loading the active phase presents some complications. In this context, carbonaceous materials offer interesting properties that can help to reduce this loading issue. However, carbonaceous materials are not considered appropriate for extrusion; hence, pure carbon monoliths cannot be obtained directly with conventional synthesis

methods [9]. Strategies such as the deposition of carbonaceous materials on ceramic monoliths or the extrusion of carbon together with binders and additives may be followed [10]. Nevertheless, in the first case, the material-to-volume ratio is very low, increasing the volume of the equipment required, while in the second case, additives affect the porosity of the material.

On this basis, pure carbon monolithic structures must be obtained without the use of additives. These structures should also have an advanced cellular design that is not based on straight and parallel channels, with the aim of favoring a turbulent circulation flow, which improves diffusion through the material's porosity and increases effectiveness in catalysis. Therefore, in this research work, a new methodology that combines the use of three-dimensional (3D) printing technology with the sol-gel process is proposed to design and manufacture carbon monoliths. This methodology enables the production of pure carbon monoliths with complex geometries that are non-achievable through conventional synthesis methods. The sophisticated carbon monoliths were used as catalytic supports, and their performance in the CO_2 methanation reaction was evaluated. Among the advantages of obtaining these porous monoliths with advanced channel designs that generate turbulent flows we can mention: 1) better interaction between the fluid and the monolith; 2) better mass transport, therefore, better material efficiency; 3) greater use of the catalyst thanks to better dispersion and anchoring of the active phase, achieving the same conversions with less catalyst; 4) decreased consumption of generally expensive and scarce raw materials (such as noble metals); and 5) capacity of treating higher flow rates.

1.2. References

[1] EPA United States Environmental Protection Agency. (2024). *Greenhouse Gas Emissions: Overview of Greenhouse Gases*, EPA. Retrieved February 16, 2024, from https://www.epa.gov/ghgemissions/overview-greenhouse-gases

[2] Liu, C., Xiao, J., Li, H., Chen, Q., Sun, D., Cheng, X., Li, P., Dang, Y., Smith, J. A., & Holmes, D. E. (2021). High efficiency in-situ biogas upgrading in a bioelectrochemical system with low energy input. *Water Research*, *197*, 117055. https://doi.org/10.1016/j.watres.2021.117055.

[3] Hao, Z., Shen, J., Lin, S., Han, X., Chang, X., Liu, J., Li, M., & Ma, X. (2021). Decoupling the effect of Ni particle size and surface oxygen deficiencies in CO_2 methanation over ceria supported Ni. *Applied Catalysis B: Environmental*, *286*, 119922. https://doi.org/10.1016/j.apcatb.2021.119922.

[4] Lin, S., Tang, R., Liu, X., Gong, L., & Li, Z. (2024). Modulating CO_2 methanation activity on Ni/CeO_2 catalysts by tuning ceria facet-induced metal-support interaction. *International Journal of Hydrogen Energy*, *51*, 462-475. https://doi.org/10.1016/j.ijhydene.2023.10.095.

[5] Modak, A., Bhanja, P., Dutta, S., Chowdhury, B., & Bhaumik, A. (2020). Catalytic reduction of CO_2 into fuels and fine chemicals. *Green Chemistry*, *22*, 4002-4033. https://doi.org/10.1039/D0GC01092H.

[6] Quindimil, A., De-La-Torre, U., Pereda-Ayo, B., Davó-Quiñonero, A., Bailón-García, E., Lozano-Castelló, D., González-Marcos, J. A., Bueno-López, A., & González-Velasco, J. R. (2020). Effect of metal loading on the CO_2 methanation: A comparison between alumina supported Ni and Ru catalysts. *Catalysis Today*, *356*, 419-432. https://doi.org/10.1016/j.cattod.2019.06.027.

[7] Davó-Quiñonero, A., Sorolla-Rosario, D., Bailón-García, E., Lozano-Castelló, D., & Bueno-López, A. (2019). Improved asymmetrical honeycomb monolith catalyst prepared using a 3D printed template. *Journal of Hazardous Materials*, *368*, 638-643. https://doi.org/10.1016/j.jhazmat.2019.01.092.

[8] Chaparro-Garnica, C. Y., Davó-Quiñonero, A., Bailón-García, E., Lozano-Castelló, D., & Bueno-López, A. (2019). Design of Monolithic Supports by 3D Printing for Its Application in the Preferential Oxidation of CO (CO-PrOx). *ACS Applied Materials & Interfaces*, *11*, 36763-36773. https://doi.org/10.1021/acsami.9b12731.

[9] Gatica, J. M., García-Cabeza, A. L., Yeste, M. P., Marín-Barrios, R., González-Leal, J. M., Blanco, G., Cifredo, G. A., Guerra, F. M., & Vidal, H. (2016). Carbon integral honeycomb monoliths as support of copper catalysts in the Kharasch–Sosnovsky oxidation of cyclohexene. *Chemical Engineering Journal*, *290*, 174-184. https://doi.org/10.1016/j.cej.2016.01.037.

[10] Gatica, J. M., Gómez, D. M., Harti, S., & Vidal, H. (2013). Monolithic honeycomb design applied to carbon materials for catalytic methane decomposition. *Applied Catalysis A: General*, *458*, 21-27. https://doi.org/10.1016/j.apcata.2013.03.016.

2

LITERATURE BACKGROUND
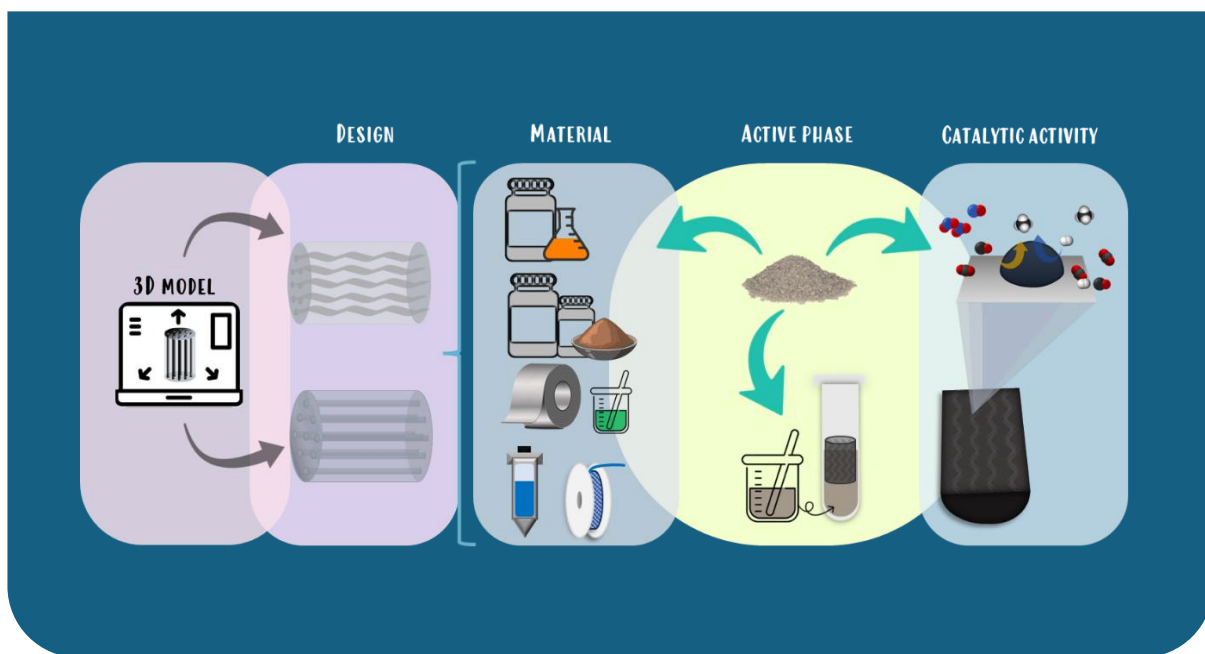
2. Literature background

This Doctoral Thesis studies the implementation of 3D printing in the manufacture of monoliths with advanced designs to use them as catalyst supports. This section serves to define the justification, hypothesis, and objectives of the study and provide an overview of the most relevant background information pertaining to the topic. The background review encompasses insight into the specific catalytic reaction under study: CO_2 methanation, the application of monolithic supports in catalysis, the primary 3D printing techniques recently introduced into the catalysis field, and the carbon gels synthesis.

2.1. CO_2 valorization – CO_2 methanation

The atmospheric CO_2 concentration, constituting close to 80% of greenhouse gases, persistently rises due to human activity, mainly from energy consumption through fossil fuel combustion [1]. This expanding trend in emissions has worrying implications for climate change, highlighting the urgent need for effective solutions. In this regard, the conversion of CO_2 into high-value fuels emerges as a promising avenue. This approach may not only aid in mitigating environmental harm but also in decreasing dependency on fossil fuels.

One method for this CO_2 valorization is hydrogenation, which produces methane, known as CO_2 methanation or Sabatier reaction [2]. The Sabatier reaction (1) is a highly exothermic reaction, usually performed at 150 to 500 °C and 1 to 100 atm in the presence of a catalyst [3-5], which leads to the production of water and methane. The resulting methane closely resembles natural gas, facilitating its direct integration into the existing natural gas grid [6].

$$CO_2 + 4H_2 \leftrightarrow CH_4 + 2H_2O, \triangle H_{298\ K} = -165\ kJ\ mol^{-1} \quad [7, 8] \tag{1}$$
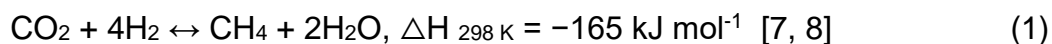
While this reaction is thermodynamically favored at low temperatures, its progress is hindered by kinetic limitations due to the chemical stability of the C=O bond in CO_2 [2, 9-11]. Consequently, adequate catalysts are needed to promote the dissociation of CO_2 and boost the reaction. Numerous researchers have proven the

catalytic activity of several metals (for instance, Ru, Rh, Pd, Fe, Cu, Co, Ir, and Ni) [12-20], generally dispersed on the surface of metal oxides (such as Al_2O_3, ZrO_2, TiO_2, and CeO_2) [7, 21-24], zeolites, or metal-organic frameworks [10, 25]. Ni-based catalysts are widely preferred owing to their great catalytic performance, high selectivity to CH_4, availability, and lower cost of Ni compared to noble metals [7-9, 20, 23, 26]. Among them, CeO_2-supported Ni catalysts have shown to improve the performance of CO_2 methanation at low temperatures. This is associated with a high amount of adsorbed CO_2, which is activated and dissociated due to considerable oxygen vacancies and the good interaction between metal and support [9, 20, 23, 27, 28].

Nevertheless, because of the high exothermicity of the CO_2 methanation, the heat of the reaction causes thermal increases and hot spot formation [4, 20]. This, in turn, may lead to catalyst deactivation by carbon deposition and Ni particle sintering [4, 7]. For this reason, additionally to look for a great catalytic activity catalyst, it is necessary to search for a better configuration that, compared to commonly used fixed-bed reactors, assists in heat management and elimination.

2.2. Monolithic supports

In general, a monolith can be defined as a uniform block built from different materials; the term's origin comes from the Greek "mono", which means single, and "lithos", which means stone [29-32]. Typically, the monolithic structures used in heterogeneous catalysis consist of uniform blocks (usually cylindrical) with parallel channels that can be produced with different sizes and cross-sectional shapes (e.g., square, triangular, circular, hexagonal, etc.). These monoliths are commonly known as honeycomb structures due to the appearance of their cross-section. An illustration of a conventional honeycomb monolithic catalyst is presented in *Figure 2.1*. This figure represents a monolithic structure coated with the active phase (catalytic component), where the surface of the channel walls functions as support for it. Monolithic catalysts have higher exposed surface area compared to powder, pellet, or granule catalysts, which, in turn, allows better distribution and accessibility of the active phase [33-35]. Moreover, their large open frontal area provides a key advantage: low flow resistance,

resulting in minimal pressure drop even at high flow rates [33, 35-37]. Monolith structures outperform conventional particle catalysts in terms of mass and heat transfer, as well as thermal and mechanical stability [38-41]. Additionally, they reduce the diffusion path length and offer easy handling and simple cleaning of particulates accumulated on the channel wall, thus improving the regeneration and reusability of the catalyst [39, 41].
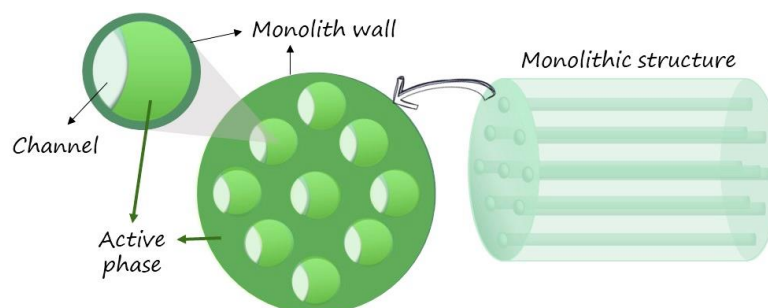
Figure 2.1. Illustration of a conventional cylindrical honeycomb monolithic structure comprising circular cross-sectional channels coated with a catalytically active phase.

The characteristics of a monolith can be defined according to its cell density, open frontal area, and exposed geometric surface area. Cell or channel density refers to the number of channels per unit of cross-sectional area, typically expressed in units of cells per square inch (cpsi) [33, 35, 37]. Open frontal area refers to the empty fraction of the monolith's cross-sectional area, excluding the width of the channel walls, through which a fluid can circulate [35, 37]. On the other hand, exposed geometric surface area corresponds to the external mass transfer area and is usually expressed in units of area per volume of monolith [33, 35]. The design of monolithic structures has been restricted by the technology available for their fabrication and the techniques feasible to support the active phases. Honeycomb monoliths are usually produced by extrusion, corrugation of sheets, or compression, and the catalytically active phases are subsequently incorporated, usually by wash coating [40, 42-45]. The deposition of highly active catalytic phases with suitable thickness, homogeneity, and adhesion to the support determines the stability of the coating as well as the catalytic activity. In this respect, the wash coating technique is reported as the most popular and adaptable

way to deposit catalysts on structured supports, using slurries or sols prepared from catalysts previously synthesized [39, 40].

The extrusion process is primarily used to produce cordierite or ceramic monoliths but can also be applied to other materials such as polymers, clays, or carbon with binders. Extrusion is effectuated using dies specifically designed to obtain the desired configuration. The extrusion process comprises several steps: 1) mixing raw materials (binders and additives); 2) plasticizing with a solvent to achieve a suitable paste consistency for shaping; 3) shaping by forcing the prepared paste through the selected die; 4) drying to remove moisture; and 5) thermal treatment (drying, calcination, curing, carbonizing, or sintering) depending on the material being treated [29, 35, 37, 46]. The corrugation method is mainly used to produce metallic monoliths, such as aluminum, iron, steel, and other alloys. This method consists of stacking and rolling alternated corrugated and flat metal sheets [35-37]. In contrast, the compression technique involves pressing a deformable material between two halves of a heated die (up to 200 °C), which product is later cooled or cured [47, 48]. However, the properties of monoliths manufactured by compression, especially porosity, may be affected [49]. Furthermore, all these methods are restricted to producing monoliths with straight parallel channels that lead to laminar flow [36]. Consequently, additive manufacturing is emerging as an alternative to the advancement of catalyst manufacturing.

2.3. 3D printing in monolithic catalysts development

Recently, AM has opened new opportunities in the catalysis field [50, 51]. Since about 85-90 % of industrial processes contain at least one catalytic step [52], the generation of catalysts that decrease the reaction activation energy and increase the selectivity of target products is of major necessity to benefit the processes efficacy. In this sense, the versatility to obtain complex structure designs, non-achievable through conventional methods but through additive manufacturing, represents an advantage in catalytic improvement. Consequently, AM is freshly being applied to produce reactors, monolithic catalysts, mixers, and ancillaries [53-56].

On the other hand, the advancement in the production of structured catalysts made of a 3D support coated by catalytically active species and their use in catalytic processes is considered an excellent alternative to traditional packed and fluidized bed systems. This is because, as previously mentioned, using structured catalysts like monoliths not only reduces the processing costs by avoiding the filtration stage but also involves a lower pressure drop and better thermal and mechanical stability regarding powders or pellets, especially for high flow rates [38-41]. Nevertheless, conventional fabrication procedures limit the design of monoliths to aligned regular channels. This configuration implies that although the flow of the feed gas is turbulent, it becomes laminar as it passes through the monolith due to viscous forces within the narrow channels. Hence, the enforced laminar flow results in its lack of uniformity and radial mass and heat transfer limitations, impeding an appropriate usage of the active phases [57]. Thus, the progress of monolith manufacturing techniques that enhance the complexity of the designs, active phase deposition, and the interaction between reactants and catalysts represent an advancement opportunity at the industrial level to diminish the costs of commonly expensive catalytic materials and increase their efficiency.

Thus far, various AM technologies have been applied to catalysis to simplify the monolithic catalyst preparation and active phase loading process. Moreover, 3D printing techniques have been used to analyze the performance of several materials (such as zeolites, metals, metal oxides, and polymers) in many processes. Along with the generally used dip-coating method (which can be applied to deposit the catalytic active phase on a printed object), this synthesis technique also allows the integration of the active phase in the monolithic structure while printing, as some studies have shown [58-64]. In this regard, the innovation of AM technology is demonstrated to be an excellent implement that helps to obtain specific, different, and complex structures, which are otherwise unattainable with conventional methods [65-68]. Moreover, the use of 3D printing techniques in combination with fluid and chemical simulation could be advantageous in optimizing heat and mass transfer [53] and, hence, catalytic

processes. The broad diversity of techniques and materials available makes the AM technology an advantageous prospect for exploring and enhancing the production of the catalyst. Monolithic catalyst manufacture through AM can be done using two strategies: obtaining them directly by 3D printing or through the generation of templates used in succeeding processing (filling, loading, or coating). Thus, the chemical composition, physicochemical properties, and monolithic structure of 3D printed catalyst materials can be customized for specific reactions or experiments. Therefore, a comparative assessment of the 3D printing techniques, materials, potential, and limitations to produce monolithic catalysts, according to different printing methods, is presented in the following sections to offer a useful review of the innovative possibilities in catalyst fabrication.

2.3.1. Additive Manufacturing Overview

Additive manufacturing (AM) is a technology developed by Charles Hull in 1986 [69], which consists of the successive addition of material, printing one layer at a time, to build up a final product. The additive manufacturing process starts by generating a 3D computer-aided design (CAD) of the desired object. This model is sliced into a stack of flat layers of patterned areas, which are printed with diverse materials and, afterward, solidified (or crosslinked) into a structure. There is a wide variety of raw materials that can be used depending on the additive manufacturing process. Among them are polymers, ceramics, composites, powders, glass, building materials, biomaterials, metals, and carbonaceous materials (with binder matrix). This technology has reduced manufacturing limitations by allowing the development of a vast range of simple and complicated geometries, with design freedom and excellent dimensional accuracy even at small scale. Furthermore, due to the advantages offered by AM, such as ease of access, high-speed production, minimization of materials wastage, and, therefore, cost-effective products [70], its applications are constantly expanding. There are several ways to classify AM processes, for example, according to their baseline technology or the type of raw material employed. Nonetheless, the most accepted classification is given by ASTM/ISO (*Figure 2.2*) and consists of seven process

categories: vat photopolymerization, powder bed fusion, material extrusion, material jetting, binder jetting, sheet lamination, and direct energy deposition [71].

Figure 2.2. Additive manufacturing technologies classified according to the type of process.

According to ASTM definition, vat photopolymerization, powder bed fusion, and direct energy deposition processes solidify the raw material either disposed in a vat container or provided from a material feeder, following each layer pattern. On the other hand, techniques grouped in the material extrusion, material jetting, and binder jetting categories deposit the building material by means of a nozzle in a build platform to be cured afterward, while in the sheet lamination technique, the printing material links without curing. ***Table 2.1*** shows a comparison of the AM categories in terms of their advantages, disadvantages, and applicability. Hereunder, an outline of the main additive manufacturing methods that have been applied so far to produce monolithic catalysts is given, therefore giving relevant and useful references in the field.

Table 2.1. Comparison of the characteristics, advantages, and disadvantages of the different additive manufacturing techniques.

Printing Technique	Process	Layer Formation Method	Typical Materials	Strengths	Weaknesses	Resolution (µm)	Printing speed	References
Vat Photopolymerization	Stereolithography (SLA)	Laser/Digital light projector	Photopolymers such as acrylates, epoxies, filled resins (glass, ceramic, metal, etc.) Preceramic polymers Monomers	Do not need support material High precision High quality Smooth surface Complexity Excellent mechanical properties Layerless structure	Costly photopolymers Requirement of post-processing treatments Poor thermal stability	>10 >10 75-162 >80	High	[75-79]
Powder Bed fusion	Laser Sintering (LS) Laser Melting (LM) Electron Beam Melting (EBM)	Laser/Electron beam	Thermoplastics Waxes Polymer, metal, and ceramic powders Alloys	High level of complexity Do not need support material Wide range of materials	Poor surface quality and accuracy caused by the fluidity of powder Requirement of post-processing treatments	>50 >20 n.d.	Moderate Moderate High	[67, 80]

Directed Energy Deposition		Melting by focused heat source	Metal wire or powder Ceramics	High single-point deposition rates Printing on irregular surfaces	Low resolution Limited materials Reduced ability to manufacture complex parts	>250	Low	[67]
Material Extrusion	Direct Ink Writing (DIW)	Extrusion from a nozzle	Plastic Metal Ceramic Zeolites Carbon based materials	Simply fabrication process Variety of materials	Reduced porosity due to binders Need of post treatment to remove additives	30-250	Low	[67, 72, 81]
	Fused Deposition Modeling (FDM)		Thermoplastic filaments (PLA, ABS, polyurethane, etc.)	Easy operation Inexpensive Good structural properties	Restriction of nozzle, diameter, and viscosity Layer-by-layer appearance Poor surface quality	50-200	Moderate	
Material Jetting	Ink Jetting	Ink-jet printing	Photopolymers Polymers Waxes Sol-gel Metals	Enable multiple materials in a single part High level of accuracy and complexity	Expensive materials and printer Limited material types Need of support material	13-16 200-300	Low	[67, 74, 82]
	Drop on Demand							

					Long process			
Binder Jetting	Aerosol Jetting	Binder drops on command	Metal and ceramics powders Polymers	Low temperature process High productivity	Low definition Poor mechanical properties	>50	Moderate	[67, 83, 84]
Sheet Lamination	Laminated Object Manufacture (LOM) Ultrasonic Lamination (UAM) Friction Stir Additive Manufacturing (FSAM)	Binding of sheets through use of sticky substance, ultrasonic welding, or friction stir welding	Paper Plastic sheets Metal foils	High volumetric build rates Large size samples Low cost	Design limitations/Not adapted to detailed structures Depends on the thickness of the laminates Bonding efficiency impacted by laser cut Misalignment of layers	Variable	n.d.	[67, 82]

2.3.2. Vat Photopolymerization

Vat photopolymerization (VPP) was the first introduced additive manufacturing process, which employs a light source to cure liquid photosensitive materials contained in a vat. There are some general characteristics required in the light curing materials, including good stability, low viscosity, suitable transmission, fast curing speed, and low curing shrinkage [72]. By means of a lens system, the scanning path is controlled to perform selective light-activated polymerization, from which the liquid photopolymer is solidified according to a pre-programmed pattern [73, 74]. The main characteristics of vat photopolymerization printing is the high precision and rapid prototyping, moreover, the active phases can be dispersed in the raw material to be used in these techniques. There are several vat polymerization techniques differentiated by the light source and mechanism used for polymerization [75]. These techniques are Stereolithography (SLA), Digital Light Processing (DLP), Continuous Liquid Interface Production (CLIP), and Volumetric Printing.

2.3.2.1. *Stereolithography*

In the stereolithography (SLA) process a beam of ultraviolet (UV) light emitted from a laser is used to react and cure photopolymer resins. The low viscosity photocurable material is deposited in a vat and a movable platform is placed inside, onto which the final product is fabricated and hold. The UV beam scans the surface of the vat in the X-Y axes following a predefined layer cross-section selectively curing the resin. After completing a layer, the build platform moves in the Z axis a layer thickness, either in bottom-up approach (*Figure 2.3a*) or top-down approach (*Figure 2.3b*), filling it with more photopolymer resin. Then, the process is repeated several times, creating successive layers until the entire object is finished. Finally, the structure is removed from the platform, cleaned, and put in a UV oven for further curing [73, 76, 85]. Compared to other techniques, the SLA process offers higher resolution and better surface quality since the resin curing does not depend on the particle size and nozzle characteristics, unlike material extrusion-based technologies.
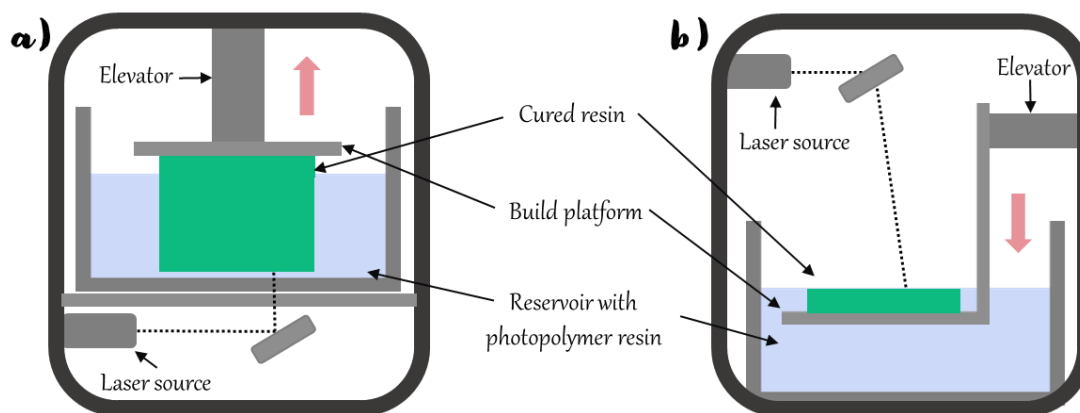
Figure 2.3. Schematic representation of SLA process: a) bottom-up approach; b) top-down approach.

Nonetheless, research utilizing the SLA technique to prepare monolithic structures for directly applying them in catalysis is limited due to the characteristics of the raw materials that restrict their use to low temperature and pressure operational conditions (***Annex 1***). Among these studies, those realized by Chaparro *et al.* [86, 87], who printed monoliths with non-conventional structures using the Visijet FTX Green resin, can be mentioned. After a stabilization treatment, the polymer became stable up to 270 and 300 °C in oxidizing and inert atmospheres, respectively, which establishes the maximum working temperature. Therefore, the catalytic performance of the monoliths was tested in the CO-PrOx reaction at atmospheric pressure with temperatures up to 250 °C. A similar maximum operating temperature was set by Franchi *et al.* [88], who produced catalytic substrates for H_2 oxidation with a high temperature resin, Formlabs FLHTAM01 High Temp V1, which has a heat distortion temperature (HDT) of 289 °C at 0.45 MPa.

Furthermore, the use of polymers also implies some trouble in dispersing and anchoring the active phase on its surface. Therefore, some pre- or post-treatments have been made to improve the deposition of the active phase, this implies additional stages in the obtention of catalytic monoliths. Different strategies have been tried to increase the loading of the active phase including i) thermal treatments; ii) attacking the polymer with different solvents such as ethanol or isopropyl alcohol before the

impregnation; iii) attacking the polymer during the impregnation by using different solvents for the catalysts suspension; iv) doping the resin liquid before the printing process; and v) structures of advanced designs containing cavities.

For instance, the previously mentioned 3D printed structures produced by Franchi *et al.* [88] were loaded with the active compound (Pd/CeO$_2$) by spin coating at 2500 rpm followed by a treatment at 200 °C in air for 3 min to consolidate the washcoat. Due to the HDT, to stabilize and activate the catalytic coat, two-steps in-situ activation procedure was performed. First a heat treatment under N$_2$ atmosphere at 260 °C for 6 h, further cooled to room temperature, and then a second step of reduction also at 260 °C for 6 h in a flow of 2.5 % H$_2$ in N$_2$. Repeated tests were performed on these supports, and results suggested that the deposition and activation procedures led to stable washcoat layers at the conditions employed. Besides, the treatment of the resin with ethanol or isopropyl alcohol was studied by Chaparro *et al.* [86]. Results showed that a chemical attack, either before or during the dip-coating process, interferes with the active phase incorporation to the monoliths, reducing the active phase anchored by about 70 % regarding impregnation without a chemical attack. According to SEM-EDX analysis, the active phase forms a layer on the surface and does not diffuse into the polymeric walls. On the other hand, thermal treatment favors the anchoring but embeds part of the catalytic phase, as shown in *Figure 2.4a-b*, hence making necessary a cleaning treatment in air to burn part of the polymer and let the active phase accessible to reagents (*Figure 2.4c-d*). The authors also investigated the effect of doping the liquid resin with different amounts of carbon and SiO$_2$ in the active phase anchoring and thermal stability of the polymeric structures. The addition of the inorganic material did not lead to changes in the thermal stability. Furthermore, the presence of both inorganic materials generated anchoring points by changing the chemistry and rugosity of the resin, thus slightly increasing the attaching capacity, especially with SiO$_2$. However, they also proved that the use of non-conventional monoliths with grooves along the structure augmented the active phase attachment and retained a similar amount of active phase regarding doped monoliths but requiring

fewer steps. This represents a great alternative and advantage considering that when using traditional monoliths (e.g. cordierite materials), the addition of inorganic materials, such as the SiO_2 or Al_2O_3, the use of binders or additives in repetitive dipping processes, and chemical or thermal treatments, are generally applied to improve active phase loading [89-94].
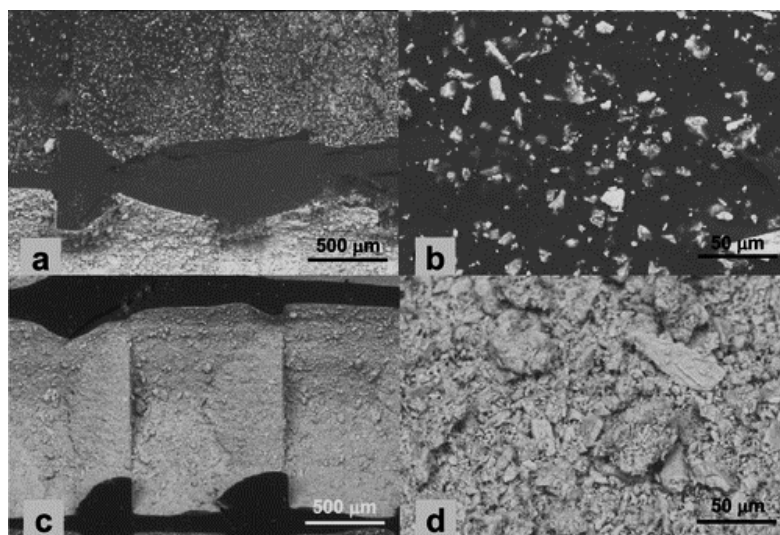
Figure 2.4. SEM images of the channels of a polymeric monolith loaded with CuO/CeO_2 active phase: (a, b) after a thermal stabilization treatment in N_2; (c, d) and after a subsequent thermal treatment in air to increase the accessibility of CuO/CeO_2. Taken from [86].

To overcome the restrictions imposed by polymers, instead of printing catalysts directly with commercial resin (**Figures 2.5a**) this AM technique can be used to create templates to fill with other materials (**Figure 2.5b**). Such is the case of the study realized by Davó *et al.* [95], who produced ceramic monoliths with different geometries to analyze the effect of their configuration on the oxidation of CO. They employed the SLA technique with Visijet FTX green polymer to print two templates for monoliths with symmetrical and asymmetrical channels, maintaining the same total area in both cases. Templates were filled with cordierite paste, and then they were removed by combustion in static air at 500 °C for later sintering of the cordierite. The CuO/CeO_2 active phase for CO oxidation was loaded by dip-coating, and no differences in the

coating between the monoliths were observed. The asymmetrical design favored turbulent regime improving the reaction rate and the radial diffusion of molecules in comparison with the symmetrical one enhancing the catalytic performance.
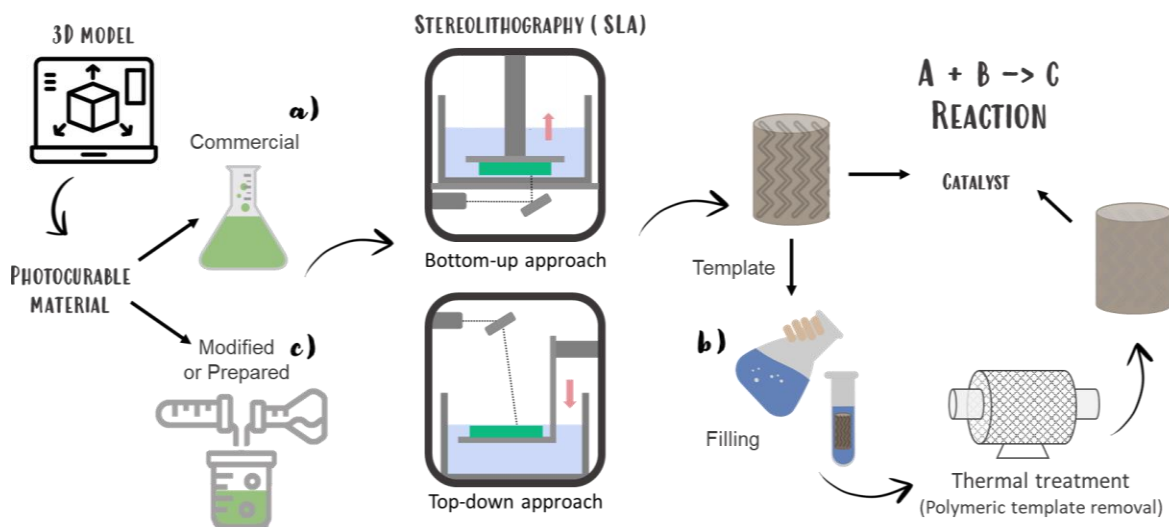
Figure 2.5. Methodologies followed to produce monolithic catalyst applying SLA technique: a) directly printing with commercial resin; b) using the 3D printed object as a template; and c) directly printing with a modified commercial resin or a prepared one.

An alternative to using monolith templates produced by this technique is the modification of the resin employed to improve its characteristics for catalysis (***Figure 2.5c***). However, this may result challenging for the attainment of a photocurable resin with low viscosity which allows dipping and recoating for its layer-by-layer treatment, and able to solidify rapidly by light-initiated polymerization. One option is the use of a photosensitive resin mixture containing prepolymers, which are polymerized by a photoinitiator under light, reactive diluents to adjust the properties of the mixture, and additives [72, 96]. Ceramic structures have been obtained by adding ceramic or glass particles to SLA resins, which after the printing process, followed thermal treatments to burn out the cross-linked polymer binder and sinter the ceramics [97, 98]. In this context, Hensleigh *et al.* [99] developed a graphene oxide-based resin (XGO) to print complex designed graphene monoliths by micro-stereolithography. To obtain the XGO resin, GO was firstly crosslinked to form a hydrogel, which was further dispersed by

sonication and added with acrylates and a photoinitiator, using N,N-dimethylformamide (DMF) as solvent. The acrylates and initiator serve to trap the XGO in the desired 3D shape, while the DMF was used to get high quality GO dispersions and eliminate amorphous carbon. Once printed, the structures were kept in solvent until dried by supercritical or freeze-drying to conserve the surface area. The 3D structures achieved around 10 µm resolution with a GO successfully reduced, showing good characteristics for catalysis.

Two-Photon Lithography (TPL) is a promising way to produce 3D printed electrodes where a substrate is covered with a photoresist, which is polymerized via laser lithography. Only certain voxels polymerize where the two lasers coincide, emitting photons at the same location; hence, the spatial resolution reaches approximately 1 µm. However, after washing away the unpolymerized photoresist, the resulting structure lacks electroactivity; thus, an annealing treatment is required to transform it into pyrolyzed glassy carbon through high-temperature heating to obtain an electroactive surface [100]. Using this technique, C. Yang *et al*. [101] fabricated free-standing microelectrodes with a carbon electroactive surface to be used as implantable neural microsensors by two-photon nanolithography followed by pyrolysis. Spherical and conical electrodes were printed and electrochemically characterized. Spherical 3D-printed microelectrodes detected dopamine in a brain slice and in vivo, demonstrating they are robust enough for tissue implantation. While TPL presents itself as a highly adaptable and promising method for creating intricate 3D structures, it has not yet reached a stage of commercial scalability due to several limitations: (1) slow processing speed, (2) absence of commercial Two-Photon Polymerization Resins (TPPRs), (3) limited processing volume, (4) constrained dynamic range resulting from a higher writing threshold, and (5) a low two-photon absorption cross-section of TPPR [102].

2.3.2.2.   *Digital Light Processing*

The digital light processing technique (DLP) works on a similar principle as SLA but employs a digital micro-mirror device (DMD) instead of a moving laser, therefore

avoiding the restriction of curing a single spot at a time. It is a bottom-up process that begins with the build platform placed one layer thickness above the vat floor (***Figure 2.6***).
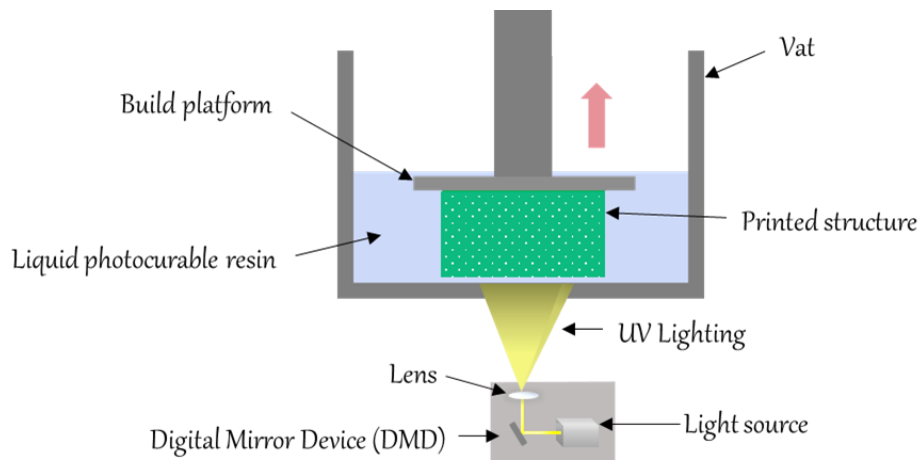
Figure 2.6. Illustrative diagram of the Digital Light Processing performance.
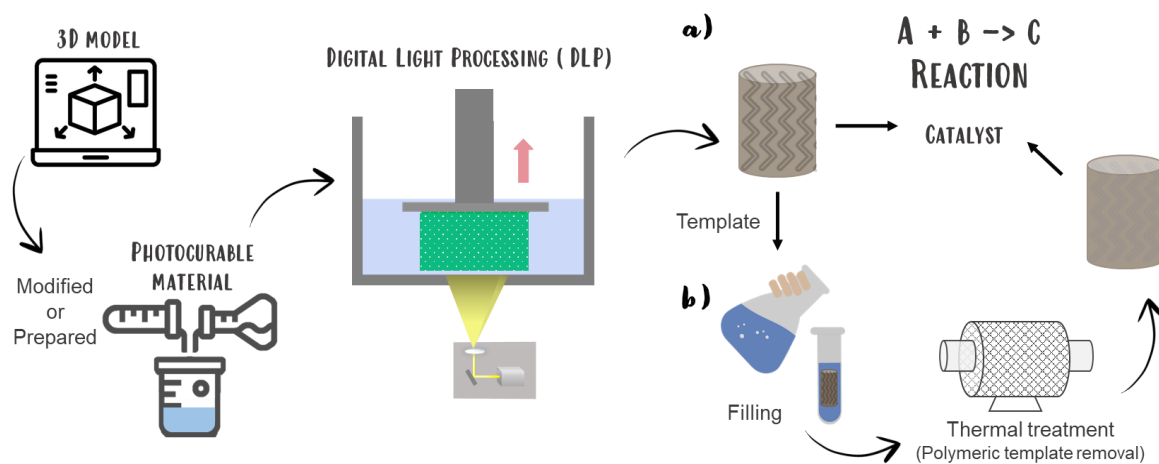
Figure 2.7. Approaches employed for manufacturing monolithic catalyst using DLP: a) straightly printing with commercial, commercial resin modified or a prepared one; and b) using the printed structure as a template.

By means of the DMD set beneath the tank, a 2D image is projected into the build platform, curing the whole coat at once within a few seconds; it is even possible to simultaneously print more than one monolith, thus reducing the printing time while improving the precision [85, 103, 104]. The method continues by tilting the vat to

separate the cured resin from the vat floor and then raising the platform one layer depth to print the next layer, and so on until the object is finished. Besides, DLP allows controlling the light intensity distribution within the 2D image to attain heterogeneous cross-linking density along the layer [73]. Due to its advantages, DLP has been used for manufacturing polymers and ceramics monolithic structures [105], and some of these works are mentioned below according to the strategy used, direct manufacturing or template production (see *Figure 2.7*).

For direct manufacturing of monoliths by DLP, most researchers have developed their own resin from zero or doped a commercial one. In this sense, among the works realized using DLP to directly produce monoliths, that of Zhakeyev *et al.* [51] can be mentioned. They integrated a 2,1,3-benzothiadiazole-based photosensitizer (St-BTZ) with a commercial resin to produce photocatalytic monoliths for furoic acid degradation. The DLP printer projected each pattern at 385 nm to cure the resin, which was later washed with isopropanol and post-cured under UV light for 1 hour. The St-BTZ was selected due to its compatibility with acrylates; moreover, it also absorbs at 385 nm, which helps to reduce over-irradiation and improve printing resolution. The optimal St-BTZ loading, 0.19 wt%, allowed the obtention of monoliths of different shapes without defects, and a uniform emission was observed when they were irradiated with a UV lamp, as presented in *Figure 2.8*.
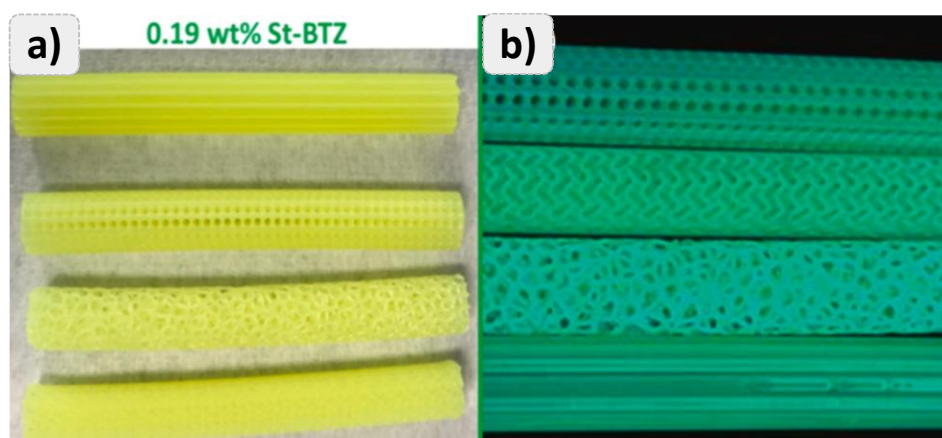
Figure 2.8. Directly DLP printed monoliths: a) cured photo-active monoliths with 0.19 wt% of St-BTZ; and b) image of the blue radiance observed owing to the St-BTZ monomers by lighting the monoliths with long-wave UV irradiation. Taken from [51].

Notwithstanding, the elaboration of light curing resins involves several factors to be considered, such as those previously mentioned in the SLA section: rapid solidification with light-induced polymerization and low viscosity to facilitate immersion and recoating. Furthermore, when adding the catalytic compounds, sedimentation should be avoided, and an appropriate solid loading must be ensured since it influences the physical properties of the resin. Too low solid content may lead to loose slurries, as well as cracking problems due to failed sintering. In contrast, too high solid content may result in viscous and heavy mixtures, long curing time or deficient curing [103]. For example, Cu_2O microparticles (0.05 – 0.5 wt%) were dispersed by Xie *et al.* [63] in a previously prepared mixture of ionic surfactant Teric G9A6, isopropanol and a commercially available photocurable resin. The resin mixture composition was established, looking for a stable formulation without perceptible phase separation for up to 24 hours at room temperature, which allows its use in DLP printing. This modified resin was employed to print heterogeneous Cu_2O catalytic monolith with meshed geometry to use it in the degradation of ofloxacin by sulfate radical-based advanced oxidation processes. After printing, the monolith was calcined at 200 °C for 2 h under N_2 atmosphere, showing structural integrity without shape changes or cracking. According to SEM images, the active phase was homogeneously distributed along the structure, and the particle size remained unchanged. Besides, XRD and XPS analyses corroborated that the main component of the monoliths was Cu_2O. Gyak *et al.* [106] generated their own resin to produce catalysts for ammonia cracking. To obtain the resin, they mixed pre-modified polyvinylsilazane (PVSZ), MEK-EC-2130Y solution containing silica nanoparticles, photoinitiators, and a UV absorber. The amount of silica nanoparticles was optimized to achieve a balance between the increase of ceramic yield and viscosity of the resin to get an acceptable resolution of the printing. Projected patterns of UV light (405 nm) were used to cure each layer within 11 seconds of UV exposure. Once the catalyst was printed, it was washed with isopropyl alcohol, followed by a post-curing with UV light, a heat treatment under argon atmosphere (up to 1000 °C), and finally, a wash coating with Ru. Catalysts exhibited high thermal stability (up to 1000 °C) and mechanical strength (78 GPa) after pyrolysis and chemical

stability after the reaction in corrosive conditions using a 2 mL min^{-1} flow. Likewise, Zhaojing *et al.* [103] prepared a resin to produce electrocatalysts for hydrogen evolution reaction. They formulated the resin with a mixture of acrylate monomers (TMPTA, TPGDA, and PUA), NiO powders (up to 56.4 wt%), TiC or Co or Fe_2O_3 powders (4.4-5.6 wt%), and additives such as stabilizer (YSZ), dispersant (BYK-111), and BYK-410 and KH-570 to reduce the viscosity and increase light curing efficiency. The slurry also required microwave ultrasound for 1 h and vacuum defoaming to get low viscosity, stability, and good dispersion properties. The authors found that a resin with about 55 wt% solid loading presented the most proper characteristics for printing with a UV wavelength of 405 nm. They printed four samples at a time, and after printing, the structures were ultrasonically cleaned with ethanol to remove residues, followed by degreasing in a muffle to remove organics, a heating treatment in a tubular furnace, and finally reduced in H_2 5 %/Ar atmosphere, observing a 15 % volume shrinkage. The process led to a surface with a gluten-like cubic structure and metals added in an amorphous state. This method generates a close connection between the catalyst and substrate, improving the electron transfer and stability during electrolysis without significant morphological or composition changes.

On the other hand, the DLP-printed templates reported so far have been filled with ceramic precursors (basically α-Al_2O_3), thermally treated, and finally covered and/or loaded with active phases (as shown in ***Annex 2***). For instance, Bogdan *et al.* [107] printed templates using DLP for obtaining conventional honeycomb monoliths with different cell densities (***Figure 2.9a***). The templates were filled with a mixture of α-Al_2O_3, Mn_2O_3, water, and sodium silicate solution; then, they were dried and calcined at 850 °C for 8 hours in air flow. The catalysts were nonporous materials, and SEM-EDS analysis (shown in ***Figure 2.9b***) corroborated the homogenous distribution of Mn, Si, and Na on alumina particles. Mn_2O_3 partially transformed into Mn_3O_4 during thermal treatment as was confirmed in XRD patterns. Some of the authors [108] followed the same procedure using a double impregnation (***Figure 2.10a***), firstly with an aqueous solution of Na_2WO_4 and then with $Mn(NO_3)_2$, realizing a drying and calcination process

after each impregnation. The elemental mapping showed a better distribution of W compared to that of Mn. The catalysts exhibited CH_4 conversion that varies between 20-30 %, and the channel size resulted in an impact on the performance of the catalyst, mainly in the products distribution for which the smaller channels led to greater selectivity, especially CO_2/CO (see **Figure 2.10b**).

Figure 2.9. Ceramic monolithic catalyst obtained by means of DLP printed templates: a) scheme of production; b) EDS images showing the homogeneous elemental distribution within the monolith channel. Adapted from [107].
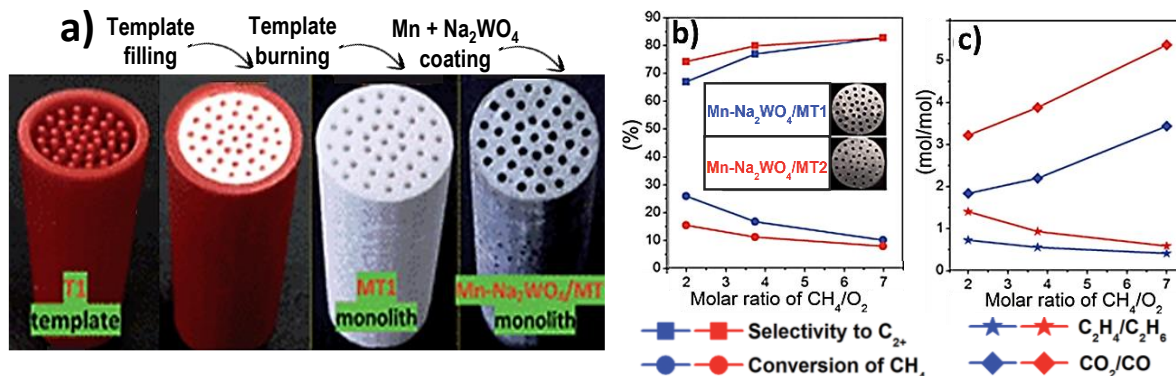
Figure 2.10. Double impregnated ceramic monolithic catalyst manufactured using DLP printed templates: a) scheme of production; b) conversion and selectivity obtained in the oxidative coupling of methane (OCM) process catalyzed with both monoliths (GHSV = 4400 cm^3 g_{cat}^{-1} h^{-1}). Adapted from [108].

Hędrzak *et al.* [109] used B9R-4-Yellow resin to obtain a mold for conventional honeycomb monolith synthesis. The template was filled with a paste of α-Al_2O_3 and

sodium silicate, subsequently dried, and calcined at 850 °C for 4 hours. After the template was removed by calcination, a layer of zeolite type MFI was deposited on monoliths by a one-pot hydrothermal process to increase the porosity of the materials (up to 73 m^2 g^{-1}), followed by an ion exchange with ammonium nitrate solutions at room temperature. SEM images showed that zeolite crystals grew randomly on the surface without any preferred orientation, and the presence of alumina in the zeolitic layer observed by EDS suggests that some alumina from the monolith could be dissolved due to hydrothermal conditions taking part in the zeolite synthesis. Alumina also controlled the acidity since acid sites were reduced with the increase in Si/Al. The catalytic performance of those monoliths was tested in the gas phase isomerization of α-pinene, obtaining the highest conversion in the monolith with the highest amount of Al (95 %). However, conversion and selectivity over all materials decreased gradually with the time on stream, which is attributed to the deposition of conjugated by-products.

A similar procedure was followed by Rokicińska *et al.* [110], who prepared a ceramic monolith covered with MFI zeolite modified with cobalt to use it in the combustion of toluene. A conventional honeycomb monolith template, made of B9R-4-Yellow resin, was filled with α-Al_2O_3 powder and sodium silicate. After removing the template by calcination, the structure was covered with MFI zeolite by means of a hydrothermal treatment to provide a higher surface area (~64 vs 0.1 m^2 g^{-1}) and ion exchange capacity. Later, some monoliths were also ion-exchanged in an ammonium nitrate solution, and, finally, both monoliths were modified with a Co-containing active phase by ion exchange or impregnation. SEM analysis corroborated that alumina particles and sodium silicate were linked and that all elements were homogenously dispersed (***Figure 2.11a-c***). The grown MFI zeolite crystals did not exhibit any specific orientation, forming a coat of 40-50 µm thickness, as presented in ***Figure 2.11d-e***. The ion-exchange method resulted in a lower Co load but a higher dispersion since Co species occupy mainly extra-framework sites in the zeolite. The monoliths showed excellent catalytic performance (~68 % conversion and ~99 % selectivity to CO_2) and stability (up to 2000 min) in the combustion of toluene.
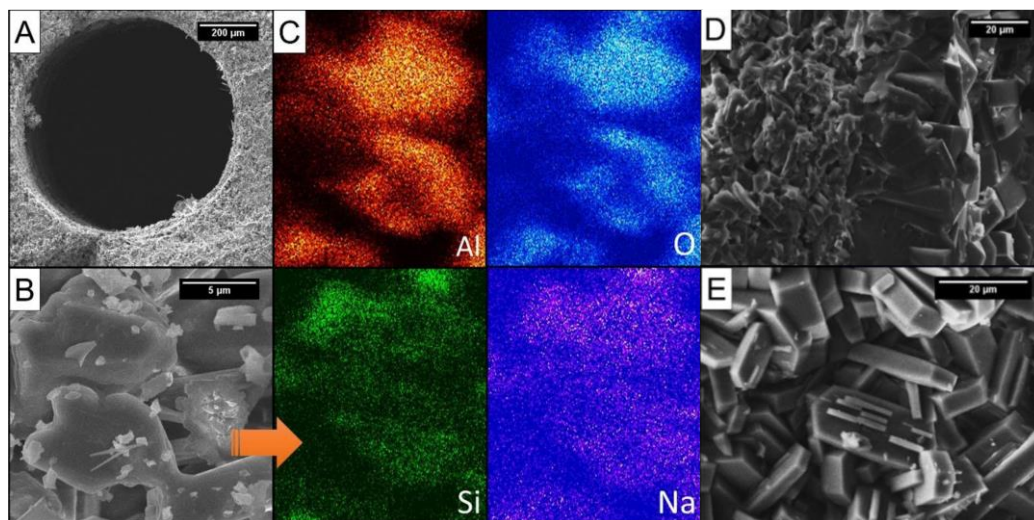
Figure 2.11. Alumina-based catalyst coated with cobalt-modified MFI zeolite for toluene combustion: a-c) SEM micrographs and elemental mapping of the ceramic monolith; and d-e) cross-section and top view of the MFI zeolite layer covering the monolith. Taken from [110].

Volumetric 3D printing and continuous liquid interface production (CLIP) are other vat photopolymerization techniques. Although they offer advantages such as higher resolution and speed printing, they have not yet been employed in the production of monolithic catalysts since SLA and DLP are much simpler and easier to use, giving good enough prints.

On the other hand, compared to commonly used methods for preparing polymer monoliths (for instance, polymerization and induced phase separation processes [111, 112]), vat photopolymerization techniques present different advantages. While traditional methods may control the porosity characteristics of the materials prepared, the structural configuration and design cannot be controlled [113-115]. Conversely, SLA and DLP methods are characterized by versatility and high resolution, leading to a wide possibility of shapes and configurations. The use of polymers, in general, is associated with a restricted maximum operation temperature. Therefore, polymer monoliths prepared so far have been employed principally in separation processes [112, 116, 117], and barely in low temperature reactions [118-120] and photocatalytic

processes [121, 122]. Consequently, when using VPP, some alternatives have been proposed for increasing structure stability, including thermal treatments of printed objects, doping commercial resins or formulation of new ones, and the production of templates filled with different materials (mostly ceramics). Thermal treatments have been shown to slightly increase the stability and allow it to work up to 250 °C, while dopant addition and template fillers enable superior temperatures (up to 850 °C depending on material composition), far surpassing conventional materials. Per contra, the preparation and use of own resins may result challenging since it implies: i) the requirement of different techniques to ensure well mixing and dispersion of solid compounds, ii) the necessity of adjusting the consistency of the samples, also avoiding sedimentation [103], and iii) application of post-treatments that may include washing and debinding to remove residues and organic compounds, post-curing, and heat treatments to stabilize the materials. At the same time, the active phase loading has been approached with different methodologies: thermally or chemically attacking the structure surface either before, during, or after wash coating, adding the catalytic compound within the resin prior to AM, and using advanced designs that produce more anchoring cavities. The first two approaches increase the loading but let it embed within the structure and no accessible for the reagents. Thus, the use of complex designs seems to be the best option for catalyst deposition. Moreover, the use of templates seems to be more useful for achieving high resolution of complex structures of a specific non-photocurable material.

2.3.3. Powder Bed Fusion

Powder bed fusion (PBF) processes continue with the principle of the additive manufacturing techniques, layer-by-layer production based on a 3D CAD. In powder bed fusion, the raw material (such as metals, polymers, and ceramics) is in the form of powder, and a heat source (laser or electron beam) is used to consolidate the material. A rolling pin disposes a powder bed onto the build platform with a certain thickness (see ***Figure 2.12***). Then, the heat source is applied to the cross-section of the powder bed according to the CAD. The build platform moves down as the layer is finished, and

the roller spreads more powder from a supply chamber to prepare the next layer [123, 124]. This process must be done inside a chamber with an inert atmosphere to avoid the oxidative degradation of the material [125]. Laser sintering (LS), Laser Melting (LM), and Electron Beam Melting (EBM) are some of the widely used PBF processes [126].
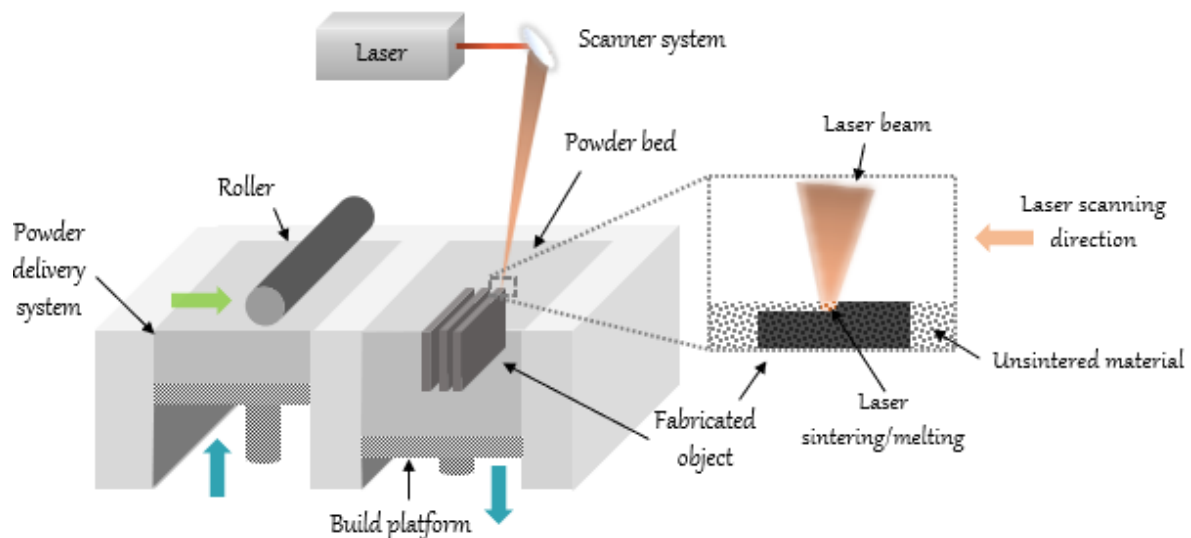
Figure 2.12. General scheme of Powder Bed Fusion printing processes.

2.3.3.1. *Laser Sintering and Laser Melting*

Selective Laser Sintering and Laser Melting are PBF processes based on the sintering technique that uses a high-power carbon dioxide laser as a tool to fabricate patterns. The laser beam selectively scans the powder, which tends to sinter or melt when the energy source is applied [127]. Sintering occurs when particles fuse only on the surface, generating pieces with inherent porosity, while in melting, a liquid state is reached where all the particles fuse completely, resulting in pieces with almost zero porosity. Among its advantages can be mentioned that no support structures are required and the unsintered material can be reused, reducing wastage [128]. Besides their high precision, both techniques allow the use of catalytically active metal materials during printing, making possible the attainment of catalysts with harsh reaction conditions. However, they present some drawbacks: i) internal stress caused by

temperature gradients [129], ii) roughness of the surfaces obtained because of the unsintered/unmolten particles added on the structure depending on the process parameters used [130], iii) the necessity of a post-treatment or coating to enable the attachment of active phases, and iv) requirement of an inert atmosphere to protect metals from oxidation [130-132]. To date, few works have been reported for the LS or LM printing of monolithic supports for catalysis. Notwithstanding, due to the generally metallic nature of raw materials used in PBF processes, the structures obtained may be used directly as catalysts using this metal base as the active phase. Moreover, it also provides them with great heat transfer, thus being advantageous for reactions that are fast and very exothermic or endothermic [133]. This was demonstrated by Fratalocchi *et al.* [134], who improved the Fischer-Tropsch process by enhancing heat transfer with periodic cellular monoliths 3D-printed in AlSi7Mg0.6 by LM. Conversions of around 80 % were achieved due to the management of Fischer-Tropsch exothermicity. This characteristic of PBF methods signifies a valuable advantage over conventional synthesis, which typically involves coating commercial monoliths with metals such as Fe, Ni, Pd, etc. [135-139]. In this sense, Qinhong *et al.* [140] printed metallic monoliths through LS to directly serve as catalysts for the conversion of C1 molecules into high-value-added fuels. Fe, Co, and Ni alloys were used to obtain the monoliths with different channel configurations. In order to enable them as a catalyst, they were activated by calcination (at 873-1073 K for 24-60 h) and reduced in H_2 (40 ml min^{-1} at 673-1073 K for 6-10 h), and in the case of the Co-catalyst, an acid treatment was done prior to the reduction to boost the catalytic centers activation. As a result, Fe and Co catalysts exhibited good performance in Fischer-Tropsch synthesis and CO_2 hydrogenation, while Ni-catalyst proficiently produces syngas by CO_2 reforming of CH_4. The characterization analyses revealed that element distribution and surface chemical states were maintained after de LS process; therefore, we can assert the technique does not affect the chemical surface properties. Moreover, thermal conductivity and temperature tolerance (1000 K) were superior to other reported materials. To analyze the advantage of design freedom, Co-catalysts of several inner geometric configurations were applied in the Fischer-Tropsch synthesis. Results

36

revealed that, although monoliths presented similar CO conversion, their structure increased and influenced the liquid fuel product selectivity, as exhibited in ***Figure 2.13***.
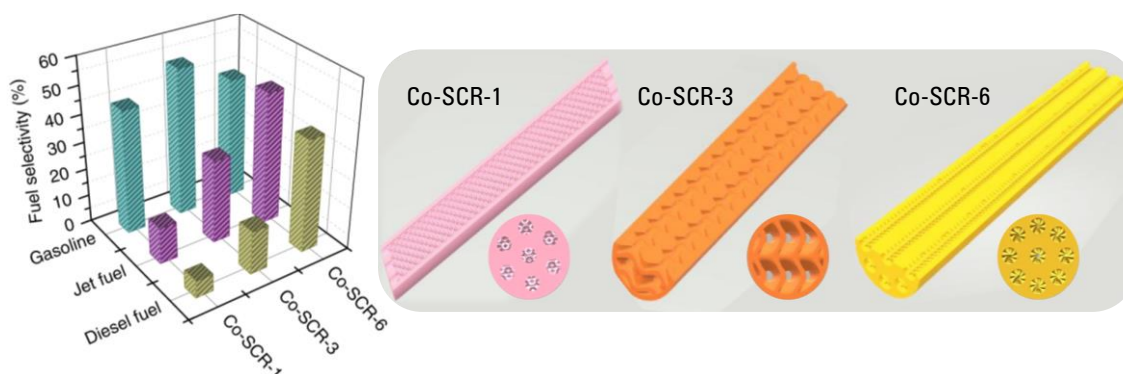
Figure 2.13. Comparison of fuel selectivity obtained from Fischer-Tropsch synthesis using monoliths with three different channel configurations. Adapted from [140].

In the same manner, Komendová *et al*. [141] realized a treatment to enable the application of a 3D printed object. They carried out an oxidation process, at 600 °C in air for 6 h, of a monolithic structure LM-printed from Ti-6Al-4V alloy to form a reactive layer of titanium oxide. Likewise, powder of stainless steel was selectively laser sintered under nitrogen atmosphere by Agueniou *et al.* [131] to fabricate metallic honeycomb monoliths with excellent heat transfer properties. This technique allowed to obtain a wall thickness of about 270 μm and a cell density of 230 cpsi. The monolith underwent a calcination process in N_2, and an aqueous slurry of Ce/Zr nickel and alumina was added with polyvinyl alcohol as a binder to enhance the wash coating of the structure. A last calcination step was performed to finally achieve a load of 0.39 mg cm^{-2} of active phase. The metal structure got a good roughness that allowed an acceptable adherence without any extra surface treatment as also observed by other authors [130] (***Figure 2.14a-b***). XRF and SEM-EDX results showed signals of Ni-Ce-Zr in the same locations, suggesting an adequate interaction between those elements. Also, the catalytic activity of the bare and coated monoliths was evaluated in the methane dry reforming. Monoliths did not show relevant deactivation after long time, and activation time was not necessary because of their great heat transfer. Due to its intrinsic nickel content, the bare monolith exhibited conversions around 40 % and 20

% for CO_2 and CH_4 at 900 °C, respectively, increasing to 95 % and 75 % in the case of the coated one. This fact highlights the opportunity of choosing an appropriate raw material that includes the active phase, thus obviating the need for its later deposition.
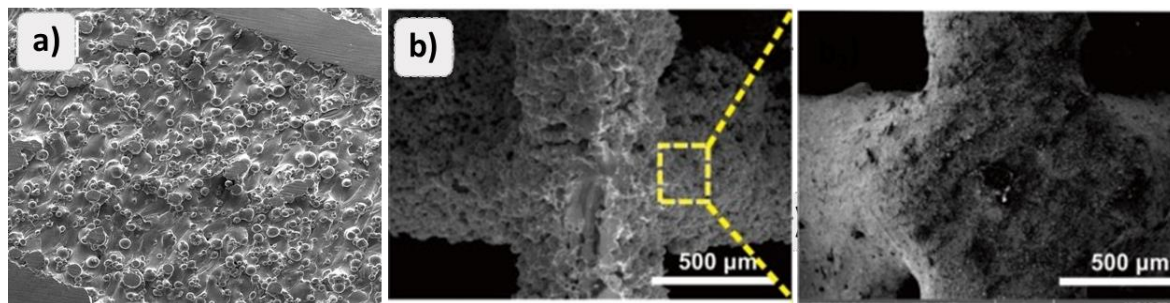
Figure 2.14. SEM images showing the roughness of metallic monoliths printed by PBF techniques. a) stainless-steel piece obtained by LS; b) SEM images of a LM printed copper monolith unpolished and polished. Taken from [130, 131].

In contrast, other authors have pointed out the necessity of carrying out different surface pretreatments to enhance the active phase fixing (*see Annex 3*). For instance, Lind *et al.* [133] 3D-printed an AlSi10Mg support for Pt and used it as a catalyst in NO oxidation. They employed laser sintering to obtain a cubic iso-reticular channeled monolith, which was further electrolytically anodized to high-surface alumina to allow the final Pt deposition. Direct anodization advantage is the chemical attachment of the oxide layer to the metal body; nonetheless, the process was challenging owing to the content of silicon (10 %) of the alloy used and the complexity of the design. The conditions leading to an acceptable alumina layer (3-4 µm) with minimum SiO_2 formation (30 %) were sulfuric acid (15 %), potential (15 V), time (15 min), and equilibrium current density (1.5-3.5 $A\,dm^{-2}$). Deposition of platinum was realized by wet impregnation, further dried, calcined (at 300 °C for 6 h in He atmosphere) and reduced with H_2 (300 °C for 3 h). SEM images revealed that Pt was homogeneously distributed through the surface and the porous layer. During the reaction, the outlet temperature only increased about 1 K thanks to the high heat transfer coefficient of the catalyst. Moreover, the catalyst exhibited around 50 % NO conversion. Lapp *et al.* [142], developed a monolith with non-intersecting straight radial and axial channels to use as

a solar receiver/reactor for the dry reforming of methane. For this, they realized LM process using a high-temperature alloy Inconel 618 as the raw material. This technique allowed them to fabricate a dense material, however, an acid etching procedure was needed to provide roughness to the surface for the catalyst to adhere. In addition, the 3D printed structure demonstrated good thermal properties and stability allowing its use up to 1200 °C. Alternatively, the catalytic phase deposition may be improved by including additives that augment the adhesion of the wash coating slurry. This is the case of the procedure followed by Gonzalez *et al.* [143], who prepared monolithic catalysts for the methanation of CO_2. They configured the channels as an arrangement of fluid guiding elements that subdivide the flow and exchange their positions along the channel (***Figure 2.15a***), returning to its initial position after going through three fluid guiding units (shown in ***Figure 2.15b***). Different monoliths were produced by changing the number and size of the fluid guiding units as a function of the polar radius and orientation angle of the gyroid (***Figure 2.15c***). To obtain the monoliths, the authors used a LM printer with stainless steel powder and realized an annealing post-treatment (900 °C in air for 12 h). Slurries of 15 % Ni and 0.5 % Ru $MgAl_2O_4$-supported were prepared along with deionized water, colloidal alumina, and PVA to adequate their properties for the wash coating. Finally, the catalysts were calcined at 500 °C for 4 h, and the load achieved with this method was around 0.220 g. Further, the improved design was shown to benefit the turbulence, mixing, and heat transfer along the monolith, therefore increasing the conversion up to 75% regarding a conventional honeycomb with parallel channels monolith (see ***Figure 2.15d***).

Contrary to the commonly used wash coating method, Cheng *et al.* [132] proposed a strategy to synthesize three-dimensional graphene (3DG) by LM printing a porous copper structure in which graphene was further in-situ grown through chemical vapor deposition (CVD). The raw material was micron-sized copper powder, mainly of spherical shape, which increases the fluidity and packing density compared to polyhedral ones. For the PBF, a Nd:YAG fiber laser of wavelength of 1060 nm was employed, allowing it to produce 20 µm thick walls under a nitrogen atmosphere.

Moreover, the authors looked for the most effective parameters of laser power and scanning speed to produce a continuous and stable melting to avoid cracks and deficient or excessive sintering (presented in ***Figure 2.16a-d***), observing good results for 350-450 mm/s and 180-200 W.
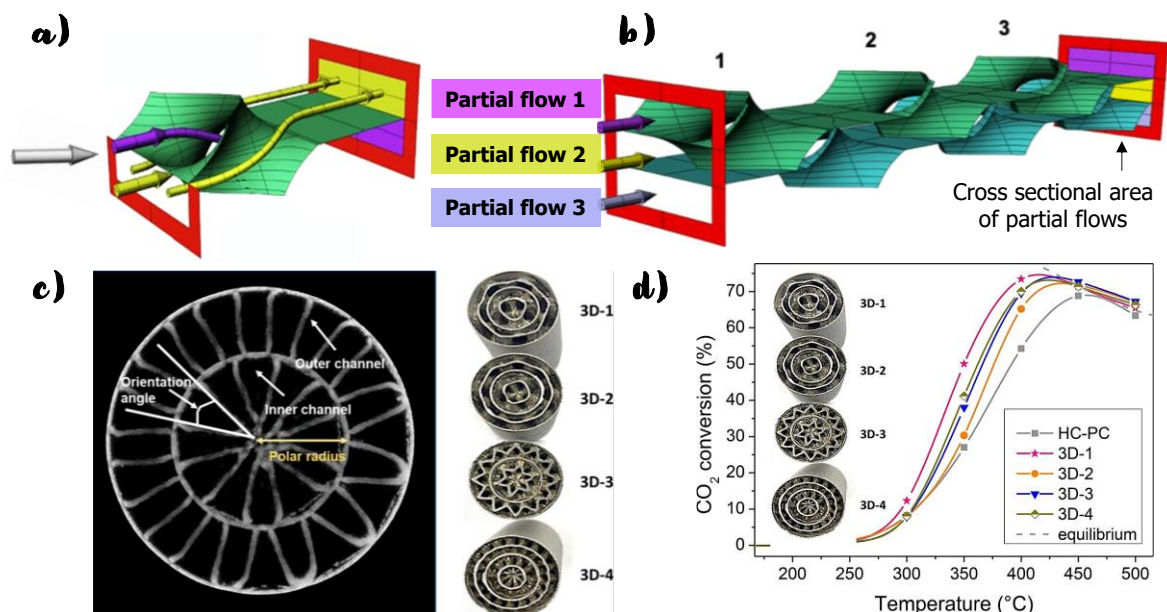
Figure 2.15. 3D printed catalysts for CO_2 methanation based on pseudo-gyroid geometries: a) illustration of a fluid guiding unit (FGU); b) arrangement of FGUs connected in series and parallel giving a different flow pattern; c) printed structures varying the number and size of the constituting channels; and d) Comparison of the CO_2 conversion at 120 L $(g-h)^{-1}$ and a H_2/CO_2 ratio of 4 achieved with 3D printed and honeycomb-parallel channel (HC-PC) monoliths. Adapted from [143].

For the CVD growth of graphene, monoliths were heated to 1000 °C under Ar and H_2 for five minutes, then a 30 cm^3 min^{-1} CH_4 flow was introduced into de reactor at ambient pressure over twenty minutes, and finally, the CH_4 flow was stopped, and the system was rapidly cooled to room temperature. XRD patterns of the printed monoliths kept similar to those of the raw material, with a light shift of the diffraction peaks to higher angles because of enhanced residual stress. Also, SEM images (***Figure 2.17***) showed good bonding of copper powder, EDS, and Raman results

confirmed the successful growth of graphene with even distribution, and the monoliths exhibited electromagnetic interference and thermal conductivity.
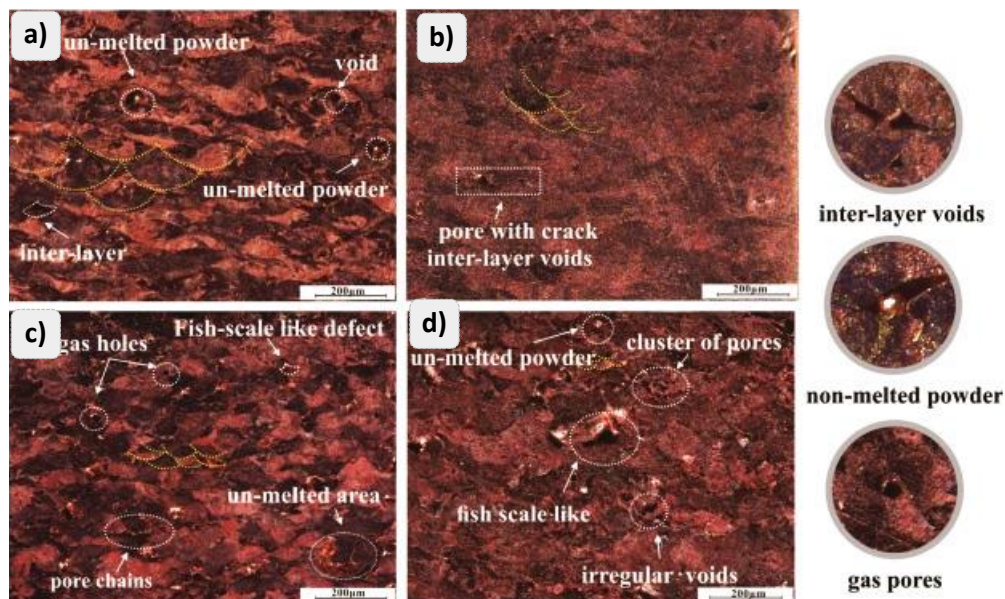
Figure 2.16. Morphology of copper samples fabricated by LM with various input energy, from excessive to low energy: a) 3000 J mm^{-3}; b) 857 J mm^{-3}; c)285 J mm^{-3}; and d) 128 J mm^{-3}. Acquired from [132].
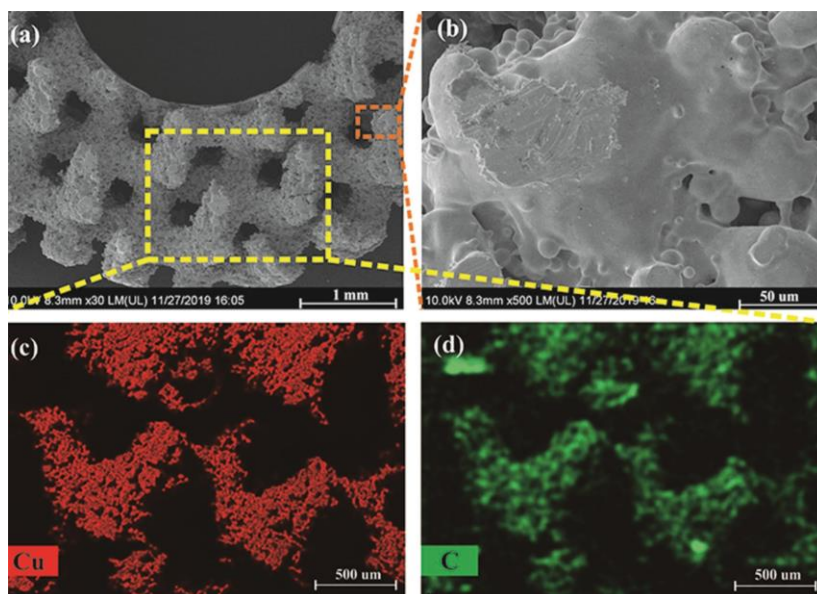
Figure 2.17. a-b) SEM micrographs of the 3DG/Cu structure; and c-d) EDS analysis of Cu and C, correspondingly. Taken from [132].

The authors followed a similar methodology to produce copper monoliths coated with a grown in-situ diamond film [130]. Before the CVD, some samples were polished by abrasive flow with a loading of 90 kg for 12 min to analyze the effect of surface roughness on the coating film. Diamond growth was performed under CH_4 and H_2 at 2000 °C for five hours. Results showed that the surface roughness benefits the diamond nucleation. Raman and SEM analysis confirmed the high density of diamond on unpolished samples. Moreover, excellent thermal conductivity was achieved in all materials, and a maximum compressive strength of 78 MPa was obtained.

2.3.3.2. *Electron Beam Melting*

Another PBF technique is the Electron Beam Melting (EBM) process, which follows the same steps that LS and LM, with the difference that it employs an electron beam at sufficient speed to work as a large area heat source to melt the powder material (***Figure 2.18***). It is considered more energy efficient since the electron beam has higher plug efficacy than the laser beam system [144].
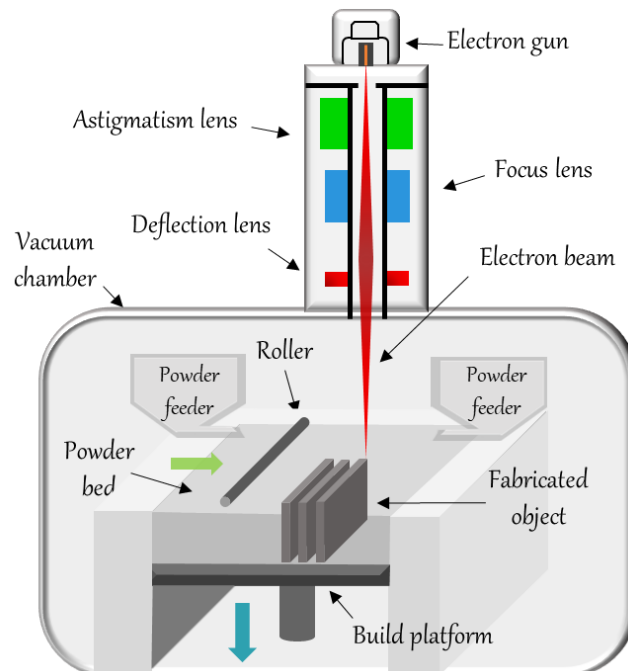
Figure 2.18. Illustration of Electron Beam Melting (EBM) system.

Nevertheless, EBM has some disadvantages, such as the need to operate in a vacuum to prevent air-electron interaction, the powder should be electrically conductive, leading to fewer material options in comparison to LS and LM, and the coarse powder needs to be pre-sintered [123, 145]. These factors lead to rougher surfaces and generally larger minimum feature sizes compared to laser processing. Besides, it is important to mention that the necessity of removing the non-melted powder may limit the monolithic geometric design and cell density, making it disadvantageous regarding other AM techniques. [146]

EBM technique has scarcely been used to prepare monolithic catalysts, probably due to its higher requirements. Among the works published in the literature (**Annex 3**), mainly focused on hydrogenation reactions, that realized by Peters *et al.* [146] may be cited. Peters *et al.* [146] prepared a Pt on alumina-coated catalyst through EBM for the dehydrogenation of perhydro-N-ethylcarbazole. The electron beam melting process was applied to a gas atomized Ti-6Al-4V alloy powder under He atmosphere and 2×10^{-3} mbar. Once printed, the excess metal powder adhered to the exterior surface of the structure was removed by "sand" blasting with the same metal powder. For coating, a solution prepared with commercial boehmite powder, dispersal, nitric acid, and a commercial active phase containing Pt was used to immerse the monolith, which was further calcined in air at 500 °C for 6 h, reaching a 3.5 g loading. Tests showed a hydrogen release capacity of 1.75 kW with up to 1.12 g_{H2} min^{-1} g_{Pt}^{-1}, as well as good reproducibility and stability at least for 48 hours.

In the same manner that in LS and LM techniques, structures obtained through EBM should undergo pretreatments to prepare their surfaces for active phase deposition. Such is the case of studies realized by Nguyen *et al.* [147, 148], who have produced different catalysts for continuous flow hydrogenation processes. Firstly, structures were printed by electron beam melting of pre-sintered 316 L stainless steel at 850 °C, and later loaded with Ni or Pd by cold spraying or electroplating, correspondingly. In this case, before the electrodeposition, materials were cleaned and activated to ensure even adhered layers of metallic palladium (done by standard

galvanostatic procedures). On the other side, nickel powder was sprayed onto the 3D printed monoliths through a plasma Giken PCS-1000 cold spray system, providing a high and uniform surface coverage on the accessible surfaces of the structures. Catalysts exhibited an optimum operating temperature of around 120 °C (12 - 20 bar) at which excellent catalytic activity for the reduction of vinyl acetate to ethyl acetate was displayed. In general, produced catalysts were efficient and versatile since they also showed good performance in other reactions, such as the reduction of alkenes, alkynes, carbonyls, nitriles, and imines.

Kundra *et al.* [55] 3D printed catalysts from nickel alloys and treated them either with chemical etching or leaching processes to activate their surfaces and use them in the hydrogenation of alkanes, aldehydes, and nitro-groups. Inconel and Monel were used as the raw materials (pre-sintered at 1050 and 600 °C, respectively), and after the electron beam melting, they were subjected to etching with Marble's reagent (***Figure 2.19 a-c***) and leaching in ammonium sulphate (***Figure 2.19d-f***), respectively, to rise the porosity and partially oxidate Ni and other metals within the alloy. After further treatment to reduce the oxides obtained, those monoliths were suitable for hydrogenation reactions. As expected, the longer the chemical etching, the higher the surface change, which kept the metal ratios the same but increased the oxygen amount due to the oxides formed. On the contrary, the Monel-catalyst resulted in a surface layer richer in nickel (Ni/Cu ratio between 4-8) after the leaching process that selectively removed copper, thus in a higher catalytic activity and selectivity towards unsubstituted double bonds.

Using a similar methodology to that followed by Cheng *et al.* [132] in LM, Knorr *et al.* [149] combined EBM of Ti-6Al-4V with chemical vapor deposition and carbide-derived carbon approach to obtain a metallic catalyst covered with microporous carbon, which was further impregnated with platinum, for the hydrogenation of ethene. Nevertheless, prior to SiC deposition, an oxidation process (550 °C in air for up to 2 h) was needed to favor the coating. Chemical vapor deposition of SiC was carried out at 950 °C with methyltrihlorosilane as a precursor, leading to a surface area of 32 m^2 g^{-1}.

Later, the structures with the carbide layer were chlorinated to obtain a carbide-derive carbon layer (800 °C for 10 – 30 min), and finally, wet impregnated with a hexachloroplatinum solution to get the 1.83 wt% Pt loaded in the Pt/EBM catalyst. High thermal and electrical conductivity were observed inherent to the material nature, as well as the high surface area of the carbon coating. Comparing the catalytic activity of the synthesized material with that of a commercial one, the Pt/EBM catalyst presented about 50 % more conversion attributed to the different diffusion lengths, and to the dispersion and accessibility of platinum.
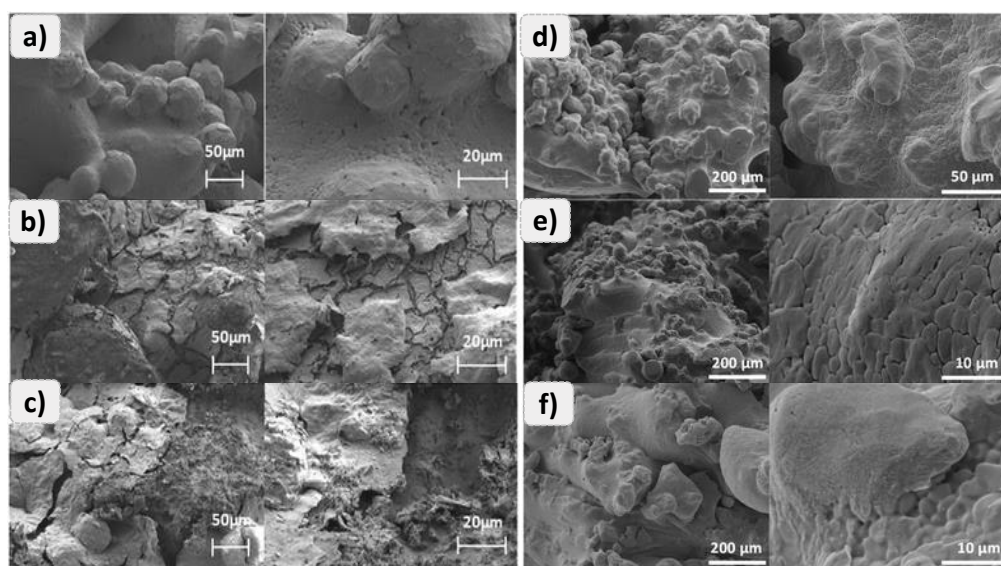
Figure 2.19. SEM micrographs of nickel alloys catalysts chemically treated: a) untreated Inconel sample; Inconel samples etched with Marble's reagent for b) 2 h, and c) 48 h; d) untreated Monel sample; Monel sample treated with e) 0.2 M ammonium persulfate, and f) 1 M ammonium sulfate. Adapted from [55].

As shown in the cited studies, PBF techniques allow the direct attainment of metallic structures, which, due to their nature, exhibit great thermal characteristics and stability, and it is possible to conform them in more complex shapes than those limited by conventional production methods. The principal raw materials used so far are stainless steel and Al, Ni, or Ti alloys. In some cases, it is also feasible to activate the metals after printing and apply them directly in catalytic processes. However, when the

loading of an active phase is required, the incorporation procedure is often arduous, implying in most cases more than one step; therefore, a cost-benefit analysis may be useful to establish its convenience. On the other side, traditional production of metal-based monoliths may include corrugating metal foils, extrusion, or pressing under high pressure, which limit the configuration and shape of channels, often with a reduced porosity [150, 151]; Likewise, other strategies, such as sol-gel process, foaming, and coating over pre-synthesized templates may offer the opportunity to adjust porosity but lack control over the structural configuration [152-156]. Conversely, PBF methods have shown their versatility to generate a wide range of designs that enhance their catalytic activity and selectivity [132, 140, 143].

2.3.4. Material Extrusion

One of the most popular additive manufacturing processes is the material extrusion technique, which presents advantages like low material wastage, simple operation, and cost-effectiveness [157, 158]. These extrusion-based technologies are suitable for employing viscoplastic materials such as ceramic pastes, hydrogels, and thermoplastics, as well as composites as raw materials [159]. The printing filaments or semiliquid materials are fed through a nozzle (when using filaments, the nozzle must be pre-heated in order to melt them), and then selectively dispensed onto a support layer upon layer. These materials are commonly used owing to their low melting temperature and melt viscosity that allow its uniform extrusion [160]. Once the extruded material cools, it solidifies again, resulting in the final print.

2.3.4.1.   *Direct Ink Writing*

Direct ink writing (DIW), also known as direct-write fabrication, robocasting, or robot-assisted shape deposition, consists of extruding a paste — known as "ink" — through a fine nozzle that moves in the X-Y direction in a controlled manner to generate patterns for each slice of a CAD model (see *Figure 2.20*). As the object is built in a layer-by-layer manner, the extruded paste impinges on the previously deposited part and fuses with it due to surface tension. This is a versatile technique that allows to

work with a broad range of materials, such as ceramics, polymers, metals, alloys, and composites. Nevertheless, there are some aspects that must be taken into consideration, such as the conditions and characteristics of the ink and the conditions of the printing and drying procedures. Principally, the rheological properties of the ink are critical as it needs good fluidity to obtain a smooth and constant extrusion and avoid ink clogging, for which it must lower its viscosity under the pressure applied during extrusion. However, it must also recover its viscosity after the deposition to have enough consistency to conserve the shape prevent structural deformation and the printed structure collapse [72, 161].
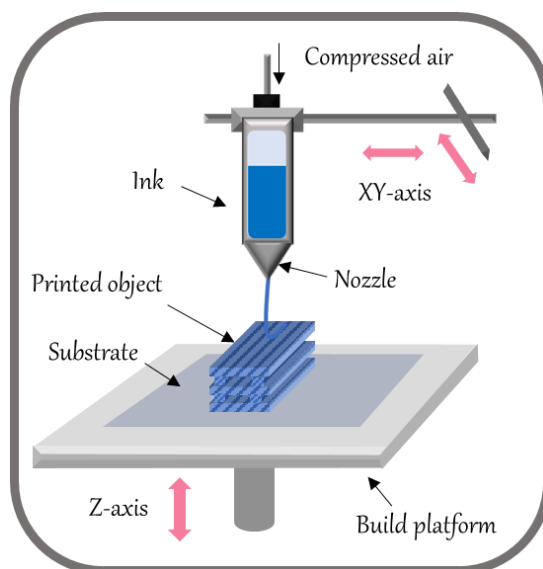
Figure 2.20. Schematic illustration of Direct Ink Writing process.

The rheological control of the slurry can be achieved by choosing the appropriate binder-material ratio and additives but also using external stimuli (such as pH, temperature, and magnetic fields) [162]. In this sense, additives not only function to obtain the appropriate rheological properties of the slurry but can also provide useful characteristics to the final printed object. Contrarily, the binder has been associated with a porosity blockage; therefore, when binders are added to the printing paste, there is commonly a calcination step to remove them [59, 61, 163-165]. The 3D structures are obtained by the disposal of the printing paste through a nozzle by air pressure or

mechanical devices, in a layer-by-layer mode, while moving according to a CAD by a robotic arm. The restrictions for the minimum possible print size, and thus cell density, depend not only on the nozzle diameter but on the rheology and ink particle size to avoid nozzle obstruction —this must be at least an order of magnitude smaller than the nozzle diameter to avoid its blockage— [161, 166, 167]. Once the printing has finished, the structure must be carefully dried to avoid shrinkages, breakages, or deformations. The drying technique, along with the printing speed, diameter of the nozzle, and viscosity of the ink, are the principal parameters that have an impact on the final properties and surface finish [162, 168]. It is important to consider that after the drying process, there is usually a shrinkage that change the desired dimension of the 3D object.

To date, this technique is the most extensively used AM technology to directly print monolithic catalysts due to the wide range of possible raw materials, some of them are listed in **Annex 4**. Among the large list of materials, ceramics have been largely used for the DIW. Such is the case of the work realized by Hossain *et al.* [169], who prepared an amorphous silica monolith by depositing an ink paste made of template-impregnated silica particles, ether solvent, and dispersant. To increase the dispersion degree, the mixture was milled at 2000 rpm, and further centrifuged also at 2000 rpm to drive out the trapped air bubbles. Silica particles adsorbed a considerable amount of water owing to their hygroscopicity; therefore, the optimal solid loading was ~27 wt%. Printed monoliths were calcined (500 °C for 2 h) and partially sintered (600 °C for 2 h), leading to the formation of micro and mesopores and a S_{BET} up to 981 m^2 g^{-1} due to the elimination of solvent and template, as well as a volume shrinkage of 22.6 %. The materials compressive strength was about 0.48 MPa.

Other broadly used materials are zeolites, which have been applied not only as a coating [170], but, unlike conventional methods, they have also been employed to conform the structure alone or doped with metal oxides. For instance, Li *et al.* [171] 3D printed HZSM-5 monoliths. The authors also studied the incorporation of SAPO-34 to control their porosity and the density of acid sites and tested them as catalysts for the

conversion of methanol to dimethyl ether. The conventionally shaped 3D-HZSM-5 monoliths were obtained by directly writing an ink prepared with HZSM-5 powder, bentonite clay powder, methylcellulose, and water on a Teflon substrate, which were further dried and calcined. The SAPO-34 was grown via a secondary growth method by immersing the HZSM-5 monoliths in a water suspension of SAPO-34 and then treating them hydrothermally. The characterization results showed the agglomeration of HZSM-5 caused by the use of binder and the calcination step. The conformation into the monolithic structure promoted a diminution in total surface area regarding powder form due to the addition of less porous binder and pore clogging with the SAPO-34 crystals grown on the HZSM-5. Moreover, whereas the use of binder during the production of the HZSM-5 monolith also affected the accessibility to acid sites, the SAPO-34 growth raised about 40 % of the strong acid sites. As a result of the reduction of acid sites and the pore clogging, a lower methanol conversion over the monoliths was observed; however, the monolithic configuration helps to increase the selectivity towards dimethyl ether. Authors also employed a similar method to incorporate SAPO-34 crystals but changed the zeolite monolith composition and used it as a catalyst for n-hexane cracking reaction [172]. To synthesize the conventional honeycomb like zeolite monoliths, HZSM-5 and HY zeolites were used together with the above-mentioned additives to prepare inks for DIW. Then, monoliths went through the same secondary growth procedure. Since the pores of HY are bigger and more accessible to the SAPO-34 solution than those of the ZSM-5, a higher growth of SAPO-34 crystals and a decrease of porosity for pore blockage were observed. The XRD analysis showed both the peaks corresponding to the zeolites ZSM-5 and HY, and the peaks attributed to the CHA framework of SAPO-34. In both cases, the coated monoliths exhibited greater amounts of strong acid sites. Although the monolithic configuration increased the selectivity to light olefins because of a better diffusion of intermediate products, the acidity enrichment boosts the aromatization to benzene, toluene, and xylene (BTX) and diminishes light olefins. Additionally, Li *et al.* [61, 165] synthesized bare and metal-doped zeolite monoliths for methanol transformation. The authors prepared pastes with ZSM-5 powder, deionized water, bentonite binder,

methylcellulose as a plasticizer, and, in the case of the doped monoliths, metals (Ce, Cr, Cu, Ga, La, Mg, Y or Zn) in its nitrate form. Conventional honeycomb monoliths were printed on an alumina substrate, dried, and finally calcined to remove the plasticizer, enhance the mechanical strength, and immobilize the metal atoms. The structure and crystallinity of the zeolite were kept; nevertheless, its surface area was reduced, mainly due to the addition of binder. It was observed some mesopore formation in bare ZSM-5 monolith which was attributed to the decomposition of methylcellulose during calcination, therefore existing a wide size distribution and shapes. However, mesopores clogging with the metal dopants was also detected. By element mapping, the homogeneous distribution of metal oxide nanoparticles was confirmed. A better performance of the 3D printed monolith catalyst in methanol conversion regarding its ZSM-5 powder counterpart was correlated to its structure, in which the coke species were less generated. Moreover, the Cr, Mg, and Y doping led to higher improvement of methanol conversion, being the catalyst doped with 10 wt% Mg the best catalyst (methanol conversion ~95 %, selectivity to ethylene and propylene of 24 % and 33 %, correspondingly).

Metal oxide/ZSM-5 or H-ZSM-5 catalysts have been elaborated by several authors following a similar strategy. Lawson *et al.* [173-176] synthesized this type of catalyst through DIW as an alternative to incipient impregnation for the dehydrogenation of propane, n-hexane cracking, and methanol conversion. ZSM-5 and H-ZSM-5 were selected as catalyst supports owing to their high surface area, pore volume, and acid site density, whilst Ga_2O_3, V_2O_5, ZrO_2, and Cr_2O_3 were chosen as dopants because of their oxidation states and redox properties. For this purpose, the authors prepared several ink pastes, including the zeolite ZSM-5/H-ZSM-5 (up to 85 wt%), different amounts and combinations of metal oxides (3.8-30 wt%), bentonite clay as binder, methylcellulose like plasticizer, and distilled water as solvent. After printing, the structures were left to dry at 25 °C and calcined either at 550 or 750 °C for 6 h. XRF spectra demonstrated the control of the loading amounts and good dispersion of the metal oxides. Likewise, XRD spectra exhibited that the crystalline structure of

zeolite was not affected by the procedure followed; however, concentrations of V_2O_5 over 2 wt% may cause the dealumination of zeolite. The N_2 physisorption results showed a greater loss in textural properties for vanadium and mixed oxides, which has been attributed to a ZSM-5 dealumination during calcination by high concentrations of V_2O_5. Catalysts probed to have excellent activity in the different reactions: the mixed metal oxides monolith produced ~40 % propane conversion, ~50 % CO_2 conversion, and 91 % propylene selectivity; Cr-doped catalyst led to 85 % n-hexane conversion with high selectivity to olefins and no BTX production; and Ga_2O_3 doped catalyst produced great methanol conversion with dimethyl ether selectivity while the other oxides were more selective to aromatic carbon. The same methodology was followed using $CaCO_3$ combined with V_2O_5, NiO, TiO_2, or Ga_2O_3, to obtain about 10 wt% metal-CaO doped H-ZSM-5 [177]. As previously seen with vanadium, results also suggested a possible interaction between titania and the zeolite, but it exhibited a better dispersion of the metal oxide phase. However, the crystalline structure of H-ZSM-5 was retained to some degree in all samples, as well as the metal dopants. Those materials, particularly the V-CaO/ZSM-5 presented excellent performance in combined CO_2 capture/oxidative dehydrogenation of ethane (ODHE) conversion (65.2 % CO_2 conversion, 36.5 % C_2H_6 conversion, with 98 % C_2H_4 selectivity). In the same manner, Farsad *et al.* [178] prepared 3D printed mixed metal oxides-HZSM-5 monolithic catalysts for the oxidative dehydrogenation of propane (ODHP). To do this, they also mixed HZSM-5, bentonite, methylcellulose, water, and different amounts of the metal oxides Ga_2O_3, V_2O_5, and ZrO_2 for obtaining extrudable pastes, which were employed in the printing of cylindrical monoliths with woodpile shaped layers. In the case of the paste containing V and Zr oxides, the viscosity was low during printing; thus, the monolith had some imperfections. According to XRD analysis, interactions between Si-OH group and oxides during calcination led to structural changes in the zeolite. Propane conversion was in the same range for all monoliths (30-40 %), showing good performance for ODHP reaction (90 % selectivity to propylene) thanks to the null affectation of the catalytic activity of the ZSM-5 and a great active sites distribution. The authors noticed the importance of selecting the metal oxides mixture since, for

example, the use of the three oxides led to the worst performance as their interactions affected their redox capabilities.

On the other hand, the DIW method has also been applied to some metallic materials. For example, stainless steel (316 L) was used as raw material for producing a monolithic catalyst for methanol conversion. The monoliths with different shape configurations produced by Lefevere *et al.* [170] were evaluated in the methanol to olefins reaction, and they showed a better performance in comparison with the packed bed, achieving around 20 % higher conversion. Tubio C.R. *et al.* [179] proposed a strategy to fabricate a palladium-alumina (Pd^0/Al_2O_3) cermet monolithic catalyst for microwave assisted organic synthesis (MAOS) employing DIW to control composition, surface area ($33.2\ cm^2\ cm^{-3}$), shape, and dimensions. The Pd^0 catalyst resulted permanently active, did not show leaching, was stable, and reusable up to 200 reaction cycles. The ink used was prepared by mixing $PdCl_2$ with Al_2O_3 (for thermal and mechanical stability) in deionized water, then adding hydroxypropyl methylcellulose (HPMC) and polyethylenimine (PEI) to adjust the characteristics of the paste for printing. Later, the samples were sintered at 1500 °C to attain a cermet material in which Pd^0 metallic species were obtained inside and on the surface of the ceramic matrix. SEM, EDS, XRD, TPR, and CO-chemisorption confirmed Pd metal already reduced was well distributed and integrated in the alumina matrix. Monoliths proved to be efficient in organic synthesis because of the synergistic effects of the metal-oxide interfaces. Besides, nanoporous gold catalysts for selective oxidation of methanol to methyl formate were prepared by Zhu *et al.* [161] following printing, annealing, and dealloying processes. Ag-Au composite inks were prepared by mixing Ag and Au clays with organic solvent and polymeric binder (atomic ratio Ag/Au= 70:30) in a planetary centrifugal mixer for 1 min. To form homogeneous Ag-Au alloys, the printed structures were annealed at 850 °C in air for 12 h. Solvent evaporation creates microporosity (1-10 μm), whereas the dealloying process creates nanoscale porosity (10-100 nm); therefore, the porosity can be adjusted by changing the solvent and polymer binder content. SEM confirmed the uniform nanoporous structure, and EDS showed a ~2

atomic % of residual Ag. The high frequency leading to good capacitance (10 times larger than powder catalyst), low pressure drop achieved for all tested flows (less than 6.8 kPa), and great catalytic activity (up to 90 % methyl formate selectivity) corroborated that the configuration of the printed nanoporous metals improved the mass transport and reaction rate for liquid and gases.

Metal-organic frameworks (MOFs) can be listed as viable structural materials of directly ink-written monoliths. In this sense, a zirconium-based MOFs monolithic catalyst was elaborated by Young *et al.* [164], who dispersed UiO-66 (52 wt%) into a mixture of polymer binders (44 wt%, TMPPTA, and EBECRYL 8413), and a photoinitiator blend (4 wt%). Monoliths were UV crosslinked upon extrusion and further thermally treated at 280 °C for 30 min. With this procedure, the final MOF content was about 74 wt%. Although heat treated catalysts presented a lower activity in catalytic hydrolysis of methyl paraoxon attributed to a partial degradation of surface active sites, they have an easier reusability compared to non-structured UiO-66. Also, Salazar *et al.* [62] prepared cuboidal and cylindrical monoliths with 90° rotated layers of iron-based MOF/SiC, which exhibited good performance in the hydroxylation of phenol with H_2O_2. The paste used in the DIW process was obtained with a pre-prepared MOF:SiC powder mixture (2.5:97.5 and 1.0 wt% Fe) combined with high and low molecular weight polyethylenimine, hydroxypropyl methylcellulose, ammonium polyacrylate, and water. After printing, a heat treatment in air at 250 °C for 1 hour was realized to raise their thermal stability. The MOF/SiC monoliths showed slight electrical conductivity (7 S m^{-1}). Although the monolith got less conversion of phenol with relation to the powder form due to a low H_2O_2 decomposition rate, this led to a reduced over-oxidation of phenol, therefore, a good selectivity (80 %) and yield (20 %) to dihydroxybenzene.

Carbon monoliths have also been synthesized through DIW, either by carbonization of templates and precursors or by introducing carbonous materials within the printing pastes. As an example of the former case, Zhou *et al.* [180] prepared porous carbon catalysts with adjustable pore sizes by means of DIW structure templates of carbon sources and SiO_2 spheres. A carbonization process at 1100 °C for

2 h in N_2 atmosphere was conducted to get the carbon replicas. Additionally, washing with NaOH was needed to complete the remotion of the SiO_2 templates (process shown in ***Figure 2.21***). SEM images of carbon catalysts showed precise replicas of the SiO_2 templates. These results, together with the low shrinkages obtained, suggest that the pore size and structure of the printed replica can be controlled by the SiO_2 template. Selective liquid phase oxidation of benzyl alcohol was used to analyze the activity of carbon catalysts, which reached up to 96 % conversion.
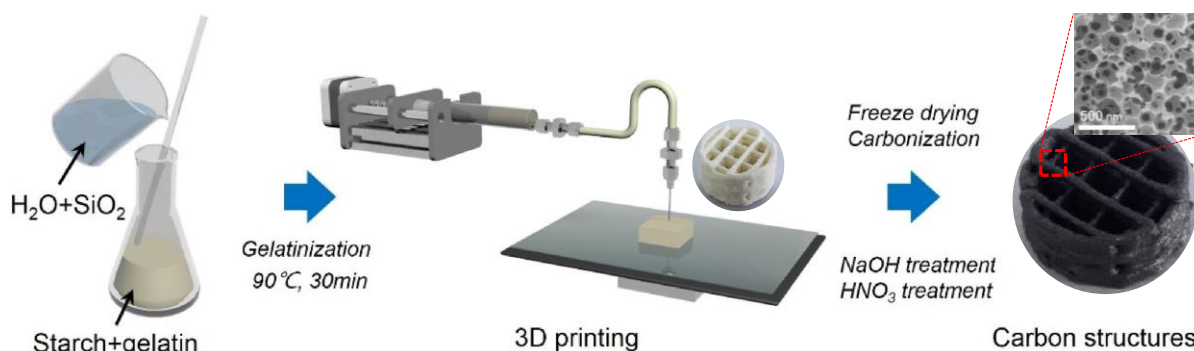
Figure 2.21. Synthesis procedure of porous carbon catalyst prepared as a replica of SiO_2 template (diameter of 200 nm). Adapted from [180].

On the contrary, Jianhua *et al.* [181] made a printing ink with graphene oxide. They printed a monolith, with woodpile layers, from an aqueous solution of large-sized graphene oxide (20 mg mL^{-1}), which can be well dispersed in water, thus presenting a good viscoelasticity without the need of additives. The resulting monolith maintained the designed shape, low density (12.8 mg cm^{-3}), and high electrical conductivity (41.1 S m^{-1}). Another graphene monolith was synthesized by Quintanilla *et al*. [182]; however, they required the use of additives to get a printable slurry. The inks were formulated by adding to deionized water, 36.6 wt% graphene nanopowder (GNP008), 8.8 wt% sodium polynaphthalenesulfonate, 2.3 wt% polyethylene glycol, and 2.8 wt% of polyehtylenimine. It is important to mention that the characteristics obtained with this paste allowed that, once printed, the structure did not collapse due to an immediate increment in viscosity of about two orders of magnitude. After the printing process, a spark plasma sintering (SPS) treatment was made to increase mechanical integrity.

The monoliths resulted in a diminution of the surface area of about 62 %, but with a good compression strength (0.1 MPa), which allows them to operate in the reaction conditions. Besides, the crystalline structure of the GNP remained after the synthesis process. These monoliths were evaluated in the catalytic wet peroxide oxidation (CWPO) of phenol, achieving high phenol conversion (85 %) but low TOC conversion (around 20 %) due to the presence of condensation species. Similarly, Middelkoop *et al.* [163] printed an advanced catalyst for CO_2 conversion into cyclic carbonates from CeZrLa/graphene mixed oxide nanocomposites. The authors mixed an aqueous solution of methylcellulose (54 wt%), CeZrLa or CeZrLa/GO nanopowders (42 wt%), and a lubrication additive (4 wt%) to obtain an ink for 3D printing. They printed woodpile layered monoliths, which were cautiously dried for several days and heat treated in an inert atmosphere at 500 °C to remove the binder and keep mechanical and thermal stability. The printed catalysts presented higher conversion and selectivity compared to their powder counterpart, which was attributed to the higher surface area with an improved distribution of the nanoparticles. According to XRD and XPS, it was confirmed that the phases of Ce, Zr, La oxides, and CeZrLa were not modified by the deposition method, printing procedure, or thermal treatment. Moreover, the catalyst supported on GO showed a greater amount of weak and medium acid sites that can be attributed to the GO. Those weak acid sites contributed to a better performance regarding the unsupported catalyst.

As a clear example of the versatility of DIW, the study realized by Long *et al.* [183] can be mentioned. The authors immobilized composites of e-E. coli/Au (engineered recombinant Escherichia coli/Au nanoparticles) into a biopolymer matrix through DIW. Sodium alginate and gelatin were added with e-E. coli/Au (5.6 – 13.8 wt% Au) to obtain a homogenous and smooth ink slurry for printing monoliths with squared straight channels. Once printed, the monolithic catalysts were introduced into a $CaCl_2$ solution to complete the crosslink reaction, and the drying process was realized by freeze-drying at -80 °C. SEM images (***Figure 2.22***) showed a homogeneous distribution of e-E. coli/Au on the surface and confocal laser scanning

microscope images (CLSM) exhibited live-cells in the catalyst. Nevertheless, during the application, no live-cells were found because of a lack of nutrients. This procedure led to a material with a compressive stress of 2 MPa, which was further used in the liquid-phase batch reduction of 4-nitrophenol with excellent activity and stability, being useful up to 7 cycles.
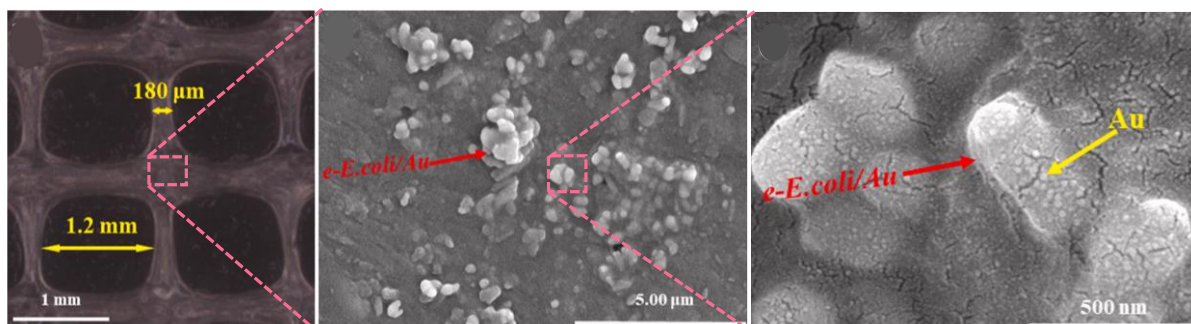
Figure 2.22. SEM images of 3D printed structure showing the uniform distribution of e-E. coli/Au into the biopolymer matrix. Extracted from [183].

Despite the capability of using a vast list of materials and compositions, as mentioned before, the inks rheological properties play a crucial role, not only during the printing process but in the successful conformation of 3D structures (*Figure 2.23a*).
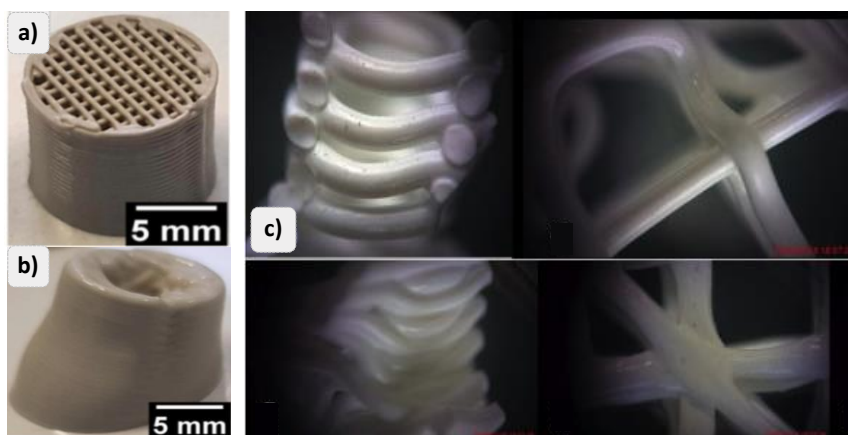
Figure 2.23. Comparison of the printing result from a) an adequate ceramic printing ink, and b) an ink with non-adequate rheological properties, c) smashing during the layer deposition because of the self-weight of the catalyst (TiO_2 monolith). Adapted from [64, 168].

If the formulated slurry does not present the needed characteristics after its deposition, some object deformation can occur (***Figure 2.23b***), as noted by Mendez *et al*. [64], who fabricated TiO_2 square-lattice double-diagonal structures by means of robocasting with a paste made of TiO_2 P25 and deionized water. Although the consistency of the paste allows the proper extrusion to form the catalyst, after the deposition a pronounced smash between layers may be observed because of the material self-weight (***Figure 2.23c***). Additionally, the porosity highly decreased due to compaction. These materials were evaluated in the photocatalytic degradation of acesulfame under UV-Vis irradiation. Although photocatalysts worked for the degradation of acesulfame, they presented a lower reactivity regarding powder form due to a decrement in the active sites that are illuminated since the smashing of the layers. Therefore, the particle size and solid content are taken into consideration, as well as some binders, plasticizers, and other additives are commonly used to adjust the slurry characteristics.

The binders employed for the preparation of inks affect not only the rheology of the paste but also the drying and calcination process requirements and the properties of the final structure. This was corroborated by Lefevere *et al*. [166], who analyzed the effect of the binder system in the 3D printed structure properties using ZSM-5 as raw material. They studied the bentonite, colloidal silica, and aluminophosphate binders within a mixture of binder with water (35 wt% single or binary binder system 50/50) and zeolite (65 wt%). Bentonite resulted in better shear-thinning behavior regarding aluminophosphate and silica (low viscosity at high shear rates and vice versa). In general, the porosity of the zeolite was reduced after its conformation in the monolithic structure due to pore blocking with the binders. Moreover, the results obtained suggest that pore size distribution is related to the particle size of the binder used, and the smaller the particle size, the smaller the pores. The mechanical strength and acidity are also dependent of the binder, achieving superior properties with the aluminophosphate. Lefevere *et al.* [184] used the methanol to olefins reaction to study the importance of binder and 3D printing architecture on catalytic properties without

changing the basic zeolite starting material. Even though all the 3D printed catalysts showed lower activity regarding the pure zeolite, bentonite, and silica single binder systems achieved good conversion of around 90 %. This decrease in activity is related to a diminution of area, diffusivity to the active sites due to porosity, and acid strength. The selectivity of the reaction was influenced by the active surface and acidity whereas the stability and activity were affected by composition as well as porosity, fiber thickness, and stacking of the layers. For this reason, the fewer strong acid sites and lower micro/mesoporosity acquired with the aluminophosphate binder led to better selectivity toward the desired products. In relation to the binary binder system, all samples exhibited almost full conversion at high temperatures, but they present differences in selectivity and stability.

Within this context, the mainly used binders are bentonite, alumina, and polymeric binders —such as polyester acrylates— (as presented in **Annex 4**). However, the former turns out to be the most employed owing to its ability to provide mechanical strength and thermal stability. On the other hand, methylcellulose is the most widely used plasticizer due to its ability to improve viscosity and impart pseudoplasticity to the inks. Nevertheless, viscosity has also been adjusted by adding hydroxypropyl methylcellulose, polyethylenimine, or polyethylene glycol. Even when binders are necessary/useful to form monolithic structures, their incorporation leads to a reduction of the surface area compared to powder raw material [172-176, 178, 185]. Furthermore, agglomeration of particles, blockage, and diminution of accessibility to active sites have also been associated with binders [171]. Conversely, some mesopore formation has been ascribed to the methylcellulose decomposition during thermal treatments [61, 165].

In addition to the incorporation of binders, the inks rheological characteristics may also be adjusted by applying different external stimuli, including temperature, pH, and light. This alternative was implemented by Elkoro *et al.* [186], who corrected the slurry characteristics by changing the pH and the printing temperature. To obtain a nanotitania monolith for photocatalytic degradation of acetaldehyde, printable slurries

were prepared by adding titanium (IV) oxide powder to water (different solid/liquid ratios) and adjusting the solution pH between 0 and 7. Maximum titania content was achieved when pH was ~0.3. This decreasing pH tendency is ascribed to a rise of the number of protons adhered to nanotitania surface. Materials prepared at pH ≤1 and T ≥150 °C did not present appreciable degeneration, whereas for pH >2 or T <150 °C, some cracking and disaggregation were observed. The use of thermal treatment increases the rutile content and particle size being greater for acid pastes. Ultraviolet-visible absorbance spectra showed a shift to higher wavelengths that, along with a decrease in the band gap, suggested the acid treatment improves the visible light absorption of materials. This method was selected since the absence of a binder avoids the decrease in surface area and leads to a better interaction of light with the catalyst, which is fundamental for photocatalysis. Likewise, Lawson *et al.* [173-176, 178] employed temperature increase to formulate their inks. They mixed zeolite (ZSM-5 or H-ZSM-5 ≤ 85 wt%), with aqueous solutions of various proportions of metal oxides (from 3.8 to 30 wt%), methylcellulose, and bentonite clay. The mixtures were shaken, then rolled at 20 rpm for 48 h at 25 °C to homogenize, and later densified at 400 rpm at 60 °C for ~3 h to achieve a printable rheology. In some cases, this external stimulus needs to be applied together with additives. For example, Zhou *et al.* [180] prepared a DIW slurry by ultrasonic dispersion and magnetic stirring at 90 °C of a mixture of carbon sources, monodispersed SiO_2 spheres, starch, gelatin, and distilled water. Once the mixture was completely gelatinized, it was cooled down to 70 °C for the printing process. The SiO_2 spheres were employed since they acted as a hard template but also increased the viscosity of the slurry, augmented the strength, and reduced the shrinkage of materials (~16 %). In this regard, the printing conditions must also be controlled to maintain the desired characteristics and ensure the final product stability. In the previously mentioned example, Zhou *et al*. [180] held the extrusion process at 70 °C to keep the desired rheological characteristics of the slurry, obtaining structure templates for carbon monoliths.

Light has been applied during printing for curing pastes containing photoinitiators. As an example, monoliths produced from a mixture of UiO-66 particles, polymer binders, and photoinitiator were crosslinked with a 365 nm UV light source upon extrusion [164]. This treatment provided structure retention for their immersion in different solvents. To further improve their stability and porosity, monoliths went through a thermal treatment at 280 °C for 30 min that degraded the polymeric binder and photoinitiator. Therefore, N_2 physisorption analysis showed the expected microporosity of UiO-66. Similarly, De Hazan *et al.* [187] synthesized 3D ceramic structures for photocatalytic decomposition of formaldehyde. The ink pastes were made by milling α-Al_2O_3 or hydroxyapatite powders with monomers used to achieve high solid loading and adjust viscosity (4-hydroxybutyl acrylate, polyethylene glycol diacrylate, bisphenol A diacrylate, and/or polyethylene glycol methacrylate), together with surfactant 2-[2-(2-Methoxyethoxy) ethoxy] acetic acid (TODS) to enhance particles dispersion, and photoinitiator, until homogeneous mixture was achieved. Those pastes were used to print monolithic catalysts and for curing the resin, every two layers, the deposition was stopped, and the piece was exposed to a 100W UV lamp for two minutes. To evaluate the effect of the curing atmosphere, some materials were cured under air and some others under argon, being the latter in which structures presented fewer cracks and smoother surfaces after sintering. Monoliths underwent subsequent thermal treatments to remove additives and densify the structure. Later, monoliths were dip-coated with a TiO_2-surfactant solution and heated to 500 °C to remove the surfactant. Authors observed that, besides the ink characteristics, the printing velocity and fiber to fiber spacing influence the fiber deformation during/after deposition; thus, the higher velocity and the lower spacing lead to less deformation. The structures were shaped after printing by rolling the flexible Al_2O_3/polymer lattices. The printed materials showed similar photocatalytic activity to that of the TiO_2 powder in formaldehyde decomposition; therefore, the conformation in 3D structure did not affect its properties.

Besides, DIW is generally utilized for directly producing catalysts, often including the active phase into the slurry for printing the structure without the need of

additional steps [53, 164, 188]. Therefore, DIW technique allows to rise the loading of active material per volume regarding coated monoliths (65 vs 33.5 wt%), as pointed out by Lefevere *et al*. [166]. In this case, Ni/Al_2O_3-based monoliths for CO_2 methanation were developed by Middelkoop *et al.* [59]. To get the active phase within the structure, Ni/Al_2O_3 catalyst was mixed with bentonite and alumina-based binders to produce the ink pastes. Those pastes were extruded to form tetragonal monoliths with mesh patterns, which, after a 500 °C treatment, presented an increase of ~30 % in specific surface area. The peaks corresponding to γ-Al_2O_3 phase were not clearly observed within the XRD diffractograms as they overlapped with the nickel aluminate $NiAl_2O_4$ phase present because of the nickel oxide-support interaction. Compared to Ni-alumina pellets and beads, structured catalysts in monolithic shape resulted in a greater CO_2 conversion (~80 %, about 20 % more than beads, and similar to pellets), and methane selectivity (~86 %, around 5 and 11 % more than beads and pellets, correspondingly) showing that the catalyst configuration is of high importance in their performance. Nonetheless, upon long exposure to high temperatures (450 °C), catalysts exhibited some shrinkage, affecting their surface area. In like manner, metal-doped ZSM-5 monoliths for methanol to olefins conversion were prepared by including 10 wt% of metal precursors into zeolite, methylcellulose, and bentonite clay mixtures [61, 165]. The incorporation of metal precursors — which were the nitrate form of Ce, Cr, Cu, Ga, La, Mg, Y or Zn — in the printing inks eliminates the additional step of ion-exchange or impregnation commonly used for doping zeolite.

Moreover, Elkoro *et al.* [58] produced Au/TiO_2 monoliths by means of the DIW technique following two different strategies: impregnating the TiO_2 with Au nanoparticles (Au NPs) before or after the printing process. For the post-printing strategy, an extrudable paste was prepared by mixing P90 TiO_2 with HCl. After printing, the structure was dried, calcined, and impregnated with an Au NPs toluene suspension for later thermal treatment. On the other hand, for the pre-printing method, the P90 TiO_2 was impregnated with the Au NPs toluene suspension, followed by the same thermal treatment and procedure for obtaining the printing paste and monolithic

structure. As observed by SEM (**Figure 2.24**), the TiO_2 dimensions were similar for both materials. Nevertheless, the materials impregnated pre-printing presented a homogeneous distribution of the Au NPs both in the surface and cross-section (**Figure 2.24a-b**), while in the post-printing monolith, a decrease of the Au NPs concentration along the cross-section was observed (**Figure 2.24c-d**). This diminution is attributed to the pore size between TiO_2 nanoparticles that reduced the Au NPs suspension diffusion during impregnation; hence, the Au NPs remained concentrated on the surface. Also, according to XPS analysis, to attain a similar Au/Ti surface ratio, the Au content needs to be more than one order of magnitude higher in the pre-printing method. Considering that the photocatalytic reaction occurs mainly at the surface, the impregnation post-printing route turns out to be the best for good performance and saving materials.
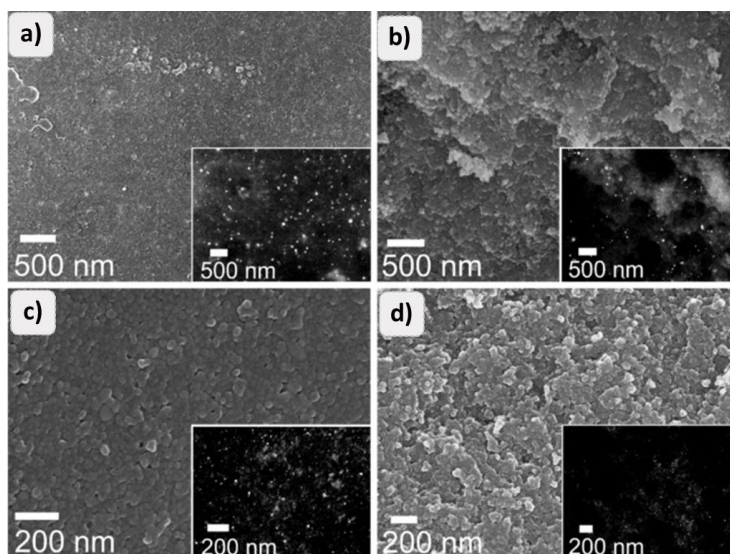
Figure 2.24. SEM images of the surfaces and cross sections of the Au/TiO_2 monoliths. a) surface of a pre-impregnated Au/TiO_2 monolith (Au 1 wt.%); b) cross section of the pre-impregnated Au/TiO_2 monolith (with Au 1 wt.%); c) surface of a post-impregnated Au/TiO_2 monolith (Au 0.1 wt.%); d) cross section of a post-impregnated Au/TiO_2 monolith (with Au 0.1 wt.%). Insets correspond to the same sample areas obtained using a backscattered electrons detector, revealing Au NPs as bright dots. Taken from [58].

Aslam *et al.* [189] also compared both methodologies for obtaining zeolite-based catalysts for syngas to alcohol conversion. In the first case, ZSM-5 zeolite powder was impregnated with ammonium molybdate tetrahydrate, cobalt (II) nitrate, and potassium nitrate prior to the preparation of the ink with silica and bentonite binders. Nevertheless, the monolith had a low surface area and collapsed before achieving the reaction conditions. In the second case, zeolite was mixed with the binders and the viscosity of the slurry was adjusted with starch. Once printed, the monolith was dried, calcined, and immersed in a solution of metal precursors with glucose for hydrothermal synthesis, which was further dried and calcined. In this approach, the inorganic binders allow to uniformly structure of a zeolite monolith that remained intact after the hydrothermal treatment. The metal precursors grew homogeneously, and synergism between molybdenum and cobalt active sites was corroborated. Also, the diffusional limitations were reduced over monoliths regarding powder, since they provide better access to catalytic active sites, leading to higher CO conversion.

Once printed, 3D structures must go through a drying process before being subjected to further post treatments. Special attention should be paid to this step due to its relevance in avoiding cracks, imperfections, or breaks in the materials, as exhibited in ***Figure 2.25***. Nevertheless, the drying procedure varies according to the raw material and composition of the inks. In this regard, Lefevere *et al.* [166] noted that the drying method depends on the characteristics of the binder system used, as they observed in the fabrication of ZSM-5 structures with three different binders (bentonite, aluminophosphate, and silica). In the case of bentonite, since it adsorbs high amounts of water, fast drying leads to ruptures in the structure; thus, a slow controlled drying at 20 °C helps to avoid defects (***Figure 2.25a-c***). On the other hand, aluminophosphate and silica pastes had low viscosity and needed speedy drying to quickly lose water and, therefore, increase their viscosities to retain their geometry without cracks (***Figure 2.25d-e***). However, regarding aluminophosphate and silica, bentonite binder leads to a greater shrinkage due to the water lose after drying.

Several drying methods have been used to avert defects in the monoliths. For instance, drying at room temperature, usually between 12 and 48 h has been used for materials based on zeolites, ceramics, and some metals [61, 167, 173, 178, 179, 189-192]. Temperatures over 80 °C have been used to dry monoliths composed of carbonous materials and some metal oxides within few hours [64, 169, 186, 193]. Contrary, longer drying was required for 3D printed structures containing Ni/Al_2O_3, which were placed in a humidity chamber for a week maintained at 85 % RH and 25 °C [59]. In some other few cases, such as the e-E. coli/Au and the SiO_2 template for carbon monolith, the authors applied a freeze-drying procedure with temperatures between -80 and -50 °C, to prevent damage within the fragile structures [180, 183]. Along with the drying method, choosing adequately the build platform material is also important for conserving the 3D printed objects without defects. Glass [58, 64, 193], alumina substrate [62, 166, 182, 194], aluminum foil [187], and Teflon [171, 175, 177, 195] are some examples of the build platform materials used for the deposition during DIW, which facilitate the removal of 3D structures, allow a homogeneous drying, thus avoid cracking. Different materials such as silicon and polytetrafluoroethylene (PTFE) films are barely utilized to prevent slippage and ease post-treatment without manipulation of soft pastes, for example those of titania and Au NPs [161, 186].
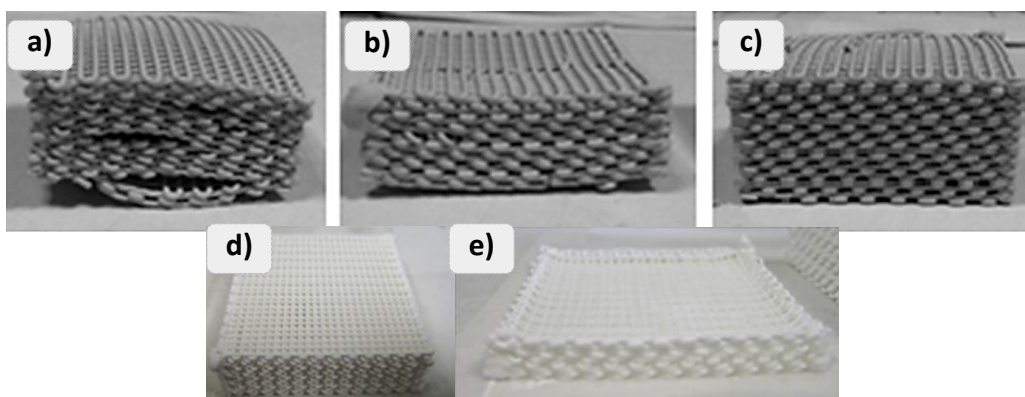
Figure 2.25. Effect of the drying process on the deformation of porous ZSM-5 materials: structures containing bentonite binder after a) fast drying with heating lamp, b) freeze drying, and c) slow drying in controlled atmosphere (80 % relative humidity, RH, and 20 °C); structures containing single silica binder after d) fast drying with

heating lamp, and e) slow drying within a regulated environment (80 % RH and 20 °C). Taken from [166].

As a result of drying and applying some stabilization treatments, most of the authors have noticed a certain shrinkage percentage, which is normally around 10 %. However, it depends on the whole fabrication process, therefore, shrinkage values from ~0.4 to almost 40 % have been reported [166, 196]. In that respect, Román-Manso *et al*. [197] synthesized silicon carbide monoliths by means of the DIW technique, analyzing the effect of the paste composition in the final structure. They employed three different ceramic powders (submicron-β-SiC: β20 and β7; and nano-β-SiC: N20) together with Al_2O_3 and Y_2O_3 as sintering additives, polyethylenimine aqueous solution as a solvent, methylcellulose as viscosifier and ammonium polyacrylate as flocculant. The smaller the particle size of the raw material, the lower the possible solid content in the ink. Despite the difference in solids content, the three inks had a highly shear thinning rheology, allowing its extrusion in the shear rate region of 30-70 s^{-1} and keeping its shape after deposition due to its great strength. Results also suggested a relation between solid content and shrinkage; the lesser the content of solids, the bigger shrinkage (28 % in N20 regarding 19 % of β7 particles). Thus, shrinkage is an important factor to take into consideration when designing the monoliths for obtaining the desired final dimension.

In another aspect, a post-treatment is often carried out on monoliths to stabilize them. For example, during the synthesis of graphene monoliths Jianhua *et al.* [181] realized a reduction process with hydroiodic acid to avoid cracking during thermal treatment caused by rapid liberation of volatile gases (1000 °C in nitrogen). Moreover, calcination or sintering processes are used to stabilize the material, enhance its mechanical strength, or foster its catalytic activity. This is the case of the 3D printed Al_2O_3 catalyst prepared by Azuaje *et al.* to act as Lewis acid in Biginelli and Hantzsch reactions in the absence of solvents [198]. The authors directly produced a woodpile layered monolith by extruding a paste made of Al_2O_3 powder, water, dispersant Darvan 821A, hydroxypropyl methylcellulose, and polyethylenimine. The structure was dried

and then sintered at 1500 °C in air to remove solvents and polymers of the ink, improve its mechanical strength, and increase its catalytic activity by increasing its Lewis acid character. The morphology and composition remain the same after 10 use cycles, as corroborated by SEM and XRD. The monolithic catalyst displayed a 15-23 % yield increment regarding alumina powder and 20-35 % compared to catalyst-free conditions, and this activity remained after ten usage cycles. In addition, monoliths led to complete consumption of the reactants in short times (20 % of the time of uncatalyzed system) without side products generation despite a lower porosity. Similarly, Tubío *et al.* [185] synthesized Al_2O_3 structures with immobilized cooper for different Ullmann reactions. The synthesis consisted of printing by DIW a paste made with Al_2O_3 powder dispersed in an aqueous solution of copper (II) nitrate, polyethylenimine, and viscosity adjusted by adding hydroxypropyl methylcellulose. The woodpile structure was dried and sintered at 1400 °C to obtain a high mechanical strength monolith. The sintering process led to the transformation of $Cu(NO_3)_2$ to CuO and $CuAl_2O_4$, which was visible with the color change and corroborated in XRD patterns. A portion of the metal is lost during the sintering because it diffuses through the structure and remains adsorbed on the supporting plate; hence, a final copper load of 2.3 wt% was attained. The SEM images showed a dense group of alumina crystals without open meso or microporosity, and a laminar structure of the copper oxide phases. Despite its low copper loading (regarding 5-10 % used in analogous systems), complete conversion was observed in a short time (2 h); therefore, the catalyst presented an excellent activity, no leaching, and stability after 10 usage cycles.

In the same manner, Quintanilla *et al.* [194] studied the immobilization of metals (Fe nanoparticles) within the structure of ceramic (SiC) honeycomb monoliths. They printed on alumina substrate an ink composed of Fe/SiC particles, deionized water, and organics for adjusting pseudoplastic behavior. After the printing process, catalysts were heat treated at 600 °C in air for 2 h to completely burn-out the organics. Later, a spark plasma sintering (SPS under Ar at 1000-1500 °C) was applied in some samples to increase mechanical integrity and induce differences in porosity. The results showed

that the SPS was crucial to diminish Fe leaching; nonetheless, as the SPS temperature increased, the porosity decreased thus the accessibility of Fe, reducing the catalytic activity. Danaci *et al.* [192] manufactured copper monoliths by 3D printing a paste made of copper powder (14-25 μm) and hydroxypropyl. After drying and calcining at 550 °C printed samples, the authors followed two methodologies: 1) conventional sintering at 880-1000 °C for 5 hours in N_2 or N_2:H_2 atmospheres or both) spark plasma sintering in the vacuum of 100 Pa. Later, sintered copper structures were coated with a solution of polyvinyl alcohol (PVA), acetic acid, water, silica, and Ni/Al_2O_3 active phase and finally calcined at 500 °C for 2 hours. When using temperatures close to the melting temperature of copper, strong bonds were attained together with a reduction in porosity. The reducing atmosphere used during sintering helped to minimize oxide content in the fibers and to obtain denser copper fibers. The copper oxide layer on the surface led to a reduction of coating adhesion. All monolithic samples showed a CO_2 conversion as high as that of the powder catalyst (50 %) at 400 °C with a slightly higher selectivity (~98 %), and higher stability for 80 h time-on-stream.

Apart from calcination and sintering processes, some materials needed different treatments in preparation for the subsequent catalyst loading. As an example, prior to the growth of MOFs through hydrothermal reaction, ceramic monoliths fabricated by Liu *et al.* [195] underwent an alkaline etching to withdraw SiO_2 nanoparticles from the surface, thereby creating additional pores. Then, monoliths were coated with polydopamine via self-polymerization of dopamine and treated through a hydrothermal process for in situ MOFs growth.

When the catalytic compound was not included in the ink, it was mostly deposited on the structure by dip-coating. In some cases, usually for metals with a smoother surface, within the coating solution, different additives (particularly polyvinyl alcohol, silica, and methylcellulose) were included to increase adherence of the active phase [170, 191, 192]. For example, the ZSM-5 coating of a stainless-steel monolith was attained by adding 1 wt% methylcellulose and 1 wt% colloidal silica to an aqueous coating slurry containing 30 wt% ZSM-5 [170]. The sintered structures underwent a

wash coating procedure, followed by drying and calcination at 550 °C to remove organic compounds. The addition of silica was necessary to increase viscosity and reduce the weight loss of the coating from 47 to 5 wt%; moreover, the deposition of zeolite augmented 80 % due to an increase in contact between particles and support. The particle size of the zeolite also influenced in the loading, the smaller the particle the higher the load.

Notwithstanding, in addition to wash coating different active phase deposition techniques, including electrodeposition, hydrothermal reactions, and chemical surface modifications, have been tried. For instance, Lin *et al.* [193] produced an electrocatalyst by 3D printing polyethyleneimine cross-linked oxygenated carbon nanotubes (O-CNT) with further nickel electrodeposition. The ink slurry containing the O-CNT, PEI, and acetic acid was deposited at room temperature onto glass wafers. After printing, samples were dried at 100 °C and calcined under nitrogen atmosphere (450-650 °C) for 1 h. Then, the nickel was electrodeposited, and samples were again dried but at 70 °C in vacuum. Element mapping confirmed the uniform distribution of C, O, and Ni on the outer surface (***Figure 2.26a***). FTIR showed CNT were cross-linked with PEI in the monolith, whereas XPS, XRD, and Raman results showed that this loading methodology acquired nickel deposited in the form of Ni and $Ni(OH)_2$. Moreover, D and G bands were observed in the Raman spectra, and I_D/I_G ratios confirmed more defective carbon generation with higher temperature annealing. The monolithic catalyst thermal treated at 650 °C presented more carbon defects, which acted as active sites for alkaline hydrogen evolution reaction.

Fumed SiO_2-based thixotropic inks were used in direct ink writing by Liu *et al.* [195] to further in situ growth of MOFs for catalytic degradation. Once printed materials were left to dry at ambient temperature for 12 h, then further dried and heated at 900 °C to form hierarchical porous ceramics (HPC). Before the MOFs growth, monoliths went through a basic etching to remove some SiO_2 nanoparticles from the surface and form more pores and coated (by dopamine self-polymerization) with polydopamine (PDA). Finally, a modified hydrothermal reaction using a MIL-100 (Fe) precursor

solution was carried out to form the 3D printed HPC-MOFs. The successful growth of MOFs on HPC was confirmed by XRD analysis. SEM images confirmed that the structural integrity was maintained after sintering and hydrothermal treatment, whereas C, O, Si, Fe, and Al elements were evenly distributed into the architectures, according to EDS results (**Figure 2.26b$_{1-2}$**). The HPC-MOFs displayed excellent catalytic degradation efficiency (~97 %) and reaction rate constants (0.16 - 0.29 min^{-1}) for different organic dyes. In the same manner, Li *et al.* [171, 172] investigated the integration of SAPO-34 in the surface of 3D printed monoliths of HZSM-5 using the secondary growth technique. This methodology consisted of dipping the HZSM-5 supports in an aqueous SAPO-34 suspension and then apply a hydrothermal treatment. Homogeneous and dense growth of SAPO-34 crystals over the HZSM-5 surface was confirmed by SEM (**Figure 2.26c$_{1-2}$**).
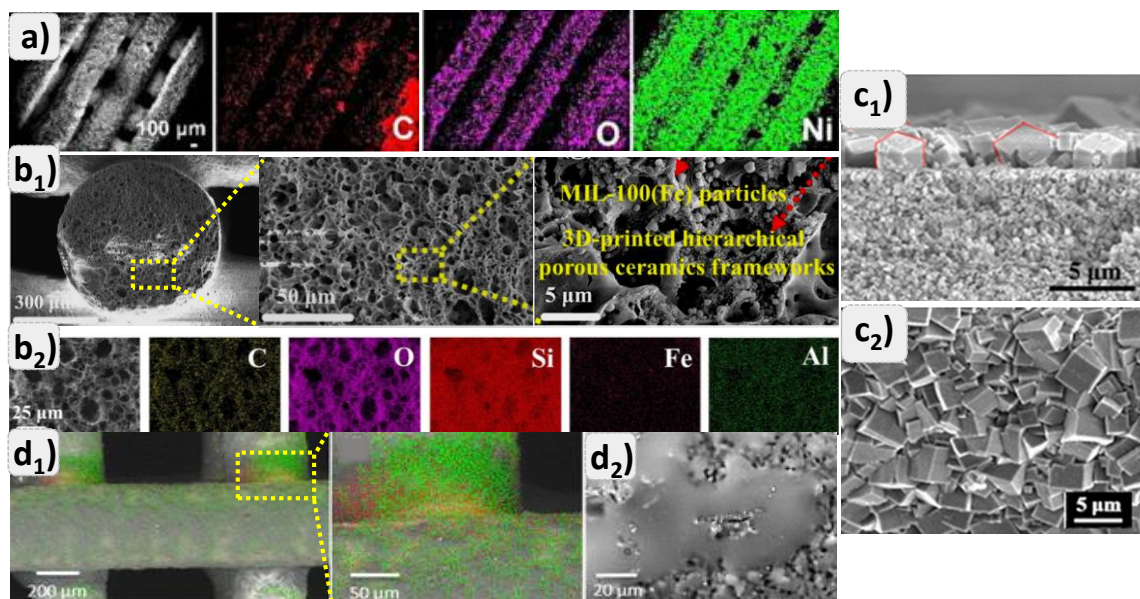
Figure 2.26. Images of active phases incorporated in 3D printed supports following different strategies: a) Elemental mapping of carbon monolithic catalyst loaded with nickel by electrodeposition (named as 3DPC-650@Ni/Ni(OH)$_2$; b$_1$) SEM, and b$_2$) EDS images of hierarchical porous ceramic structure hydrothermally treated to in situ MOFs growth; c$_1$) lateral and c$_2$) top view images of the load of SAPO-34 grown through hydrothermal treatment — SAPO-34 cubic crystals on 3D-HZSM5 monolith surfaces,

marked with red frames —; d$_1$) EDS and d$_2$) SEM images of PI-Pd composite deposited on silica monolith surface by chemical modification. Adapted from [171, 193, 195, 196].

In another way, a chemical surface modification was used to obtain monolithic catalysts with immobilized palladium to test in the Suzuki reaction. Sanchez *et al.* [196] employed the DIW technique to print a silica monolith whose surface was further chemically modified. The silica monolith was generated from a paste of SiO$_2$, poly(vinyl butyral-co-vinyl alcohol-co-vinyl acetate) (PVB-PVA-PVAc, 80 wt % vinyl butyral), polyethylene glycol, and 2-propanol. Posterior to printing, the monoliths were dried, deagglomerated (400 °C) to remove solvent and polymers, and sintered (1500 °C) to attain mechanical and chemical stability. Later, the monolith underwent a chemical surface modification via submersion in a solution containing polyimide resin, Pd(AcO)$_2$, and anhydrous N,N-dimethylformamide (DMF). The authors selected this strategy to deposit the catalytic species only in the surface of the monolith since metal introduction inside the mass of the support (without porosity, 0.3 m^2 g^{-1}) would not be accessible to the reagents, thus representing an unnecessary expense. As confirmed by SEM, PI-Pd composite was deposited on the monolithic silica surface, and carbon from the resin and Pd (1.6 mg Pd) were present exclusively on the monolith surface (presented in **Figure 2.26d$_{1-2}$**). The catalyst was stable with almost no changes in its activity after 10 cycles of use; moreover, negligible leaching of Pd was detected.

Additionally, Sanchez *et al.* [68] also realized a similar procedure to generate monoliths with immobilized copper and palladium. In this case, the functionalization consisted of a surface activation with H$_2$O$_2$, followed by a silanization with (3-aminopropyl) trimethoxysilane (APTS) or [3-(2-aminoethylamino) propyl] trimethoxysilane (AAPTS) to modify the material surface preparing it for the final metalation to immobilize Cu or Pd, respectively. It was also corroborated that the Cu and Pd loaded (0.6 mg and 1.6 mg, respectively) were present only on the surface of the monoliths with a homogeneous distribution. The leaching of Cu and Pd was negligible, representing less than 0.07 %.

The DIW technique has demonstrated its advantages compared to traditional methods for directly producing monolithic catalysts. Among these advantages, its compositional versatility expands its capability to generate a large range of materials not achievable through usual extrusion, pressing, or corrugating foil techniques. In this regard, the technique allows for the incorporation of additives, thus altering the characteristics of the catalysts produced (e.g., porosity, chemical or mechanical strength, etc.). The incorporation of active phases within the ink paste is another alternative presented in this method and may be considered depending on the porosity and availability they will have for the reagents during its application. Additionally, the generation of complex structures, a general benefit of AM technology, is also proved.

2.3.4.2. Fused Deposition Modeling

Fused deposition modeling (FDM), also named fused filament fabrication (FFF), is one of the most employed AM techniques [199]. In FDM the raw material filament is unwound from a reel and then supplied to an extrusion nozzle. The filament reaches its melting point as it passes through the nozzle, which accurately extrudes and deposits it on the print bed. The extruder moves in the X-Y direction over the build platform according to the required geometry while extruding the plastic to form each layer (**Figure 2.27** presents a schema of FDM system).
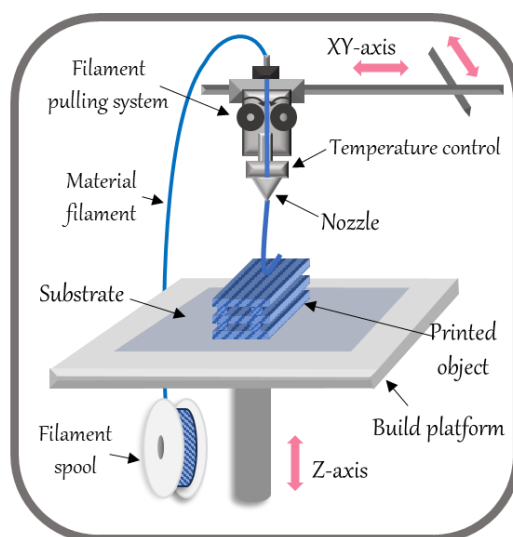
Figure 2.27. Schematic illustration of the fused deposition modeling (FDM) technique.

It should be mentioned that the printing speed and printing chamber temperature have been proven to significantly impact in the 3D printed object features [200]. Too high speeds lead to structures malformation and nozzle clogging, therefore moderated speeds are preferred to acquire consistent and quality structures. Moreover, keeping the printing chamber temperature aids in preventing the structure from bending from the platform during printing. When deposition has finished, the fused material cools and solidifies on the heat bed, which is maintained at a lower temperature to ease this process [201]. Nevertheless, the temperature difference between the extruder end and the print platform is reduced to avoid imperfections in the printed structure, such as breaks or warping due to the change in temperature [202]. The extruder temperature is fixed depending on the properties of the filament but is usually set around 220 °C; instead, the build platform temperature depends also on its material — such as glass, adhesive foils, and Teflon —, values ranging from 70 and 120 °C have been reported [203-206].

On the other hand, for FDM technique thermoplastic filaments of polylactic acid (PLA), acrylonitrile butadiene styrene (ABS), polyester, and polyurethane are commonly used. Nonetheless, these thermoplastic polymers have low glass transition temperature and low surface area, and their properties may be affected by heat, which reduces their catalytic applications [72, 205]. Consequently, the use of commercial filaments for producing monolithic catalysts has been poorly studied (see **Annex 5**). In particular, FDM was applied by Hock *et al.* [204] to fabricate advanced polymeric monoliths, which were further functionalized to act as acid catalysts in sucrose hydrolysis. The authors employed a commercial high impact polystyrene (HIPS) filament to print monoliths with an orthogonal orientation of woodpile pattern layers. For printing, the nozzle was heated to 220 °C to extrude the filament, while the build platform was kept at 90 °C to ensure adhesion. Once printed, the HIPS monoliths were immersed in a 96 wt% H_2SO_4 solution at 22 °C for times varying between 1 h to 7 days to introduce sulfonic acid groups. After this time, they were washed with water until reaching a neutral pH. This functionalization method was chosen due to its

reproducibility and the larger mechanical strength achieved regarding other treatments at higher temperatures. No structural changes were observed in the monoliths even after 7 days of sulfonation, from which a sulfonation degree above 0.7 mmol g^{-1} was attained. Optimal treatment was set for three days in which the sulfonation degree was 0.48 mmol g^{-1}. Functionalized monoliths showed better catalytic performance in the hydrolysis of sucrose regarding a commercial reference catalyst, sulfonic acid-functionalized by ion exchange, even though commercial catalyst has about 7-10 times more sulfonic acid groups. This improvement has been ascribed not only to the better mass transfer which boosts the reaction kinetics, but to a greater availability to the sulfonic acid groups. Authors corroborated the increased mixing when using complex channel structures compared to straight channeled monoliths; this is based on the Reynolds number.

To extend the chemical functioning of commercial thermoplastics for catalytic reactions, some researchers have opted to modify them to prepare their own filaments. For example, Hock *et al.* [203] synthesized nanoporous hyper-crosslinked polymers, which were further mixed with different thermoplastics (PLA, PVA, PS, or a mixture) to extrude a filament of 3 mm of diameter. The filament extrusion was realized at around 200 °C; however, the higher the content of hyper-crosslinked polymers, the higher the temperature required. The fused deposition was realized at around 220 °C, over an adhesive foil at 120 °C to assure the adhesion of deposited material during printing. With this procedure, a 40 wt% loading of nanoporous solid materials, together with a specific surface area of ~ 171 m^2 g^{-1} was attained. Besides, the channel geometry proved to be significant for reaction purposes due to hydrodynamic properties, pressure drop, and residence time distribution. In a similar manner, an alumina-based filament was extruded by *Li et al.* [206]. The filaments were prepared by mixing thermoplastic elastomer (TPE), grafted polyolefin, and alumina. The authors used these filaments to print monoliths with conventional straight channels and biaxial channels (*Figure 2.28a*), which were evaluated in the plasma-catalytic oxidation of toluene. Once the monoliths were printed, they were submerged into cyclohexane to

remove binders and later subjected to a sintering treatment and an immersion reaction to load Mn-Co nanospheres. Some defects were observed within the structures because of clogging of the nozzle and an irregular extrusion since a variability in the filament dimensions. Layers from the FDM printing are clearly observable in the SEM images of the radial channels (***Figure 2.28b***) as well as the porosity among sintered alumina nanoparticles (***Figure 2.28c***). A bigger amount of Mn-Co loaded in the advanced design (0.234 vs 0.102 wt%) was attributed to a higher specific surface area and better mass transfer during the immersion reaction. SEM images of axial channels of a coated monolith are presented in ***Figures 2.28d-f,*** showing Mn-Co nanospheres of about 680 nm covering the Al_2O_3 surface. The conventional design reduced up to 95 % of the by-products obtained by the powder counterpart, whereas the radial channels increased the energy efficiency with a negligible rise in by-products. Radial channels were more relevant at lower input power because they provided a conduit for high-energy electrons, thus increasing the catalytic oxidation of toluene (***Figure 2.28g***).
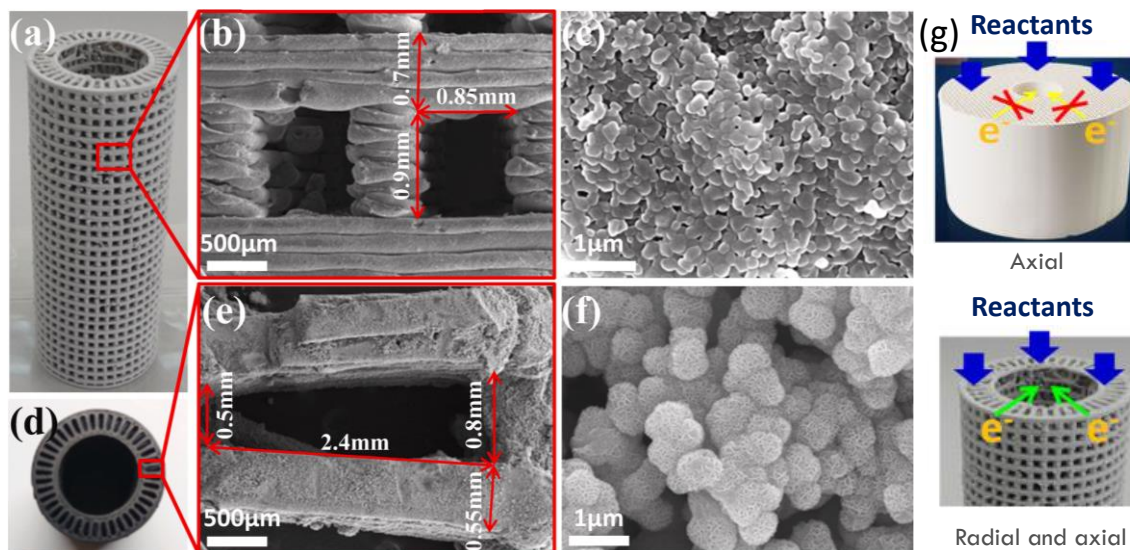
Figure 2.28. Mn-Co nanospheres coated Al_2O_3 monolith with axial and radial channels for plasma-catalytic oxidation of toluene. a-c) Photograph and SEM micrographs of the 3D printed Al_2O_3 monolith (radial channels); d-f) Photograph and SEM micrographs of

the Mn-Co nanospheres coated structure; and g) Effect of radial channels in high-energy electrons transport. Adapted from [206].

Some studies have been realized with the incorporation of active compounds into the filaments, thus obviating a second step to deposit them after printing. Among those studies, the one carried out by Evans *et al.* [207], in which they synthesized a catalyst of Zeolitic-based MOFs with chemically active porous surface, can be pointed out. Zeolitic-based MOFs were evenly integrated into polylactic acid (PLA) and thermoplastic polyurethane (TPU) matrices with high loadings close to 50 wt%. Those composites were extruded at 185 °C into filaments (1.6 mm diameter) and used in the FDM process. After printing, the structures underwent a solvent exchange either in CH_3OH or acetone, followed by an activation step at 75 °C, which did not generate any morphological changes. Besides, this activation led to an increase in thermal stability in accordance with the reduction in mass loss from 100 to 200 °C observed in TGA measurements. Thus, these materials are also limited to work under this temperature. XRD results confirmed the retention of the ZIF-8 crystallinity after the fabrication procedure, while N_2 isotherms show the high surface areas achieved, 531-706 m^2 g^{-1}. Although some MOFs particles remained embedded in the plastic matrices, they conserved their characteristic ability to perform chemical interactions. Filaments of TiO_2 nanoparticles incorporated in ABS thermoplastic were developed by Skorsi *et al.* [200] to be used in photodegradation. ABS polymer was chosen since it has higher stability and less propensity to decompose during extrusion in comparison to other commercial polymers. The filaments were created by dispersing mixtures of ABS and TiO_2 nanoparticles (0-10 wt% TiO_2, larger contents led to printing difficulties) in acetone for several hours at 35 °C and sonication. Later, the solution was placed in a Teflon substrate at 80 °C to evaporate the solvent so it could be fed to an extruder to get the 1.75 mm-wide filaments. These filaments were used to 3D print photocatalyst for the degradation of rhodamine 6G, in which the presence of TiO_2 was confirmed by XRD. Although FTIR results exhibited that TiO_2 interacts with polymer and increases its degradation during processing, the larger TiO_2 contents presented increased

mechanical strength. Additionally, TiO_2 within the printed matrix was able to quench the intrinsic fluorescence of the rhodamine 6G up to 22 % after 4 h of sunlight exposure. Martín de Vidales *et al.* [60] also made their own TiO_2 doped filaments to 3D print floating photocatalysts for degradation of methylene blue (MB). To prepare the filament, they mixed granulated low-density polyethylene (LDPE) and TiO_2 with a dispersing agent. Then, the mixture was extruded, and the filaments were used in the FDM printer to obtain square meshed structures. The 3D printed structure resulted in an increase in degradation since a higher active surface is available to oxidize the MB, and, compared to TiO_2 powder, the structure has the additional benefit of not requiring a separation step. Carbon materials have also been integrated into filaments for FDM. This is the case of the study reported by Gnanasekaran *et al.* [205], who prepared their own filaments of polymer and nanocomposites of carbon nanotubes (CNT) and graphene. To formulate their filaments, they dispersed CNT or graphene in isopropanol by sonication. Then, a certain amount of thermoplastic polybutylene terephthalate (PBT) was added, and later, the isopropanol was left to evaporate at 90 °C. After drying, the melt mixed composite was fed to an extruder to get filaments of 3 mm diameter. Those filaments were used in a FDM printer in which the nozzle was heated between 200 and 260 °C for the deposition and, to prevent the material warping, double-sided tape was set as printing substrate over the platform at 70 °C. TEM images showed that the graphene platelets were perfectly dispersed without agglomeration when printing at low temperatures. Contrary, for higher temperatures, some voids are generated, driving to surface roughness. In relation to their functioning, CNT-based materials presented better conductive and mechanical characteristics and performance regarding the graphene-based structure. The preparation of these conductive polymers is very interesting for electrochemical applications where the conductivity of the 3D printed electrodes is mandatory for the final application. Thus, the preparation of good conductive filaments in which the polymeric matrix does not affect the conductive properties of the conductive materials used is a hot topic theme of study. C.Y. Foo *et al*. [208] studied the preparation of printable graphene-based conductive filament to create a range of 3D printed electrodes (3DEs) for its use as

supercapacitors and photochemical sensors. This 3D printed electrode showed a promising capacitive performance (98.4 F g^{-1}) and stable cycling stability (up to 100 charge/discharge cycles) as well as a good sensing behavior with a photocurrent response that exceeded expectations (~724.1 µA) and a lower detection limit (0.05 µM) than a conventional ITO/FTO glass electrode. In turn, Z. Rymansaib *et al*. [209] prepared new conductive blends suitable for 3D printing by adding CNFs and graphite flake microparticles to thermoplastic polystyrene. For that, the polystyrene was first dissolved in the appropriate solvent, and the conductive additives were added. Once the solvent has completely evaporated, the solid thermoplastic composite is extruded into composite conductive filament using a heated aluminum barrel at 220 °C equipped with a 2 mm orifice. A compromise of good electrical conductivity and excellent electrode surface properties with good mechanical and printing characteristics was achieved with 80 wt% polystyrene, 10 wt% carbon nanofibers, 10 wt% graphite flakes. The electrode obtained with this formulation was used in the detection of trace metals, obtaining a good performance comparable to results achieved with other types of conventional electrodes.

Despite the possibility of this methodology being applied to diverse active compounds, the combination with thermoplastics maintains the limitation of the operational temperature; moreover, results suggest that a big part of the particles remains embedded in the plastic matrix together with the porosity blockage, also reducing its activity and cost-effectiveness. In addition to this methodology, there are other alternatives to structure novel catalytic materials: printing with more than one material (when using a FDM printer with a double head) to produce a composite product [125]; and using the FDM to create templates of the desired structure for filling them with appropriate materials, and then eliminate the template through thermal treatment. The latter option has already been studied for the synthesis of carbonous and ceramic catalysts. In this regard, Chaparro *et al.* [57, 210, 211] proposed a strategy that combines the FDM and sol-gel polymerization processes, which has enabled the obtention of integral carbon monoliths with complex channel architecture and tailorable

porosity. The influence of the channel geometry and carbon porosity on CuO/CeO_2 catalytic performance was identified with the CO-PrOx reaction. The synthesis methodology consisted of printing polymeric templates from FDM of Co-polyester (CPE+, selected owing to its high chemical stability), which served as a negative of complex interconnected channels. Later, those printed templates were put into glass tubes and filled with a solution of resorcinol, formaldehyde, and water in different ratios (R/W). The controlled polymerization process was held at room temperature for 1 day, at 50 °C for 1 day, and at 80 °C for the subsequent 5 days. Once this process had finished, the organic gel was unmolded and dried for its further slow carbonization (in N_2 atmosphere at 900 °C for 2 h). The selected active phase, Cu/CeO_2, was loaded via dip-coating in an ethanolic solution, achieving a deposition of ~110 mg. Drying and thermal treatment at 250 °C in air was also realized. According to TGA analysis, thermal stability was affected by active phase distribution; however, all supported catalysts exhibited stability up to 500 °C in oxidizing conditions, thus being useful in a wide range of reactions and overcoming the limitations imposed by previous methodology. The pore size distribution and macropore volume are related to the size and interconnection of primary particles, which can be controlled by varying the water content for polymerization. The higher the water content, the greater the particle size and lower their interconnection leaving larger pore size and macropore volume. As the pore size and macroporosity increase, the active phase distribution along the carbon improves thus the catalytic activity as well. Nevertheless, too high-water content generates heterogeneous pore size distribution and leads to preferential flow pathways. High and stable CO conversion (~98 %) and CO selectivity (~99 %) were achieved at 104 °C. Authors followed the same procedure to produce carbon monoliths but employed them as support for Ni/CeO_2 catalyst for CO_2 methanation [211]. The textural and chemical properties of carbon can be tuned to improve the dispersion and attaching of active phases. They noted that their novel design forced turbulent flow regime within the channels, thus enhancing the CO_2 methanation rate about 25 % at 300 °C. This approach allowed the fabrication of pure and integral carbon monoliths with specific and complex designed channels not attainable by conventional methods,

as well as a controlled porosity. Similarly, Li *et al.* [212] combined template printing by FDM and the polymerization process to generate carbon monoliths. In this case, the authors employed a PLA filament to print templates made of cylinder, tetrahedron, and tetrakaidecahedron periodic units. Those templates were filled with a phenol-formaldehyde paste to later follow polymerization, calcination, and wash coating processes. High structural integrity, precise replica of the templates, but a high shrinkage of about 67 % were obtained in the fabricated monoliths. The tortuous channels in the monoliths synthesized with tetrahedron units led to a CO conversion increase of about 32 % regarding straight channels, which is related to the reactant and products transport enhancement between the catalyst surface and fluid, as well as the heat release.

In relation to the use of ceramic fillers, an equivalent methodology was followed by Alimi *et al.* [38] to obtain alumina monoliths with immobilized palladium for its use in the epoxidation of styrene. Polylactic acid (PLA) filament was fused to print the conventional monolithic template, which was further filled with γ-Al_2O_3 and sodium silicate, dried, and calcined for the final immobilization of palladium nanoparticles by deposition-precipitation method. The XRD analysis confirmed the obtention of ordered silica since the characteristic peaks of Al_2O_3 were observed, though those peaks were reduced after the addition of palladium nanoparticles. In terms of porosity, an increment in the surface area from the powder to the monolith was observed, probably due to the incorporation of SiO_2; however, this area was later reduced because of pore blockage with Pd. The authors observed that the lower the flow rate, the greater the conversion, and that a low residence time prevents the formation of side products. As expected for its endothermic nature, the styrene conversion raised (58 %) with the increment in temperature (>85 °C) with a good selectivity (70 %) to styrene oxide. Also, the high surface area to volume ratio between the substrate and the catalyst helped to improve the conversion. It is important to highlight the effectiveness of the deposition method since the samples presented only 0.3 % of the Pd leached after 7 cycles.

This methodology has been proven to enable the synthesis of monoliths of different geometries with an excellent replica of the templates. The use of filler materials such as carbon precursors and ceramics has improved the catalysts chemical properties and stability. Additionally, compared to other synthesis methods, which require the use of binders and plasticizers, the absence of additives in the fillers allows for keeping unchanged the desired characteristics of the precursors (e.g., surface area and active sites). Also, the need for some additional steps, like polymerization, carbonization, or sintering, is compensated by the increase in their possible catalytic applications. Notwithstanding, authors have reported the existence of shrinkage in the final structure (varying from 10 to 67 % depending on the materials and process conditions), which must be taken into consideration while designing the monoliths.

2.3.5. Binder Jetting

The binder jetting (BJT) technology consists of the injection layer-by-layer of a liquid binder agent on a powder bed to build the object (***Figure 2.29***). The process begins with the deposition of a powder coat of a certain thickness on a build platform. Then, by means of a print head, the binder is injected to selectively join or fuse the material according to the CAD pattern. Later, the build platform is moved, and a new powder coat is disposed to continue with the printing process [125]. Due to the residual powder and the binder, no support structure is needed [213]. Once the printing is finished and the binder is completely set, the so-called "green object" is removed from the printing bed, and excess powder is withdrawn by compressed air. In order to grant mechanical properties, the curing of the binder, and sintering are done [214].

Compared to powder bed processes such as LM and LS, a wider range of materials can be used since there is no restriction of melting point [125, 213, 214]. Nevertheless, several factors such as materials used (the relationship of the properties of powders and binders), layer thickness, and delay time of spreading a new layer must be taken into account to prevent defects in the printed object [216]. Because of those

drawbacks, the binder jetting methodology has practically not been used in the production of 3D structures for supporting catalysts.
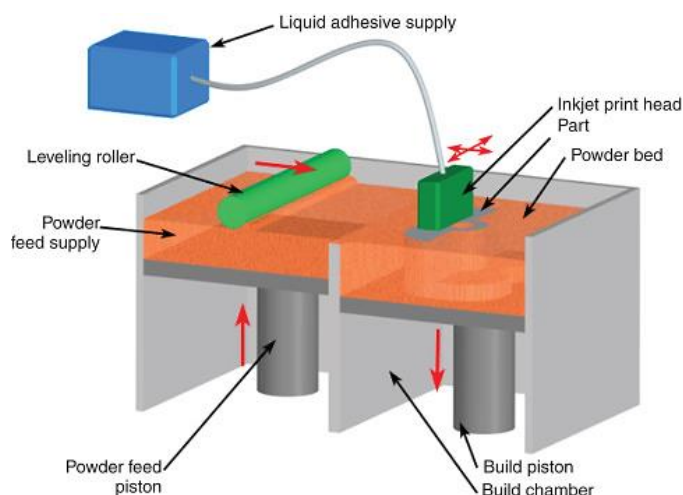
Figure 2.29. Schematic of the binder jetting (BJT) printing process. Taken from [215].

In this regard, Bui *et al.* [217, 218] have reported the use of the BJ technique to produce catalysts, initially in pellet configuration but later in monolithic shape. In their first approach, the authors applied the binder jetting technique to print spherical and cylindrical pellets of Ni-Al catalyst for CO_2 methanation. Later, the authors also leveraged this procedure to obtain a monolithic shaped catalyst and compared it to the DIW process [219]. In this case, alumina monolithic supports were fabricated by both DIW and BJ and later loaded with Pt by dip-coating to test them in the dehydrogenation of perhydro-dibenzyltoluene. For the BJ process, the authors prepared the bed material by mixing boehmite and bayerite powdered binders with polyvinylpyrrolidone (PVP) to bind the powder upon contact with the printing liquid. On the other hand, the printing liquid formulation consisted of boehmite, isopropyl alcohol, and butanediol. After printing, the sample is depowdered, dried, and calcined (600 °C for 2-4 h) to remove PVP binder. Then, a further infiltration with an aqueous solution of boehmite to introduce additional particles into the porous particle framework and increase stability, was realized. In comparison, the DIW ink was formulated just with boehmite and acetic acid. A calcination step was carried out in the same way for both techniques (1100 °C for 3 h), followed by the dip-coating with $H_3Pt(SO_3)_2(OH)$. While DIW creates smoother

surfaces, the BJ process produces more porous and rougher surfaces. In this respect, the porosity of BJ catalyst seems to be affected by the addition of binders; therefore, with the debinding treatment the surface area increased, whereas from the calcination step a reduction is observed probably due to some Ni sintering. Also, the BJ printed structure exceeded the designed dimensions, which is caused by hardware related printing inaccuracies or bleeding (which is a macroscopic flow of binder caused by high ink saturation level). Besides, shrinkage is 3 times higher than that of the DIW support for low calcination temperatures and is almost the same for 1000-1200 °C calcined structures (~12 %). At calcination temperatures above 1000 °C, the compressive strength of DIW increases almost 4 times regarding BJ, though, for both materials, this treatment led to a drastic surface area reduction. The Pt loading resulted in higher for the BJ monolith since it contained more meso and macropores; however, both catalysts showed equal dehydrogenation rates of about 2.7 $gH_2 \, g_{Pt}^{-1}min^{-1}$.

Taking this case, the achievement of the desired design and dimensions is apparently harder with the binder jetting technique since the deposition of the binder ink is not as precise as other AM technologies presented above. Moreover, the use of binders, as usually observed with other techniques, implies a porosity blockage, and thus a post-treatment to eliminate them from the structures is needed. Nevertheless, the liquid ink properties are not as challenging as those required for preparing inks for DIW or resins for vat photopolymerization processes. Therefore, when controlling the printing hardware and ink level, binder jetting may be an attractive option for producing monolithic catalysts with rough surfaces. This characteristic can be used as an asset by avoiding the necessity of pre-treatments that are often required to facilitate the deposition of active compounds on other materials.

2.3.6. Sheet Lamination

The sheet lamination (SHL) technique, also named laminated object manufacturing (LOM), consists of laminating a sheet of printing material with the help of rollers, then bonding and cutting (or vice versa, depending on the configuration of the equipment) consecutive layers of the material until the construction of the piece is

completed (**Figure 2.30**). To bond layers different thermal and mechanical sources of energy are used, involving bonding mechanisms such as adhesive bonding, thermal bonding, sheet metal clamping, and ultrasonic welding [220]. The cutting is made with a laser (usually CO_2) or a blade (mechanical cutting), with a depth of the thickness of a layer following a pattern generated by a computer program [125].

This is a hybrid additive manufacturing process, which allows the construction of larger parts at higher production speeds, also avoiding defects caused by solidification process, however, in some cases a final processing is required to improve the surface quality. Moreover, traditional SHL is not able to produce multi-material structures, and the capability for obtaining complex geometries is not comparable with other AM techniques since it is not adapted to finely detailed structures and depends on the shape and thickness of the sheets [220, 221]. In consequence, the limitations of laminated object manufacturing have inhibited its application in catalyst synthesis.
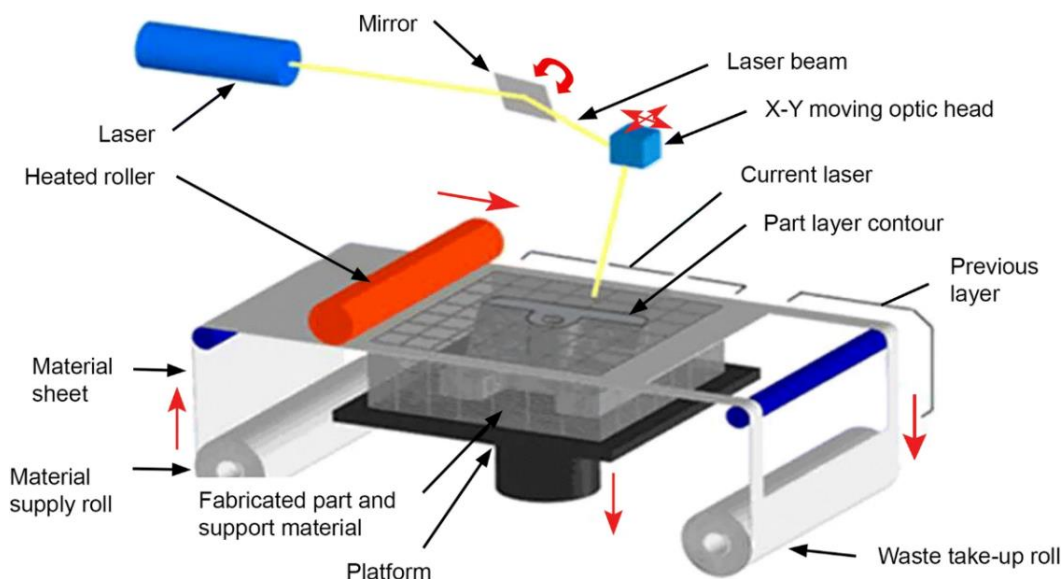
Figure 2.30. Schematic of the sheet lamination (SHL) printing process. Taken from [222].

Scarcely, the work realized by Lei *et al.* [223] can be pointed out, who proposed the combination of LM and laminated object manufacturing to obtain a novel catalyst for hydrogen production via methanol steam reforming. 316 L stainless steel sheets

were produced by laser melting, subsequently cleaned and coated with an aqueous solution of $Cu(NO_3)_2$, $Zn(NO_3)_2$, $Al(NO_3)_3$, $Zr(NO_3)_4$, and Al_2O_3 to strength the adhesion. Later, multiple hexahedral mesh sheets were bonded through sheet lamination to conform a structure with periodic units. This material had a large specific surface area and connectivity, and some surface roughness that favored the active phase adhesion was also observed. Additionally, the catalyst displayed a good performance in methanol steam reforming (reaching up to 90 % methanol conversion), which also resulted in superior compared to a commercial stainless-steel fiber sintered felt (~10 % higher). Whereas the structure of commonly used metal foams for this catalytic process cannot be entirely controlled or reproduced [224-226], the procedure proposed by Lei *et al.* allows to obtain reproducible materials with a high exposed surface area for depositing the active phase.

2.3.7. Structure Geometry Effect

Thus far, the research of additive manufacturing applied as an innovative tool in monolithic catalysts synthesis has been focused on the modification or generation of new materials — either resins, inks, or filaments —, adjustment of printing techniques, and/or implementation of post printing treatments to modify the structure or load it with other compounds. Notwithstanding, most works report the use of additive manufacturing to prepare monoliths of conventional configuration of straight and parallel channels, and few studies have been realized to analyze the effect of channel geometries on catalytic performance. However, it is important to point out that additionally to the properties provided by the diverse available materials and additive manufacturing techniques, 3D printing offers the possibility of designing the channel geometry, therefore exceeding the limit of straight configuration imposed by conventional synthesis methods. This may result in a huge advantage in reactions where diffusion, mixing and/or heat transfer limit the performance, regardless of the base material (either polymer, ceramic, carbon, metal, etc.).
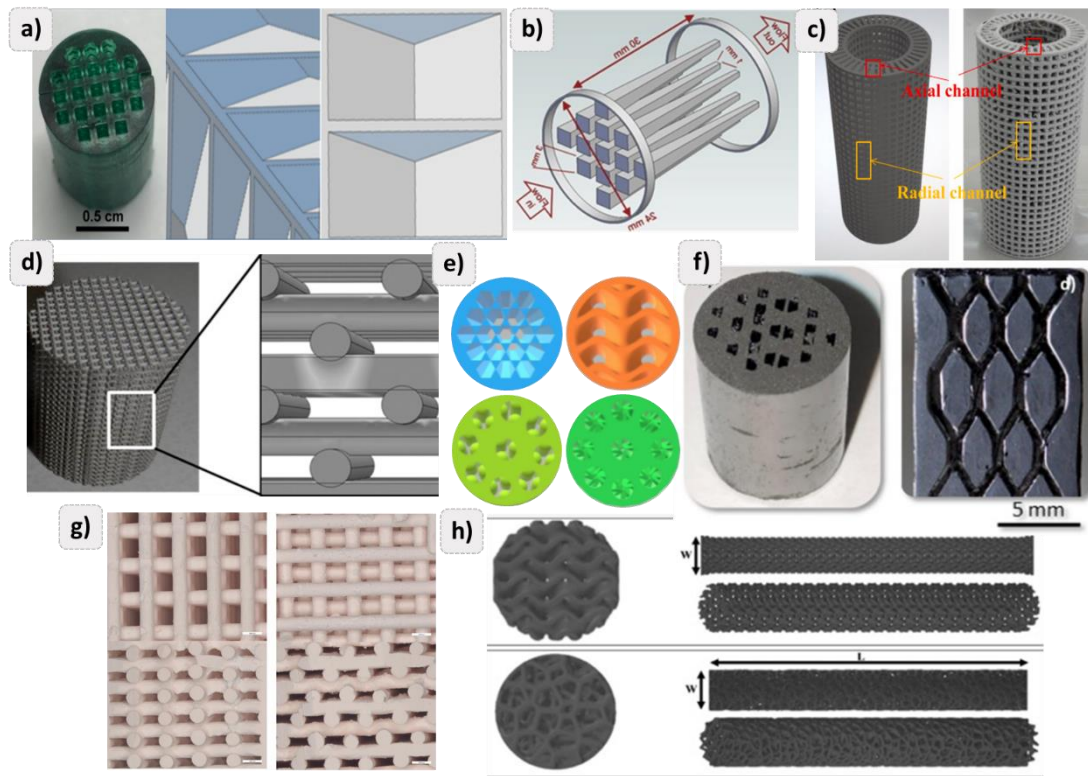
Figure 2.31. Examples of novel and non-straight channels designs: a) prismatic cavities along the channels [86]; b) asymmetrical channels [95]; c) incorporation of axial and radial channels [206]; d) stacked zigzag channels [191]; e) periodic lattices of different shapes [140]; f) interconnected crisscrossed channels [57]; g) stacked woodpile-like layers [184]; and h) Gyroid and Voroni periodic units [51].

In regard to the scarce non-traditional monolithic structures developed so far the following modifications can be mentioned: i) addition of circular or square grooves lengthwise the channels (***Figure 2.31a***), ii) asymmetrical channels with reduction of the cross section (***Figure 2.31b***), iii) combination of axial and radial channels (***Figure 2.31c***), iv) zigzag shaped channels (***Figure 2.31d***), v) pseudo-random and periodic lattices (***Figure 2.31e***), and vi) interconnected channels — either by crisscrossed channels (***Figure 2.31f***), stacking woodpile like layers with different offset angles (***Figure 2.31g***), or use of periodic units or fluid guiding elements (***Figure 2.31h***) —. One of the benefits of using complex designs is the amelioration of the deposition of active phases, as corroborated by Chaparro *et al.* [86]. The authors used SLA

technique to print two non-conventionally shaped monoliths with hollows through the structure (**Figure 2.31a**). They explored and compared the effect of the active phase anchoring of those grooves and the doping of the liquid resin with inorganic materials. The results demonstrated that the use of the advanced design leads to load similar quantities of active phase in relation to doped monoliths while necessitating a reduced number of steps.

Furthermore, some authors have reported the advantages of their novel and sophisticated monolith designs in comparison to conventional honeycomb like structures. The principal effect of non-straight channels has been proven to be the generation of turbulence within them due to tortuous paths, contrary to conventional straight channels, which force laminar flow, creating radial diffusion limitations [95, 204]. This, in turn, boosts the interaction between reagents and catalyst, increases the fluid diffusion and mass transfer, as well as improves the heat transfer [184]. In relation to catalytic activity, the transfer improvement is associated with better and faster transportation of reactants and products between the catalyst surface and the fluid, consequently resulting in an augment of reaction rates and conversions [51, 57, 140].

In that respect, Chaparro *et al.* [210] compared a carbon monolith of interconnected crisscrossed channels (that split and join successively along the structure, as shown in **Figure 2.31f**) with a carbon monolith of conventional straight channels to analyze the influence of the channel geometry on their catalytic performance. The carbon monoliths were used as supports of Cu/CeO_2 active phase in the preferential oxidation of CO in the presence of H_2. Due to their porosity, the active phase was loaded both in the surface and carbon matrix. Results showed that the gas diffusion through the channels and carbon matrix is influenced by the design. The tortuous path in the advanced design favors the turbulent flow regime despite the flow rate employed. This implies an improvement of the gas diffusion through the carbon network which, in turn, increases the active phase accessibility and its interaction with the reactants. Together with the activity and availability of the Cu/CeO_2, the catalytic efficiency enhanced with the non-straight channels as observed in the T_{50}

(Temperature to achieve the 50 % of CO conversion) that decreased around 13 °C (using 240 mL min^{-1}) regarding the conventional straight-channeled monolith.

Utilizing the flexibility offered by 3D printing, C. Chaparro-Garnica *et al.* [87] reimagined the conventional concept of channeled monoliths for catalysis, creating advanced non-channeled monolithic (NCM) supports (**Figure 2.32a**-*ii*). These supports are constructed from multiple transversal discs featuring active phase deposits, with strategically placed slits allowing gas circulation. The advantages of this new NCM were evaluated in the CO-PrOx reaction. Remarkably, this material exhibited superior catalytic activity compared to traditional channeled monoliths (**Figure 2.32a**-*i*), showcasing the potential of this innovative approach for enhanced catalytic processes. Turbulence manifests within the fluid pathway in the NCM, facilitating the transfer of reagents and products to and from the active sites within the fluid bulk, thereby promoting the rate of chemical reactions. Additionally, the non-channeled monolith enhances heat dispersion through its convoluted pathways, thereby reducing local temperatures at the active sites. Consequently, the transportation of reactants and products within the monoliths plays a pivotal role, with the inner geometry of the monoliths exerting a significant influence on this process.

Hajimirzaee *et al.* [167] prepared cordierite non-linear channel catalysts washcoated with a Pd:Pt/Al$_2$O$_3$ active phase for the oxidation of methane. Cordierite was obtained by a solid-state reaction at 1200 °C after 3D printing a paste made with cordierite precursors, water, and ethylene glycol. The structure was printed using diverse offset angles between meshed layers (**Figure 2.32b**); nevertheless, the walls obtained were 70 % thicker than a commercial monolith due to limitations for extruding the paste. Therefore, less open area is achieved, especially for lower offset angles, leading to higher backpressure compared to commercial straight channels cordierite monoliths. On the positive side, turbulence is induced causing irregular fluctuations and mixing so a better catalytic activity is reached. At moderate and high inlet temperatures, in which the reaction rate is controlled by mass transfer, the turbulence produced within the non-straight channels also increases reaction rates, despite the

fact it had a minor cell density and lower amount of precious metal in relation to conventional diesel oxidation catalyst, making it more cost-effective. Besides, the same methodology was followed by the authors using a commercial porcelain paste fixing the offset angle between layers in 90° [190]. The nozzle blockage with the highly viscous ink difficulted the use of a nozzle smaller than 0.7 mm in diameter, thus limiting the cell density that resulted in 4 folds lower than a conventional diesel oxidation catalyst (DOC) employed as reference. The catalyst was also evaluated in the methane oxidation but in a dual fuel system. Similar conclusions were attained since the 3D structure induces internal turbulence, thus improving internal and external mass transfer which increases the reaction rate.
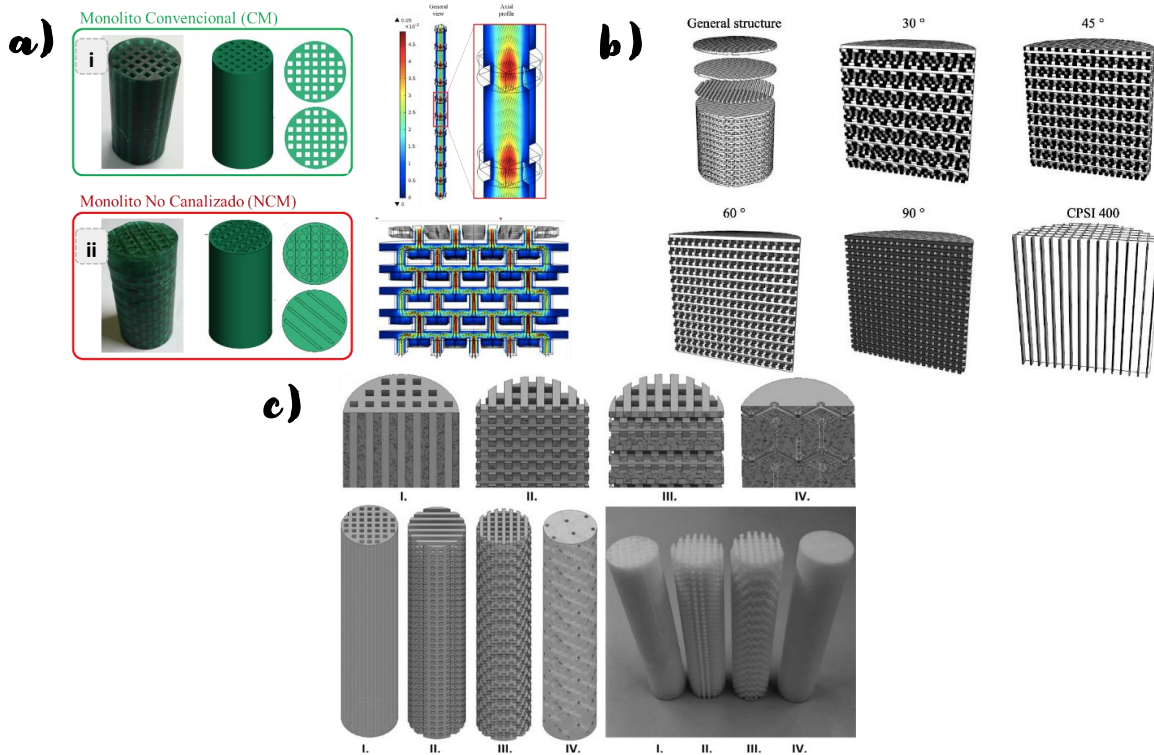
Figure 2.32. a) Geometry of conventional honeycomb monolith (CM) with straight channels (i) and advanced non-channeled (NCM) design composed by several transversal discs containing deposits for the active phase loading and slits through which the gas circulates (ii), and velocity profiles inside of NCM, adapted from [87]; b) General structure and cross sectional view of 3D printed ceramic substrates utilizing different offset angles between meshed layers from [167]; and c) Four geometry

designs used for FDM of polymeric monoliths: straight channels (I), orthogonal mesh layers (II), shifted orthogonal mesh layers (III), and diamond structure in which each channel connects to three other channels in a tetrahedral node (IV) from [203].

The effect of the channel geometry on the hydrodynamic properties, pressure drop, and residence time distribution was analyzed by Hock *et al.* [203]. They obtained cylindrical monoliths with varying geometries of transport channels by a fused deposition modeling (FDM) 3D printer from thermoplastic polymers (**Figure 2.32c**). The hydrodynamic properties, pressure drop, and residence time distribution are affected by the monolith design. Monoliths with less complex structures (I and II) present minor pressure drop, whereas monoliths with significantly higher tortuosity of the pore channels result in higher pressure drops (III and IV). However, the effect of the channel geometry in the catalytic performance was not analyzed.

Moreover, the heat transfer also helps in exothermic reactions to the heat release, thus avoiding the generation of hot spots within the material. In that context, Gonzalez et al. [143] prepared advanced-designed monolithic catalysts for CO_2 methanation using stainless steel powder in LM printing. The channel configuration was based on different sized flow guiding elements used to bifurcate the stream and switch its position throughout the catalyst. The obtained results evidenced that the highest sized channels performed better than the others. This was attributed to a favored radial heat transfer, mixing, and turbulence established, which enhanced the catalytic activity and obtained almost 75 % conversion at 400 °C. Moreover, it was not possible to establish a linear relation between the channels size and their catalytic activity; however, all of them presented better performance and selectivity regarding parallel straight channels used as reference. Lefevere *et al.* [170] used DIW to obtain ZSM-5-coated stainless steel (316L) monoliths with woodpile-like layers of straight or zigzag channels. Monolithic catalyst achieved higher conversions of methanol compared to its powder counterpart (approximately 20 %), while maintaining the selectivity over 99 %. These results were attributed to better diffusional transport and since the dehydration of methanol to dimethyl ether is an exothermic reaction, the

structures could help to remove the heat of the reaction. Additionally, the monolith with "zigzag" tortuous channels favors turbulence, thus raising the yield of light olefins. A similar procedure but with a different coat (Ni/alumina) was realized to test the catalytic activity in CO_2 methanation [191]. In which the improvement of CO_2 conversion (around 30 %) over the "zigzag" channeled monoliths due to a higher contact reagent-catalyst was also confirmed.

Likewise, other benefits of advanced designs have been observed: enlargement of the temperature region in which chemical control is maintained since transport limitations imposed in straight channels are overcome [87]; the possibility of adjusting the catalytic product distribution due to material selectivity [140]; smaller pressure drop compared to powder counterpart [107, 212]; even with fewer amount of active phase, the dispersion together with the promoted turbulence allows greater conversions regarding conventional catalyst, thus resulting more cost-effective; and the higher cell density, the higher catalytic activity due to distribution and accessibility of active sites [107].

2.4. Carbon gels

Carbon gels are nanostructured porous carbons obtained through carbonization of organic gels [227-229]. Sol-gel polycondensation of organic monomers such as resorcinol (R) and formaldehyde (F), first outlined by Pekala [230], is the conventionally used method to synthesize those organic gels [227-229, 231]. This synthesis consists of four steps: 1) sol mixture preparation; 2) gelation and curing of the gel, for which the presence of a catalyst, concentration of solids, the initial pH, temperature, and time play a critical role; 3) drying; and 4) carbonization.

On the other hand, for the gelation and curing the polycondensation of resorcinol and formaldehyde follows two stages. In the first stage, formaldehyde molecules undergo an addition reaction with the free positions on the aromatic ring of resorcinol, resulting in the formation of hydroxymethyl-R derivatives. Successively, a condensation reaction occurs through the hydroxyl groups, with water being produced

as a byproduct. This process leads to the formation of poly-aromatic compounds, where the rings are linked to each other via methylene or methylene-ether bridges [228]. The addition reaction is catalyzed by bases, while the condensation reaction is catalyzed by acids [228, 232]. As a result, the polycondensation of resorcinol-formaldehyde yields clusters of macromolecules, which further react with each other to form colloidal particles [233]. Initially, these particles are independent, forming a colloidal solution (sol). Over time, through Brownian motion, they begin to aggregate due to the reactions occurring on their surface groups to finally form a gel with an intertwined structure [233].

According to the previously described process, carbon gels are known to be versatile porous materials whose properties and structure at the nano, micro, and macroscopic levels can be adjusted by appropriately selecting the reagents, reagents ratios, catalyst, and synthesis conditions (such as pH, temperature, and polymerization time) [227-229, 231, 234, 235]. These factors significantly influence the synthesis as they can, for example, alter the interactions between molecules or favor either the addition or condensation reactions by modifying the solution pH. The post-treatment conditions, including drying methods and carbonization procedure, are also important to avoid shrinkage and collapsing of porous structure [227, 233]. Moreover, these materials can be prepared in different shapes, including powder, pellets, monoliths, thin films, or coatings, which facilitates their application in a wide range of processes.

2.5. Justification

In over 80% of industrial processes, catalysts play a vital role in overcoming kinetic limitations, reducing activation energy demand, and enhancing selectivity towards desired products. Traditional catalytic supports, such as powder, granules, or pellets used in catalytic beds, often struggle to manage sizable volumes efficiently. Achieving optimal system configuration to minimize pressure drop, improve fluid dynamics, and maximize catalyst efficiency is crucial in industrial settings. Monolithic structured catalysts have demonstrated superior performance compared to packed bed systems, particularly in handling high flow rates.

Monolithic supports are commonly produced by extrusion, pressing of different materials, or corrugation of metallic sheets, with active phases loaded onto the exposed surfaces of their walls. However, these supports often exhibit low porosity and may require pre-treatment or pre-coating to enhance surface area and catalyst adhesion. Moreover, their synthesis methods constrain the geometry of monolith channels to straight and parallel configurations. Although conventional honeycomb monoliths perform adequately at high flow rates with low pressure drop, their straight channels promote laminar flow due to friction forces, leading to reduced interaction between reagents and active phases. The recent introduction of 3D printing technology in catalysis represents a promising opportunity for innovative design and production of structured catalytic materials. The versatility of 3D printing allows for the controlled production of pieces with diverse compositions and adapted shapes, overcoming current limitations in monolith manufacturing.

On the other hand, in light of increasing concerns about global warming and greenhouse gas emissions, the promotion of sustainable energy sources, such as biogas generated from organic waste and anaerobic digestion, has become imperative. However, the enrichment of biogas to improve its applicability involves separating CO_2 content, which cannot be released into the environment due to pollution concerns. Therefore, valorizing the substantial CO_2 volumes from biogas facilities is crucial for maintaining biogas' status as a renewable fuel. Among various CO_2 valorization routes, methanation appears promising, as methane produced can be injected directly into the natural gas grid. However, the energy-demanding dissociation of CO_2 and the exothermic nature of the methanation reaction pose challenges, including catalyst sintering and deactivation. Hence, precise catalyst selection is essential to enhance methanation activity and improve mass and heat transfer properties to prevent catalyst deactivation and ensure productivity.

The integration of 3D printing with the properties of the sol-gel process will enable to obtain carbon monolithic supports with sophisticated structures, unattainable through conventional methods, for use as catalysts in CO_2 methanation. These novel

designs will promote turbulent fluid flow regimes within the channels, enhancing heat and mass transfer and improving reagents-catalyst interaction and heat elimination. Additionally, the characteristic porosity of pure carbon will facilitate active phase deposition, leading to a more homogeneous distribution accessible to reagent flow.

2.6. Hypothesis

The integration of 3D printing for creating intricate channel molds, along with the versatility of the sol-gel process, presents an opportunity to fabricate monolithic carbon supports for catalysts with sophisticated designs. These advanced designs are structured to enhance the interaction between reagent flow and the active phase embedded within the support, thereby augmenting the catalytic efficiency of a reaction of significant socioeconomic and environmental importance, such as CO_2 methanation. This advancement holds promise for surpassing the capabilities of currently available supports.

2.7. Objectives

2.7.1. General objective

The main objective of this Doctoral Thesis is to develop carbon monoliths with adapted geometry using additive manufacturing technology and sol-gel process to enhance their efficacy as catalytic supports. The production of carbon monoliths with advanced and complex channel geometries, non-attainable through conventional synthesis methods, is effectuated by 3D printing polymeric templates of the desired channel configurations. The synthesized carbon monoliths are used as catalyst supports by wash coating them with the catalytically active compound Ni/CeO_2 to evaluate their performance in CO_2 valorization by the methanation reaction. The effect of the proposed novel geometries on their catalytic functioning is analyzed, as well as the comparison of a commercially available conventional honeycomb cordierite monolithic catalyst.

As an additional work apart from the Thesis project, it is aimed to analyze the performance of advanced oxidation processes, using sulfate radicals, for degrading

metformin in aqueous solution. To assess the significance different operational conditions —initial metformin concentration (C_{A0}), oxidant concentration (C_{ox}), temperature (T), and pH— on metformin degradation through an analysis of variance (ANOVA). Finally, to propose a degradation pathway by analyzing the products obtained from degradation and determine their toxicity.

2.7.2. Specific objectives

To validate the hypothesis and achieve the general objective of the thesis, which aims to prepare catalyst supports through 3D printing to improve the performance of conventional supports, the following specific objectives are proposed:

- Analyze the influence of the straight channel configuration in a commercial honeycomb cordierite monolith on the catalytic performance of the Ni/CeO$_2$ active phase in CO$_2$ methanation at atmospheric pressure.

- Design intricate channel geometries utilizing 3D printing technology, non-based on straight and parallel configuration, to increase the residence time of gases inside the channels and promote turbulent circulation regime, thereby improving the interaction catalyst-fluid and the performance of the monoliths.

- Employ Fused Deposition Modeling technique (FDM) to 3D print polymeric templates which serve as negatives for the designed channels.

- Produce carbon monolithic supports by filling the printed templates with a carbon gel precursor solution and subsequently removing the polymeric templates through a controlled carbonization process.

- Synthesize a catalytic active phase for the CO$_2$ methanation reaction, consisting of Ni supported on CeO$_2$, and load it onto the carbon supports.

- Characterize the chemical and physical properties of the active phase, both in powder and supported on the carbon monoliths, to assess its distribution along the structure and the effect of the loading process.

- Evaluate the catalytic performance of the prepared monoliths in CO_2 conversion to methane via the methanation reaction at atmospheric pressure while analyzing the effect of the designed geometries.

In relation to the study of metformin degradation in aqueous solution by sulfate radicals, the specific objectives considered are as follows:

- Establish an appropriate experimental response surface design to analyze the significance of operational conditions, initial metformin concentration (C_{A0}), oxidant concentration (C_{ox}), temperature (T), and pH, on metformin degradation.
- Perform metformin degradation through advanced oxidation processes using a $UV/S_2O_8^{2-}$ system, and according to the experimental design, investigate the influence of variables on degradation through an analysis of variance.
- Estimate the mineralization percentage (%TOC) by analyzing the Total Organic Carbon (TOC) and assess the significance of the studied factors on the %TOC.
- Identify degradation byproducts through mass spectrometry and propose a degradation mechanism.
- Determine the toxicity of the final solutions based on the growth inhibition percentage of cell biomass of *Chlamydomonas reinhardtii* culture (CC-125), to conclude on the appropriateness of the method.

2.8. References

[1] EPA United States Environmental Protection Agency. (2024). *Greenhouse Gas Emissions: Overview of Greenhouse Gases*, EPA. Retrieved February 16, 2024, from https://www.epa.gov/ghgemissions/overview-greenhouse-gases

[2] Chen, Y., Zhang, Y., Fan, G., Song, L., Jia, G., Huang, H., Ouyang, S., Ye, J., Li, Z., & Zou, Z. (2021). Cooperative catalysis coupling photo-/photothermal effect to drive Sabatier reaction with unprecedented conversion and selectivity. *Joule, 5*, 3235-3251. https://doi.org/10.1016/j.joule.2021.11.009.

[3] Canales, R., Gil-Calvo, M., & Barrio, V. L. (2023). UV- and visible-light photocatalysis using Ni–Co bimetallic and monometallic hydrotalcite-like materials for enhanced CO2 methanation in Sabatier reaction. *Heliyon*, *9*, e18456. https://doi.org/10.1016/j.heliyon.2023.e18456.

[4] Kiani, A., Dubois, L., Chauvy, R., Lippi, R., & Daiyan, R. (2024). Renewable Methane Production. In A. Martin (Ed.), *Encyclopedia of Sustainable Technologies* (2nd Ed.). Vol. 3, pp 313-30. Elsevier. https://doi.org/10.1016/B978-0-323-90386-8.00040-1.

[5] Uchida, H., Harada, M.R. (2019). Chapter 5.3.3 - Application of Hydrogen by Use of Chemical Reactions of Hydrogen and Carbon Dioxide. In P. E. V. de Miranda (Ed.), *Science and Engineering of Hydrogen-Based Energy Technologies* (pp. 279-289). Academic Press. https://doi.org/10.1016/B978-0-12-814251-6.00013-7.

[6] Tsiotsias, A. I., Charisiou, N. D., Yentekakis, I. V., & Goula, M. A. (2020). Capture and Methanation of CO2 Using Dual-Function Materials (DFMs). *Chemistry Proceedings, 2*(1), 35. https://doi.org/10.3390/ECCS2020-07567.

[7] Freccero, R., Spennati, E., Garbarino, G., & Riani, P. (2024). Intermetallic based materials for Sabatier reaction: Surface understanding, performance assessment and comparison with commercial catalyst. *Applied Catalysis B: Environmental*, 343, 123532. https://doi.org/10.1016/j.apcatb.2023.123532.

[8] Wai, S., Ota, Y., & Nishioka, K. (2021). Performance analysis of Sabatier reaction on direct hydrogen inlet rates based on solar-to-gas conversion system. *International Journal of Hydrogen Energy, 46*, 26801-26808. https://doi.org/10.1016/j.ijhydene.2021.05.156.

[9] Alli, Y. A., Oladoye, P. O., Ejeromedoghene, O., Bankole, O. M., Alimi, O. A., Omotola, E. O., Olanrewaju, C. A., Philippot, K., Adeleye, A. S., & Ogunlaja, A. S. (2023). Nanomaterials as catalysts for CO2 transformation into value-added

products: A review. *Science of The Total Environment*, *868*, 161547. https://doi.org/10.1016/j.scitotenv.2023.161547.

[10] Gómez-Flores, K. A., Solís-García, A., Jimenez, S. A., Cervantes-Gaxiola, M. E., Castillo-López, R. I., Ruelas, J. P., Gómez, S. A., Flores-Aquino, E., & Zepeda, T. A. (2024). Modulating selectivity in CO2 methanation through rhodium catalysts supported on zirconia-chemically grafted SBA-15. *Molecular Catalysis, 558*, 114035. https://doi.org/10.1016/j.mcat.2024.114035.

[11] Mustafa, A., Lougou, B. G., Shuai, Y., Wang, Z., & Tan, H. (2020). Current technology development for CO2 utilization into solar fuels and chemicals: A review. *J Energy Chem*, *49*, 96-123. https://doi.org/10.1016/j.jechem.2020.01.023.

[12] Wang, H., Yao, H., Pan, L., Cui, L., Wang, Y., Tao, Z., & Li, D. (2023). Theoretical research the mechanism on the Ir/Ni (111) catalyst surface for CO2 methanation reaction. *Molecular Catalysis*, *550*, 113605. https://doi.org/10.1016/j.mcat.2023.113605.

[13] Wijayapala, R., Yu, F., Pittman, C. U., & Mlsna, T. E. (2014). K-promoted Mo/Co- and Mo/Ni-catalyzed Fischer–Tropsch synthesis of aromatic hydrocarbons with and without a Cu water gas shift catalyst. *Applied Catalysis A: General*, *480*, 93-99. https://doi.org/10.1016/j.apcata.2014.04.044.

[14] Wieclaw-Solny, L., Wilk, A., Chwola, T., Krótki, A., Tatarczuk, A., & Zdeb, J. (2016). Catalytic carbon dioxide hydrogenation as a prospective method for energy storage and utilization of captured CO2. *Journal of Power Technologies*, *96*(4), 213-218.

[15] Shen, L., Xu, J., Zhu, M., & Han, Y. (2020). Essential role of the support for nickel-based CO2 methanation catalysts. *ACS Catalysis*, *10*, 14581-14591. https://doi.org/10.1021/acscatal.0c03471.

[16] Wang, J., Qin, D., Lan, J., Cheng, Y., Zhang, S., Guo, Q., Wu, J., Wu, D., and You, J. (2015). Rh-catalysed direct cyclisation of 1,4-naphthoquinone and 9,10-phenanthraquinone with alkyne: facile access to 1,8-dioxapyrenes and 1,12-dioxaperylenes as orange and red-emitting luminophores, *Chem.Commun. 51*, 6337-6339. https://doi.org/10.1039/C5CC00312A.

[17] Wang, C., Guan, E., Wang, L., Chu, X., Wu, Z., Zhang, J., ... Xiao, F. (2019). Product selectivity controlled by nanoporous environments in zeolite crystals enveloping rhodium nanoparticle catalysts for CO2 hydrogenation. *J.Am.Chem.Soc. 141*, 8482-8488, https://doi.org/10.1021/jacs.9b01555.

[18] Guo, Y., Mei, S., Yuan, K., Wang, D., Liu, H., Yan, C., & Zhang, Y. (2018). Low-temperature CO2 methanation over CeO2-supported Ru single atoms, nanoclusters, and nanoparticles competitively tuned by strong metal–support interactions and H-spillover effect. *ACS Catalysis*, *8*, 6203-6215. https://doi.org/10.1021/acscatal.7b04469.

[19] Jiménez, V., Sánchez, P., Panagiotopoulou, P., Valverde, J. L., & Romero, A. (2010). Methanation of CO, CO2 and selective methanation of CO, in mixtures of CO and CO2, over ruthenium carbon nanofibers catalysts. *Applied Catalysis A: General, 390*, 35-44. https://doi.org/10.1016/j.apcata.2010.09.026.

[20] Renda, S., Ricca, A., & Palma, V. (2021). Study of the effect of noble metal promotion in Ni-based catalyst for the Sabatier reaction. *Int. J. Hydrogen Energy, 46*, 12117-12127. https://doi.org/10.1016/j.ijhydene.2020.05.093.

[21] Solis-Garcia, A., Louvier-Hernandez, J. F., Almendarez-Camarillo, A., & Fierro-Gonzalez, J. C. (2017). Participation of surface bicarbonate, formate and methoxy species in the carbon dioxide methanation catalyzed by ZrO2-supported Ni. *Applied Catalysis B: Environmental, 218*, 611-620. https://doi.org/10.1016/j.apcatb.2017.06.063.

[22] Matsubu, J. C., Yang, V. N., & Christopher, P. (2015). Isolated metal active site concentration and stability control catalytic CO2 reduction selectivity. Journal of the *American Chemical Society, 137*, 3076-3084. https://doi.org/10.1021/ja5128133.

[23] Ashok, J., Pati, S., Hongmanorom, P., Tianxi, Z., Junmei, C., & Kawi, S. (2020). A review of recent catalyst advances in CO2 methanation processes. *Catalysis Today, 356*, 471-489. https://doi.org/10.1016/j.cattod.2020.07.023.

[24] Khuenpetch, A., Choi, C., Reubroycharoen, P., & Norinaga, K. (2022). Development of a kinetic model for CO2 methanation over a commercial Ni/SiO2 catalyst in a differential reactor. *Energy Reports, 8*, 224-233. https://doi.org/10.1016/j.egyr.2022.10.194.

[25] Zhen, W., Gao, F., Tian, B., Ding, P., Deng, Y., Li, Z., ... Lu, G. (2017). Enhancing activity for carbon dioxide methanation by encapsulating (111) facet Ni particle in metal–organic frameworks at low temperature. *Journal of Catalysis, 348*, 200-211. https://doi.org/10.1016/j.jcat.2017.02.031.

[26] Jabotra, G., Yadav, P. K., Kumar, S., & Sharma, S. (2023). CO2/CO methanation over Ru and Ni supported γ-Al2O3: A study on the effect of the stoichiometry of reactant gases. *Molecular Catalysis, 547*, 113365. https://doi.org/10.1016/j.mcat.2023.113365.

[27] Tada, S., Shimizu, T., Kameyama, H., Haneda, T., & Kikuchi, R. (2012). Ni/CeO2 catalysts with high CO2 methanation activity and high CH4 selectivity at low temperatures. *International Journal of Hydrogen Energy, 37*, 5527-5531. https://doi.org/10.1016/j.ijhydene.2011.12.122

[28] Ratchahat, S., Sudoh, M., Suzuki, Y., Kawasaki, W., Watanabe, R., & Fukuhara, C. (2018). Development of a powerful CO2 methanation process using a structured

Ni/CeO2 catalyst. *Journal of CO2 Utilization, 24*, 210-219. https://doi.org/10.1016/j.jcou.2018.01.004.

[29] Tomašić, V., & Jović, F. (2006). State-of-the-art in the monolithic catalysts/reactors. *Applied Catalysis A: General*, *311*, 112-121. https://doi.org/10.1016/j.apcata.2006.06.013.

[30] Hu, R., Chen, Y., Zhang, C., Jiang, S., Hou, H., & Duan, G. (2024). Porous monoliths from polyimide: Synthesis, modifications and applications. *Progress in Materials Science, 144*, 101284. https://doi.org/10.1016/j.pmatsci.2024.101284.

[31] Huang, L., Chen, G., Zhang, G., Fang, Y., Zhu, W., & Xin, Y. (2024). Construction of a highly efficient adsorbent for one-step purification of recombinant proteins: Functionalized cellulose-based monolith fabricated via phase separation method. *Carbohydr. Polym., 335*, 122046. https://doi.org/10.1016/j.carbpol.2024.122046.

[32] Masini, J. C., & Svec, F. (2017). Porous monoliths for on-line sample preparation: A review. *Anal. Chim. Acta, 964*, 24-44. https://doi.org/10.1016/j.aca.2017.02.002.

[33] Heck, R. M., Gulati, S., & Farrauto, R. J. (2001). The application of monoliths for gas phase catalytic reactions. *Chemical Engineering Journal, 82,* 149-156. https://doi.org/10.1016/S1385-8947(00)00365-X.

[34] Yokota, T., Takahata, Y., Katsuyama, T., & Matsuda, Y. (2001). A new technique for preparing ceramics for catalyst support exhibiting high porosity and high heat resistance. *Catalysis Today, 69*, 11-15. https://doi.org/10.1016/S0920-5861(01)00349-2.

[35] Govender, S., & Friedrich, H. B. (2017). Monoliths: A review of the basics, preparation methods and their relevance to oxidation. *Catalysts, 7*(2), 62. https://doi.org/10.3390/catal7020062.

[36] Avila, P., Montes, M., & Miró, E. E. (2005). Monolithic reactors for environmental applications: A review on preparation technologies. *Chemical Engineering Journal, 109*, 11-36. https://doi.org/10.1016/j.cej.2005.02.025.

[37] Williams, J. L. (2001). Monolith structures, materials, properties and uses. *Catalysis Today, 69*, 3-9. https://doi.org/10.1016/S0920-5861(01)00348-0.

[38] Alimi, O. A., Ncongwane, T. B., & Meijboom, R. (2020). Design and fabrication of a monolith catalyst for continuous flow epoxidation of styrene in polypropylene printed flow reactor. *Chemical Engineering Research and Design, 159*, 395-409. https://doi.org/10.1016/j.cherd.2020.04.025.

[39] Troncoso, F. D., & Tonetto, G. M. (2022). Highly stable platinum monolith catalyst for the hydrogenation of vegetable oil. *Chemical Engineering and Processing - Process Intensification, 170*, 108669. https://doi.org/10.1016/j.cep.2021.108669.

[40] Roustapisheh, M., Karami, D., & Mahinpey, N. (2022). The fabrication of Ce promoted Ni/Mg/Al mixed oxides hydrotalcite washcoated alloy, monolith catalyst for catalytic steam cracking of vacuum gas oil. *Catalysis Today, 397-399*, 497-510. https://doi.org/10.1016/j.cattod.2021.06.022.

[41] Hajili, E., Suo, Z., Sugawara, A., Asoh, T., & Uyama, H. (2022). Fabrication of chitin monoliths with controllable morphology by thermally induced phase separation of chemically modified chitin. *Carbohydrate Polymers, 275*, 118680. https://doi.org/10.1016/j.carbpol.2021.118680.

[42] Aranzabal, A., Iturbe, D., Romero-Sáez, M., González-Marcos, M. P., González-Velasco, J. R., & González-Marcos, J. A. (2010). Optimization of process parameters on the extrusion of honeycomb shaped monolith of H-ZSM-5 zeolite. *Chem. Eng. J., 162*, 415-423. https://doi.org/10.1016/j.cej.2010.05.043.

[43] Chafik, T. (2021). Towards harnessing local natural clay in power to X technologies: Review on syngas production using low cost catalyst extruded as

honeycomb monolith. *Materials Today: Proceedings, 37*, 3834-3839. https://doi.org/10.1016/j.matpr.2020.08.403.

[44] Santos, D. F. M., Soares, O. S. G. P., Figueiredo, J. L., Sanz, O., Montes, M., & Pereira, M. F. R. (2020). Preparation of ceramic and metallic monoliths coated with cryptomelane as catalysts for VOC abatement. *Chemical Engineering Journal, 382*, 122923. https://doi.org/10.1016/j.cej.2019.122923.

[45] Yang, Z., Li, D., Zhao, Y., Miao, Y., Rao, J., Cai, D., ... Zhou, Y. (2019). In situ ZrC/Si-B-C-N monoliths prepared by sol-gel and reactive hot-pressing: Processing, microstructure, mechanical properties and oxidation behavior. *J. Alloys Compounds, 811*, 151687. https://doi.org/10.1016/j.jallcom.2019.151687.

[46] Forzatti, P., Ballardini, D., & Sighicelli, L. (1998). Preparation and characterization of extruded monolithic ceramic catalysts. *Catalysis Today, 41*, 87-94. https://doi.org/10.1016/S0920-5861(98)00040-6.

[47] Greene, J. P. (2021). Compression Molding. In J. P. Greene (Ed.), *Automotive Plastics and Composites* (pp. 265-278). William Andrew Publishing.

[48] Hasan, Z., Rahman, M. Z., Saha, B., & Ador, S. H. (2023). Composite materials from synthetic and natural sources: Fabrication techniques and applications. *In Reference Module in Materials Science and Materials Engineering*. Elsevier.

[49] Plieva, F. M., Seta, E. D., Galaev, I. Y., & Mattiasson, B. (2009). Macroporous elastic polyacrylamide monolith columns: Processing under compression and scale-up. *Separation and Purification Technology, 65*, 110-116. https://doi.org/10.1016/j.seppur.2008.03.026.

[50] Laguna, O. H., Lietor, P. F., Godino, F. J. I., & Corpas-Iglesias, F. A. (2021). A review on additive manufacturing and materials for catalytic applications: Milestones, key concepts, advances and perspectives. *Materials Design, 208*, 109927. https://doi.org/10.1016/j.matdes.2021.109927.

[51] Zhakeyev, A., Jones, M. C., Thomson, C. G., Tobin, J. M., Wang, H., Vilela, F., & Xuan, J. (2021). Additive manufacturing of intricate and inherently photocatalytic flow reactor components. *Additive Manufacturing, 38*, 101828. https://doi.org/10.1016/j.addma.2020.101828.

[52] Védrine, J. C. (2019). Importance, features and uses of metal oxide catalysts in heterogeneous catalysis. *Chinese Journal of Catalysis, 40*, 1627-1636. https://doi.org/10.1016/S1872-2067(18)63162-6.

[53] Zhu, J., Wu, P., Chao, Y., Yu, J., Zhu, W., Liu, Z., & Xu, C. (2022). Recent advances in 3D printing for catalytic applications. *Chemical Engineering Journal, 433*, 134341. https://doi.org/10.1016/j.cej.2021.134341.

[54] Kundra, M., Sultan, B. B. M., Ng, D., Wang, Y., Alexander, D. L. J., Nguyen, X., Xie, Z., & Hornung, C. H. (2020). Continuous flow semi-hydrogenation of alkynes using 3D printed catalytic static mixers. *Chemical Engineering and Processing - Process Intensification, 154*, 108018. https://doi.org/10.1016/j.cep.2020.108018.

[55] Kundra, M., Zhu, Y., Nguyen, X., Fraser, D., Hornung, C. H., & Tsanaktsidis, J. (2022). 3D printed nickel catalytic static mixers made by corrosive chemical treatment for use in continuous flow hydrogenation. *Reaction Chemistry & Engineering, 7*, 284-296. https://doi.org/10.1039/D1RE00456E.

[56] Hu, X., Karnetzke, J., Fassbender, M., Drücker, S., Bettermann, S., Schroeter, B., Pauer, W., Moritz, H., Fiedler, B., Luinstra, G., & Smirnova, I. (2020). Smart reactors – Combining stimuli-responsive hydrogels and 3D printing. *Chemical Engineering Journal, 387*, 123413. https://doi.org/10.1016/j.cej.2019.123413.

[57] Chaparro-Garnica, C. Y., Bailón-García, E., Davó-Quiñonero, A., Lozano-Castelló, D., & Bueno-López, A. (2022). Sponge-like carbon monoliths: Porosity control of 3D-printed carbon supports and its influence on the catalytic

performance. *Chemical Engineering Journal, 432*, 134218. https://doi.org/10.1016/j.cej.2021.134218.

[58] Elkoro, A., Soler, L., Llorca, J., & Casanova, I. (2019). 3D printed microstructured Au/TiO2 catalyst for hydrogen photoproduction. *Applied Materials Today, 16*, 265-272. https://doi.org/10.1016/j.apmt.2019.06.007.

[59] Middelkoop, V., Vamvakeros, A., de Wit, D., Jacques, S. D. M., Danaci, S., Jacquot, C., de Vos, Y., Matras, D., Price, S. W. T., & Beale, A. M. (2019). 3D printed Ni/Al2O3 based catalysts for CO2 methanation - a comparative and operando XRD-CT study. *Journal of CO2 Utilization, 33*, 478-487. https://doi.org/10.1016/j.jcou.2019.07.013.

[60] Martín de Vidales, M. J., Nieto-Márquez, A., Morcuende, D., Atanes, E., Blaya, F., Soriano, E., & Fernández-Martínez, F. (2019). 3D printed floating photocatalysts for wastewater treatment. *Catalysis Today, 328*, 157-163. https://doi.org/10.1016/j.cattod.2019.01.074.

[61] Magzoub, F., Li, X., Al-Darwish, J., Rezaei, F., & Rownaghi, A. A. (2019). 3D-printed ZSM-5 monoliths with metal dopants for methanol conversion in the presence and absence of carbon dioxide. *Applied Catalysis B: Environmental, 245*, 486-495. https://doi.org/10.1016/j.apcatb.2019.01.008.

[62] Salazar-Aguilar, A. D., Quintanilla, A., Vega-Díaz, S. M., Casas, J. A., Miranzo, P., Osendi, M. I., & Belmonte, M. (2021). Iron-based metal-organic frameworks integrated into 3D printed ceramic architectures. *Open Ceramics, 5*, 100047. https://doi.org/10.1016/j.oceram.2020.100047.

[63] Xie, Y., Yu, Y., Xie, H., Huang, F., & Hughes, T. C. (2022). 3D-printed heterogeneous Cu2O monoliths: Reusable supports for antibiotic treatment of wastewater. *Journal of Hazardous Materials, 436*, 129170. https://doi.org/10.1016/j.jhazmat.2022.129170.

[64] Mendez-Arriaga, F., de la Calleja, E., Ruiz-Huerta, L., Caballero-Ruiz, A., & Almanza, R. (2019). TiO2 3D structures for environmental purposes by additive manufacturing: Photoactivity test and reuse. *Materials Science in Semiconductor Processing, 100*, 35-41. https://doi.org/10.1016/j.mssp.2019.04.034.

[65] Zhou, X., & Liu, C. (2017). Three-dimensional Printing for Catalytic Applications: Current Status and Perspectives. *Advanced Functional Materials, 27*(34), 1701134. https://doi.org/10.1002/adfm.201701134.

[66] Shen, H., Zou, R., Zhou, Y., Guo, X., Guan, Y., Na, D., ZHANG, J., FAN, X., & JIAO, Y. (2022). Additive manufacturing of sodalite monolith for continuous heavy metal removal from water sources. *Chinese Journal of Chemical Engineering, 42*, 82-90. https://doi.org/10.1016/j.cjche.2021.12.016.

[67] Tang, J., Guo, X., Chang, H., Hu, K., Shen, Z., Wang, W., Liu, M., Wei, Y., Huang, Z., & Yang, Y. (2021). The preparation of SiC ceramic photosensitive slurry for rapid stereolithography. *Journal of the European Ceramic Society, 41*(15), 7516-7524. https://doi.org/10.1016/j.jeurceramsoc.2021.08.029.

[68] Díaz-Marta, A. S., Tubío, C. R., Carbajales, C., Fernández, C., Escalante, L., Sotelo, E., Guitián, F., Barrio, V. L., Gil, A., & Coelho, A. (2018). Three-Dimensional Printing in Catalysis: Combining 3D Heterogeneous Copper and Palladium Catalysts for Multicatalytic Multicomponent Reactions. *ACS Catalysis, 8*(1), 392-404. https://doi.org/10.1021/acscatal.7b02592.

[69] Bhatia, A., & Sehgal, A. K. (2021). Additive manufacturing materials, methods and applications: A review. *Materials Today: Proceedings, 81*, 1060-1067. https://doi.org/10.1016/j.matpr.2021.04.379.

[70] Blyweert, P., Nicolas, V., Fierro, V., & Celzard, A. (2021). 3D printing of carbon-based materials: A review. *Carbon, 183*, 449-485. https://doi.org/10.1016/j.carbon.2021.07.036.

[71] Gibson, I., Rosen, D., & Stucker, B. (2015). Development of Additive Manufacturing Technology. In I. Gibson, D. Rosen, & B. Stucker (Eds.), *Additive Manufacturing Technologies: 3D Printing, Rapid Prototyping, and Direct Digital Manufacturing* (pp. 19-42). Springer New York.

[72] Li, N., Tong, K., Yang, L., & Du, X. (2022). Review of 3D printing in photocatalytic substrates and catalysts. *Materials Today Energy, 23,* 101100. https://doi.org/10.1016/j.mtener.2022.101100.

[73] Andreu, A., Su, P., Kim, J., Ng, C. S., Kim, S., Kim, I., Lee, J., Noh, J., Subramanian, A. S., & Yoon, Y. (2021). 4D printing materials for vat photopolymerization. *Additive Manufacturing, 44,* 102024. https://doi.org/10.1016/j.addma.2021.102024.

[74] Pazhamannil, R. V., & Govindan, P. (2021). Current state and future scope of additive manufacturing technologies via vat photopolymerization. *Materials Today: Proceedings, 43*, 130-136. https://doi.org/10.1016/j.matpr.2020.11.225.

[75] Al Rashid, A., Ahmed, W., Khalid, M. Y., & Koç, M. (2021). Vat photopolymerization of polymers and polymer composites: Processes and applications. *Additive Manufacturing, 47*, 102279. https://doi.org/10.1016/j.addma.2021.102279.

[76] Bai, X., Ding, G., Zhang, K., Wang, W., Zhou, N., Fang, D., & He, R. (2021). Stereolithography additive manufacturing and sintering approaches of SiC ceramics. *Open Ceramics, 5*, 100046. https://doi.org/10.1016/j.oceram.2020.100046.

[77] Lee, B. J., Hsiao, K., Lipkowitz, G., Samuelsen, T., Tate, L., & DeSimone, J. M. (2022). Characterization of a 30 μm pixel size CLIP-based 3D printer and its enhancement through dynamic printing optimization. *Additive Manufacturing, 55*, 102800. https://doi.org/10.1016/j.addma.2022.102800.

[78] Loterie, D., Delrot, P., & Moser, C. (2020). High-resolution tomographic volumetric additive manufacturing. *Nature Communications, 11*, 852. https://doi.org/10.1038/s41467-020-14630-4.

[79] Amini, A., Guijt, R. M., Themelis, T., De Vos, J., & Eeltink, S. (2023). Recent developments in digital light processing 3D-printing techniques for microfluidic analytical devices. *Journal of Chromatography A, 1692*, 463842. https://doi.org/10.1016/j.chroma.2023.463842.

[80] Wang, Y., Chen, Y., Wen, C., Huang, K., Chen, Z., Han, B., & Zhang, Q. (2023). The process planning for additive and subtractive hybrid manufacturing of powder bed fusion (PBF) process. *Materials Design, 227*, 111732. https://doi.org/10.1016/j.matdes.2023.111732.

[81] Lamnini, S., Elsayed, H., Lakhdar, Y., Baino, F., Smeacetto, F., & Bernardo, E. (2022). Robocasting of advanced ceramics: Ink optimization and protocol to predict the printing parameters - A review. *Heliyon, 8*, e10651. https://doi.org/10.1016/j.heliyon.2022.e10651.

[82] Mora, S., Pugno, N. M., & Misseroni, D. (2022). 3D printed architected lattice structures by material jetting. *Materials Today, 59*, 107-132. https://doi.org/10.1016/j.mattod.2022.05.008.

[83] Miyanaji, H., Momenzadeh, N., & Yang, L. (2018). Effect of printing speed on quality of printed parts in Binder Jetting Process. *Additive Manufacturing, 20*, 1-10. https://doi.org/10.1016/j.addma.2017.12.008.

[84] Porter, Q., Moghadasi, M., Pei, Z., & Ma, C. (2023). Dense and strong ceramic composites via binder jetting and spontaneous infiltration. *Ceramics International, 49*(11), 17363-17370. https://doi.org/10.1016/j.ceramint.2023.02.104.

[85] Azam, F. I., Rani, A. M. A., Razak, M. A. A., Ali, S., & Aliyu, A. A. (2021). Additive Manufacturing Processes, Challenges and Applications: A Review. *Progress in Engineering Technology III* (pp. 93-111). Springer International Publishing.

[86] Chaparro-Garnica, C. Y., Davó-Quiñonero, A., Bailón-García, E., Lozano-Castelló, D., & Bueno-López, A. (2019). Design of Monolithic Supports by 3D Printing for Its Application in the Preferential Oxidation of CO (CO-PrOx). *ACS Applied Materials & Interfaces, 11*(38), 36763-36773. https://doi.org/10.1021/acsami.9b12731.

[87] Chaparro-Garnica, C. Y., Jordá-Faus, P., Bailón-García, E., Ocampo-Pérez, R., Aguilar-Madera, C. G., Davó-Quiñonero, A., Lozano-Castelló, D., & Bueno-López, A. (2020). Customizable Heterogeneous Catalysts: Nonchanneled Advanced Monolithic Supports Manufactured by 3D-Printing for Improved Active Phase Coating Performance. *ACS Applied Materials & Interfaces, 12*(46), 54573-54584. https://doi.org/10.1021/acsami.0c14703.

[88] Franchi, F. S., Ambrosetti, M., Balzarotti, R., Bracconi, M., Groppi, G., & Tronconi, E. (2022). Rich H2 catalytic oxidation as a novel methodology for the evaluation of mass transport properties of 3D printed catalyst supports. *Catalysis Today, 383*, 123-132. https://doi.org/10.1016/j.cattod.2021.04.004.

[89] Chava, R., Purbia, D., Roy, B., Janardhanan, V. M., Bahurudeen, A., & Appari, S. (2021). Effect of Calcination Time on the Catalytic Activity of Ni/γ-Al2O3 Cordierite Monolith for Dry Reforming of Biogas. *International Journal of Hydrogen Energy, 46*(11), 6341-6357. https://doi.org/10.1016/j.ijhydene.2020.11.125.

[90] Zang, M., Zhao, C., Wang, Y., Chen, S., Liu, X., & Zhang, Y. (2019). Ceramic-monolith-supported La0.8Ce0.2MnO3 catalysts for toluene oxidation. *Materials Letters, 253*, 196-200. https://doi.org/10.1016/j.matlet.2019.05.135.

[91] Patil, P., Nakate, U. T., Harish, K., Pavan, S. P., Rakesh, N. P., Selvakumar, D., & Kumar, N. S. (2020). Au sensitized La–CeO2 catalyst coated ceramics monoliths for toluene catalysis application. *Materials Chemistry and Physics, 240*, 122269. https://doi.org/10.1016/j.matchemphys.2019.122269.

[92] Tan, L., & Tan, B. (2020). Functionalized hierarchical porous polymeric monoliths as versatile platforms to support uniform and ultrafine metal nanoparticles for heterogeneous catalysis. *Chemical Engineering Journal, 390*, 124485. https://doi.org/10.1016/j.cej.2020.124485.

[93] Barbato, P. S., Di Benedetto, A., Landi, G., & Lisi, L. (2015). CuO/CeO2 based monoliths for CO preferential oxidation in H2-rich streams. *Chemical Engineering Journal, 279*, 983-993. https://doi.org/10.1016/j.cej.2015.05.079.

[94] Cifuentes, B., Cifuentes, A., Bustamante, F., Soler, L., Llorca, J., & Cobo, M. (2021). Monoliths washcoated with AuCu catalysts for CO removal in an ethanol fuel processor: Effect of CeO2–SiO2 dual support on the catalytic performance and reactor cost. *International Journal of Hydrogen Energy, 46*(3), 2166-2181. https://doi.org/10.1016/j.ijhydene.2020.10.122.

[95] Davó-Quiñonero, A., Sorolla-Rosario, D., Bailón-García, E., Lozano-Castelló, D., & Bueno-López, A. (2019). Improved asymmetrical honeycomb monolith catalyst prepared using a 3D printed template. *Journal of Hazardous Materials, 368*, 638-643. https://doi.org/10.1016/j.jhazmat.2019.01.092.

[96] Aktitiz, İ., Varol, R., Akkurt, N., & Saraç, M. F. (2020). In-situ synthesis of 3D printable mono- and Bi-metallic (Cu/Ag) nanoparticles embedded polymeric structures with enhanced electromechanical properties. *Polymer Testing, 90*, 106724. https://doi.org/10.1016/j.polymertesting.2020.106724.

[97] Gao, Y., & Ding, J. (2020). Low solid loading, low viscosity, high uniform shrinkage ceramic resin for stereolithography based additive manufacturing. Procedia Manufacturing, 48, 749-754. https://doi.org/10.1016/j.promfg.2020.05.109.

[98] Weng, Z., Zhou, Y., Lin, W., Senthil, T., & Wu, L. (2016). Structure-property relationship of nano enhanced stereolithography resin for desktop SLA 3D printer. *Composites Part A: Applied Science and Manufacturing, 88*, 234-242. https://doi.org/10.1016/j.compositesa.2016.05.035.

[99] Hensleigh, R. M., Cui, H., Oakdale, J. S., Ye, J. C., Campbell, P. G., Duoss, E. B., Spadaccini, C. M., Zheng, X., & Worsley, M. A. (2018). Additive manufacturing of complex micro-architected graphene aerogels. *Materials Horizons, 5*(6), 1035-1041. https://doi.org/10.1039/C8MH00668G.

[100] Chang, Y., Cao, Q., & Venton, B. J. (2023). 3D printing for customized carbon electrodes. *Current Opinion in Electrochemistry, 38*, 101228. https://doi.org/10.1016/j.coelec.2023.101228.

[101] Yang, C., Cao, Q., Puthongkham, P., Lee, S. T., Ganesana, M., Lavrik, N. V., & Venton, B. J. (2018). 3D-Printed Carbon Electrodes for Neurotransmitter Detection. *Angewandte Chemie International Edition, 57*(43), 14255-14259. https://doi.org/10.1002/anie.201809992.

[102] Jaiswal, A., Rastogi, C. K., Rani, S., Singh, G. P., Saxena, S., & Shukla, S. (2023). Two decades of two-photon lithography: Materials science perspective for additive manufacturing of 2D/3D nano-microstructures. *iScience, 26*(4), 106374. https://doi.org/10.1016/j.isci.2023.106374.

[103] Han, Z., Wang, G., Zhang, J., & Tang, Z. (2022). Direct photo-curing 3D printing of nickel-based electrocatalysts for highly-efficient hydrogen evolution. *Nano Energy, 102*, 107615. https://doi.org/10.1016/j.nanoen.2022.107615.

[104] Zhao, J., Li, Q., Jin, F., & He, N. (2021). Digital light processing 3D printing Kevlar composites based on dual curing resin. *Additive Manufacturing, 41*, 101962. https://doi.org/10.1016/j.addma.2021.101962.

[105] Zhang, Y., Li, S., Zhao, Y., Duan, W., Liu, B., Wang, T., & Wang, G. (2021). Digital light processing 3D printing of AlSi10Mg powder modified by surface coating. *Addit. Manuf., 39*, 101897. https://doi.org/10.1016/j.addma.2021.101897.

[106] Gyak, K., Vishwakarma, N. K., Hwang, Y., Kim, J., Yun, H., & Kim, D. (2019). 3D-printed monolithic SiCN ceramic microreactors from a photocurable preceramic resin for the high temperature ammonia cracking process. *Reaction Chemistry & Engineering, 4*(8), 1393-1399. https://doi.org/10.1039/C9RE00201D.

[107] Bogdan, E., Michorczyk, B., Rokicińska, A., Basta, M., Myradova, M., Kuśtrowski, P., & Michorczyk, P. (2021). Monolithic composites with geometry controlled by polymeric 3D printed templates: Characterization and catalytic performance in OCM. *Appl.Surf. Sci., 553*, 149554. https://doi.org/10.1016/j.apsusc.2021.149554.

[108] Michorczyk, P., Hędrzak, E., & Węgrzyniak, A. (2016). Preparation of monolithic catalysts using 3D printed templates for oxidative coupling of methane. *Journal of Materials Chemistry A, 4*(46), 18753-18756. https://doi.org/10.1039/C6TA08629B.

[109] Hędrzak, E., Węgrzynowicz, A., Rachwalik, R., Sulikowski, B., & Michorczyk, P. (2019). Monoliths with MFI zeolite layers prepared with the assistance of 3D printing: Characterization and performance in the gas phase isomerization of α-pinene. *Applied Catalysis A: General, 579*, 75-85. https://doi.org/10.1016/j.apcata.2019.04.017.

[110] Rokicińska, A., Drozdek, M., Bogdan, E., Węgrzynowicz, A., Michorczyk, P., & Kuśtrowski, P. (2021). Combustion of toluene over cobalt-modified MFI zeolite dispersed on monolith produced using 3D printing technique. *Catalysis Today, 375*, 369-376. https://doi.org/10.1016/j.cattod.2020.04.005.

[111] Yoneda, S., Han, W., Hasegawa, U., & Uyama, H. (2014). Facile fabrication of poly(methyl methacrylate) monolith via thermally induced phase separation by utilizing unique cosolvency. *Polymer, 55*(12), 3212-3216. https://doi.org/10.1016/j.polymer.2014.05.031.

[112] Chae, J. A., Oh, Y., Kim, H. J., Choi, G. B., Lee, K. M., Jung, D., Kim, Y. A., & Kim, H. (2019). Preparation of compressible polymer monoliths that contain mesopores capable of rapid oil–water separation. *Polymer Chemistry, 10*(39), 5142-5150. https://doi.org/10.1039/c9py00967a.

[113] Shen, Y., Qi, L., & Mao, L. (2012). Macroporous polymer monoliths with a well-defined three dimensional skeletal morphology derived from a novel phase separator for HPLC. *Polymer, 53*(19), 4128-4134. https://doi.org/10.1016/j.polymer.2012.07.019.

[114] Xin, Y., Fujimoto, T., & Uyama, H. (2012). Facile fabrication of polycarbonate monolith by non-solvent induced phase separation method. *Polymer, 53*(13), 2847-2853. https://doi.org/10.1016/j.polymer.2012.04.029.

[115] Sun, X., Sun, G., & Wang, X. (2017). Morphology modeling for polymer monolith obtained by non-solvent-induced phase separation. *Polymer, 108,* 432-441. https://doi.org/10.1016/j.polymer.2016.12.026.

[116] Ye, J., Qian, C., Dong, Y., Zhu, Y., & Fu, Y. (2023). Development of organic solvent-induced shape memory poly(ethylene-co-vinyl acetate) monoliths for expandable oil absorbers. *European Polymer Journal, 183*, 111730. https://doi.org/10.1016/j.eurpolymj.2022.111730.

[117] Han, J., Xie, K., Du, Z., Zou, W., & Zhang, C. (2015). β-Cyclodextrin functionalized polystyrene porous monoliths for separating phenol from wastewater. *Carbohydrate Polymers, 120*, 85-91. https://doi.org/10.1016/j.carbpol.2014.12.011.

[118] Liu, J., Tobin, J. M., Xu, Z., & Vilela, F. (2015). Facile synthesis of a conjugated microporous polymeric monolith via copper-free Sonogashira–Hagihara cross-coupling in water under aerobic conditions. *Polymer Chemistry, 6*(37), 7251-7255. https://doi.org/10.1039/C5PY00772K.

[119] Kuzmicz, D., Coupillaud, P., Men, Y., Vignolle, J., Vendraminetto, G., Ambrogi, M., Taton, D., & Yuan, J. (2014). Functional mesoporous poly(ionic liquid)-based copolymer monoliths: From synthesis to catalysis and microporous carbon production. *Polymer, 55*(14), 3423-3430. https://doi.org/10.1016/j.polymer.2014.04.032.

[120] Xin, Y., Sakamoto, J., van der Vlies, A. J., Hasegawa, U., & Uyama, H. (2015). Phase separation approach to a reactive polycarbonate monolith for "click" modifications. *Polymer, 66*, 52-57. https://doi.org/10.1016/j.polymer.2015.04.008.

[121] Kuppusamy, S., Jagadeesan, D., Mohan, A. M., Pavoor Veedu, A., Jiji, A. E., John, A. M., & Deivasigamani, P. (2023). NH2-MIL-125 MOF integrated translucent mesoporous polymer monolith as dual-light responsive new-generation photocatalyst for the expeditious decontamination of perennial pharmaceuticals. *Journal of Environmental Chemical Engineering, 11*, 110355. https://doi.org/10.1016/j.jece.2023.110355.

[122] Chae, J. A., Jeong, S., Kim, H. J., Tojo, T., Oh, Y., Chi, W. S., Yoon, H., & Kim, H. (2021). Fibrous mesoporous polymer monoliths: macromolecular design and enhanced photocatalytic degradation of aromatic dyes. *Polymer Chemistry, 12*(17), 2464-2470. https://doi.org/10.1039/D1PY00049G.

[123] Roehling, J. D., Khairallah, S. A., Shen, Y., Bayramian, A., Boley, C. D., Rubenchik, A. M., DeMuth, J., Duanmu, N., & Matthews, M. J. (2021). Physics of large-area pulsed laser powder bed fusion. *Additive Manufacturing, 46*, 102186. https://doi.org/10.1016/j.addma.2021.102186.

[124] Goodridge, R., & Ziegelmeier, S. (2017). Powder bed fusion of polymers. In M. Brandt (Ed.), *Laser Additive Manufacturing* (pp. 181-204). Woodhead Publishing.

[125] Chaparro-Garnica, C.Y. (2021). *Design of monolithic supports by 3D printing for its application in catalysis.* [Doctoral Thesis, University of Alicante] http://hdl.handle.net/10045/119082.

[126] Soundararajan, B., Sofia, D., Barletta, D., & Poletto, M. (2021). Review on modeling techniques for powder bed fusion processes based on physical principles. *Additive Manufacturing, 47*, 102336. https://doi.org/10.1016/j.addma.2021.102336.

[127] Zhang, J., Zheng, W., Wu, J., Yu, K., Ye, C., & Shi, Y. (2021). Effects of particle grading on properties of silica ceramics prepared by selective laser sintering. *Ceram. Int., 48*(1), 1173-1180. https://doi.org/10.1016/j.ceramint.2021.09.202.

[128] Qadri, S. I. A. (2021). A critical study and analysis of process parameters of selective laser sintering Rapid prototyping. *Materials Today: Proceedings, 49*(5), 19080-1988. https://doi.org/10.1016/j.matpr.2021.08.153.

[129] Schwentenwein, M., & Homa, J. (2015). Additive Manufacturing of Dense Alumina Ceramics. International Journal of Applied Ceramic Technology, 12(1), 1-7. https://doi.org/10.1111/ijac.12319.

[130] Cheng, K., Xiong, W., Li, Y., Tang, D., Geng, H., Sun, M., Hao, L., Wang, H. S., & Zhang, H. (2021). In-situ deposition of diamond on functionally graded copper scaffold for improved thermal conductivity and mechanical properties. *Materials Letters, 299*, 130050. https://doi.org/10.1016/j.matlet.2021.130050.

[131] Agueniou, F., Vidal, H., López, J. de D., Hernández-Garrido, J. C., Cauqui, M. A., Botana, F. J., Calvino, J. J., Galvita, V. V., & Gatica, J. M. (2021). 3D-printing of metallic honeycomb monoliths as a doorway to a new generation of catalytic

devices: the Ni-based catalysts in methane dry reforming showcase. *Catalysis Communications, 148*, 106181. https://doi.org/10.1016/j.catcom.2020.106181.

[132] Cheng, K., Xiong, W., Li, Y., Hao, L., Yan, C., Li, Z., Liu, Z., Wang, Y., Essa, K., Lee, L., Gong, X., & Peijs, T. (2020). In-situ deposition of three-dimensional graphene on selective laser melted copper scaffolds for high performance applications. *Composites Part A: Applied Science and Manufacturing, 135*, 105904. https://doi.org/10.1016/j.compositesa.2020.105904.

[133] Lind, A., Vistad, Ø., Sunding, M. F., Andreassen, K. A., Cavka, J. H., & Grande, C. A. (2020). Multi-purpose structured catalysts designed and manufactured by 3D printing. *Mater. Des., 187*, 108377. https://doi.org/10.1016/j.matdes.2019.108377.

[134] Fratalocchi, L., Groppi, G., Visconti, C. G., Lietti, L., & Tronconi, E. (2020). Adoption of 3D printed highly conductive periodic open cellular structures as an effective solution to enhance the heat transfer performances of compact Fischer-Tropsch fixed-bed reactors. *Chemical Engineering Journal, 386*, 123988. https://doi.org/10.1016/j.cej.2019.123988.

[135] Rodrigues, C. S. D., Guimarães, V., Pereira, M. F. R., Soares, O. S. G. P., & Madeira, L. M. (2022). Gaseous toluene abatement by the heterogeneous Fenton-like process using iron/carbon-coated monolith as catalyst: Proof of concept. *J. Environ. Manage., 322*, 116084. https://doi.org/10.1016/j.jenvman.2022.116084.

[136] Sampaio, E. F. S., Soares, O. S. G. P., Pereira, M. F. R., Rodrigues, C. S. D., & Madeira, L. M. (2023). Fe-containing carbon-coated monoliths prepared by CVD in gaseous toluene abatement - parametric analysis of the Fenton process. *Catalysis Today, 418*, 114143. https://doi.org/10.1016/j.cattod.2023.114143.

[137] Li, Z., Cai, W., Song, L., Hu, Y., Xing, W., & Gui, Z. (2023). Catalysis co-calcination: An available and energy-saving approach to prepare metal/carbon

materials with well hydrophobicity and photo-thermal conversion performance. *Appl. Surf. Sci., 639*, 158253. https://doi.org/10.1016/j.apsusc.2023.158253.

[138] Saud, S., Nguyen, D. B., Bhattarai, R. M., Matyakubov, N., Nguyen, V. T., Ryu, S., Jeon, H., Kim, S. B., & Mok, Y. S. (2022). Plasma-catalytic ethylene removal by a ZSM-5 washcoat honeycomb monolith impregnated with palladium. *J. Hazard. Mater., 426*, 127843. https://doi.org/10.1016/j.jhazmat.2021.127843.

[139] Katheria, S., Deo, G., & Kunzru, D. (2019). Rh-Ni/MgAl2O4 catalyst for steam reforming of methane: Effect of Rh doping, calcination temperature and its application on metal monoliths. *Applied Catalysis A: General, 570*, 308-318. https://doi.org/10.1016/j.apcata.2018.11.021.

[140] Wei, Q., Li, H., Liu, G., He, Y., Wang, Y., Tan, Y. E., Wang, D., Peng, X., Yang, G., & Tsubaki, N. (2020). Metal 3D printing technology for functional integration of catalytic system. *Nature Communications, 11*, 4098. https://doi.org/10.1038/s41467-020-17941-8.

[141] Komendová, M., Nawada, S., Metelka, R., Schoenmakers, P. J., & Urban, J. (2020). Multichannel separation device with parallel electrochemical detection. *J. Chromatography A, 1610*, 460537. https://doi.org/10.1016/j.chroma.2019.460537

[142] Lapp, J. L., Lange, M., Rieping, R., de Oliveira, L., Roeb, M., & Sattler, C. (2017). Fabrication and testing of CONTISOL: A new receiver-reactor for day and night solar thermochemistry. *Applied Thermal Engineering, 127*, 46-57. https://doi.org/10.1016/j.applthermaleng.2017.08.001.

[143] González-Castaño, M., Baena-Moreno, F., Navarro de Miguel, J. C., Miah, K. U. M., Arroyo-Torralvo, F., Ossenbrink, R., Odriozola, J. A., Benzinger, W., Hensel, A., Wenka, A., & Arellano-García, H. (2022). 3D-printed structured catalysts for CO2 methanation reaction: Advancing of gyroid-based geometries. *Energy Convers. Manag., 258*, 115464. https://doi.org/10.1016/j.enconman.2022.115464.

[144] Kumar, S. (2014). Selective Laser Sintering/Melting. In S. Hashmi, G. F. Batalha, C. J. Van Tyne, & B. Yilbas (Eds.), *Comprehensive Materials Processing* (pp. 93-134). Elsevier, Oxford.

[145] Rahmati, S. (2014). Direct Rapid Tooling. In S. Hashmi, G. F. Batalha, C. J. Van Tyne, & B. Yilbas (Eds.), *Comprehensive Materials Processing* (pp. 303-344). Elsevier, Oxford.

[146] Peters, W., Eypasch, M., Frank, T., Schwerdtfeger, J., Körner, C., Bösmann, A., & Wasserscheid, P. (2015). Efficient hydrogen release from perhydro-N-ethylcarbazole using catalyst-coated metallic structures produced by selective electron beam melting. *Energy & Environmental Science, 8*(3), 641-649. https://doi.org/10.1039/C4EE03461A.

[147] Nguyen, X., Carafa, A., & Hornung, C. H. (2018). Hydrogenation of vinyl acetate using a continuous flow tubular reactor with catalytic static mixers. *Chemical Engineering and Processing - Process Intensification, 124*, 215-221. https://doi.org/10.1016/j.cep.2017.12.007.

[148] Hornung, C. H., Nguyen, X., Carafa, A., Gardiner, J., Urban, A., Fraser, D., Horne, M. D., Gunasegaram, D. R., & Tsanaktsidis, J. (2017). Use of Catalytic Static Mixers for Continuous Flow Gas–Liquid and Transfer Hydrogenations in Organic Synthesis. *Organic Process Research & Development, 21*(9), 1311-1319. https://doi.org/10.1021/acs.oprd.7b00180.

[149] Knorr, T., Heinl, P., Schwerdtfeger, J., Körner, C., Singer, R. F., & Etzold, B. J. M. (2012). Process specific catalyst supports—Selective electron beam melted cellular metal structures coated with microporous carbon. *Chemical Engineering Journal, 181-182*, 725-733. https://doi.org/10.1016/j.cej.2011.10.009.

[150] Koo, K. Y., Eom, H. J., Kwon, S. C., Jung, U. H., & Yoon, W. L. (2017). Ru-coated metal monolith catalyst prepared by novel coating method for hydrogen production

via natural gas steam reforming. *Catalysis Today, 293-294*, 129-135. https://doi.org/10.1016/j.cattod.2016.11.016.

[151] Le, Z., Zhang, W., Li, W., Tan, J., Li, R., Wang, X., Kaneti, Y. V., Jiang, X., Chu, J., Yamauchi, Y., & Hu, M. (2020). Metal-Organic Powder Thermochemical Solid-Vapor Architectonics toward Gradient Hybrid Monolith with Combined Structure-Function Features. Matter, 3(3), 879-891. https://doi.org/10.1016/j.matt.2020.07.002.

[152] Gao, F., Tang, Y., Liu, J., Pan, K., Zhou, M., Qian, G., Liu, M., Yu, F., Dan, J., & Dai, B. (2023). Nickel foam supported CuCe mixed metal oxide as monolith catalyst for NO removal. *Chemical Engineering Journal, 474*, 145713. https://doi.org/10.1016/j.cej.2023.145713.

[153] Wang, J., Yang, J., Zhu, H., Li, B., & Zhu, S. (2023). In-situ construction of hierarchically porous MOF monoliths using high internal phase emulsion templates. *Chem. Eng. J., 456*, 141026. https://doi.org/10.1016/j.cej.2022.141026.

[154] Sheikh, M. U. D., Naikoo, G. A., Thomas, M., Bano, M., & Khan, F. (2015). Surfactant-assisted morphological tuning of porous metallic silver sponges: facile synthesis, characterization and catalytic performance. *Journal of Sol-Gel Science and Technology, 76*(3), 572-581. https://doi.org/10.1007/s10971-015-3807-0.

[155] Sharma, M., Mishra, A., Mehta, A., Choudhury, D., & Basu, S. (2017). Enhanced catalytic and antibacterial activity of nanocasted mesoporous silver monoliths: kinetic and thermodynamic studies. *Journal of Sol-Gel Science and Technology, 81*(3), 704-710. https://doi.org/10.1007/s10971-016-4260-4.

[156] Sharma, M., Hazra, S., & Basu, S. (2017). Synthesis of heterogeneous Ag-Cu bimetallic monolith with different mass ratios and their performances for catalysis and antibacterial activity. *Advanced Powder Technology, 28*(12), 3085-3094. https://doi.org/10.1016/j.apt.2017.09.023.

[157] Jeyachandran, P., Bontha, S., Bodhak, S., Balla, V. K., & Doddamani, M. (2021). Material extrusion additive manufacturing of bioactive glass/high density polyethylene composites. *Composites Science and Technology, 213*, 108966. https://doi.org/10.1016/j.compscitech.2021.108966.

[158] Casini, M. (2022). Chapter 8 - Advanced building construction methods. In Casini, M. (Ed.) *Construction 4.0* (pp. 405-470). Woodhead Publishing.

[159] Mollah, M. T., Comminal, R., Serdeczny, M. P., Pedersen, D. B., & Spangenberg, J. (2021). Stability and deformations of deposited layers in material extrusion additive manufacturing. *Additive Manufacturing, 46*, 102193. https://doi.org/10.1016/j.addma.2021.102193.

[160] Rao, Y., Wei, N., Yao, S., Wang, K., & Peng, Y. (2021). A process-structure-performance modeling for thermoplastic polymers via material extrusion additive manufacturing. *Additive Manufacturing, 39*, 101857. https://doi.org/10.1016/j.addma.2021.101857.

[161] Zhu, C., Qi, Z., Beck, V. A., Luneau, M., Lattimer, J., Chen, W., ... & Biener, J. (2018). Toward digitally controlled catalyst architectures: Hierarchical nanoporous gold via 3D printing. *Science Advances, 4*(3), eaas9459. https://doi.org/10.1126/sciadv.aas9459.

[162] Ma, S., Fu, S., Zhao, S., He, P., Ma, G., Wang, M., ... & Zhou, Y. (2021). Direct ink writing of geopolymer with high spatial resolution and tunable mechanical properties. *Additive Manufacturing, 46*, 102202. https://doi.org/10.1016/j.addma.2021.102202.

[163] Middelkoop, V., Slater, T., Florea, M., Neațu, F., Danaci, S., Onyenkeadi, V., ... & Kellici, S. (2019). Next frontiers in cleaner synthesis: 3D printed graphene-supported CeZrLa mixed-oxide nanocatalyst for CO2 utilisation and direct

propylene carbonate production. *Journal of Cleaner Production, 214*, 606-614. https://doi.org/10.1016/j.jclepro.2018.12.274.

[164] Young, A. J., Guillet-Nicolas, R., Marshall, E. S., Kleitz, F., Goodhand, A. J., Glanville, L. B. L., ... & Chin, J. M. (2019). Direct ink writing of catalytically active UiO-66 polymer composites. *Chemical Communications, 55*(15), 2190-2193. https://doi.org/10.1039/C8CC10018G.

[165] Li, X., Rezaei, F., & Rownaghi, A. A. (2019). Methanol-to-olefin conversion on 3D-printed ZSM-5 monolith catalysts: Effects of metal doping, mesoporosity and acid strength. *Microporous and Mesoporous Materials, 276*, 1-12. https://doi.org/10.1016/j.micromeso.2018.09.016.

[166] Lefevere, J., Protasova, L., Mullens, S., & Meynen, V. (2017). 3D-printing of hierarchical porous ZSM-5: The importance of the binder system. *Materials Design, 134*, 331-341. https://doi.org/10.1016/j.matdes.2017.08.044.

[167] Hajimirzaee, S., & Doyle, A. M. (2020). 3D printed catalytic converters with enhanced activity for low-temperature methane oxidation in dual-fuel engines. *Fuel, 274*, 117848. https://doi.org/10.1016/j.fuel.2020.117848.

[168] Shahzad, A., & Lazoglu, I. (2021). Direct ink writing (DIW) of structural and functional ceramics: Recent achievements and future challenges. *Composites Part B: Engineering, 225*, 109249. https://doi.org/10.1016/j.compositesb.2021.109249.

[169] Hossain, S. S., Son, H., Gao, B., Park, S., & Bae, C. (2023). Development of tri-modal-pore architecture of silica monolith via extrusion-based 3D printing and employing rice husk ash. *Materials Today Communications, 34*, 105246. https://doi.org/10.1016/j.mtcomm.2022.105246.

[170] Lefevere, J., Gysen, M., Mullens, S., Meynen, V., & Van Noyen, J. (2013). The benefit of design of support architectures for zeolite coated structured catalysts for

methanol-to-olefin conversion. *Catalysis Today, 216,* 18-23. https://doi.org/10.1016/j.cattod.2013.05.020.

[171] Magzoub, F., Li, X., Lawson, S., Rezaei, F., & Rownaghi, A. A. (2020). 3D-printed HZSM-5 and 3D-HZM5@SAPO-34 structured monoliths with controlled acidity and porosity for conversion of methanol to dimethyl ether. *Fuel, 280,* 118628. https://doi.org/10.1016/j.fuel.2020.118628.

[172] Li, X., Li, W., Rezaei, F., & Rownaghi, A. (2018). Catalytic cracking of n-hexane for producing light olefins on 3D-printed monoliths of MFI and FAU zeolites. *Chem. Eng. J., 333*, 545-553. https://doi.org/10.1016/j.cej.2017.10.001.

[173] Lawson, S., Newport, K. A., Axtell, A., Boucher, C., Grant, B., Haas, M., ... & Rownaghi, A. A. (2021). Structured Bifunctional Catalysts for CO2 Activation and Oxidative Dehydrogenation of Propane. *ACS Sustainable Chemistry & Engineering, 9*(21), 5716-5727. https://doi.org/10.1021/acssuschemeng.1c00882.

[174] Magzoub, F., Lawson, S., Rezaei, F., & Rownaghi, A. A. (2021). Directly Printed Oxide/ZSM-5 Bifunctional Catalysts for Methanol Conversion to Dimethyl Ether with Exceptional Stability, Conversion, and Selectivity. *Energy & Fuels, 35*(3), 2619-2629. https://doi.org/10.1021/acs.energyfuels.0c04279.

[175] Lawson, S., Farsad, A., Rezaei, F., Ludlow, D., & Rownaghi, A. A. (2021). Direct Ink Writing of Metal Oxide/H-ZSM-5 Catalysts for n-Hexane Cracking: A New Method of Additive Manufacturing with High Metal Oxide Loading. *ACS Applied Materials & Interfaces, 13*(1), 781-794. https://doi.org/10.1021/acsami.0c20752.

[176] Lawson, S., Farsad, A., Adebayo, B., Newport, K., Schueddig, K., Lowrey, E., ... & Rownaghi, A. A. (2021). A Novel Method of 3D Printing High-Loaded Oxide/H-ZSM-5 Catalyst Monoliths for Carbon Dioxide Reduction in Tandem with Propane Dehydrogenation. *Advanced Sustainable Systems, 5*(5), 2000257. https://doi.org/10.1002/adsu.202000257.

[177] Lawson, S., Baamran, K., Newport, K., Rezaei, F., & Rownaghi, A. A. (2022). Formulation and processing of dual functional Adsorbent/Catalyst structured monoliths using an additively manufactured contactor for direct Capture/Conversion of CO2 with cogeneration of ethylene. *Chemical Engineering Journal, 431*, 133224. https://doi.org/10.1016/j.cej.2021.133224.

[178] Farsad, A., Lawson, S., Rezaei, F., & Rownaghi, A. A. (2021). Oxidative dehydrogenation of propane over 3D printed mixed metal oxides/H-ZSM-5 monolithic catalysts using CO2 as an oxidant. *Catalysis Today, 374*, 173-184. https://doi.org/10.1016/j.cattod.2020.10.002.

[179] Tubio, C. R., Malatini, C., Barrio, V. L., Masaguer, C. F., Amorín, M., Nabgan, W., ... & Coelho, A. (2023). 3D printing of a palladium-alumina cermet monolithic catalyst: catalytic evaluation in microwave-assisted cross-coupling reactions. *Mater. Today Chem., 27*, 101355. https://doi.org/10.1016/j.mtchem.2022.101355.

[180] Zhou, X., & Liu, C. (2020). Three-dimensional printing of porous carbon structures with tailorable pore sizes. *Catalysis Today, 347*, 2-9. https://doi.org/10.1016/j.cattod.2018.05.044.

[181] Ma, J., Wang, P., Dong, L., Ruan, Y., & Lu, H. (2019). Highly conductive, mechanically strong graphene monolith assembled by three-dimensional printing of large graphene oxide. *Journal of Colloid and Interface Science, 534*, 12-19. https://doi.org/10.1016/j.jcis.2018.08.096.

[182] Quintanilla, A., Carbajo, J., Casas, J. A., Miranzo, P., Osendi, M. I., & Belmonte, M. (2020). Graphene-based nanostructures as catalysts for wet peroxide oxidation treatments: From nanopowders to 3D printed porous monoliths. *Catalysis Today, 356*, 197-204. https://doi.org/10.1016/j.cattod.2019.06.026.

[183] Long, L., Pei, R., Liu, Y., Rao, X., Wang, Y., Zhou, S., & Zhan, G. (2022). 3D printing of recombinant Escherichia coli/Au nanocomposites as agitating paddles

towards robust catalytic reduction of 4-nitrophenol. *Journal of Hazardous Materials, 423*, 126983. https://doi.org/10.1016/j.jhazmat.2021.126983.

[184] Lefevere, J., Mullens, S., & Meynen, V. (2018). The impact of formulation and 3D-printing on the catalytic properties of ZSM-5 zeolite. *Chemical Engineering Journal, 349*, 260-268. https://doi.org/10.1016/j.cej.2018.05.058.

[185] Tubío, C. R., Azuaje, J., Escalante, L., Coelho, A., Guitián, F., Sotelo, E., & Gil, A. (2016). 3D printing of a heterogeneous copper-based catalyst. *Journal of Catalysis, 334*, 110-115. https://doi.org/10.1016/j.jcat.2015.11.019.

[186] Elkoro Ugarteburu, A., & Casanova, I. (2018). 3D Printing of Structured Nanotitania Catalysts: A Novel Binder-Free and Low-Temperature Chemical Sintering Method. *3D printing and Additive Manufacturing, 5*(3), 220-226 https://doi.org/10.1089/3dp.2017.0164.

[187] de Hazan, Y., Thänert, M., Trunec, M., & Misak, J. (2012). Robotic deposition of 3d nanocomposite and ceramic fiber architectures via UV curable colloidal inks. *Journal of the European Ceramic Society, 32*(6), 1187-1198. https://doi.org/10.1016/j.jeurceramsoc.2011.12.007.

[188] Ge, Y., Zhang, T., Zhou, B., Wang, H., Zhang, Z., Shen, J., & Du, A. (2018). Nanostructured resorcinol-formaldehyde ink for 3D direct writing. *Journal of Materials Research, 33*(14), 2052-2061. https://doi.org/10.1557/jmr.2018.104.

[189] Aslam, W., Ahmed, M. H., Qui, T., & Konarova, M. (2020). Syngas to higher alcohols synthesis over 3D printed KMoCo/ZSM5 monolith. *Chemical Engineering Journal Advances, 3*, 100024. https://doi.org/10.1016/j.ceja.2020.100024.

[190] Hajimirzaee, S., Shaw, D., Howard, P., & Doyle, A. M. (2021). Industrial scale 3D printed catalytic converter for emissions control in a dual-fuel heavy-duty engine. *Chem. Eng. Sci., 231*, 116287. https://doi.org/10.1016/j.ces.2020.116287.

[191] Danaci, S., Protasova, L., Shen, J., Bouwen, W., Bengaouer, A., & Marty, P. (2016). Efficient CO2 methanation over Ni/Al2O3 coated structured catalysts. *Catalysis Today, 273*, 234-243. https://doi.org/10.1016/j.cattod.2016.04.019.

[192] Danaci, S., Protasova, L., Snijkers, F., Bouwen, W., Bengaouer, A., & Marty, P. (2018). Innovative 3D-manufacture of structured copper supports post-coated with catalytic material for CO2 methanation. *Chemical Engineering and Processing: Process Intensification, 127*, 168-177. https://doi.org/10.1016/j.cep.2018.03.023.

[193] Lin, Y., Zhu, W., & Li, Y. (2022). Hierarchical monolithic carbon with high transfer performance for hydrogen evolution reaction. *Journal of Energy Chemistry, 73*, 41-48. https://doi.org/10.1016/j.jechem.2022.05.019.

[194] Quintanilla, A., Casas, J. A., Miranzo, P., Osendi, M. I., & Belmonte, M. (2018). 3D-Printed Fe-doped silicon carbide monolithic catalysts for wet peroxide oxidation processes. *Applied Catalysis B: Environmental, 235*, 246-255. https://doi.org/10.1016/j.apcatb.2018.04.066.

[195] Liu, D., Jiang, P., Li, X., Liu, J., Zhou, L., Wang, X., & Zhou, F. (2020). 3D printing of metal-organic frameworks decorated hierarchical porous ceramics for high-efficiency catalytic degradation. *Chemical Engineering Journal, 397*, 125392. https://doi.org/10.1016/j.cej.2020.125392.

[196] Sanchez Díaz-Marta, A., Yáñez, S., Tubío, C. R., Barrio, V. L., Piñeiro, Y., Pedrido, R., ... & Coelho, A. (2019). Multicatalysis Combining 3D-Printed Devices and Magnetic Nanoparticles in One-Pot Reactions: Steps Forward in Compartmentation and Recyclability of Catalysts. *ACS Applied Materials & Interfaces, 11*(27), 25283-25294. https://doi.org/10.1021/acsami.9b08119.

[197] Román-Manso, B., De Pablos, Á., Belmonte, M., Osendi, M.I., & Miranzo, P. (2014). Microstructural designs of spark-plasma sintered silicon carbide ceramic

scaffolds. *Boletín de la Sociedad Española de Cerámica y Vidrio, 53*(2), 93-100. https://doi.org/10.3989/cyv.132014.

[198] Azuaje, J., Tubío, C. R., Escalante, L., Gómez, M., Guitián, F., Coelho, A., ... & Sotelo, E. (2017). An efficient and recyclable 3D printed α-Al2O3 catalyst for the multicomponent assembly of bioactive heterocycles. *Applied Catalysis A: General, 530,* 203-210. https://doi.org/10.1016/j.apcata.2016.11.031.

[199] Jain, P., & Kuthe, A. M. (2013). Feasibility Study of Manufacturing Using Rapid Prototyping: FDM Approach. *Procedia Engineering, 63,* 4-11. https://doi.org/10.1016/j.proeng.2013.08.275.

[200] Skorski, M. R., Esenther, J. M., Ahmed, Z., Miller, A. E., & Hartings, M. R. (2016). The chemical, mechanical, and physical properties of 3D printed materials composed of TiO2-ABS nanocomposites. *Journal of Applied Polymer Science, 17*(2), 89-97. https://doi.org/10.1080/14686996.2016.1152879.

[201] Paul, S. (2021). Finite element analysis in fused deposition modeling research: A literature review. *Measurement, 178*, 109320. https://doi.org/10.1016/j.measurement.2021.109320.

[202] Cano-Vicent, A., Tambuwala, M. M., Hassan, S. S., Barh, D., Aljabali, A. A. A., Birkett, M., Arjunan, A., & Serrano-Aroca, Á. (2021). Fused deposition modelling: Current status, methodology, applications and future prospects. *Additive Manufacturing, 47,* 102378. https://doi.org/10.1016/j.addma.2021.102378.

[203] Hock, S., & Rose, M. (2020). 3D-Structured Monoliths of Nanoporous Polymers by Additive Manufacturing. *Chemie Ingenieur Technik, 92*(4), 525-531. https://doi.org/10.1002/cite.201900149.

[204] Hock, S., Rein, C., & Rose, M. (2022). 3D-Printed Acidic Monolithic Catalysts for Liquid-Phase Catalysis with Enhanced Mass Transfer Properties. *Chem. Cat. Chem, 14*, e202101947. https://doi.org/10.1002/cctc.202101947.

[205] Gnanasekaran, K., Heijmans, T., van Bennekom, S., Woldhuis, H., Wijnia, S., de With, G., & Friedrich, H. (2017). 3D printing of CNT- and graphene-based conductive polymer nanocomposites by fused deposition modeling. *Additive Manufacturing, 9*, 21-28. https://doi.org/10.1016/j.apmt.2017.04.003.

[206] Li, T., Gonzalez-Gutierrez, J., Raguž, I., Holzer, C., Li, M., Cheng, P., Kitzmantel, M., Shi, L., & Huang, L. (2021). Material extrusion additively manufactured alumina monolithic structures to improve the efficiency of plasma-catalytic oxidation of toluene. *Addit. Manuf., 37*, 101700. https://doi.org/10.1016/j.addma.2020.101700.

[207] Evans, K. A., Kennedy, Z. C., Arey, B. W., Christ, J. F., Schaef, H. T., Nune, S. K., & Erikson, R. L. (2018). Chemically Active, Porous 3D-Printed Thermoplastic Composites. *ACS Applied Materials & Interfaces, 10*(17), 15112-15121. https://doi.org/10.1021/acsami.7b17565.

[208] Foo, C. Y., Lim, H. N., Mahdi, M. A., Wahid, M. H., & Huang, N. M. (2018). Three-Dimensional Printed Electrode and Its Novel Applications in Electronic Devices. *Scientific Reports, 8*, 7399. https://doi.org/10.1038/s41598-018-25861-3.

[209] Rymansaib, Z., Iravani, P., Emslie, E., Medvidović-Kosanović, M., Sak-Bosnar, M., Verdejo, R., & Marken, F. (2016). All-Polystyrene 3D-Printed Electrochemical Device with Embedded Carbon Nanofiber-Graphite-Polystyrene Composite Conductor. *Electroanalysis, 28*, 1517-1523. https://doi.org/10.1002/elan.201600017.

[210] Chaparro-Garnica, C., Bailón-García, E., Lozano-Castelló, D., & Bueno-López, A. (2021). Design and fabrication of integral carbon monoliths combining 3D printing and sol–gel polymerization: effects of the channel morphology on the CO-PROX reaction. *Catalysis Science & Technology, 11*(18), 6490-6497. https://doi.org/10.1039/D1CY01104A.

[211] Chaparro-Garnica, C., Bailón-García, E., Davó-Quiñonero, A., Da Costa, P., Lozano-Castelló, D., & Bueno-López, A. (2021). High Performance Tunable Catalysts Prepared by Using 3D Printing. *Materials, 14*(17), 5017. https://doi.org/10.3390/ma14175017.

[212] Li, Y., Chen, S., Cai, X., Hong, J., Wu, X. E., Xu, Y., ... & Chen, B. H. (2018). Rational design and prepare of hierarchical monolith through 3D printing for syngas methanation. *Journal of Materials Chemistry A, 6*, 6254-6261. https://doi.org/10.1039/C8TA01597J.

[213] Tancogne-Dejean, T., Roth, C. C., & Mohr, D. (2021). Rate-dependent strength and ductility of binder jetting 3D-printed stainless steel 316L: Experiments and modeling. *International Journal of Mechanical Sciences, 207*, 106647. https://doi.org/10.1016/j.ijmecsci.2021.106647.

[214] Lecis, N., Mariani, M., Beltrami, R., Emanuelli, L., Casati, R., Vedani, M., & Molinari, A. (2021). Effects of process parameters, debinding and sintering on the microstructure of 316L stainless steel produced by binder jetting. *Mater. Sci. Eng. A, 828*, 142108. https://doi.org/10.1016/j.msea.2021.142108.

[215] Moritz, T., & Maleksaeedi, S. (2018). Additive manufacturing of ceramic components. In *Additive Manufacturing* (pp. 105-161). Butterworth-Heinemann.

[216] Hamano, R., Nakagawa, Y., Irawan, V., & Ikoma, T. (2021). Mechanical anisotropy and fracture mode of binder jetting 3D printed calcium sulfate moldings. *Additive Manufacturing, 25*, 101160. https://doi.org/10.1016/j.apmt.2021.101160.

[217] Bui, H. M., Großmann, P. F., Gros, T., Blum, M., Berger, A., Fischer, R., Szesni, N., Tonigold, M., & Hinrichsen, O. (2022). 3D printed co-precipitated Ni-Al CO2 methanation catalysts by Binder Jetting: Fabrication, characterization and test in a single pellet string reactor. *Applied Catalysis A: General, 643*, 118760. https://doi.org/10.1016/j.apcata.2022.118760.

[218] Bui, H. M., Fischer, R., Szesni, N., Tonigold, M., Achterhold, K., Pfeiffer, F., & Hinrichsen, O. (2022). Development of a manufacturing process for Binder Jet 3D printed porous Al2O3 supports used in heterogeneous catalysis. *Additive Manufacturing, 50*, 102498. https://doi.org/10.1016/j.addma.2021.102498.

[219] Bui, H. M., Großmann, P. F., Berger, A., Seidel, A., Tonigold, M., Szesni, N., Fischer, R., Rieger, B., & Hinrichsen, O. (2023). Comparison of Direct Ink Writing and Binder Jetting for additive manufacturing of Pt/Al2O3 catalysts for the dehydrogenation of perhydro-dibenzyltoluene. *Chemical Engineering Journal, 458,* 141361. https://doi.org/10.1016/j.cej.2023.141361.

[220] Derazkola, H. A., Khodabakhshi, F., & Simchi, A. (2020). Evaluation of a polymer-steel laminated sheet composite structure produced by friction stir additive manufacturing (FSAM) technology. *Polymer Testing, 90*, 106690. https://doi.org/10.1016/j.polymertesting.2020.106690.

[221] Bhatt, P. M., Kabir, A. M., Peralta, M., Bruck, H. A., & Gupta, S. K. (2019). A robotic cell for performing sheet lamination-based additive manufacturing. *Additive Manufacturing, 27*, 278-289. https://doi.org/10.1016/j.addma.2019.02.002.

[222] Mercado, F., & Rojas Arciniegas, A. (2020). Additive manufacturing methods: techniques, materials, and closed-loop control applications. The International J. *Adv. Manuf. Technol., 109*, 17-31. https://doi.org/10.1007/s00170-020-05663-6.

[223] Lei, H., Li, J., Wang, Q., Xu, Z., Zhou, W., Yu, C., & Zheng, T. (2019). Feasibility of preparing additive manufactured porous stainless steel felts with mathematical micro pore structure as novel catalyst support for hydrogen production via methanol steam reforming. *International Journal of Hydrogen Energy, 44*(47), 24782-24791. https://doi.org/10.1016/j.ijhydene.2019.07.187.

[224] Ha, C., Wang, Z., Wang, C., Qin, J., Zhou, Z., Wang, S., Liu, Z., & Li, B. (2024). High-performance catalyst of methanol steam reformer based on Cu foam with

nanofiber architectures. *International Journal of Hydrogen Energy, 52*(2), 1163-1174. https://doi.org/10.1016/j.ijhydene.2022.07.110.

[225] Wu, Q., Wang, Y., Mei, D., & Si, S. (2022). Development of methanol steam reforming microreactor based on stacked wave sheets and copper foam for hydrogen production. *International Journal of Hydrogen Energy, 47*(11), 6282-6294. https://doi.org/10.1016/j.ijhydene.2021.11.221.

[226] Yu, H., Chen, H., Pan, M., Tang, Y., Zeng, K., Peng, F., & Wang, H. (2007). Effect of the metal foam materials on the performance of methanol steam micro-reformer for fuel cells. *Applied Catalysis A: General, 327*(1), 106-113. https://doi.org/10.1016/j.apcata.2007.05.003.

[227] Flores-López, S. L., Ramírez-Montoya, L. A., Casal, M. D., Montes-Morán, M. A., Menéndez, J. A., & Arenillas, A. (2021). Tortuosity of the porous structure of carbon gels. *Carbon, 171*, 921-930. https://doi.org/10.1016/j.carbon.2020.09.079.

[228] Bailón-García, E. (2016). *Hidrogenación selectiva de aldehídos A, B-Insaturados y fotodegradación de contaminantes con catalizadores basados en xerogeles de carbón*, [Doctoral Thesis, University of Granada] http://hdl.handle.net/10481/42973.

[229] Figueiredo, J. L. (2019). Carbon gels with tuned properties for catalysis and energy storage. *Journal of Sol-Gel Science and Technology, 89*(1), 12-20. https://doi.org/10.1007/s10971-018-4633-y.

[230] Pekala, R. W. (1989). Organic aerogels from the polycondensation of resorcinol with formaldehyde. *Journal of Materials Science, 24*(9), 3221-3227. https://doi.org/10.1007/BF01139044.

[231] Rey-Raap, N., Menéndez, J. A., & Arenillas, A. (2014). RF xerogels with tailored porosity over the entire nanoscale. *Microporous and Mesoporous Materials, 195*, 266-275. https://doi.org/10.1016/j.micromeso.2014.04.048.

[232] Morales-Torres, S., Maldonado-Hódar, F. J., Pérez-Cadenas, A. F., & Carrasco-Marín, F. (2010). Textural and mechanical characteristics of carbon aerogels synthesized by polymerization of resorcinol and formaldehyde using alkali carbonates as basification agents. *Physical Chemistry Chemical Physics, 12*(39), 10365-10372. https://doi.org/10.1039/C003396K.

[233] Yamamoto, T., Yoshida, T., Suzuki, T., Mukai, S. R., & Tamon, H. (2002). Dynamic and Static Light Scattering Study on the Sol-Gel Transition of Resorcinol-Formaldehyde Aqueous Solution. *Journal of Colloid and Interface Science, 245*(2), 391-396. https://doi.org/10.1006/jcis.2001.8006.

[234] Rey-Raap, N., Arenillas, A., & Menéndez, J. A. (2017). Carbon Gels and Their Applications: A Review of Patents. In Bettotti, P. (Ed.) *Submicron Porous Materials* (pp. 25-52). Springer International Publishing.

[235] Al-Muhtaseb, S., & Ritter, J. A. (2003). Preparation and Properties of Resorcinol–Formaldehyde Organic and Carbon Gels. *Advanced Materials, 15*(2), 101-114. https://doi.org/10.1002/adma.200390020.

[236] Brookes, K. J. A. (2015). 3D printing materials in Maastricht. *Mater. Perform. Charact., 4*(3), 68-78. https://doi.org/10.1016/j.mprp.2015.02.009.

[237] Kulkarni, A., Sorarù, G. D., & Pearce, J. M. (2020). Polymer-derived SiOC replica of material extrusion-based 3-D printed plastics. *Additive Manufacturing, 32*, 100988. https://doi.org/10.1016/j.addma.2019.100988

3

EXPERIMENTAL PROCEDURES

3.1. Materials

In a first approach, for the catalytic evaluation of monolithic structures of conventional shape, and the analysis of the influence of cell density on their performance in CO_2 methanation, commercial cordierite monoliths of 200, 400, and 500 cpsi were used. These commercial cylindrical honeycomb monoliths (2.3 cm in diameter and 3.5 in length), with straight channels of square cross-section, were supplied by Céramiques Techniques et Industrielles (CTI), France.

To improve the catalytic efficiency, sophisticated carbon monoliths with novel configurations were produced. The methodology used consisted of three principal steps: i) production of thermoplastic templates of complex channel designs through 3D printing (fused deposition modeling, with CPE filaments); ii) xerogel synthesis by means of a controlled sol-gel process using a resorcinol-formaldehyde-water solution; iii) polymeric template elimination and carbon attainment through carbonization in an N_2 atmosphere at 850 °C, at 1.5 °C min^{-1}, for 2 h.

The active phase used for the methanation of CO_2 was Ni/CeO_2, which was obtained by incipient wetness impregnation of CeO_2 (previously prepared from the thermal decomposition of $Ce(NO_3)_3$) with $Ni(NO_3)_2$ followed by calcination. Once obtained, the active phase was loaded onto cordierite and carbon monoliths by dip coating.

The designs used to print the polymeric templates, the synthesis procedures for the active phase and carbon monoliths, as well as the impregnation method, are thoroughly detailed in Chapters 4 to 6.

3.2. Characterization techniques

The physico-chemical characteristics of monolithic structures are correlated with their catalytic performance and are a key factor in determining their suitability in catalysis. The monoliths produced and used in this research project were characterized to analyze and understand their behavior.

The thermal stability was studied through thermogravimetric analysis (TGA) in air up to 900 °C. This analysis allows to determine the maximum operating temperature as well as the effect of the active phase incorporation. The mechanical stability of the samples was evaluated by means of compressive stress-strain curves obtained through compression tests.

The morphology of the structures, including the surface of the channels and their walls, was studied by means of scanning electron microscopy (SEM). Moreover, the active phase distribution obtained with the dip coating method was assessed with chemical mapping using energy dispersive X-ray spectroscopy (EDS).

The porosity of the active phase and ceramic and carbon monoliths was estimated by adsorption isotherms, either using N_2 at -196 °C and/or CO_2 at 0°C. The Brunauer-Emmett-Teller (BET) and Dubinin-Radushkevich (DR) equations were employed to calculate the specific surface area (S_{BET}) and micropore volume (V_{micro}). The total pore volume was taken as the N_2 volume adsorbed at a relative pressure of 0.95. Besides, the wider porosity was determined by Hg-porosimetry.

The surface chemistry of the CeO_2 and the Ni/CeO_2 active phase was examined through X-ray photoelectron spectroscopy (XPS). Additionally, their crystalline structure, as well as the impact of the loading process, was studied using X-ray diffraction (XRD) and Raman spectroscopy.

A more detailed description of the analytical procedures and the operational conditions used is provided in the corresponding chapters of this thesis.

3.3. Catalytic evaluation

The catalytic behavior of the different catalysts produced was evaluated in the CO_2 methanation, also known as the Sabatier reaction. The results were used to establish the effect of the monolithic configuration on their effectiveness. The reaction system consisted of flow controllers for the reagent feeding to a quartz cylindrical reactor located in a tubular furnace with temperature control. A monolith was placed in the middle of the quartz reactor, and a cold trap was integrated at the outlet to collect

the water vapor produced during the reaction. A detailed schema of the reaction system configuration is shown in Chapter 4.

The reaction was monitored by analyzing the outflow gases CO2 and CH4 with infrared gas sensors (Edinburgh Instruments LTD 034/00700). A reduction treatment (100 mL min^{-1} of 10% H_2 in Ar) at 500 °C for 1.5 h was carried out before each reaction. Once finished, the system was allowed to cool down to 150 °C to change the inlet flow to the reactive mixture consisting of 10% CO_2 and 40% H_2 balanced in Ar, with total flows between 100 and 500 mL min^{-1}. Temperature increments of 25 °C were applied to reach 450 °C, holding each temperature for 20 min. The catalytic performance was evaluated based on the CO_2 conversion, reaction rate, and selectivity to CH_4.

A more detailed description of the reaction system, the operational conditions, and the catalytic tests is provided in Chapters 4 to 6 of the thesis.

4

MODELING AND EXPERIMENTAL ANALYSIS OF CO_2 METHANATION REACTION USING Ni/CeO_2 MONOLITHIC CATALYST
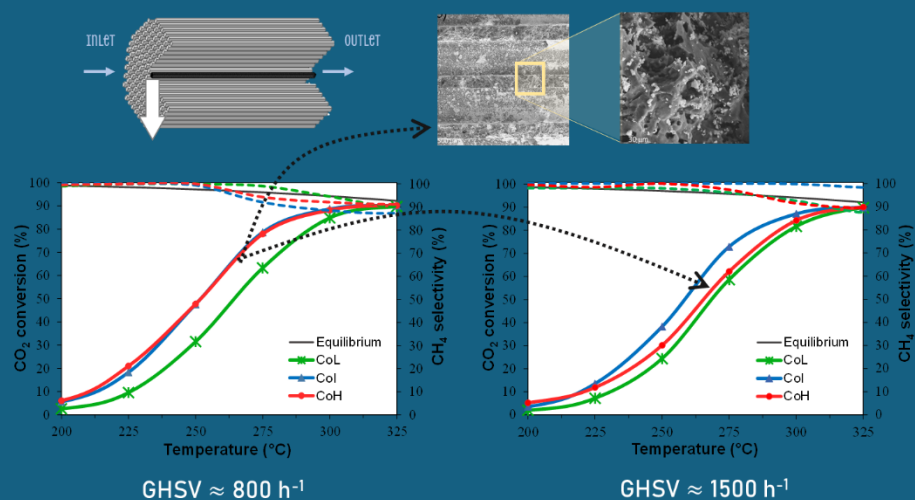
4.1. Introduction

The carbon dioxide conversion to value-added products appears as a promising alternative to reduce the environmental problems caused by CO_2-dominated greenhouse gases. Several techniques have been employed for CO_2 reduction, including thermochemical [1–3], biochemical [4,5], electrochemical [6–9], and photochemical [10–12]. Among the technologies mentioned above for CO_2 valorization, the thermochemical transformation through catalytic hydrogenation to methane has gained attention since it is a strategy that can treat two environmental issues at a time: the accumulation of greenhouse gases in the atmosphere and the energy demand [13–16].

The catalytic CO_2 hydrogenation to methane, also known as CO_2 methanation or Sabatier reaction (Eq. 1), is a high exothermic equilibrium reaction [17,18].

$$CO_2 + 4H_2 \leftrightarrow CH_4 + 2H_2O, \triangle H_{298\,K} = -164.9 \text{ kJ mol}^{-1} \tag{1}$$
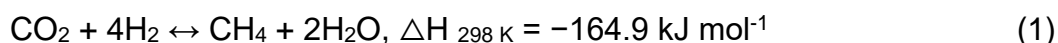
This process has several environmental implications such as: i) carbon sequestration since CO_2 methanation offers a potential pathway for carbon capture and storage (CCS) by converting CO_2 into methane helping to mitigate climate change; ii) utilization of CO_2: methanation provides a means of utilizing CO_2 as a feedstock for the production of methane, an useful fuel or chemical feedstock, rather than allowing them to be released directly into the atmosphere; iii) renewable energy storage: methane produced through CO_2 methanation can be used as a renewable energy storage medium. It can be stored and transported through existing natural gas infrastructure [19] providing a means of storing excess renewable energy generated from sources such as wind and solar power for use during periods of low generation. Overall, while CO_2 methanation offers potential environmental benefits such as carbon sequestration and renewable energy storage, its environmental implications depend on factors such as the source of hydrogen, energy efficiency of the process, methane leakage, and land use impacts. Therefore, careful assessment and management of these factors are necessary to maximize the environmental benefits of CO_2 methanation while minimizing its potential negative impacts.

The Sabatier reaction is thermodynamically favored at low temperatures; however, it is kinetically limited due to the high carbon dioxide stability and hydrogen activation [19]. Therefore, stable, and efficient catalysts are needed to improve the reaction conditions and increase the reaction rate of CO_2 methanation. In this sense, catalysts based on Ni species supported on different oxides (namely CeO_2, Al_2O_3, TiO_2, SiO_2, ZrO_2, and so on) are the most commonly used in industrial scale methanation processes [13,20,21]. Regarding other metals, metallic nickel results are attractive because of its high catalytic activity, high methane selectivity, and relatively low cost [21,22]. On the other hand, among the previously mentioned supports, CeO_2 is recognized to promote CO_2 methanation, enhancing CH_4 formation. Also, CeO_2 improves the metal-support interaction, resulting in an excellent low-temperature catalytic performance [23,24]. Nevertheless, during exothermic CO_2 methanation, the temperature increases, forming hot spots and leading to catalyst deactivation by Ni particles agglomeration/sintering and carbon deposition [25]. Hence, the catalyst structure has an essential role in enabling good heat and mass transfer inside the reactor to get high stability and activity.

Compared to packed-bed systems, structured systems using monolithic catalysts present several advantages, such as better heat exchange and fluid processing and a significant reduction in pressure drop, allowing to treat high feed flows. Moreover, using monolithic catalysts also results in easier manipulation, separation, and cleaning processes at an industrial scale. Typically, monolithic structures used for supporting catalytic active phases are either ceramic or metallic [26–29]. In that regard, few studies employing monolithic structures supporting catalytic active phases for CO_2 methanation have been developed. Fukuhara et al. [30] prepared a CO_2 methanation catalyst by wash coating an aluminum honeycomb monolith with a Ni/CeO_2-propanol suspension. The catalyst produced showed high activity and selectivity owing to better mass and heat transfer properties. Danaci et al. [31] investigated the performance of a stainless-steel monolithic structure coated with Ni/Al_2O_3 for CO_2 methanation. The results showed improvement using the metallic

support compared to the powder catalyst (an increase of CO_2 conversion near to 90 %, and stable methane selectivity at around 95-99 %). Nonetheless, they have noticed the importance of the slurry properties in coating adhesion on metallic supports, for which was needed the addition of acid to avoid agglomeration of particles and binder to provide suitable viscosity and suspension stability. Hence, the requirement and influence of surface pretreatments and/or coating additives on the catalytic properties is a disadvantage of this type of material.

Ceramic materials, among which cordierite is the most widely used, offer high thermal and chemical stability and better active phase adherence in comparison to metallic ones [32–34]. In this context, NiFe catalyst was prepared on alumina-washcoated cordierite monolith by Huynh et al. (2020), which allowed them to treat high flow rate (500 mL min^{-1}), achieving great methane yield from CO_2 methanation. Besides, Vita et al. (2020) studied the behavior of a cordierite monolith loaded with 25 wt% Ni/GDC (gadolinium-doped-ceria) towards the conversion of CO_2 to CH_4. The catalyst facilitated the temperature distribution, thus avoiding coking and sintering, along with enabling high space velocity operation with great stability and CO_2 conversion (~70 %). Furthermore, other configuration parameters, such as hydrodynamic design, are also determining for its usefulness in selective oxidation processes [37,38]. With an increase in cell density a larger surface to volume ratio is gained, leading to a greater amount of deposited and accessible active phase, and, therefore, a higher CO-PROX activity is expected [39]. However, some authors have observed that dynamic performance is deteriorated due to a mass transfer inhibition by molecular diffusion in VOC abatement or adsorption kinetics [40,41]. However, a lack of information exists about the behavior of cordierite monoliths and the effect of cell density, flow rates, and the active phase distribution along the monolith porosity on the catalytic performance for the CO_2 methanation.

Considering the above, this chapter aims to evaluate the performance of Ni/CeO$_2$-coated cordierite monoliths in the Sabatier reaction as a way for improving the catalytic activity in the treatment of high CO_2 flow rates. Moreover, different cell

densities (200, 400, and 500 cpsi) were employed to study the influence of monolith configuration on CO_2 conversion and selectivity to CH_4. Additionally, an appropriate mathematical model is established to analyze the fluid dynamics of the materials, as well as to predict the velocity profiles inside the channels of the catalytic structure used. Therefore, the understanding achieved in this chapter is very promising for the development and improvement of monolithic catalysts for CO_2 methanation and works towards achieving the sustainability and environmental protection goals.

4.2. Experimental

4.2.1. Catalyst preparation

4.2.1.1. Active phase synthesis

Firstly, the CeO_2 was obtained by thermal decomposition of cerium nitrate hexahydrate ($Ce(NO_3)_3 \cdot 6H_2O$, ≥ 99.5 % from Alfa Aesar) by calcination in a muffle at 500 °C for 4 h. Then, the Ni/CeO_2 active phase was prepared by incipient wetness impregnation of the CeO_2 with an ethanolic solution of nickel (II) nitrate hexahydrate ($Ni(NO_3)_2 \cdot 6H_2O$, ≥ 97 % Sigma-Aldrich) to attain 10 wt% of Ni. Subsequently, the impregnated CeO_2 was calcined at 600 °C for 5 h to decompose the salt and obtain the final Ni/CeO_2 active phase.

4.2.1.2. Active phase loading

The previously obtained Ni/CeO_2 was deposited onto commercial cordierite monoliths with three different cell densities (200, 400, and 500 cpsi, named CoL, CoI, and CoH, correspondingly) using the dip-coating method. These cylindrical honeycomb cordierite monoliths, of approximately 2.3 cm in diameter and 3.5 cm in length, are composed by straight channels with a square cross-section (**Figure 4.1**) and were supplied by CTI (Céramiques Techniques et Industrielles; France). The monoliths were immersed into a Ni/CeO_2 ethanolic suspension (10 wt%). Then, they were dried for 12 h at room temperature while rotating horizontally to obtain homogeneous distribution of the Ni/CeO_2, and later at 80 °C overnight. The exceeding active phase not anchored to the monoliths that can block the channels was dropped using compressed air. The amount of Ni/CeO_2 loaded was corroborated by the weight difference of the dried

monoliths after each impregnation, and the process was repeated until achieving 800 ± 5 mg of Ni/CeO$_2$ per monolith.

Figure 4.1. Commercial honeycomb cordierite monoliths used for evaluation of CO$_2$ methanation.

4.2.2. Catalyst characterization

To get information about the surface area of the Ni/CeO$_2$ powder catalyst, adsorption isotherms (N$_2$ at -196 °C) were obtained employing a Quantachrome Autosorb-6B equipment. The samples were degassed at 110 °C for 8 h before the gas adsorption measurements. The surface chemistry of the active phase Ni/CeO$_2$ and the CeO$_2$ support was analyzed using X-ray photoelectron spectroscopy (XPS) with a K-ALPHA Thermo Scientific device. The X-ray source utilized was Al-Kα radiation at 1486.6 eV. Besides, its crystalline structure was studied by X-ray diffraction (XRD) and Raman spectroscopy. Raman analysis was done by a JASCO NRS-5100 dispersive micro-Raman microscope with a Green Diode 532 nm, 30 mW (Elforlight G4-30; Nd:YAG). The XRD patterns of the catalyst were measured using an X-Ray Diffractometer Bruker D8 DISCOVER with CuKα-ray radiation (λ =1.54178 Å) in the 2θ range of 10 – 90° at a step size of 1° min^{-1}. The average crystal size (*d*) was determined using the Scherrer equation (2) [42,43].

$$d = \frac{K \cdot \lambda}{B \cdot cos\theta} \qquad (2)$$

Where d is the crystallite size, B is the full width at half maximum in radians, K is the shape factor (0.94), l is the X-ray wavelength (0.15 nm) and q is the diffraction angle in radians.

The porosity of the ceramic monoliths was analyzed by Hg-porosimetry using a Micromeritics AutoPore IV 9500 equipment. The analysis was conducted from an initial pressure of 5 psi up to 30, 500 psi, with 10 seconds of equilibration time between points. The contact angle and surface tension used for pore size calculations were $\theta = 130°$ and $\gamma = 485$ dyne/cm, respectively. The active phase distribution on the cordierite monoliths was analyzed by scanning electron microscopy (SEM) using a SUPRA40VP Variable Pressure Scanning Electron Microscope (VP-FESEM) from Zeiss equipped with an EDX detector X-max 50 for microanalysis and chemical mapping.

Moreover, compression tests were realized to analyze the mechanical properties of ceramic monoliths. Firstly, the monolith samples were cut into cylinders 1.5 cm high, and the bases were sanded to obtain smooth and even surfaces. The tests were carried out with a constant approach speed of 1 mm-min^{-1} utilizing a Shimadzu AGS-J 10 kN instrument, and the compression test direction was top to bottom. The corresponding compressive stress–strain curves were analyzed to obtain the Young's modulus (E), and the maximum strength (σ) were determined from stress-strain curve analysis.

4.2.3. Catalytic tests

The monolithic catalysts performance and the effect of cell density were analyzed in the methanation of carbon dioxide. A monolith was fixed in a quartz cylindrical reactor and placed in a furnace with temperature control, as shown in **Figure 4.2**. A cold trap was settled at the outlet of the reactor to retain the water produced, and the outflow gases CO_2 and CH_4 were analyzed by infrared gas sensors (Edinburgh Instruments LTD 034/00700). Prior to each experiment, the monolith to be studied was treated in a reducing atmosphere at 500 °C for 1.5 h. Afterwards, the system was let to cool down to 150 °C, so the inlet flow was changed to the reaction gas mixture (10 % CO_2, and 40 % H_2 balanced in Ar) with total flows ranging from 100 to 500 mL min^{-1}. The temperature was increased up to 450 °C in steps of 25 °C, holding each temperature for 20 min. The CO_2 conversion ($\%C_{CO_2}$) and selectivity to CH_4 ($\%S_{CH_4}$) were calculated to evaluate the catalytic performance according to the following equations:

$$\%C_{CO_2}(\%)=\frac{F\ CO_{2in}\ -\ F\ CO_{2out}}{F\ CO_{2in}}\times100\% \tag{3}$$

$$\%S_{CH_4}(\%)=\frac{FCH_4}{F\ CO_{2in}\ -\ F\ CO_{2out}}\times100\% \tag{4}$$

Where $FCO_{2\ in}$, $FCO_{2\ out}$, and FCH_4 refer to the volumetric flow of CO_2 in the inlet and outlet of the reactor, and the volumetric flow of CH_4 obtained, respectively.
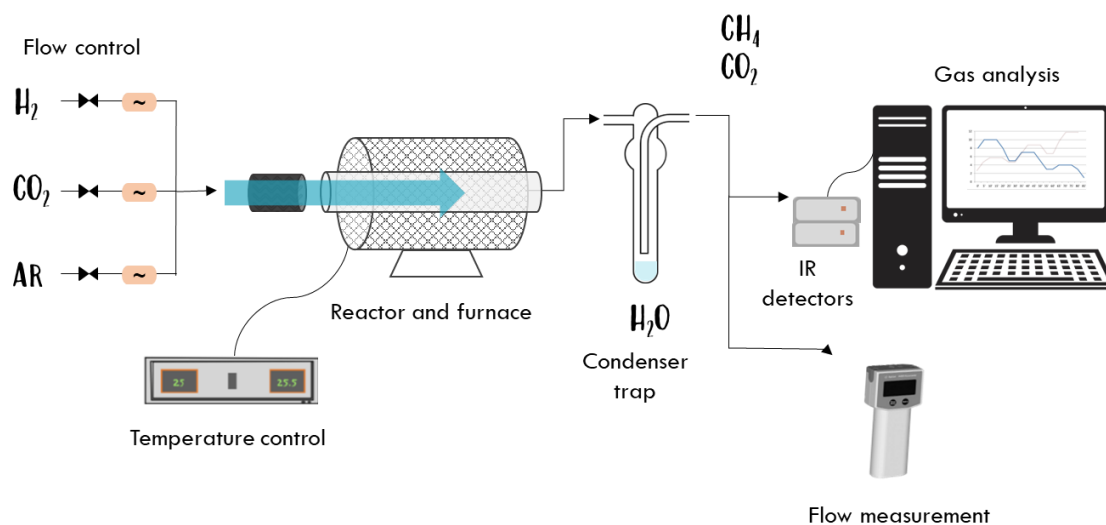
Figure 4.2. Experimental reaction system setup scheme.

4.2.4. Mathematical model

The experimental data were interpreted with a mathematical model involving the mass and momentum balances for the reaction gas mixture. The mass transfer was analyzed considering the mass transport of CO_2 and H_2 from the bulk to the external surface of the reactive monolith walls. It is assumed that the monolith has low porosity; thus, the solute diffusion is negligible. According to the chemical reaction (1), the mathematical model includes nine partial differential equations. Three equations correspond to the momentum balance, one equation states the gas-phase mass balance, and additionally, there is one mass balance for each chemical species including argon, since, although it is a nonreactive compound, the species molar fractions depend on all the gases, and they must sum one in total. For momentum

balance, we used the $\kappa - \epsilon$ mathematical model, considering the possibility of the flow developing turbulence inside the monolith for all the experimental cases.

The momentum balance is given by:

$$\rho \frac{\partial \boldsymbol{u}}{\partial t} + \rho(\boldsymbol{u} \cdot \nabla)\boldsymbol{u} = -\nabla p + \nabla \cdot \mathbf{K} \tag{5}$$

With,

$$\mathbf{K} = (\mu + \mu_T)[\nabla \boldsymbol{u} + (\nabla \boldsymbol{u})^T] \tag{6}$$

Here μ_T is the turbulent viscosity computed as follows:

$$\mu_T = \rho C_\mu \frac{\kappa^2}{\epsilon} \tag{7}$$

The turbulent kinetic energy κ obeys the following partial differential equation:

$$\rho \frac{\partial \kappa}{\partial t} + \rho(\boldsymbol{u} \cdot \nabla)\kappa = \nabla \cdot \left[\left(\mu + \mu_T \frac{\mu_T}{\sigma_\kappa}\right)\nabla\kappa\right] + P_\kappa - \rho\epsilon \tag{8}$$

While the rate of dissipation of turbulent kinetic energy is given by:

$$\rho \frac{\partial \epsilon}{\partial t} + \rho(\boldsymbol{u} \cdot \nabla)\epsilon = \nabla \cdot \left[\left(\mu + \mu_T \frac{\mu_T}{\sigma_\epsilon}\right)\nabla\epsilon\right] + C_{\epsilon 1}\frac{\epsilon}{\kappa}P_\kappa - C_{\epsilon 2}\rho\frac{\epsilon^2}{\kappa} \tag{9}$$

The term associated to the rate of deformation is defined as:

$$P_\kappa = \mu_T\{\nabla\boldsymbol{u}\colon[\nabla\boldsymbol{u} + (\nabla\boldsymbol{u})^T]\} \tag{10}$$

In addition, $\boldsymbol{\rho}$ represents the fluid mass density, $\boldsymbol{u}$ is the vector of velocity, t is the time, p is the pressure, and $\boldsymbol{\mu}$ is the fluid viscosity. The gas-phase mass balance is given by the continuity equation written as:

$$\frac{\partial \rho}{\partial t} + \nabla \cdot (\rho\boldsymbol{u}) = 0 \tag{11}$$

The mass balance for each chemical species in terms of molar concentration, C, are shown in equations (12-16), for which D_i refers to the molecular diffusivity of the *i*-compound in Ar.

For CO₂ $\dfrac{\partial C_{CO_2}}{\partial t} + \nabla \cdot \left(\boldsymbol{u}C_{CO_2}\right) = \nabla \cdot (D_{CO_2}\nabla C_{CO_2})$ $\tag{12}$

For H₂ $\dfrac{\partial C_{H_2}}{\partial t} + \nabla \cdot \left(\boldsymbol{u}C_{H_2}\right) = \nabla \cdot (D_{H_2}\nabla C_{H_2})$ $\tag{13}$

For CH$_4$ $\quad \dfrac{\partial C_{CH_4}}{\partial t} + \nabla \cdot \left(\boldsymbol{u}C_{CH_4}\right) = \nabla \cdot \left(D_{CH_4}\nabla C_{CH_4}\right)$ (14)

For H$_2$O $\quad \dfrac{\partial C_{H_2O}}{\partial t} + \nabla \cdot \left(\boldsymbol{u}C_{H_2O}\right) = \nabla \cdot \left(D_{H_2O}\nabla C_{H_2O}\right)$ (15)

For Ar $\quad \dfrac{\partial C_{Ar}}{\partial t} + \nabla \cdot \left(\boldsymbol{u}C_{Ar}\right) = \nabla \cdot \left(D_{Ar}\nabla C_{Ar}\right)$ (16)

Initial values of primary variables (molar concentrations, pressure, and velocity) used to solve numerically the model are considered as:

At $\;t = 0$ min $\;\; C_{CO_2} = C_{CO_2}^0, \; C_{H_2} = C_{H_2}^0, \; C_{CH_4} = C_{CH_4}^0, \; C_{H_2O} = C_{H_2O}^0,$

$$C_{Ar} = C_{Ar}^0, \qquad \boldsymbol{u} = \boldsymbol{0}, \quad p = 1 \text{ atm}$$ (17)

Further, boundary conditions were stated at the inlet and outlet of the monolith. For the inlet boundary, the velocity and molar concentrations are determined as:

$$C_{CO_2} = C_{CO_2}^{in}, \quad C_{H_2} = C_{H_2}^{in}, \quad C_{CH_4} = C_{CH_4}^{in}, \quad C_{H_2O} = C_{H_2O}^{in}, \quad C_{Ar} = C_{Ar}^{in}$$

$$-\boldsymbol{n} \cdot \boldsymbol{u} = u^{in}$$ (18)

Where $\boldsymbol{n}$ is the unit normal vector pointing outward the inlet boundary. The inlet velocity u^{in} is computed through the flow area and volumetric flow rate as follows:

$$u^{in} = \frac{Q}{A}$$ (19)

Whereas, at the outlet boundary the pressure is fixed, and the species flow is only due to advection:

$$\boldsymbol{n} \cdot (D_{CO_2}\nabla C_{CO_2}) = 0, \quad \boldsymbol{n} \cdot (D_{H_2}\nabla C_{H_2}) = 0, \quad \boldsymbol{n} \cdot (D_{CH_4}\nabla C_{CH_4}) = 0,$$

$$\boldsymbol{n} \cdot (D_{H_2O}\nabla C_{H_2O}) = 0, \quad \boldsymbol{n} \cdot (D_{Ar}\nabla C_{Ar}) = 0, \; p = 1 \text{ atm}$$ (20)

The nonslip and impenetrability conditions are enforced for the velocity vector at the monolith surface, $\boldsymbol{u} = \boldsymbol{0}$. Meanwhile, at the reactive surface of the monolith the normal fluxes of chemical species are stated as:

$$\boldsymbol{n} \cdot (D_{CO_2}\nabla C_{CO_2}) = -r_m, \quad \boldsymbol{n} \cdot (D_{H_2}\nabla C_{H_2}) = -4r_m,$$

$$\boldsymbol{n} \cdot (D_{CH_4}\nabla C_{CH_4}) = r_m,$$ (21)

$$\boldsymbol{n} \cdot (D_{H_2O}\nabla C_{H_2O}) = 2r_m, \quad \boldsymbol{n} \cdot (D_{Ar}\nabla C_{Ar}) = 0$$

The auxiliary relations of the total molar concentration, molar fraction of species *i*, partial pressure of species *i*, and the mass density of the gaseous mixture obtained from the average molar mass M, are given by the following equations:

$$C = C_{CO_2} + C_{H_2} + C_{CH_4} + C_{H_2O} + C_{Ar} \tag{22}$$

$$y_i = \frac{C_i}{C} \tag{23}$$

$$p_i = y_i p \tag{24}$$

$$M = \Sigma_i y_i M_i; \quad \rho = MC \tag{25}$$

The molecular diffusivity coefficients D_i as function of the temperature (T) were estimated with the following correlations (temperature in K and diffusivity in cm² s⁻¹):

$$D_{CO_2-Ar} = \frac{0.00143T^{1.75}}{(1)(41.8807)^{0.5}[26.9^{1/3} + 16.2^{1/3}]^2} = 7.2346 \; x \; 10^{-6}T^{1.75} \tag{26}$$

$$D_{H_2-Ar} = \frac{0.00143T^{1.75}}{(1)(3.8383)^{0.5}[6.12^{1/3} + 16.2^{1/3}]^2} = 3.8406 \; x \; 10^{-5}T^{1.75} \tag{27}$$

$$D_{CH_4-Ar} = \frac{0.00143T^{1.75}}{(1)(22.8894)^{0.5}[25.14^{1/3} + 16.2^{1/3}]^2} = 1.0027 \; x \; 10^{-5}T^{1.75} \tag{28}$$

$$D_{H_2O-Ar} = \frac{0.00143T^{1.75}}{(1)(24.8318)^{0.5}[13.1^{1/3} + 16.2^{1/3}]^2} = 1.2012 \; x \; 10^{-5}T^{1.75} \tag{29}$$

The chemical reaction rate of CO₂ methanation is described by a Hougen-Watson type expression [44]:

$$r_m = \rho_{cat} \frac{kK_{CO_2}K_{H_2}^4 p_{CO_2} p_{H_2}^4}{\left(1 + K_{CO_2}p_{CO_2} + K_{H_2}p_{H_2}\right)^5}(1 - \beta) \tag{30}$$

Where r_m (mol m⁻³s⁻¹) is the CO₂ methanation reaction rate, ρ_{cat} (kg m⁻³) is the catalyst density, and β is the approach-to-equilibrium coefficient defined as:

$$\beta = \frac{p_{CH_4}p_{H_2O}^2}{0.009 p_{CO_2} p_{H_2}^4 K_{eq}} \tag{31}$$

Here k is the rate constant of CO_2 methanation reaction (mol $kg_{cat}^{-1}s^{-1}$), p_i (i = CO_2, H_2, CH_4 and H_2O) is the partial pressure (atm) of species i, K_i is the surface adsorption equilibrium constant for species i (atm^{-1}), and K_{eq} is the overall Sabatier reaction equilibrium constant (atm^{-2}). The expressions for these variables are given as:

$$k = 1.0635x10^{11}exp\left(\frac{-124850}{RT}\right) \tag{32}$$

$$K_{CO_2} = 9.099x10^{-7}exp\left(\frac{69691.8}{RT}\right) \tag{33}$$

$$K_{H_2} = 9.6104x10^{-4}exp\left(\frac{39942.0}{RT}\right) \tag{34}$$

$$K_{eq} = exp\left[\left(\frac{28183}{T^2}+\frac{17430}{T}-8.2536log(T)+2.8032x10^{-3}T\right)+33.165\right] \tag{35}$$

4.3. Results and discussions

4.3.1. *Materials characterization*

4.3.1.1. *Physicochemical characterization of the active phase*

The specific surface area (S_{BET}) and micropore volume (V_{micro}) were determined by applying the Brunauer-Emmett-Teller and Dubinin-Radushkevich equations to the N_2 isotherm, resulting in low surface areas. The volume of N_2 adsorbed at $P/P_0=0.95$ was considered as the total pore volume (V_{total}), while the mesopore volume (V_{meso}) was calculated by the difference between the V_{total} and V_{micro}. As shown in *Figure 4.3*, type IV isotherms were obtained for the CeO_2 and Ni/CeO_2 samples, which according to the IUPAC classification correspond to mesoporous materials. The isotherms present a low N_2 uptake at low relative pressures, meaning they contain low micropore volume. As the relative pressures increased, the N_2 uptake augmented, and a hysteresis loop is observed in both cases, which is attributed to the presence of mesopores. It is seen that the hysteresis loop closes at high relative pressures due to the existence of wide mesopores, possibly produced during the calcination. Moreover, the addition of Ni on the CeO_2 surface led to mesopores blockage, as shown with the

diminution of S_{BET} and V_{meso} (see ***Table 4.1***), suggesting that Ni particles are dispersed on the CeO_2 surface blocking part of the porosity of the material.
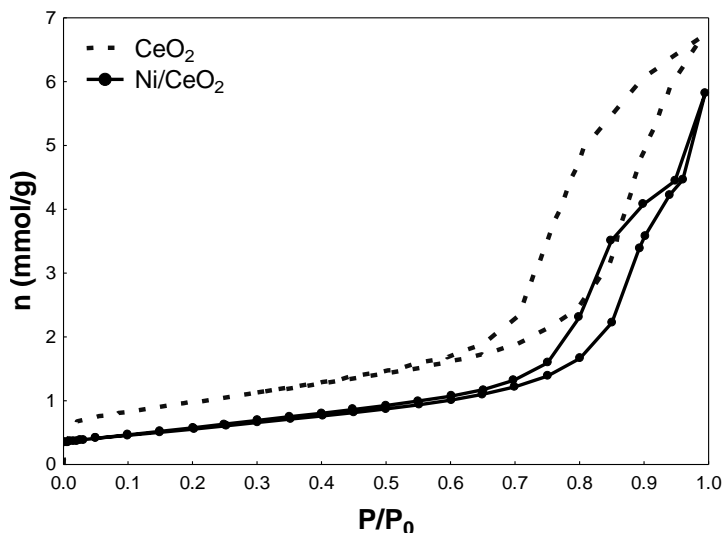
Figure 4.3. N_2 adsorption−desorption isotherms at −196 °C of CeO_2 and Ni/CeO_2 powdered catalyst.

Table 4.1. N_2 sorption characterization of CeO_2 and Ni/CeO_2 powdered active phase.

Sample	S_{BET} $(m^2 g^{-1})$	V_{total} $(cm^3 g^{-1})$	V_{micro} $(cm^3 g^{-1})$	V_{meso} $(cm^3 g^{-1})$
CeO_2	78	0.21	0.04	0.17
Ni/CeO_2	45	0.15	0.02	0.13

The crystal structure of CeO_2 and the catalytic compound was analyzed by X-ray diffraction and Raman spectroscopy, and the results are presented in ***Figures 4.4*** and ***4.5***, respectively. The X-ray diffractograms of both samples (***Figure 4.4***) revealed the characteristic peaks of the fluorite face-centered cubic (FCC) crystalline structure of ceria (JCPDS 00-034-0394) at 28.5, 33.1, 47.6, and 56.5°, corresponding to the (111), (200), (220), and (311) planes [45]. Besides, the Ni/CeO_2 analysis showed additional little peaks at 37.2, 43.3, and 63° ascribed to (111), (200), and (220) crystallographic planes of the FCC of NiO (JCPDS 00-047-1049) [46]. The lattice parameter of CeO_2 calculated from XRD data was 0.5411 nm, which stays in accordance with the value reported in JCPDS 00-034-0394. The incorporation of nickel

slightly displaced the CeO_2 peaks in Ni/CeO_2 active phase, which is also manifested in the increase of the lattice parameter of CeO_2 to 0.5420, thus implying that some nickel cations are introduced into the crystal lattice of ceria. Instead, NiO particles are assumed to be mainly distributed on the CeO_2 surface. The crystal sizes of CeO_2 and Ni/CeO_2 were obtained by the Scherrer equation [42,43]. The addition of nickel did not cause a significant change in the average size of the ceria crystals since the results were similar for both the pure CeO_2 (8.77 nm) and the catalytic Ni/CeO_2 (9.27 nm).
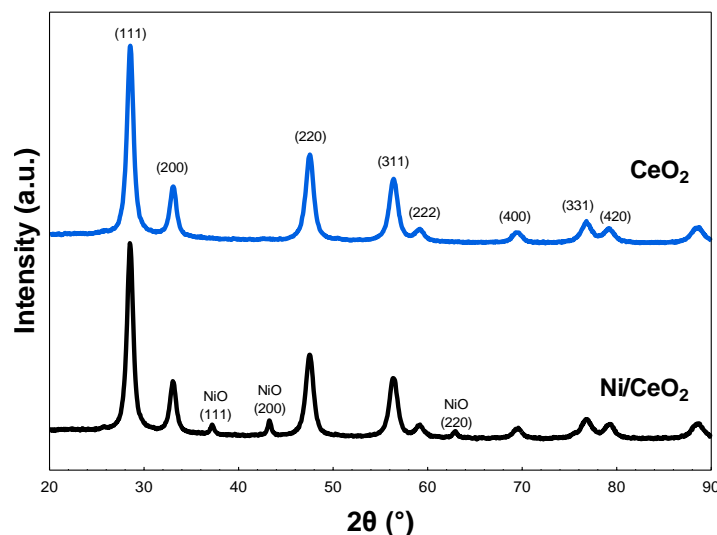
Figure 4.4. X-ray diffractograms of CeO_2 support and Ni/CeO_2 active phase.

As plotted in ***Figure 4.5***, Raman spectra of pure ceria contains a single band at 463.9 cm^{-1}, attributed to the F_{2g} mode of the fluorite-type cubic crystal structure of CeO_2 [47–49]. This peak corresponds to a symmetric Ce-O stretching vibration occurring around its equilibrium position in the octahedral sites of the cubic cell [48,50,51]. Owing to the presence of nickel and its interaction with ceria, the F_{2g} peak shifted to 459.5 cm^{-1} in the spectra of Ni/CeO_2 active phase [50]. Further, a small shoulder is present in the spectra of Ni/CeO_2 catalyst between 500 and 660 cm^{-1}, which is assigned to oxygen vacancies located at interfacial sites between Ni and CeO_2 [52].

These results evidence the insertion of Ni^{2+} cations into the CeO_2 network, replacing Ce^{4+} cations, and the oxygen vacancies are created to compensate the positive charge imbalance and relax crystal tensions due to the smaller size of the Ni^{2+}

cations. The oxygen vacancies act as crucial cooperative sites in addition to metal active sites, since they bind adsorbates more strongly than normal oxide sites, promoting the dissociation [53,54]. In conclusion, Ni/CeO_2 characterization by N_2 adsorption, XRD and Raman spectroscopy evidence the formation of NiO particles on the CeO_2 surface and inserption of Ni^{2+} cations into the CeO_2 framework. High catalytic activity of this active phase for CO_2 methanation has been related with the presence of two type of active sites: oxygen vacant sites associated to the Ni^{2+}-CeO_2 entities that are efficient for CO_2 chemisorption and dissociation, and metal Ni, obtained upon surface NiO nanoparticles reduction, which is expected to dissociate H_2.
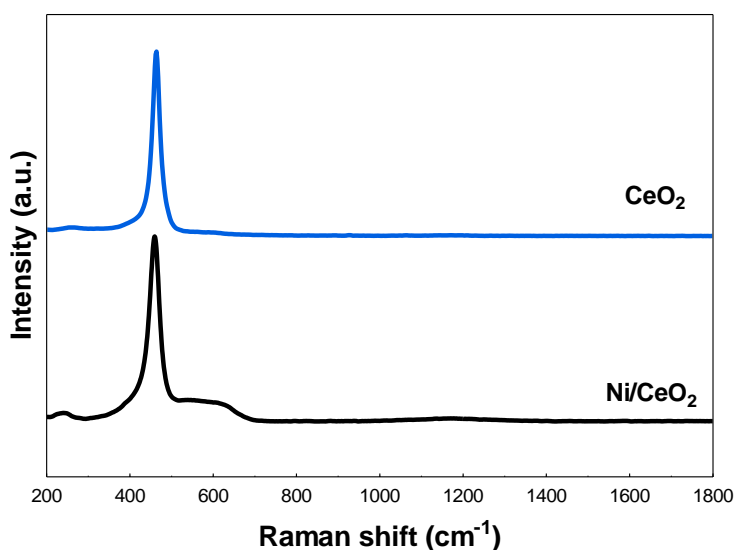
Figure 4.5. Raman spectra of CeO_2 support and Ni/CeO_2 active phase.

The surface chemistry of the Ni/CeO_2 active phase and CeO_2 support was analyzed by XPS. Ce_{3d}, O_{1s}, and Ni_{2p} XPS spectral regions are shown in ***Figure 4.6.*** 5 doublets are required to deconvolve the Ce_{3d} region (***Figure 4.6a***). The peaks pairs at 882.0-900.3 eV, 888.2-907.0 eV, 898.0-916.3 are attributed to $Ce^{4+,}$ whereas the peaks at 880.3-898.6 eV and 884.0-902.3 eV are assigned to Ce^{3+}. The proportion of Ce^{3+} detected by XPS must be related with the reducibility of the surface. B. Sellers-Antón et al. [55] show that the reducibility of the surface is improved by the addition of Ni, mainly if this Ni is incorporated during the synthesis due to the higher dispersion and Ce-Ni contact in this case. Consequently, it is expected that the amount of Ce^{3+}

detected by XPS increases in Ni/CeO$_2$ active phase regarding CeO$_2$ support. The surface Ce^{3+} content obtained by XPS was 18.9 and 22.5 for CeO$_2$ and Ni/CeO$_2$, respectively, due to the improved surface reducibility which confirm the successful synthesis of Ni/CeO$_2$. This effect must be also observed in the O$_{1s}$ region. The O$_{1s}$ region requires two peaks for deconvolution (see **Figure 4.6b**): one peak centered at 529.0 eV, associated with surface lattice oxygen (O$_{latt}$), and another peak centered at 531.0 eV, attributed to adsorbed oxygen species (O$_{ads}$). Typically, O$_{ads}$ species are present at oxygen vacancies, so a higher concentration of O$_{ads}$ species suggests a greater population of oxygen vacancies. Therefore, the ratio of surface O$_{ads}$ to O$_{latt}$ can serve as an indicator of surface reducibility. The O$_{ads}$/O$_{latt}$ ratio was 0.22 and 0.32 for CeO$_2$ and Ni/CeO$_2$, respectively indicating that Ni improves the ceria surface reducibility. Finally, the Ni$_{2p3/2}$ region of active phase was depicted in **Figure 4.6c**. In this spectral region, a primary band is observed within the 851–859 eV range, accompanied by a satellite structure at higher binding energies (859–866 eV). To deconvolute the Ni$_{2p3/2}$ region, three peaks are necessary, occurring around 853.2, 855.0, and 857.2 eV. These peaks correspond to surface Ni^{2+} species within the NiO structure (surface NiO species), Ni^{2+} species closely associated with the ceria surface (NiO-Ce species), and Ni^{3+} or Ni(OH)$_2$ species, respectively [55,56].
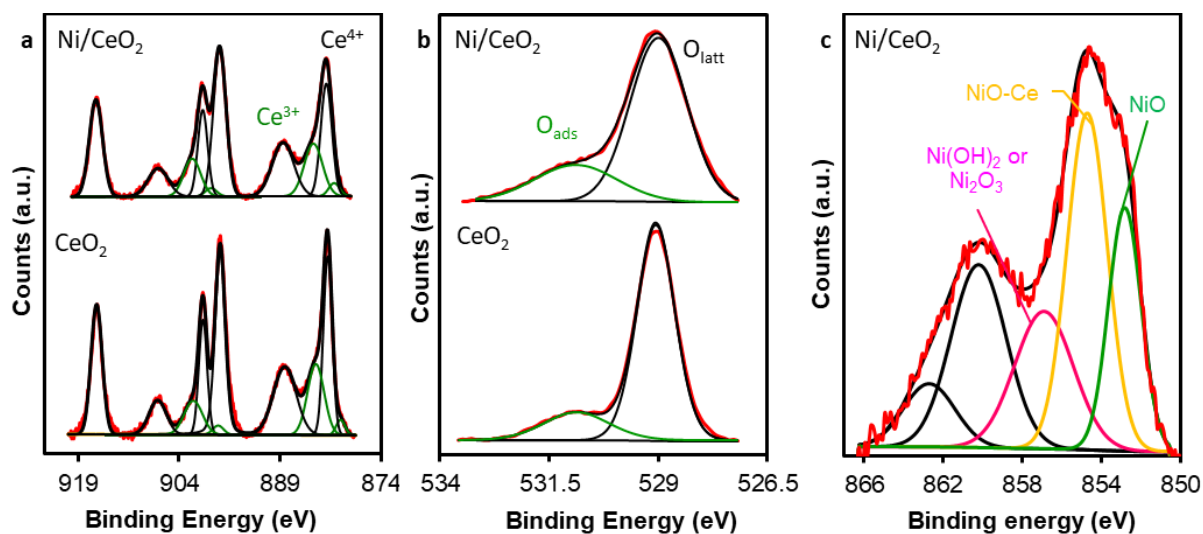
Figure 4.6. XPS results: a) Ce$_{3d}$, b) O$_{1s}$, and c) Ni$_{2p3/2}$ regions.

4.3.1.2. Characterization of ceramic catalysts

To determine the meso and macro porosity of the bare monolithic materials, mercury porosimetry characterization was performed. The pore volume and pore size distribution are presented in ***Figure 4.7*** a and b, respectively. Results corroborated the low porosity of cordierite monoliths; however, a significant difference is observed in the CoH material regarding the CoL and CoI. The porosity profile of CoH monolith (***Figure 4.7a***) shows a larger increment of the intrusion volume in the macropores range up to mesopores of about 26 nm. Besides, a wider distribution of pore diameter was found in this material (***Figure 4.7b***).
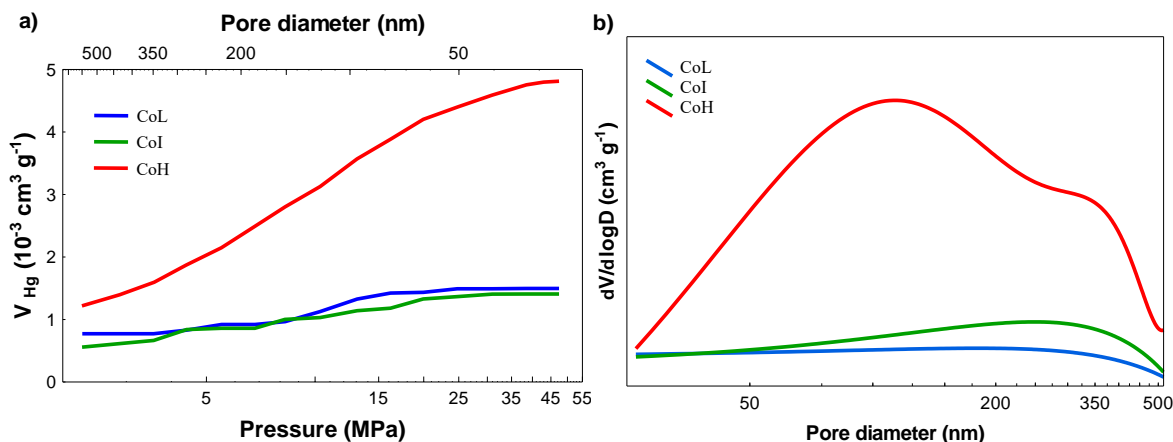
Figure 4.7. Results of mercury porosimetry of the three different cell densities cordierite monoliths: a) cumulative intrusion curves; and b) pore size distribution.

SEM analysis was performed to observe the morphology and active phase distribution on the cordierite monoliths (***Figures 4.8a-c***). It is observed that the surfaces of cordierite monoliths walls are rough, exhibiting some irregular pores with sizes on the order of macropores, which is consistent with the Hg-porosimetry results and has also been observed in this type of material by other authors [57,58]. Their low porosity leads to a limited diffusion of the active phase during the impregnation; therefore, most of the load is concentrated on the surface of the channels, especially for monoliths CoL and CoI (***Figures 4.8a-b***). It is also evident that, in the case of the low cell density, the active phase layer results thicker than in the other two monoliths due to the smaller exposed surface available for deposition. Notwithstanding, the bigger pore volume of

CoH monolith resulted in a higher diffusion of the Ni/CeO$_2$ ethanolic solution during impregnation, thus, in a higher amount of the active phase introduced into the channels walls (as depicted in **Figure 4.8c**).
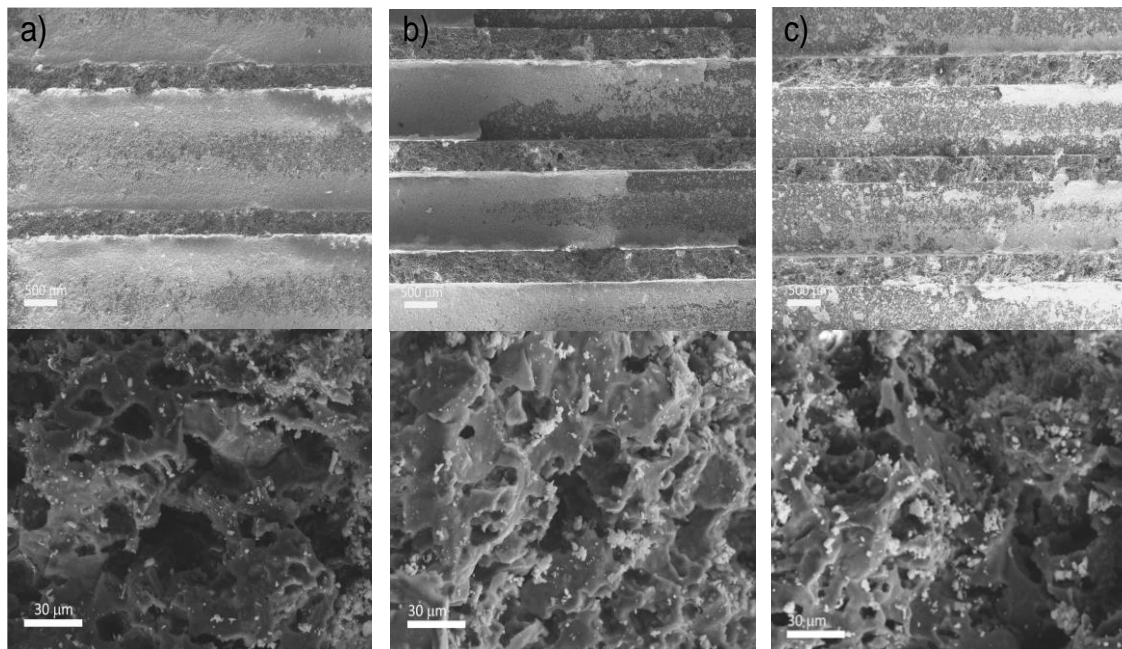
Figure 4.8. SEM micrographs of cordierite monoliths loaded with Ni/CeO$_2$: a) CoL; b) CoI; and c) CoH. Top images: monolith channels and down images: channel walls.

This was also corroborated by chemical mapping (see **Figure 4.9)**, where it can be observed that the active phase is not only uniformly distributed along the channels but also within their walls. Cerium (**Figure 4.9a**) and nickel (**Figure 4.9b**) were detected inside the walls in the case of the CoH monolith. Furthermore, it is essential to note that during the preparation of samples for SEM analysis, part of the active phase coating, especially in low and intermediate cell densities, detached when cutting them. This separation can be attributed to its concentration in the walls and the poor attachment resulting from the low porosity.

The mechanical properties of the monoliths with different cell densities were evaluated through stress-strain curves (**Figure 4.10**) obtained by compression along the channels. The maximum compressive stress values achieved were 10.96, 15.15, and 19.10 MPa for the low, intermediate, and high cell densities, respectively (**Table**

4.2). These results are in accordance with the amount and thickness of the channels, which contribute to greater mechanical strength.
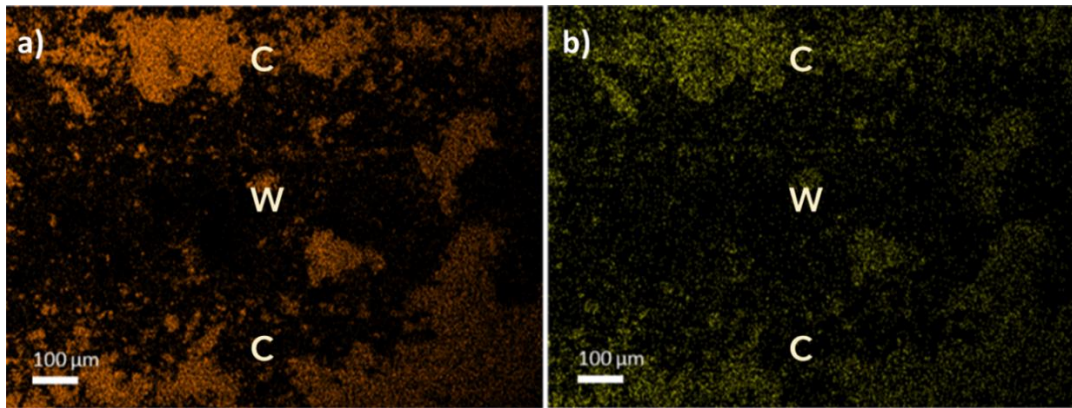
Figure 4.9. Chemical mapping of the active phase Ni/CeO$_2$ deposited in the CoH ceramic monolith within the channels (C) and walls (W): a) Ce; and b) Ni.
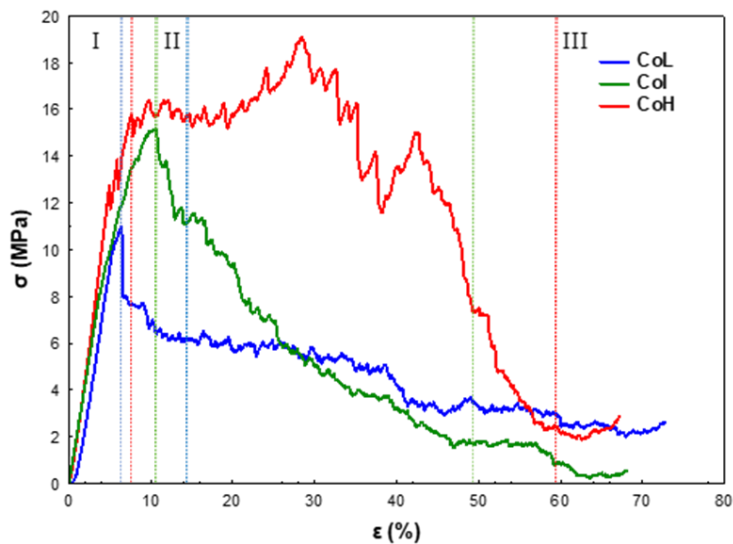
Figure 4.10. Stress-strain curves of cordierite monoliths of different cell densities.

Table 4.2. Maximum compressive stress (σ_{max}) and Young's modulus (E) of cordierite monoliths obtained from stress-strain curves.

Sample	$\sigma_{máx}$ MPa	E MPa
CoL	10.96	135
CoI	15.15	158
CoH	19.1	210

The deformation process can generally be classified into three regions (I, II, and III) based on the compressive stress-strain behavior. The first region (I) comprises the almost linear increase in compressive stress as the strain increment occurs. This behavior is attributed to the elastic buckling of cell walls. Afterward, the stress-strain curve reaches maximum stress, and a rapid drop in the compressive stress appears in region II. This rapid drop results from the fast transition of elastic buckling to plastic buckling of cell walls, followed by debonding fractures at cell/cell interfaces [59]. For the case of high cell density, a slight plateau region is appreciated, which may indicate a viscoelastic behavior [60]. The stress maintains a roughly constant value lower than the maximum compression stress in region III, where a continuous fracture of the cell walls was observed.

4.3.2. Catalytic results

The catalytic performance of the Ni/CeO_2-loaded cordierite monoliths was analyzed in the CO_2 methanation under 10 % CO_2 and 40 % H_2 in Ar balance, at total flows varying from 100 to 500 mL min^{-1}. The reaction rates normalized by weight of active phase are depicted in **Figure 4.11**. As exhibited in **Figure 4.11a**, the low cell density monolith works under diffusional control at flows below 400 mL min^{-1}. In contrast, attributed to higher active phase dispersion, this behavior is observed up to 300 mL min^{-1} for intermediate and high cell density monoliths (**Figure 4.11b-c**), where chemical control is achieved. However, flow rates higher than 400 mL min^{-1} cause a decrease in the reaction rate. Under diffusional control, an increment in volumetric flow enhances the reactants supply to the catalyst and facilitates the withdrawal of the products. Conversely, excessively high injection rates force the gas to flow inside the straight channels, leading to a laminar flow regime. In this regime, the flow is non-uniform because of the friction with the walls, resulting in significantly higher velocities in the center of the channel compared to the proximity of the walls [61,62]. Consequently, the interaction with the catalyst walls is diminished and, thus, the effectiveness is also reduced.

The effect of the flow rate was more significant in monoliths with higher cell densities, which may be promoted by their lower open frontal area speeding the reagents flow. The open frontal area refers to the part of the cross-section of the monolith that is free for the flow of gas and depends on the cell density, wall thickness, and washcoat layer [63]. Owing to the characteristics of the cell density (surface to volume ratio ~45 regarding ~20), the CoI and CoH monoliths achieve a better distribution of Ni/CeO_2 than CoL. However, when the reactive mixture is supplied to these materials, it is further induced to flow inside the channels, interacting less with the active phase.
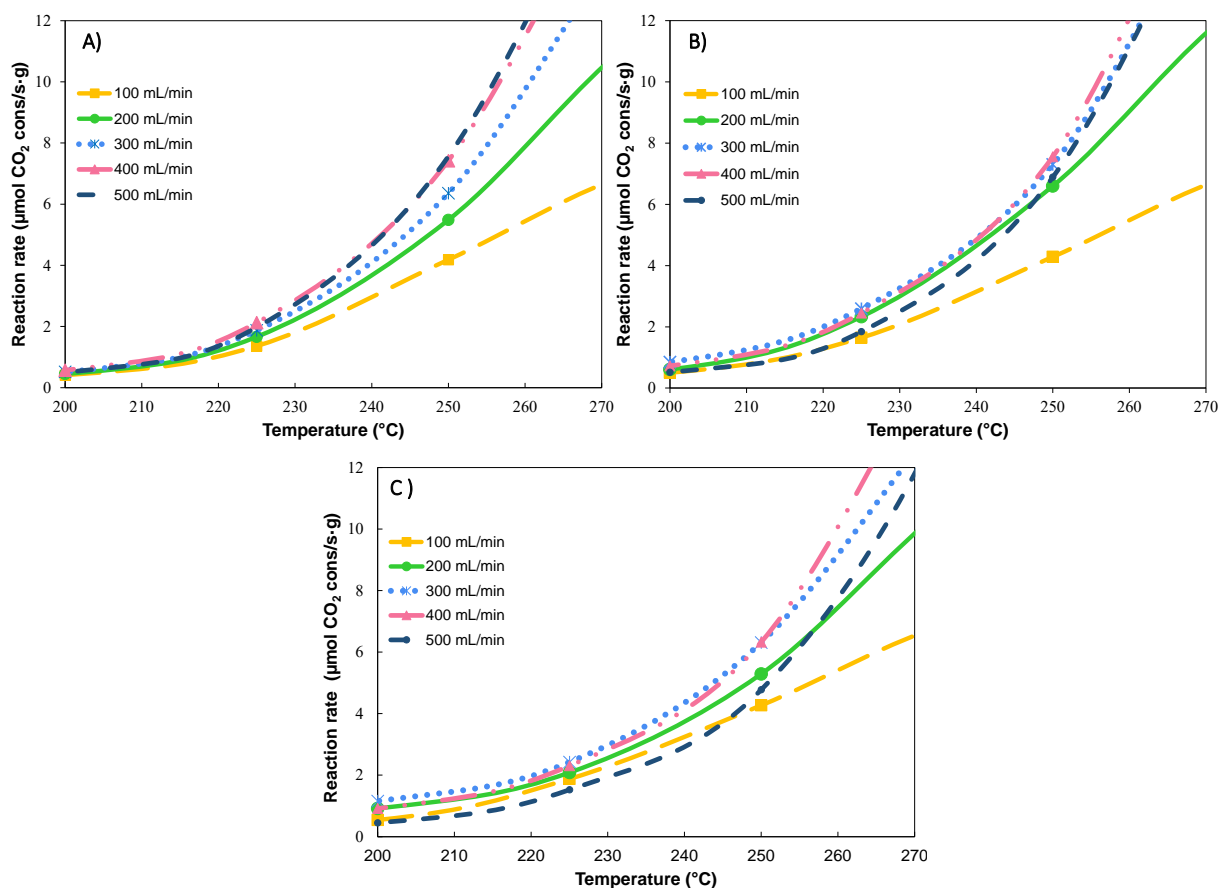
Figure 4.11. Reaction rate normalized by weight of Ni/CeO_2 supported on commercial cordierite monoliths of different cell densities: a) ~200 cpsi; b) ~400 cpsi; and c) ~500 cpsi.

The effect of the flow rate was observed in the CO_2 conversion obtained with different cell densities (***Figure 4.12***). For the CoL monolith (***Figure 4.12a***), increasing

the flow rate from 100 to 200 mL min^{-1} results in a higher minimum temperature required for the reaction to take place; though, rising from 300 to 500 mL min^{-1} does not represent a significant change in the conversion of CO_2. In contrast, ***Figure 4.12b*** shows CoH monolith is more affected by gas flow rate changes. For the CoH monolith, larger flow rates clearly affect the performance of the catalyst, requiring up to 50 °C more to treat 500 mL min^{-1} compared to 100 mL min^{-1}. The increase in the minimum reaction temperature may be attributed to both the introduction of the active phase in the channel's walls (as observed in SEM), and the reduction of diffusion caused by the straight design. These factors together result in poor contact between the reactive gas mixture and the Ni/CeO$_2$, which makes part of the active phase inaccessible and unusable, principally that inside the walls.
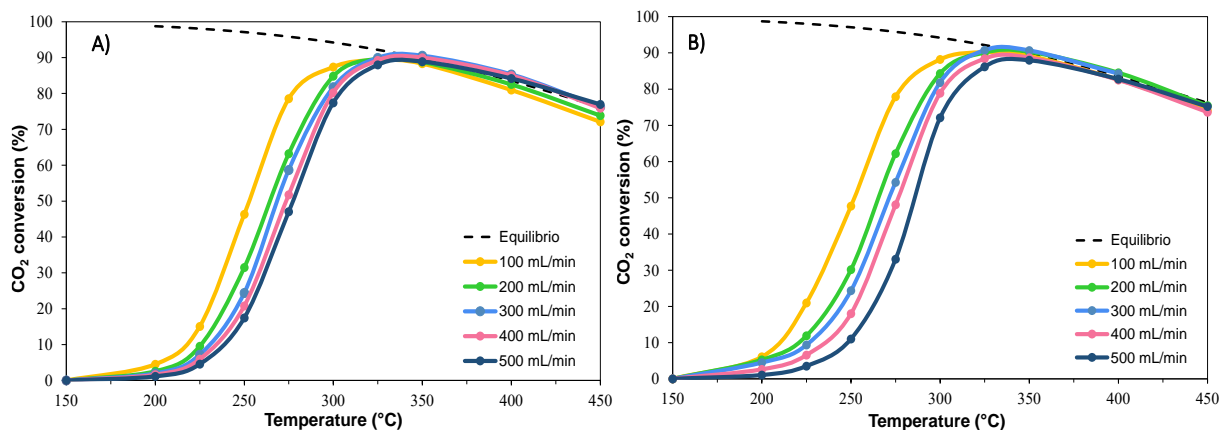
Figure 4.12. CO_2 conversion obtained with Ni/CeO$_2$-loaded commercial cordierite monoliths of: a) ~200 cpsi; and b) ~500 cpsi.

Further, the catalytic activities of the three cordierite monoliths using similar gas hourly space velocities, were assessed (***Figure 4.13***). It is evident that higher cell densities exhibit improved catalytic activity, this is associated with their greater exposed surface area in which the Ni/CeO$_2$ is distributed, and the gases can react. In the case of lower GHSV (***Figure 4.13a***), both CoI and CoH monoliths displayed similar performances, achieving superior CO_2 conversion (about 15 %) and reaching total conversion at a lower temperature (around 16 °C less) compared to CoL. Although CoH has a slightly bigger surface to volume ratio in relation to CoI (44.9 and 42.3, correspondingly), and thus better activity could be expected, the Ni/CeO$_2$ introduced

inside its channels walls resulted useless and reduced the benefit of CoH configuration. This effect is more prominent when employing higher GHSV (***Figure 4.13b***). As the reagents flow increased, diffusion through the walls diminished to a greater extent, leading to a notable reduction in the catalytic activity in the CoH material.

On the other hand, a slight decrease in the selectivity to CH_4 is observed, which may be related to the temperature reached over the catalyst. The high catalyst surface-to-bulk gas volume ratio results in a great rate of heat produced over the catalyst surface and heat transferred to the gas phase [39]. Therefore, the surface may get hotter with the potential formation of hot spots, which in turn, can activate the reverse water-gas shift reaction (RWGSR) [22]. This explains the increase in conversion while obtaining slightly lower selectivity.
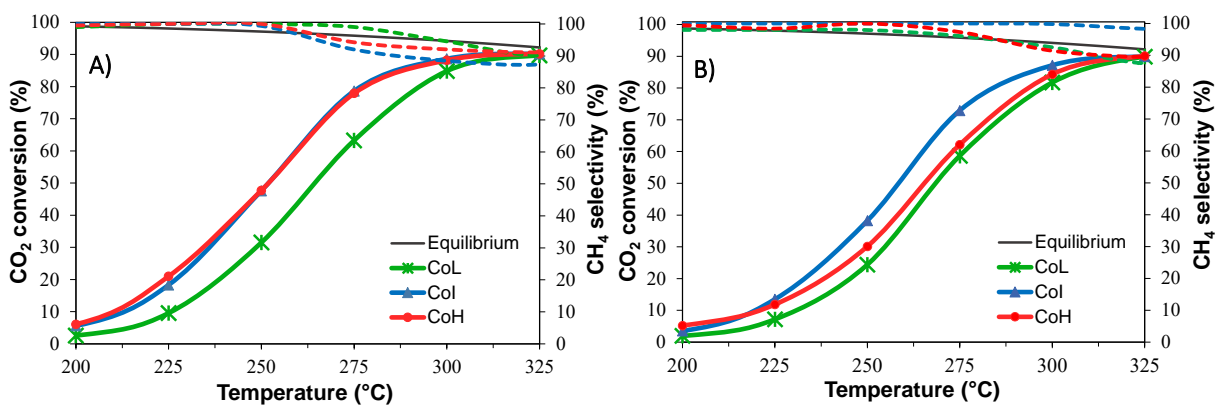
Figure 4.13. CO_2 conversion (continuous line) and selectivity to CH_4 (dashed line) obtained for CO_2 methanation with cordierite monoliths of different cell densities considering the same gas hourly space velocity: a) GHSV≈ 800 h^{-1}; and b) GHSV≈ 1500 h^{-1}.

4.3.3. Fluid dynamic study

The mathematical model formulated in Equations (5) to (28) was numerically solved using the software Comsol Multiphysics. This software utilizes advanced numerical routines for solving coupled partial differential equations through the finite element method. For this method, the geometrical domain is divided into multiple subdomains, where the unknown variables are calculated at each time step. ***Figure***

4.14 shows the geometric representation of the monolithic catalyst and the gridmesh used in one of the channels.
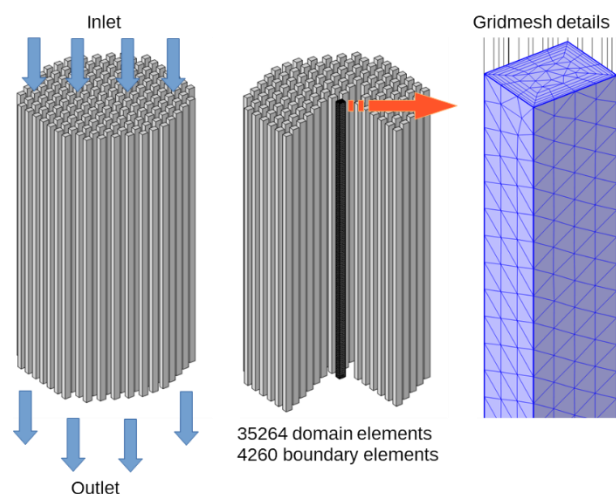
Figure 4.14. Computational geometry of the monolithic catalyst and the triangular grid mesh used for one channel.
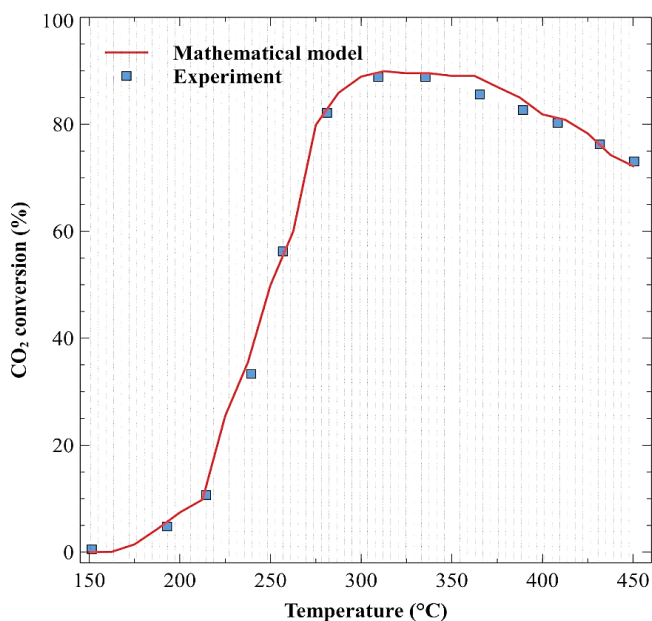
Figure 4.15. Comparison of CO_2 conversion calculated via the numerical solution of the mathematical model with the experimental data obtained in the laboratory for the CoL monolith (200 cpsi) treating a volumetric flow of 100 mL min^{-1}.

Due to the simple geometry of the straight channels, the numerical solution of the mathematical model can be performed in just one of the channels, under the

assumption that mass and momentum transport, as well as the chemical reaction rates, are equal in all the channels. We verified that the gridmesh containing 35,264 triangular elements is enough to yield accurate and consistent solutions of the mathematical model. Once the mathematical model is programmed and solved in Comsol Multiphysics, its predictability is assessed by comparing the CO_2 conversion (see *Figures 4.15* and *4.16*). According to the curves plotted in *Figure 4.15*, the mathematical model solution shows good agreement with the experimental results considering the monolith of 200 cpsi and a gas injection rate of 100 mL min^{-1}. The error, quantified as the area between the curves plotted in *Figure 4.15*, is approximately 313.4 %/°C.
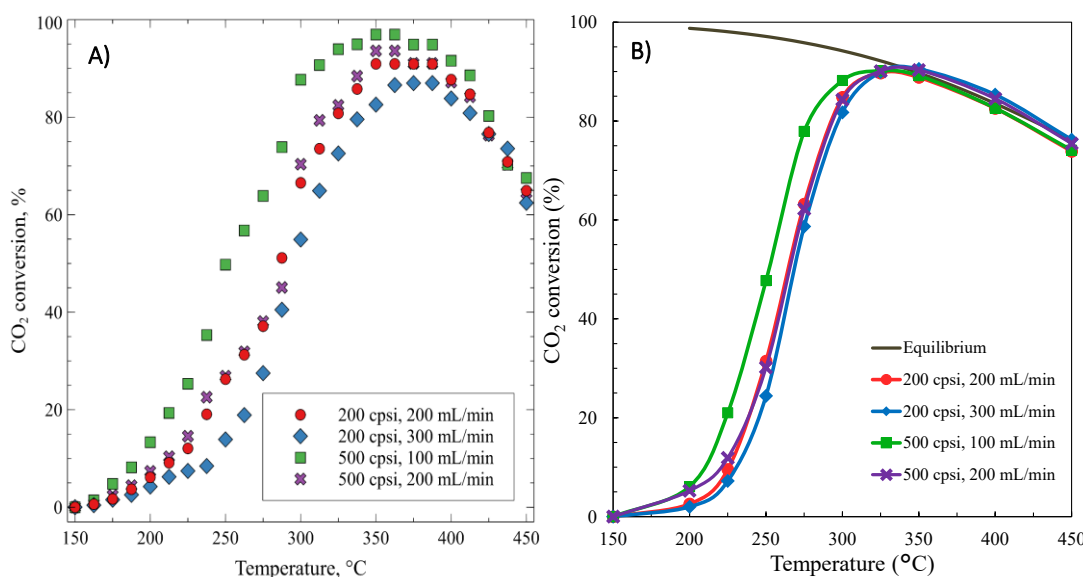
Figure 4.16. CO_2 conversion obtained with Ni/CeO$_2$-loaded commercial cordierite monoliths with 200 cpsi and 500 cpsi for different gas flows: a) calculated via the numerical solution of the mathematical model; and b) experimental data.

The velocity profile of the gas mixture inside the monolith channels is of great importance to understand the efficiency of supplying reactants to the reactive sites and removing the products through the gas stream. For this purpose, the fluid velocity achieved in the CoL monolith for a 200 mL min^{-1} gas injection is depicted in *Figure 4.17*. The velocity profile rapidly acquires a stationary state and, therefore, it is not necessary to analyze the velocity at each time step. In general, a radial profile is

162

developed on the transverse section of the channel, and such profile is kept from the entrance to the exit. As expected, the maximum velocity is found at the center of the channel. The absence of vortices is observed, which could eventually hinder the diffusion of the gaseous reagents into the monolithic structure. Nevertheless, this diffusion can be enhanced by designing monoliths with tortuous channels that promote turbulence within the channels [64]. The maximum velocity achieved when injecting 200 mL min^{-1} is about 0.01127 m s^{-1}.
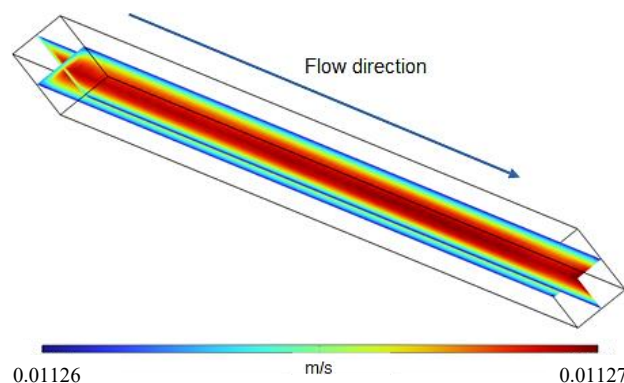
Figure 4.17. 3D velocity profile of the reactive gas mixture inside one of the channels of the CoL monolithic catalyst at a flow of 200 mL min^{-1}.

This behavior was also corroborated in the CoH monolith at different inlet flows (see **Figure 4.18**). It is also noticeable that, for the smaller channel (CoH) the same increase in reagents flow (100 mL min^{-1}) produces a higher rise in fluid velocity (around 2 times) compared to the larger channel of CoL monolith (approximately 1.5 times). This augment in velocity leads to lower diffusion through the CoH channel walls. Consequently, the interaction and use of the deposited active phase, mainly in the walls is reduced, supporting the previously mentioned catalytic results.

The local concentrations of CO_2 and CH_4 inside the channel of the CoL monolith with a flow rate of 100 mL min^{-1} were estimated and graphed in **Figure 4.19**. In this figure we have selected the time when temperature reaches 350 °C, which are the conditions for maximum CO_2 conversion. The maximum methane concentration reaches 4.5 mol m^{-3}, while the maximum concentration of CO_2 is that of feed conditions near the entrance, and eventually it drastically diminishes through the monolith

channel. In the analyzed case, most of the methane is produced from the middle and towards the exit of the monolith, while CO_2 is simultaneously consumed. In general, both chemical species develop linear streamlines along the monolith channel.
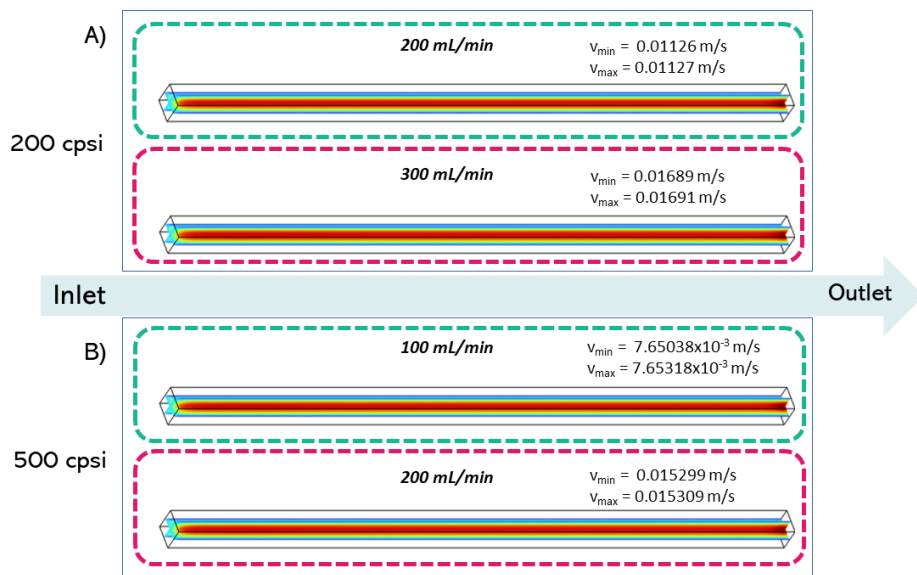
Figure 4.18. Comparison of the 3D velocity profiles of the reactive gas mixture at different flows to achieve similar gas hourly space velocities (green box GHSV ≈ 800 h^{-1}, and pink box GHSV ≈ 1500 h^{-1}) inside one of the channels of: a) CoL monolith; and b) CoH monolith.
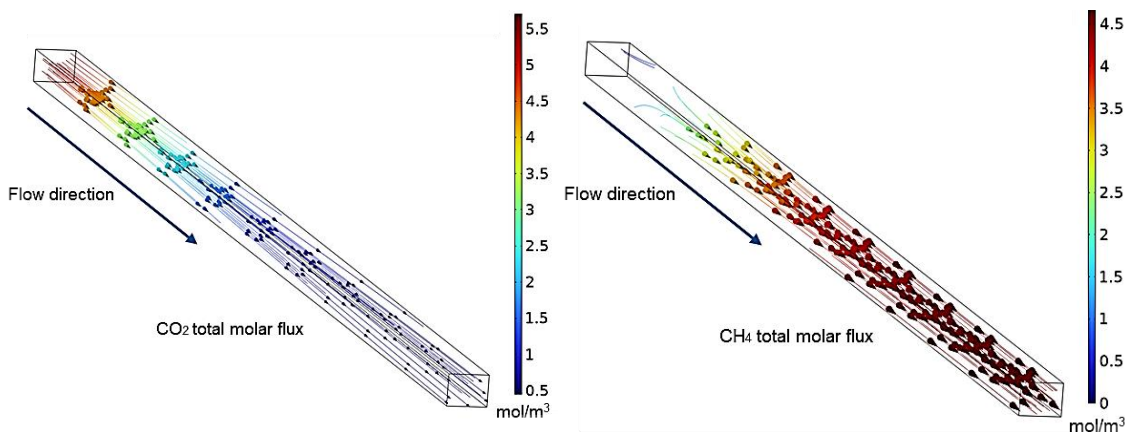
Figure 4.19. Molar concentration and main trajectories of the CO_2 and CH_4 in one channel of the CoL monolithic catalyst. Flow rate of 100 mL min^{-1} at 350 °C.

Finally, ***Figure 4.20*** shows the variation of the ratio of CH_4 to CO_2 concentrations along the channel, evaluated at the center of the channel, for various temperatures. As

observed, there is one entrance length of about 5 mm where the methane commences to be produced significantly. As temperature rises to 350 °C, methane is massively produced throughout most of the monolith, mainly near the exit. The maximum concentration ratio reached, approximately 10, is achieved at 350 °C. It is also evident that at higher temperatures, the higher CH_4/CO_2 ratio (lower than 10) is reached closer to the entrance (450 °C) and the middle (400 °C), after which concentrations remain constant. Therefore, we can affirm that the 3.5 cm long monolith is proper for working at the lowest temperature that allows achieving higher conversion without misusing the catalyst.
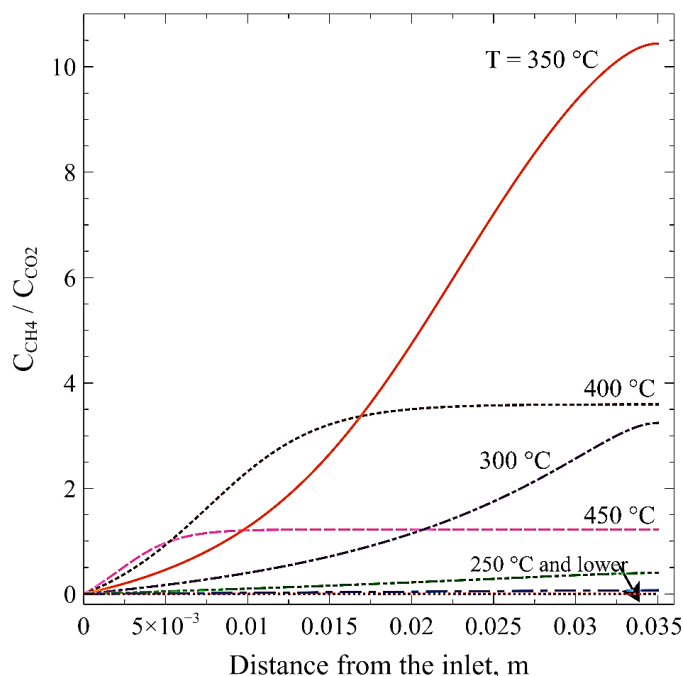
Figure 4.20. Ratio of CH_4 to CO_2 concentrations assessed at the center of the channel of the 200 cpsi monolith with a volumetric flow rate of 100 mL min^{-1}.

4.4. Conclusions

The influence of the cell density configuration of monolithic catalysts was investigated in the Sabatier reaction for CO_2 conversion using cordierite monoliths. Ni/CeO_2 was selected as the active phase, which was loaded on commercial cordierite monoliths of three different cell densities (200, 400, and 500 cpsi) by means of

immersion into an ethanolic suspension. The low porosity of the CoL and CoI materials led to concentration of the active phase on the channels' surface due to a limited diffusion of the ethanolic suspension through the structure. However, in the case of the CoH monolith, owing to a larger pore volume, some Ni/CeO_2 was deposited into the channel's walls, as observed in SEM and EDS micrographs.

The catalytic evaluation indicated diffusional control at flows below 500 mLmin^{-1} for the CoL monolith, whereas CoI and CoH materials achieved chemical control at flows above 300 mL min^{-1}. Though, larger increase in volumetric flow in CoI and CoH materials led to a decrease in reaction rate since their lower open frontal area speeded the reagents flow through the channels, reducing the interaction with the catalysts. Regarding the CO_2 conversion, the three materials were analyzed at the same GHSV. Results confirmed the benefit of attaining a better distribution and availability of Ni/CeO_2 by means of the bigger surface to volume ratio in high cell densities. Notwithstanding, despite the greater exposed surface area of CoH monolith, the introduction of active phase into the walls repercussed on its accessibility. Therefore, CO_2 conversion was reduced at high GHSV, in which the reagents diffusion through the ceramic material was further diminished, thus, the active phase introduced into the walls was misused.

Furthermore, a comprehensive mathematical model was formulated and successfully solved through Comsol Multiphysics software to simulate the reaction of methanation of CO_2. The model exhibited acceptable convergency with the experimental data and helped to study the fluid dynamics of the monolithic support as well as the velocity profile within the channels. In this sense, a radial profile, with the maximum velocity of the fluid at the center of the channel, is formed close to the inlet and kept to the outlet. Additionally, an entry length of about 0.5 cm was observed when analyzing the concentration of CO_2 and CH_4. Moreover, it was observed a maximum production of 4.5 mol m^{-3} of CH_4 at 350 °C utilizing the whole monolith length. Lastly, the streamlines of chemical species were linearly established along the channel.

Overall, the cell density is an important factor controlling the catalytic activity but the control of the Ni/CeO_2 distribution on the porosity of the monolith is also mandatory

to optimize the active phase catalytic performance since repercussed on its accessibility. Hence, the insights gained from this analysis hold great promise for advancing and refining monolithic catalysts used in CO_2 methanation, contributing to the pursuit of sustainability and environmental conservation objectives.

4.5. References

[1] Amica, G., & Gennari, F. C. (2022). Synergistic effect of MgH2 doping with Ni and carbon nanotubes on thermochemical CO2 recycling process for CH4-H2 mixtures production. *International Journal of Hydrogen Energy, 47*, 428–442. https://doi.org/10.1016/j.ijhydene.2021.10.007

[2] González-Castaño, M., González-Arias, J., Bobadilla, L. F., Ruíz-López, E., Odriozola, J. A., & Arellano-García, H. (2023). In-situ DRIFTS steady-state study of CO2 and CO methanation over Ni-promoted catalysts. *Fuel, 338*, 127241. https://doi.org/10.1016/j.fuel.2022.127241

[3] Shuai, Y., Zhang, H., Guene Lougou, B., Jiang, B., Mustafa, A., Wang, C.-H., Wang, F., & Zhao, J. (2021). Solar-driven thermochemical redox cycles of ZrO2 supported NiFe2O4 for CO2 reduction into chemical energy. *Energy, 223*, 120073. https://doi.org/10.1016/j.energy.2021.120073

[4] Nisar, A., Khan, S., Hameed, M., Nisar, A., Ahmad, H., & Mehmood, S. A. (2021). Bio-conversion of CO2 into biofuels and other value-added chemicals via metabolic engineering. *Microbiological Research, 251*, 126813. https://doi.org/10.1016/j.micres.2021.126813

[5] Sharma, T., Sharma, A., Xia, C. L., Lam, S. S., Khan, A. A., Tripathi, S., Kumar, R., Gupta, V. K., & Nadda, A. K. (2022). Enzyme mediated transformation of CO2 into calcium carbonate using purified microbial carbonic anhydrase. *Environ. Res., 212*, 113538. https://doi.org/10.1016/j.envres.2022.113538

[6] Albo, J., Perfecto-Irigaray, M., Beobide, G., & Irabien, A. (2019). Cu/Bi metal-organic framework-based systems for an enhanced electrochemical transformation of CO_2 to alcohols. *Journal of CO2 Utilization, 33*, 157–165. https://doi.org/10.1016/j.jcou.2019.05.025

[7] Oßkopp, M., Löwe, A., Lobo, C. M. S., Baranyai, S., Khoza, T., Auinger, M., & Klemm, E. (2022). Producing formic acid at low pH values by electrochemical CO_2 reduction. *Journal of CO2 Utilization, 56*, 101823. https://doi.org/10.1016/j.jcou.2021.101823

[8] Song, X., Jia, S., Xu, L., Feng, J., He, L., Sun, X., & Han, B. (2022). Towards sustainable CO_2 electrochemical transformation via coupling design strategy. *Mater. Today Sustain., 19*, 100179. https://doi.org/10.1016/j.mtsust.2022.100179

[9] Wang, T., Zhang, J., Li, F., Liu, B., & Kawi, S. (2022). Recent progress of electrochemical reduction of CO_2 by single atom catalysts. *Materials Reports: Energy, 2*, 100140. https://doi.org/10.1016/j.matre.2022.100140

[10] Kuramochi, Y., Ishitani, O., & Ishida, H. (2018). Reaction mechanisms of catalytic photochemical CO_2 reduction using Re(I) and Ru(II) complexes. *Coordination Chemistry Reviews, 373*, 333–356. https://doi.org/10.1016/j.ccr.2017.11.023

[11] Pashchenko, D. (2022). Photochemical hydrocarbon fuel regeneration: Hydrogen-rich fuel from CO_2. *International Journal of Hydrogen Energy, 47*(46), 25531–25540. https://doi.org/10.1016/j.ijhydene.2022.06.002

[12] Yaashikaa, P. R., Senthil Kumar, P., Varjani, S. J., & Saravanan, A. (2019). A review on photochemical, biochemical and electrochemical transformation of CO_2 into value-added products. *Journal of CO2 Utilization, 33*, 131–147. https://doi.org/10.1016/j.jcou.2019.05.017.

[13] Chen, H., Liu, P., Liu, J., Feng, X., & Zhou, S. (2021). Mechanochemical in-situ incorporation of Ni on MgO/MgH2 surface for the selective O-/C-terminal catalytic hydrogenation of CO2 to CH4. *Journal of Catalysis, 394*, 397–405. https://doi.org/10.1016/j.jcat.2020.10.026

[14] Cordero-Lanzac, T., Ramirez, A., Cruz-Fernandez, M., Zander, H.-J., Joensen, F., Woolass, S., Meiswinkel, A., Styring, P., Gascon, J., & Olsbye, U. (2023). A CO2 valorization plant to produce light hydrocarbons: Kinetic model, process design and life cycle assessment. *Journal of CO2 Utilization, 67*, 102337. https://doi.org/10.1016/j.jcou.2022.102337

[15] Fan, W. K., & Tahir, M. (2021). Recent trends in developments of active metals and heterogenous materials for catalytic CO2 hydrogenation to renewable methane: A review. Journal of Environmental Chemical Engineering, 9, 105460. https://doi.org/10.1016/j.jece.2021.105460

[16] Shewchuk, S. R., Mukherjee, A., & Dalai, A. K. (2021). Selective carbon-based adsorbents for carbon dioxide capture from mixed gas streams and catalytic hydrogenation of CO2 into renewable energy source: A review. *Chemical Engineering Science, 243*, 116735. https://doi.org/10.1016/j.ces.2021.116735.

[17] Navarro, J. C., Centeno, M. A., Laguna, O. H., & Odriozola, J. A. (2018). Policies and motivations for the CO2 valorization through the Sabatier reaction using structured catalysts. A review of the most recent advances. *Catalysts, 8*(12), 578. https://doi.org/10.3390/catal8120578.

[18] Renda, S., Ricca, A., & Palma, V. (2021). Study of the effect of noble metal promotion in Ni-based catalyst for the Sabatier reaction. *Int. J. Hydrogen Energy, 46*(49), 12117–12127. https://doi.org/10.1016/j.ijhydene.2020.05.093.

[19] Chen, Y., Zhang, Y., Fan, G., Song, L., Jia, G., Huang, H., Ouyang, S., Ye, J., Li, Z., & Zou, Z. (2021). Cooperative catalysis coupling photo-/photothermal effect to

drive Sabatier reaction with unprecedented conversion and selectivity. *Joule, 5*(12), 3235–3251. https://doi.org/10.1016/j.joule.2021.11.009

[20] Frontera, P., Macario, A., Ferraro, M., Antonucci, P., & Styring, P. (2017). Supported catalysts for CO2 methanation: A review. *Catalysts, 7*(2), 59. https://doi.org/10.3390/catal7020059

[21] Gómez, L., Martínez, I., Navarro, M. V., García, T., & Murillo, R. (2022). Sorption-enhanced CO and CO2 methanation (SEM) for the production of high purity methane. *Chem. Eng. J., 440*, 135842. https://doi.org/10.1016/j.cej.2022.135842

[22] De Piano, G., Gamboa, J. J. A., Condó, A. M., Bengió, S., & Gennari, F. C. (2022). Bimetallic Ni-Fe catalysts for methanation of CO2: Effect of the support nature and reducibility. *Applied Catalysis A: General, 634*, 118540. https://doi.org/10.1016/j.apcata.2022.118540.

[23] Laosiripojana, N., & Assabumrungrat, S. (2006). Catalytic steam reforming of ethanol over high surface area CeO2: The role of CeO2 as an internal pre-reforming catalyst. *Applied Catalysis B: Environmental, 66*, 29–39. https://doi.org/10.1016/j.apcatb.2006.01.011.

[24] Prakash, A. S., Shivakumara, C., & Hegde, M. S. (2007). Single step preparation of CeO2/CeAlO3/γ-Al2O3 by solution combustion method: Phase evolution, thermal stability and surface modification. *Materials Science and Engineering: B, 139*, 55–61. https://doi.org/10.1016/j.mseb.2007.01.034.

[25] Zhang, D., Zhang, J., Li, R., Chen, H., Hao, Q., Bai, Y., Shang, J., Zhang, L., & Ma, X. (2023). Coal char supported Ni catalysts prepared for CO2 methanation by hydrogenation. *International Journal of Hydrogen Energy, 48 (39), 14608-14621*. https://doi.org/10.1016/j.ijhydene.2023.01.042.

[26] Colman-lerner, E., Peluso, M. A., Sambeth, J., & Thomas, H. (2016). Cerium, manganese and cerium/manganese ceramic monolithic catalysts. Study of VOCs and PM removal. *Journal of Rare Earths, 34*, 675–682. https://doi.org/10.1016/S1002-0721(16)60078-9.

[27] Forzatti, P., Ballardini, D., & Sighicelli, L. (1998). Preparation and characterization of extruded monolithic ceramic catalysts. *Catalysis Today, 41*, 87–94. https://doi.org/10.1016/S0920-5861(98)00040-6.

[28] Kucharczyk, B., Tylus, W., Okal, J., Chęcmanowski, J., & Szczygieł, B. (2017). The Pt-NiO catalysts over the metallic monolithic support for oxidation of carbon monoxide and hexane. *Chemical Engineering Journal, 309*, 288–297. https://doi.org/10.1016/j.cej.2016.10.032.

[29] Quan, C., Gao, N., & Wu, C. (2018). Utilization of NiO/porous ceramic monolithic catalyst for upgrading biomass fuel gas. *Journal of the Energy Institute, 91*, 331–338. https://doi.org/10.1016/j.joei.2017.02.008.

[30] Fukuhara, C., Hayakawa, K., Suzuki, Y., Kawasaki, W., & Watanabe, R. (2017). A novel nickel-based structured catalyst for CO_2 methanation: A honeycomb-type Ni/CeO_2 catalyst to transform greenhouse gas into useful resources. *Applied Catalysis A: General, 532*, 12–18. https://doi.org/10.1016/j.apcata.2016.11.036.

[31] Danaci, S., Protasova, L., Lefevere, J., Bedel, L., Guilet, R., & Marty, P. (2016). Efficient CO_2 methanation over Ni/Al_2O_3 coated structured catalysts. *Catalysis Today, 273*, 234–243.https://doi.org/10.1016/j.cattod.2016.04.019.

[32] Al-Harbi, O. A., Özgür, C., & Khan, M. M. (2015). Fabrication and characterization of single phase cordierite honeycomb monolith with porous wall from natural raw materials as catalyst support. *Ceramics International, 41*(3), 3526–3532. https://doi.org/10.1016/j.ceramint.2014.11.009.

[33] Chaparro-Garnica, C. Y., Bailón-García, E., Davó-Quiñonero, A., Lozano-Castelló, D., & Bueno-López, A. (2022). Sponge-like carbon monoliths: Porosity control of 3D-printed carbon supports and its influence on the catalytic performance. *Chem. Eng. J., 432*, 134218. https://doi.org/10.1016/j.cej.2021.134218.

[34] Pratap, S. R., Shamshuddin, S. Z. M., Thimmaraju, N., & Shyamsundar, M. (2020). Cordierite honeycomb monoliths coated with Al(III)/ZrO2 as an efficient and reusable catalyst for the Knoevenagel condensation: A faster kinetics. *Arab. J. Chem., 13*(6), 2734–2749. https://doi.org/10.1016/j.arabjc.2018.07.005.

[35] Huynh, H. L., Tucho, W. M., & Yu, Z. (2020). Structured NiFe catalysts derived from in-situ grown layered double hydroxides on ceramic monolith for CO2 methanation. *Green Energy & Environment, 5*(4), 423–432. https://doi.org/10.1016/j.gee.2020.09.004.

[36] Vita, A., Italiano, C., Pino, L., Laganà, M., Ferraro, M., & Antonucci, V. (2020). High-temperature CO2 methanation over structured Ni/GDC catalysts: Performance and scale-up for Power-to-Gas application. *Fuel Processing Technology, 202*, 106365. https://doi.org/10.1016/j.fuproc.2020.106365.

[37] García-Moncada, N., Navarro, J. C., Odriozola, J. A., Lefferts, L., & Faria, J. A. (2022). Enhanced catalytic activity and stability of nanoshaped Ni/CeO2 for CO2 methanation in micro-monoliths. *Catalysis Today, 383*, 205–215. https://doi.org/10.1016/j.cattod.2021.02.014.

[38] Vega, G., Quintanilla, A., Menendez, N., Belmonte, M., & Casas, J. A. (2021). 3D honeycomb monoliths with interconnected channels for the sustainable production of dihydroxybenzenes: towards the intensification of selective oxidation processes. *Chemical Engineering and Processing - Process Intensification, 165*, 108437. https://doi.org/10.1016/j.cep.2021.108437.

[39] Barbato, P. S., Di Benedetto, A., Landi, G., & Lisi, L. (2015). CuO/CeO2 based monoliths for CO preferential oxidation in H2-rich streams. *Chemical Engineering Journal, 279*, 983–993. https://doi.org/10.1016/j.cej.2015.05.079.

[40] Lawson, S., Adebayo, B., Robinson, C., Al-Naddaf, Q., Rownaghi, A. A., & Rezaei, F. (2020). The effects of cell density and intrinsic porosity on structural properties and adsorption kinetics in 3D-printed zeolite monoliths. *Chemical Engineering Science, 218*, 115564. https://doi.org/10.1016/j.ces.2020.115564.

[41] Santos, D. F. M., Soares, O. S. G. P., Figueiredo, J. L., Sanz, O., Montes, M., & Pereira, M. F. R. (2020). Preparation of ceramic and metallic monoliths coated with cryptomelane as catalysts for VOC abatement. *Chemical Engineering Journal, 382*, 122923. https://doi.org/10.1016/j.cej.2019.122923.

[42] Scherrer, P. (1912). Bestimmung der inneren Struktur und der Größe von Kolloidteilchen mittels Röntgenstrahlen. In R. Zsigmondy (Ed.), *Kolloidchemie Ein Lehrbuch* (pp. 387–409). Springer Berlin Heidelberg. https://doi.org/10.1007/978-3-662-33915-2_7.

[43] Burton, A. W., Ong, K., Rea, T., & Chan, I. Y. (2009). On the estimation of average crystallite size of zeolites from the Scherrer equation: A critical evaluation of its application to zeolites with one-dimensional pore systems. *Micropor. Mesopor. Mater., 117*(1-2), 75–90. https://doi.org/10.1016/j.micromeso.2008.06.010.

[44] Chein, R. Y., Chen, W. Y., & Yu, C. T. (2016). Numerical simulation of carbon dioxide methanation reaction for synthetic natural gas production in fixed-bed reactors. *Journal of Natural Gas Science and Engineering, 29*, 243–251. https://doi.org/10.1016/j.jngse.2016.01.019.

[45] Tana, M., Zhang, J., Li, J., Li, H., Li, Y., & Shen, W. (2009). Morphology-dependent redox and catalytic properties of CeO2 nanostructures: Nanowires, nanorods and nanoparticles. *Catalysis Today*, *148*(1-2), 179–183.

https://doi.org/10.1016/j.cattod.2009.02.016.

[46] Nguyen, K., Hoa, N. D., Hung, C. M., Le, D. T. T., Duy, N. V., & Hieu, N. V. (2018). A comparative study on the electrochemical properties of nanoporous nickel oxide nanowires and nanosheets prepared by a hydrothermal method. *RSC Advances, 8*(34), 19449–19455. https://doi.org/10.1039/C8RA02862A.

[47] Kumaran, C., Baskaran, I., Sathyaseelan, B., Senthilnathan, K., Manikandan, E., & Sambasivam, S. (2022). Effect of doping of iron on structural, optical and magnetic properties of CeO2 nanoparticles. *Chemical Physics Letters, 808*, 140110. https://doi.org/10.1016/j.cplett.2022.140110.

[48] Lee, M. (2017). A Raman Study of CeO2 Nanomaterials with Different Morphologies. [Master Thesis, Friedrich-Alexander University Erlangen-Nürnberg].

[49] Rui, N., Zhang, X., Zhang, F., Liu, Z., Cao, X., Xie, Z., Zou, R., Senanayake, S. D., Yang, Y., Rodriguez, J. A., & Liu, C.-J. (2021). Highly active Ni/CeO2 catalyst for CO2 methanation: Preparation and characterization. *Applied Catalysis B: Environmental, 282*, 119581. https://doi.org/10.1016/j.apcatb.2020.119581.

[50] Muduli, S., Sahoo, T. R., (2023). Green synthesis and characterization of CeO2 and Ni-doped CeO2 nanoparticles and its dielectric properties. *Materials Today: Proceedings, 74*, 697–702. https://doi.org/10.1016/j.matpr.2022.10.278.

[51] Winter, L. R., Chen, R., Chen, X., Chang, K., Liu, Z., Senanayake, S. D., Ebrahim, A. M., & Chen, J. G. (2019). Elucidating the roles of metallic Ni and oxygen vacancies in CO2 hydrogenation over Ni/CeO2 using isotope exchange and in situ measurements. *Applied Catalysis B: Environmental, 245*, 360–366. https://doi.org/10.1016/j.apcatb.2018.12.069.

[52] Lin, S., Li, Z., & Li, M. (2023). Tailoring metal-support interactions via tuning CeO2 particle size for enhancing CO2 methanation activity over Ni/CeO2 catalysts. *Fuel, 333*, 126369. https://doi.org/10.1016/j.fuel.2022.126369.

[53] Li, R., Zhang, J., Shi, J., Li, K., Liu, H., & Zhu, X. (2022). Regulation of metal-support interface of Ni/CeO2 catalyst and the performance of low temperature chemical looping dry reforming of methane. *Journal of Fuel Chemistry and Technology, 50*(12), 1458–1470. https://doi.org/10.1016/S1872-5813(22)60032-X.

[54] Xu, X., Liu, L., Tong, Y., Fang, X., Xu, J., & Jiang, D. (2021). Facile Cr 3+ -Doping Strategy Dramatically Promoting Ru/CeO 2 for Low-Temperature CO 2 Methanation: Unraveling the Roles of Surface Oxygen Vacancies and Hydroxyl Groups. *ACS Catalysis, 11*(10), 5762–5775. https://doi.org/10.1021/acscatal.0c05468.

[55] Sellers-Antón, B., Bailón-García, E., Cardenas-Arenas, A., Davó-Quiñonero, A., Lozano-Castelló, D., & Bueno-López, A. (2020). Enhancement of the Generation and Transfer of Active Oxygen in Ni/CeO2 Catalysts for Soot Combustion by Controlling the Ni–Ceria Contact and the Three-Dimensional Structure. *Environ. Sci. Technol., 54*(4), 2439–2447. https://doi.org/10.1021/acs.est.9b07682.

[56] Cárdenas-Arenas, A., Quindimil, A., Davó-Quiñonero, A., Bailón-García, E., Lozano-Castelló, D., De-La-Torre, U., Pereda-Ayo, B., González-Marcos, J. A., & González-Velasco, J. R. (2020). Design of active sites in Ni/CeO2 catalysts for the methanation of CO2: tailoring the Ni-CeO2 contact. *Applied Materials Today, 19*, 100591. https://doi.org/10.1016/j.apmt.2020.100591.

[57] Brussino, P., Bortolozzi, J. P., Milt, V. G., Banús, E. D., & Ulla, M. A. (2016). NiCe/γ-Al2O3 coated onto cordierite monoliths applied to Oxidative Dehydrogenation of Ethane (ODE). *Catalysis Today, 273*, 259–265. https://doi.org/10.1016/j.cattod.2016.02.055.

[58] Tang, X., Wang, C., Gao, F., Han, W., Yi, H., Zhao, S., Zhou, Y., & Liu, Y. (2021). Mn-Fe-Ce multiple oxides with Al2O3 coating supported onto honeycomb cordierite monoliths for NO catalytic oxidation. *Colloids and Surfaces A: Physicochemical and Engineering Aspects, 611*, 125790. https://doi.org/10.1016/j.colsurfa.2020.125790.

[59] Lee, H. S., Hong, S. H., Lee, J. R., & Kim, Y. K. (2002). Mechanical behavior and failure process during compressive and shear deformation of honeycomb composite at elevated temperatures. *Journal of Materials Science, 37*(6), 1265–1272. https://doi.org/10.1023/A:1014344228141.

[60] Dorado, B., Moreno-Sanabria, L., García, E., Belmonte, M., Miranzo, P., & Osendi, M. I. (2023). 3D printing of cordierite materials from raw reactive mixtures. *Ceram. Int., 49*(4), 4578–4585. https://doi.org/10.1016/j.ceramint.2022.09.343.

[61] Caenn, R., Darley, H. C. H., & Gray, G. R. (2017). The Rheology of Drilling Fluids. In R. Caenn, H. C. H. Darley, & G. R. Gray (Eds.), *Composition and Properties of Drilling and Completion Fluids* (7th ed., pp. 151–244). Gulf Professional Publishing. https://doi.org/10.1016/B978-0-12-804751-4.00006-7.

[62] Kundu, P. K., Cohen, I. M., & Dowling, D. R. (2016). Laminar Flow. In P. K. Kundu, I. M. Cohen, & D. R. Dowling (Eds.), *Fluid Mechanics* (6th ed., pp. 409–467). Academic Press. https://doi.org/10.1016/B978-0-12-405935-1.00009-5.

[63] Cornejo, I., Garreton, G., & Hayes, R. E. (2021). On the Use of Dual Cell Density Monoliths. *Catalysts, 11*(9), 1075. https://doi.org/10.3390/catal11091075.

[64] Aguilar-Madera, C. G., Ocampo-Pérez, R., Bailón-García, E., Herrera-Hernández, E. C., Chaparro-Garnica, C. Y., Davó-Quiñonero, A., Lozano-Castelló, D., Bueno-López, A., & García-Hernández, E. (2021). Mathematical Modeling of Preferential CO Oxidation Reactions under Advection–Diffusion Conditions in a 3D-Printed Reactive Monolith. *Industrial & Engineering Chemistry Research, 60*(32), 11689–11698. https://doi.org/10.1021/acs.iecr.1c01483.

5

ADVANCING CARBON-BASED CATALYSTS FOR CO$_2$ METHANATION: EXPLORING THE IMPACT OF CELL GEOMETRY AND DENSITY THROUGH 3D PRINTING OF MONOLITHIC STRUCTURES
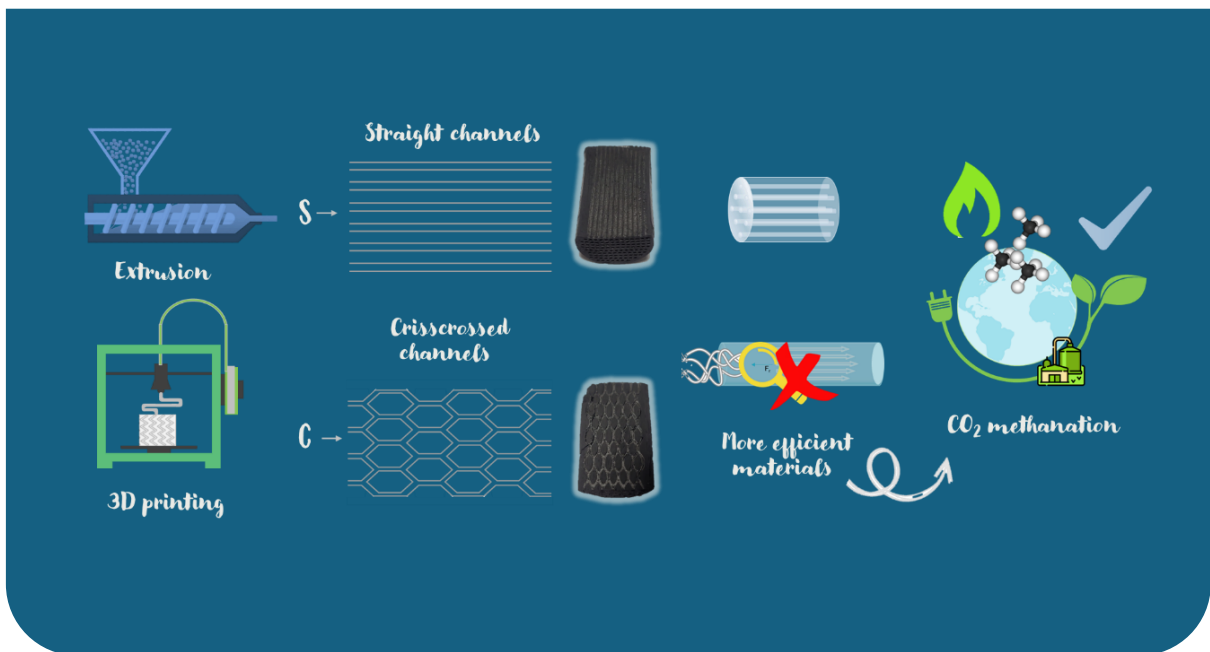
5.1. Introduction

Carbon dioxide is an abundant greenhouse gas found in the atmosphere which causes severe environmental damage. Nonetheless, the utilization of CO_2 in methane production through its hydrogenation, also known as the Sabatier reaction (Eq. 1), would not only reduce the greenhouse gas concentration in the atmosphere but would also be able to partially fulfill the world's energy demand. However, the high stability of CO_2 demands a great energy input to make its dissociation possible [1], thus the use of efficient catalysts is needed to overcome this limitation.

$$CO_2 + 4H_2 \leftrightarrow CH_4 + 2H_2O, \triangle H_{298\,K} = -164.9 \text{ kJ mol}^{-1} \text{ [2,3]} \tag{1}$$
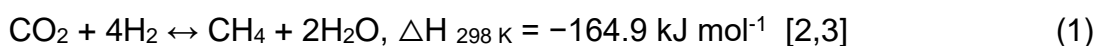
In that respect, noble- and transition-metals supported on various oxides are the main materials utilized in CO_2 hydrogenation [4–7]. Among the principal supporting oxides used, CeO_2 improves low-temperature CO_2 methanation performance since its oxygen vacancies reduce the CO_2 adsorbed on it, thereby leading to higher conversion [8]. Ni-based catalysts distinguish owing to the high activity and selectivity to CH_4 formation together with the relatively low price of nickel [7]. However, the particle size, the distribution of Ni on ceria, their interaction, the amount of oxygen vacancies, and their thermal and mechanical stability influence their effectiveness [9].

Moreover, due to the high exothermic character of the reversible CO_2 hydrogenation reaction, the potential hot spot generation may, in turn, lead to catalyst deactivation by coke deposition and particle sintering [10,11]. Then, regarding the problem this implies for the industrial operation, it is important to search not only for great catalytic activity but an appropriate configuration to remove the heat generated. Although the conformation of the catalyst may influence the heat and mass transfer, hence favor or disfavor its effectiveness, this factor is barely studied, and conversely, most research focuses on the active phase and the reaction mechanism.

To surpass common challenges associated with powdered catalysts and to facilitate their application in industrial-scale continuous flow processes, there is growing interest in utilizing monolithic structures as supports. Honeycomb monoliths, this is, uniform blocks with straight and parallel channels, typically metallic or ceramic,

have been coated with active phases and used in gas-solid systems. This type of structure has proven its advantages over fixed-bed reactors: i) lower pressure drop owing to its high open frontal area for the fluid flow [12–14] , ii) improved heat and mass transfer which helps to smooth temperature gradients thus avoiding hot spots, an increasing reagents-active phase interaction, respectively [12,14–16], iii) higher processing fluid rates that result in larger efficiency and productivity [14,17], and iv) better mechanical stability which reduces attrition and makes it easier to handle, separate, and clean [16,18,19].

Certain studies have shown that the incorporation of active phases for Sabatier reaction into monolithic supports enhances their stability and catalytic performance. For instance, Li et al. [20,21] synthesized monolithic Ni-foam catalysts coated with a Ni-Al_2O_3 composite layer through a modified wet chemical etching. These catalysts exhibited good CO_2 conversion and CH_4 selectivity at 320 °C and 0.1 MPa with a gas hourly space velocity (GHSV) of 5000 h^{-1}. Moreover, the results and computational fluid dynamics simulation confirmed that the monolithic catalysts have better catalytic performance in CO_2 methanation than the particulate catalyst due to improved heat transfer, which reduces hot spot temperature formation. Navarro et al. [22] also analyzed the effect of structuring a catalyst for the Sabatier reaction into a monolith but they used a conventional honeycomb metallic structure. To prepare a cylindrical monolith with parallel straight channels, two stainless steel sheets were cleaned and rolled. Then, the monolith was pre-treated and washcoated with a Ru-Ni/$MgAl_2O_4$ active phase, followed by a calcination process. Although the structured catalyst presented higher stability compared to the powder form, signal of no hot spots' formation, some issues were detected: sintering of the active phase during catalyst manufacturing, and low residence time and transfer limitations at larger flow rates due to the shape of the channels. On the other side, an aluminum honeycomb monolith was washcoated with a Ni-based catalyst by Fukuhara et al. [23] to use it in CO_2 methanation. Compared to its granulated form, the monolithic catalyst presented a better removal of the exothermic energy generated. Moreover, they observed that

stacking small pieces of the monolithic catalyst to generate a random flow path resulted in an improvement of the heat and mass transfer, and thus, in a higher catalytic performance of about 5-10 % at 250-350 °C and at 70 mL min^{-1} flow rate. Additionally, this arrangement did not exhibit diminution of the catalytic activity when increasing the flow rate, conversely to the granulated form. Therefore, it is suggested that the activity of the monolithic catalyst may be controlled by modifying its configuration and geometry.

Notwithstanding, while traditional techniques for manufacturing monolithic structures —i.e., material extrusion or pressing, and foils corrugation— enable shaping of the cross section, they constrain the channels to be straight and parallel. Besides, the structure geometry is not precisely controlled with those methods, and straight channels are associated with forcing a laminar flow regardless of the inlet flow regime [24,25]. This laminar regime imposes a non-uniform velocity with a notable difference between walls and the center of the channels, where the maximum velocity, up to twice the average velocity, is found [26]. This fluid flow profile disfavors the interaction between reagents and catalyst. Furthermore, raw materials are generally ceramic or metallic, leading to some complication for the active phase loading, hence, usually requiring pre-treatment to facilitate the coating. Conversely, carbon materials offer an easier deposition process which results in a better distribution of the active phase (more accessibility for reagents), in addition to their textural properties and chemical stability. However, carbon is not an appropriate raw material for traditional production methods.

Recently, the use of 3D printing in the catalysts' development has emerged as an opportunity to beat composition and design restrictions. Therefore, in the present chapter an innovative methodology, which integrates the 3D printing technology with the sol-gel process, is proposed as an alternative to fabricate advanced structured carbon catalysts. Monoliths with crisscrossed channels and straight channels (used for comparison) were produced from sol-gel polymerization, where polymeric templates printed by fused deposition modeling were included. The advantages of combining

both methods allow the manufacture of pure carbon monoliths of controlled and complex designs, non-achievable through conventional methods. Later, monoliths were loaded with Ni/CeO_2 active phase to prove them in the catalytic CO_2 methanation. This non-straight channel design may favor turbulent regime, increasing the reagents-catalyst interaction and, thus, the active phase leverage and catalyst efficiency. Besides, different cell densities of both designs were produced to thoroughly investigate the effect of monolithic geometry on catalytic performance.

5.2. Experimental

5.2.1. Catalyst preparation

5.2.1.1.   Active phase synthesis

Cerium nitrate hexahydrate ($Ce(NO_3)_3·6H_2O$, ≥ 99.5 % from Alfa Aesar) was calcined in a muffle at 500 °C for 4 h to obtain CeO_2 for later preparing the Ni/CeO_2 active phase. The CeO_2 was impregnated with 10 wt% of Ni by incipient wetness impregnation of a nickel (II) nitrate hexahydrate ($Ni(NO_3)_2·6H_2O$, ≥ 97 % Sigma-Aldrich) ethanolic solution. Afterwards, a calcination step at 600 °C for 5 h was carried out to decompose the salt and attain the Ni/CeO_2 active phase.

5.2.1.2.   Synthesis of carbon monoliths

Carbon monolithic supports were prepared by combining 3D printing fused deposition modeling (FDM) technique, with a controlled sol-gel process. The FDM was used to obtain polymeric templates of two different channel designs (**Figure 5.1**), one of conventional straight channels and a crisscrossed channels design, named as S and C, respectively. Additionally, different cell densities of both designs (~160 cpsi, ~240 cpsi, and ~420 cpsi, labeled by their design initial letter followed by L, I, or H, correspondingly) were prepared to evaluate their influence on catalytic performance. The designs were done using Cubify Invent software and later printed with a co-polyester filament in an UltiMaker[2+] 3D printer.

The sol-gel procedure was carried out from a solution of resorcinol (R), formaldehyde (F), and water (W), considering the molar ratios R/W= 1/15 and R/F=

1/2. The printed templates were placed into glass tubes of approximately 2.7 cm of internal diameter, then the R-F-W mixture was added, and the tubes were sealed. The polymerization process consisted of holding the materials 1 day at room temperature, 1 day at 50 °C, and 5 days at 80 °C. When the polymerization was finished, the organic monoliths were removed from the tubes and immersed in acetone for 3 days to interchange it with the water contained in their structure. This interchange was realized to avoid pore detriment and to facilitate drying at room temperature. These organic monoliths were carbonized with a heating rate of 1.5 °C min^{-1} up to 850 °C for 2 h in N_2 atmosphere to, firstly, melt and remove the polymeric template, and finally obtain the carbon monoliths. Carbon monoliths exhibited a dimension shrinkage of about 20 % regarding the organic monoliths, hence a final diameter of ~2.1 cm and 3.5 cm length were obtained.
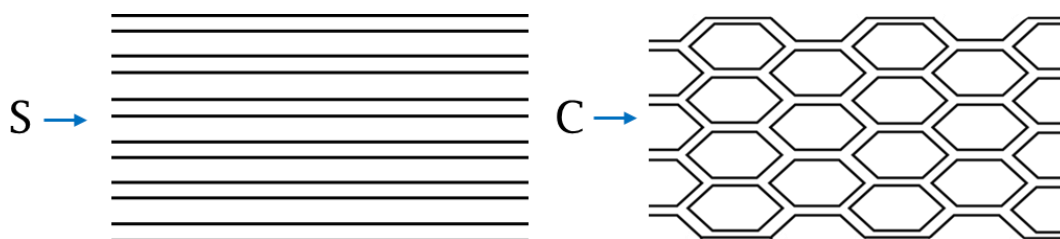
Figure 5.1. Channel geometry designs: conventional straight channels (S), and advanced design of crisscrossed channels (C).

5.2.1.3. *Active phase loading*

Carbon monoliths were loaded with the active phase by dip-coating them in an ethanolic suspension of 10 wt% Ni/CeO_2. Later, the monoliths were rotated horizontally at ambient temperature for 12 h to dry and ensure even distribution, and then were dried at 80 °C overnight. The active phase not anchored to the surface of the monoliths that can obstruct the channels was removed with compressed air. The Ni/CeO_2 loading was verified by measuring the weight difference following the impregnation. This process was recurred up to achieving a Ni/CeO_2 loading of 800 ± 5 mg in each monolith.

5.2.2. Catalyst characterization

Regarding the Ni/CeO$_2$ powder, X-ray diffraction (XRD) and Raman spectroscopy were used to study its crystalline structure and the effect of its deposition on the carbon monoliths. The X-ray diffraction patterns were measured in the 2θ range between 10° and 90° at 1° min^{-1} using a Bruker D8 DISCOVER X-Ray diffractometer (CuKα-ray radiation, λ= 1.5406 Å) with a PILATUS3R 100K-A detector. Whereas, Raman analysis was realized with a Green Diode (Elforlight G4-30; Nd:YAG, λ= 532 nm) in a Raman microscope JASCO NRS-5100. X-ray photoelectron spectroscopy (XPS) analysis was conducted on both the CeO$_2$ support and the active phase Ni/CeO$_2$ to study their surface chemistry. The analysis was performed using a Kratos Axis Ultra-DLD spectrometer with an X-ray source emitting Al-Kα radiation at 1486.6 eV.

On the other hand, the surface area of CeO$_2$ and Ni/CeO$_2$ was obtained by N$_2$ adsorption isotherms (at -196°C). Moreover, the porosity of the carbon structures was also evaluated through adsorption isotherms of N$_2$ at -196 °C and CO$_2$ at 0 °C, and Hg-porosimetry. Prior to N$_2$ and CO$_2$ adsorption analyses, the samples were degassed at 110 °C during 8 h, using a Quantachrome Autosorb-6B equipment. For Hg-porosimetry, samples were degassed at 50 °C for 12 h and then analyzed in a Poremaster 60 GT (Quantachrome) equipment in the pressure range of 7 to 390,000 KPa. Pore size calculations were realized considering a contact angle of θ = 140° and surface tension of γ = 480 dyne cm^{-1}.

The morphology of carbon monoliths and the distribution of the active phase on them were studied by scanning electron microscopy (SEM). For this analysis a SUPRA 40VP microscope from Zeiss equipped with a X-Max 50 mm detector was used. Moreover, thermal and mechanical stability were analyzed through thermogravimetric analysis (TGA) and compression tests, correspondingly. Thermal stability of carbon monoliths, bare and loaded with Ni/CeO$_2$, in oxidizing atmosphere was analyzed in a SDT 2960 DSC-TGA device, heating with a 10 °C min^{-1} rate up to 900 °C under air flow. For the compression tests, 1.5 cm high monolithic samples with sanded bases (to ensure flat and uniform surfaces) were used. The tests were carried out with a top

to bottom compression direction and constant approach speed of 1 mm min^{-1} in a Shimadzu AGS-J 10 kN equipment.

5.2.3. Catalytic tests

The effect of channel geometry was analyzed by evaluating the catalytic performance of both monolith designs and different cell densities in the CO_2 methanation. The reaction system consisted of flow controllers for the reagent feeding to a quartz cylindrical reactor located in a tubular furnace with temperature control (see ***Figure 4.2***). At the outlet of the reactor a cold trap was used to retain the water vapor produced in the reaction. For each catalytic test, a monolith was placed into the quartz reactor and the reaction was monitored by analyzing the outflow gases CO_2 and CH_4 with infrared gas sensors (Edinburgh Instruments LTD 034/00700). A reduction treatment (100 mL min^{-1} of 10% H_2 in Ar) at 500 °C for 1.5 h was carried out before the reaction. Once finished, the system was let to cool down to 150 °C to change the inlet flow to the reactive mixture consisting of 10% CO_2 and 40% H_2 balanced in Ar, in total flows between 100 and 500 mL min^{-1}. Temperature increments of 25 °C were applied to reach 450 °C, holding each temperature for 20 min. The catalytic performance was evaluated with the CO_2 conversion, reaction rate, and selectivity to CH_4 obtained.

5.3. Results and discussion

5.3.1. Characterization of the physical and chemical properties of the catalysts

As demonstrated in the previous chapter, XPS analysis was performed to elucidate the chemistry of the active phase surface [27]. Based on the Ce_{3d}, O_{1s}, and Ni_{2p} XPS spectral regions obtained from the analysis of both the CeO_2 support and the Ni/CeO_2 (see ***Figure 4.6***), the successful synthesis of the active phase was corroborated by the following findings: i) the proportion of surface Ce^{3+}/Ce^{4+} increased in the Ni/CeO_2 sample, presenting a higher Ce^{3+} content (22.5) compared to that of CeO_2 (18.9). This increase is associated with improved surface reducibility resulting from the high dispersion of Ni and Ce-Ni contact; ii) the ratio between adsorbed oxygen species (O_{ads}), located at oxygen vacancies, and surface lattice oxygen (O_{latt}),

O_{ads}/O_{latt}, increased with Ni incorporation from 0.22 in CeO_2 to 0.32 in Ni/CeO_2, which denotes an increment in oxygen vacancies and thus in ceria surface reducibility; and iii) the $Ni_{2p3/2}$ region exhibited three peaks corresponding to surface Ni^{2+} species, including surface NiO species, Ni^{2+} species leagued to ceria surface (NiO-Ce species), and Ni^{3+} or $Ni(OH)_2$ species.
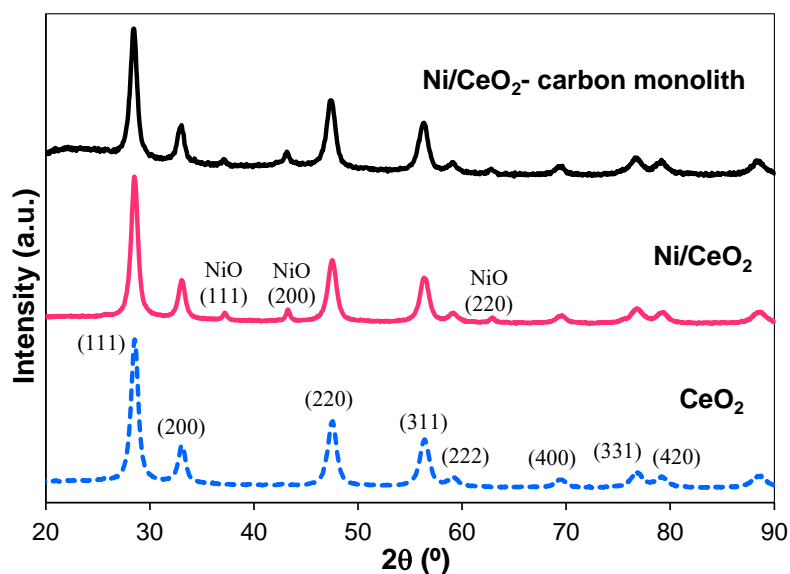
Figure 5.2. X-ray diffractogram of CeO_2 and Ni/CeO_2, both powder and supported (carbon monolith - Ni/CeO_2).

On the other hand, the crystalline structure of ceria and the active phase in powder form and loaded on the carbon monoliths was studied. The XRD diffractograms of all samples (***Figure 5.2***) exhibited distinctive peaks indexed to the (111), (200), (220), (311), (400), (331), and (420) crystal faces of the face-centered cubic structure of ceria (JCPDS 00-034-0394) [28]. Moreover, the lattice constant of CeO_2 was determined from the X-ray diffraction measurements, resulting in 0.5411 nm which is consistent with reported values [29,30]. The XRD patterns of both, the Ni/CeO_2 and the monolith impregnated displayed further peaks at 37.2, 43.2, and 63° that were assigned to the planes (111), (200), and (220) of the face-centered cubic phase of NiO (according to JCPDS 00-047-1049) [31]. Additionally, a change in the lattice constant of CeO2 in the active phase (0.5420) is observed by a sligh displacement of the CeO_2 peaks in both the Ni/CeO_2 powder and supported forms. The increase in lattice

186

constant with the integration of Ni indicates that some Ni cations were inserted into the crystal lattice of CeO_2. Nevertheless, the introduction of Ni did not result in a significant increase in the average size of CeO_2 crystals from pure (10.5 nm) to Ni/CeO_2 (11.0 nm), as calculated using the Scherrer equation. The XRD pattern of the Ni/CeO_2 impregnated monolith did not present any significant change in the crystalline structure compared to the powder form of the active phase, indicating that the impregnation process and the interaction with the carbon monolith do not modify the crystalline structure.

Figure 5.3 shows the comparison between Raman spectra of pure CeO_2, Ni/CeO_2, and a carbon monolith impregnated with Ni/CeO_2. In the case of pure ceria, its spectra is composed of a unique band centered at 464 cm^{-1}. This band has been ascribed to the F_{2g} vibrational mode of the crystalline fluorite-type cubic structure of ceria, corresponding to a symmetric Ce-O stretching vibration [32–34].
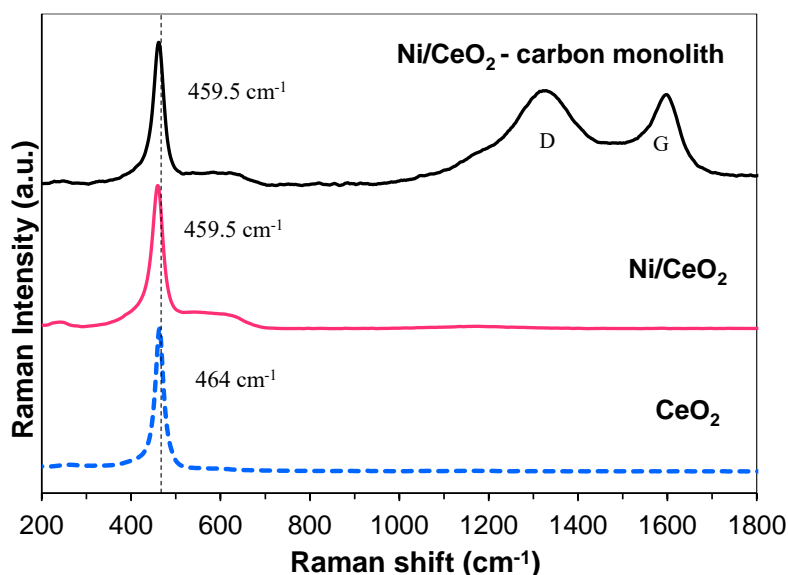
Figure 5.3. Raman spectra of CeO_2 and Ni/CeO_2 both powdered and supported (carbon monolith - Ni/CeO_2).

Regarding the other two spectra, the incorporation of nickel which interacts with the ceria surface, leads to a shift in the F_{2g} peak to approximately 459.5 cm^{-1} [34,35]. Besides, the band at approximately 600 cm^{-1} can be assigned to the oxygen defect-induced mode (D) of ceria that indicates the oxygen vacancy on the interface between

Ni and the CeO_2 surface [36–38]. Together with metal active sites, oxygen vacancies play a crucial role in the dissociation process owing to a stronger binding affinity for adsorbates compared to other oxide sites [37,39]. Finally, the spectra of impregnated monolith also shows the D (~1325 cm^{-1}) and G (~1580 cm^{-1}) Raman typical bands for carbon materials [40,41]. Nevetheless, no significant differences in the 459.5 cm^{-1} and 600 cm^{-1} bands for Ni/CeO_2 and the Ni/CeO_2-impregnated monolith were observed. These results suggest that the loading process, as well as the interaction of the active phase with the carbon material, does not affect the chemical nature of the Ni/CeO_2. Therefore, the catalytic results obtained using the catalysts produced can be directly assigned to the structural design of the monoliths.
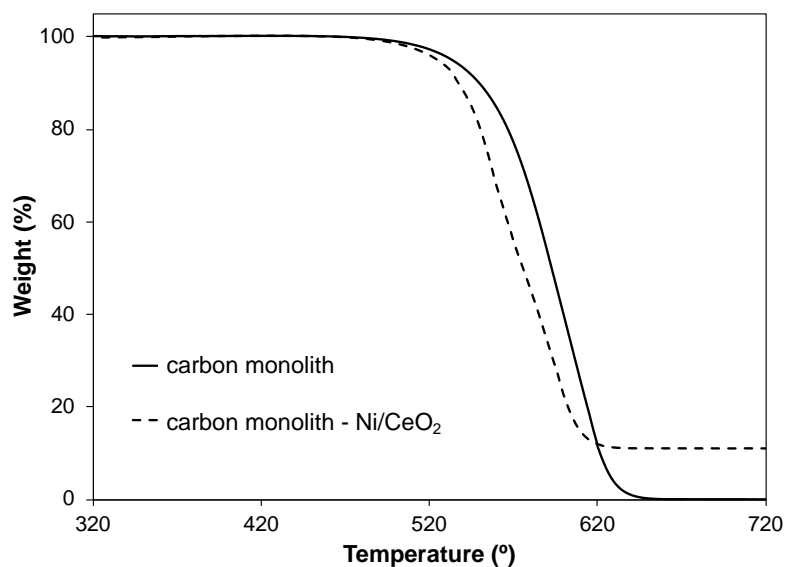
Figure 5.4. Thermogravimetric analysis in air of carbon monolith and Ni/CeO_2 loaded monolith.

Due to its importance in catalysis, the thermal stability of a carbon support and a Ni/CeO_2-supported carbon catalyst was evaluated in oxidant atmosphere by thermogravimetric analysis, and the results are presented in **Figure 5.4**. The results indicate that, even with the active phase loading, the Ni/CeO_2-supported carbon catalysts are stable up to approximately 500 °C under oxidizing conditions. Therefore, they can be used as catalysts for the methanation of CO_2.

The results of N_2 sorption on ceria and the active phase were evaluated through the Brunauer-Emmett-Teller and Dubinin-Radushkevich equations to calculate the specific surface area (S_{BET}) and micropore volume (V_{micro}). The catalytic compounds resulted mesoporous since the isotherms obtained (see ***Figure 4.3***) correspond to type IV of the IUPAC classification. The total pore volume was taken as the N_2 volume adsorbed at a relative presure of 0.95. Then, mesopore volume was considered as the difference between total and micro pore volumes, and results are presented in ***Table 4.1***. The low V_{micro} calculated correspond to the little adsorption of N_2 seen at low relative pressures. Whereas, the rise in N_2 adsorption together with a hysteresis loop closing at higher P/P_0 show the presence of wide mesopores. The dispersion of nickel particles on the CeO_2 surface caused pores obstruction, which is seen in the decrease of porosity (see ***Table 4.1***).
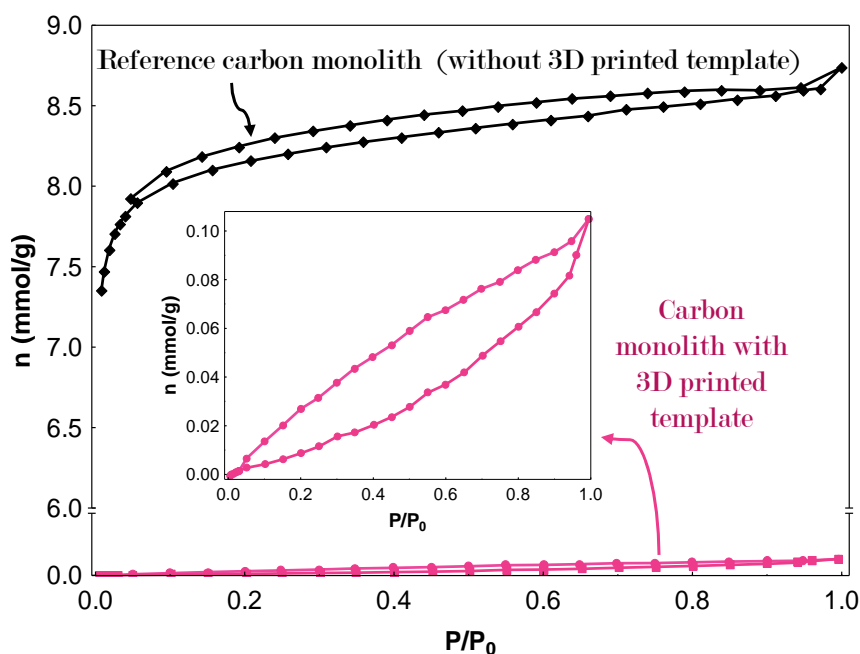
Figure 5.5. N_2 adsorption−desorption isotherms at −196 °C of carbon monolith obtained with 3D printed template, and carbon monolith without template.

On the other hand, the textural properties of the carbon supports are presented in ***Table 5.1***. In the N_2 isotherm of the carbon monolith without template, a closed neck and a flat plateau are identified, wich indicates a very low mesopore volume and the presence of homogeneous microporosity (***Figure 5.5***). In the case of carbon monoliths

obtained with 3D printed template, a blockage of the surface hinders the accessibility of N_2 into the carbon bulk and, therefore, it is difficult to obtain this information (***Figure 5.5***). This blocking can be associated with the fact that part of the polymeric template is carbonized at the organic gel-template interface during the pyrolysis treatment.

Table 5.1. Textural characteristics of carbon monoliths obtained with 3D printed template, and carbon monoliths without template.

Sample	N_2 adsorption		CO_2 adsorption		Mercury porosimetry
	S_{BET} (m^2/g)	V_{total} (cm^3/g)	S_{micro} (m^2/g)	L_0 (nm)	V_{macro} (cm^3/g)
Carbon monolith without template	639	0.29	1026	0.61	1.06
Carbon monolith with template	-	-	843	0.79	1.06

S_{BET}= BET surface area, W_0= micropore volume, S_{mic}= micropore surface, L_0= micropore wide, and V_{macro}= macropore volume

Likewise, information about the narrow microporosity was obtained from CO_2 adsorption and confirms the blocking of porosity by the presence of the template (***Table 5.1***). A decrease in the micropore surface (S_{micro}) was identified when the templates were used. However, this behavior is similar for any template design (conventional straight channels, and advanced design of crisscrossed channels), confirming that the only variable among the catalysts in this study is the design of the monoliths.
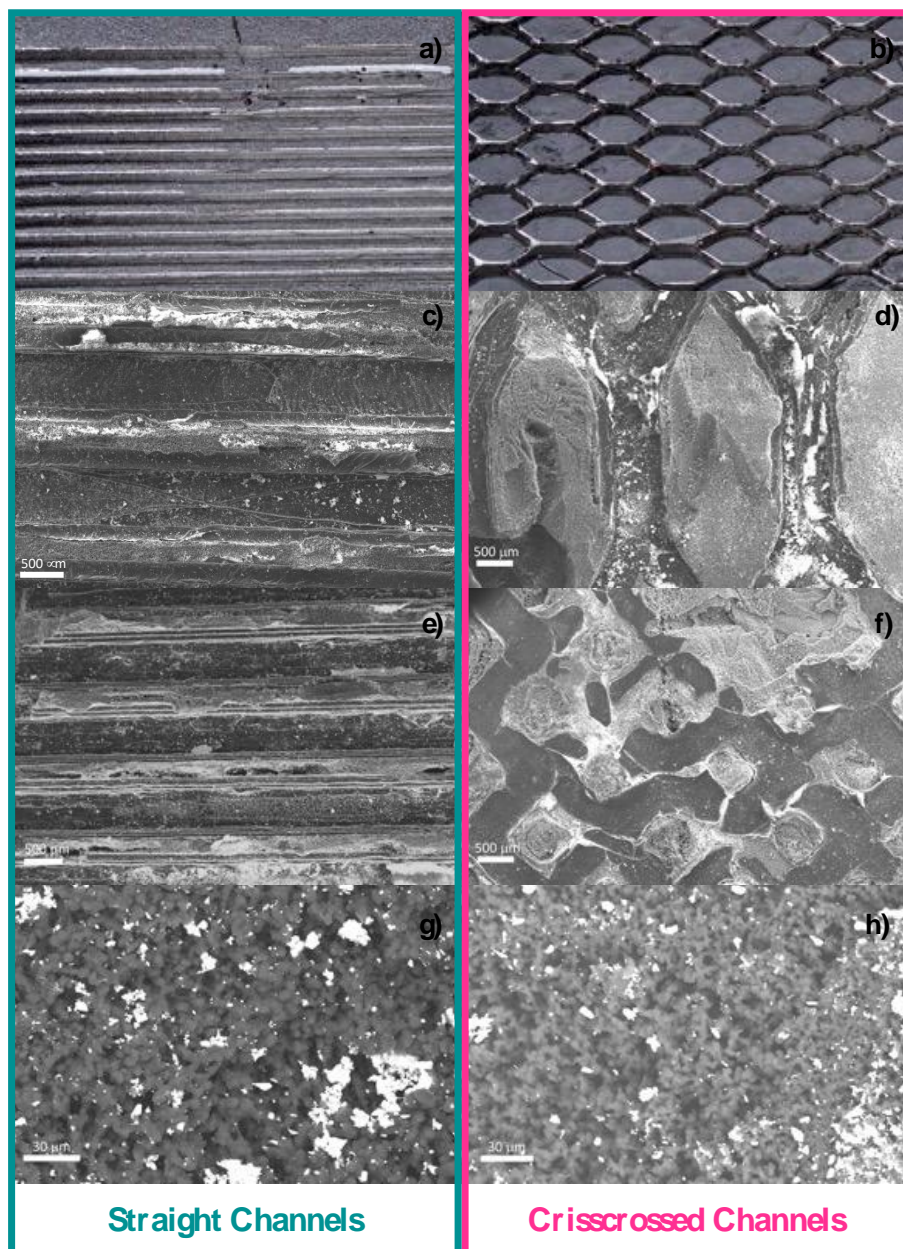
Figure 5.6. Photographs and SEM images of the straight channel carbon monoliths (left) and the crisscrossed channel carbon monoliths (right) impregnated with Ni/CeO$_2$. a) and b) photographs of both designs without impregnation of catalyst; c) and e) straight channels of different cell density; d) and f) crisscrossed channels of different cell density; g) and h) distribution of the active phase in the porous structure of the two different designs.

The textural properties of these carbon monoliths also have a significant contribution from macropores, as detected by mercury porosimetry. As seen in **Table 5.1**, the macroporosity of the carbon monoliths has not been affected by the presence of the templates. Furthermore, this macroporosity favors the dispersion of the active phase both on the surface of the channels and within the porous structure of the carbon, as identified in the SEM images (**Figure 5.6**).

The amount of Ni/CeO$_2$ active phase supported in the different designs was very similar (800 ± 5 mg) and was dispersed homogeneously in each monolith during the dip-coating process. However, note that designs with lower cell density (**Figure 5.6c and 5.6d**) favor greater dispersion of the Ni/CeO$_2$ active phase on the surface of the channels compared to designs with higher cell density (**Figure 5.6e and 5.6f**). This indicates that increasing the cell density of the monoliths favors the diffusion of the active phase within its porous structure. Consequently, a design that induces turbulence in the path of the reaction gases can enhance the accessibility of that active phase. Furthermore, the walls of the carbon monoliths are composed of primary particles that are fused to form a coral structure, which allows obtaining a porosity of the order of microns (as shown in **Figure 5.6g and 5.6h**). Just as already mentioned, this macroporosity enhances the dispersion of the active phase and, subsequently, facilitates its interaction with the reaction gases.

Cell density also affects the mechanical properties of monolithic supports. As can be seen in **Figure 5.7**, an increase in the cell density of the monoliths negatively affects their mechanical resistance. For both designs, monoliths with higher cell density have a lower value of maximum stress (σ_{max}) at the point of failure. However, crisscrossed channel monoliths have greater strength compared to straight channel monoliths of similar cell density. In other words, by increasing the cell density, the volume occupied by the carbon structure decreases, therefore, its mechanical resistance also decreases.
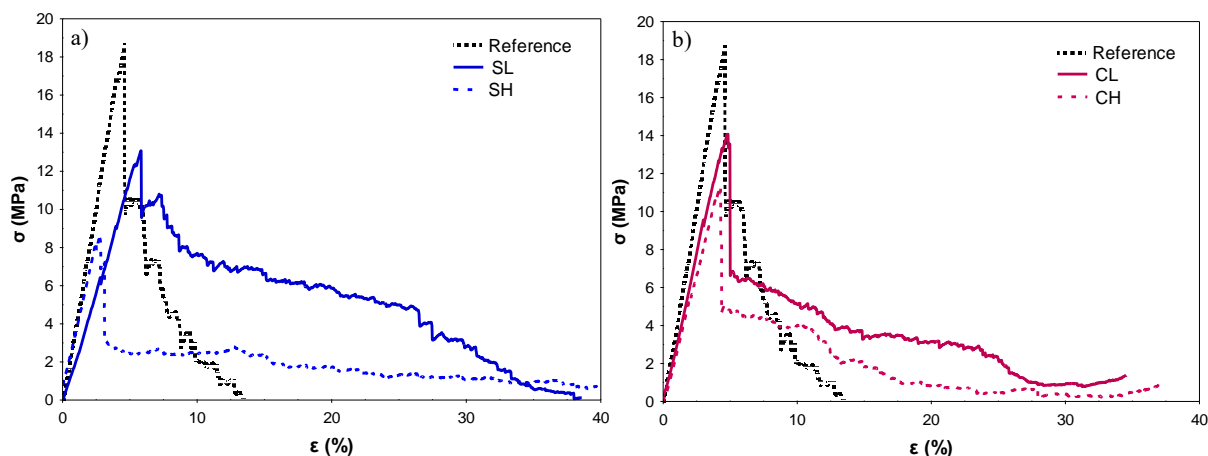
Figure 5.7. Stress-strain curves of carbon monoliths of both cell geometries compared to a monolith without channels (Reference). a) straight channels; and b) crisscrossed channels.

5.3.2. Catalytic results

The catalytic performance of the Ni/CeO$_2$ active phase supported on monoliths of different designs was studied in the CO$_2$ methanation, increasing the flow rates of the reaction gases from 100 to 500 mL min^{-1}. As expected, the design of the channels influences the interaction between the reaction gases and the active phase [42]. To analyze the influence of the channel design on mass diffusion, the reaction rate was determined for the different flows (***Figure 5.8***).
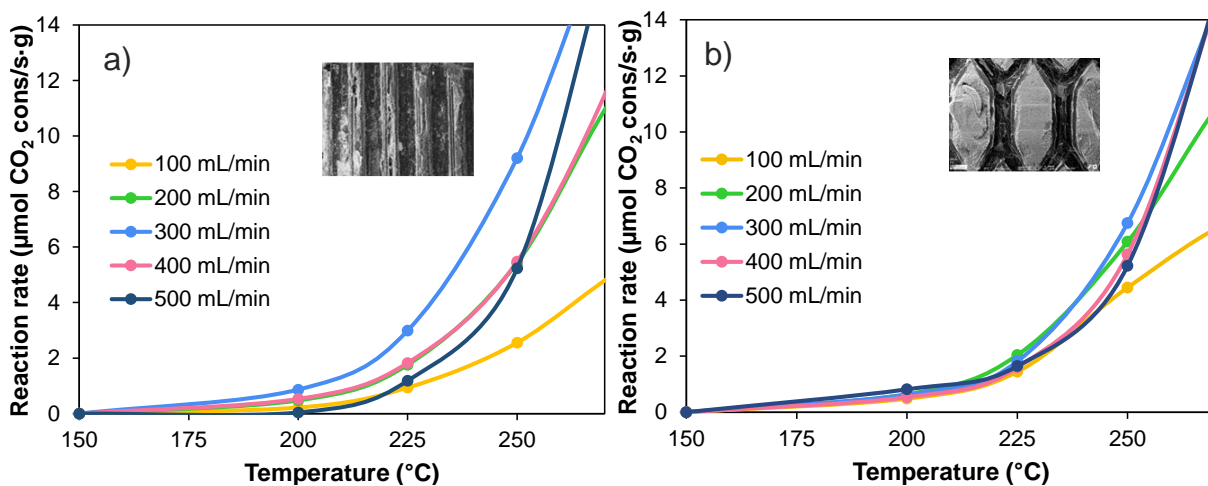
Figure 5.8. CO$_2$ conversion rate normalized by weight of Ni/CeO$_2$ supported on carbon monolith: a) straight channels; and b) crisscrossed channels.

In straight channels monoliths, it is observed that the reaction rate varies significantly as the reaction gases flow increases, which indicates that the reaction rate is under diffusion control. That is, when the flow rate is increased, the amount of available reactants increases, therefore, the reaction rate increases. However, at higher flow rates, there is a drop in CO_2 conversion rates because a large part of the reactants cannot access the active phase due to diffusion limitations (as seen in **Figure 5.8a**). A different behavior is observed in the crisscrossed channels monoliths (**Figure 5.8b**). In this case, the tortuous path followed by the reaction gases improves their diffusion and accessibility to the Ni/CeO_2 active phase, favoring the chemical control of the reaction up to approximately 230 ºC. Note that up to this temperature, the increase in reactants (flow rate) does not lead to significant variations in the CO_2 conversion rate. Thus, it is clear that the design of crisscrossed channels mitigates the diffusion problems that arise in a conventional straight channels monolith and favors the use of the active phase supported both on the surface of the channels and within the porous structure.
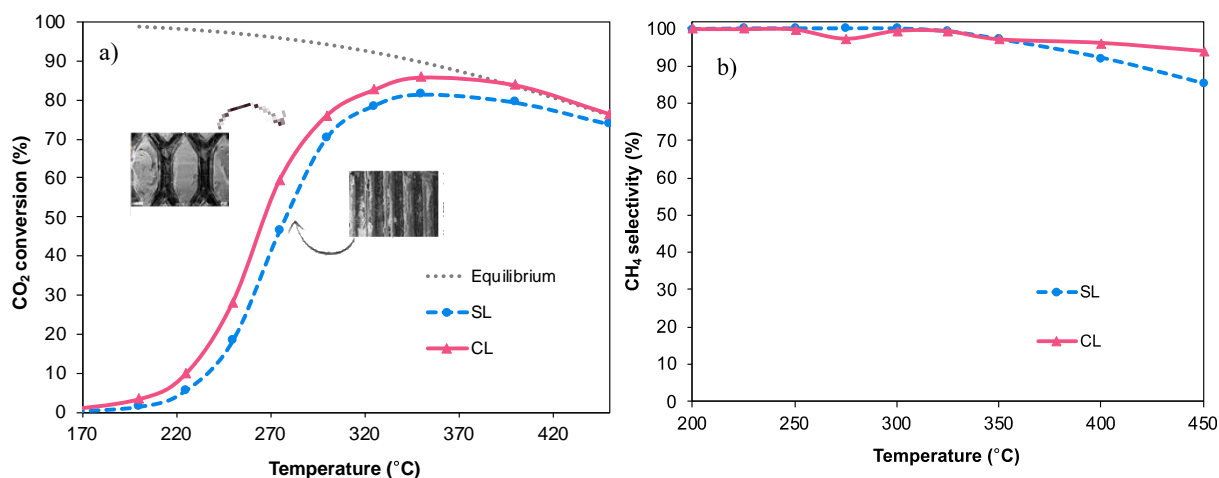
Figure 5.9. CO_2 methanation tests over Ni/CeO_2-carbon monolithic catalysts prepared with low cell density for straight (SL) and crisscrossed (CL) channel designs; GHSV ≈ 6500 h^{-1}. a) CO_2 conversion; and b) selectivity to CH_4.

The effect that the channel design has on the catalytic performance can also be observed in the CO_2 conversion profiles. As seen in **Figure 5.9a**, a test carried out on

monolithic catalysts of similar cell density (160 cpsi) at a space velocity of approximately 6500 h^{-1} confirms that the crisscrossed channels design allows obtaining greater catalytic performance compared to a straight channels design; using the same amount of active phase (800 ± 5 mg). For its part, CH_4 selectivity (*Figure 5.9b*) maintains a similar behavior in both monolithic catalysts up to the temperature where their maximum conversion is approximately reached. From this point on, selectivity to CH_4 shows a slightly more marked drop in monolithic catalysts with a straight channel design.
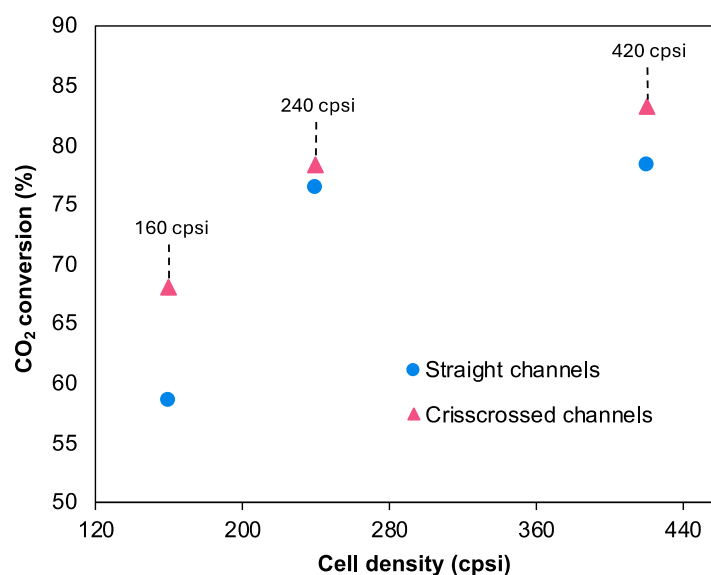
Figure 5.10. CO_2 conversion at 325 ºC and GSHV ≈ 12000 h^{-1} for the straight channels (S) and crisscrossed channels (C) monoliths with different cell densities (cpsi).

To investigate the effect of cell density on the catalytic activity of both designs, a series of catalytic tests were carried out, setting the space velocity (GSHV ≈ 12000 h^{-1}) so that the only variables under study were channels design and cell density. *Figure 5.10* shows the CO_2 conversion obtained for each monolithic catalyst at 325 ºC and a space velocity of 12000 h^{-1}. As previously mentioned, the crisscrossed channels design allows obtaining greater catalytic performance of the Ni/CeO_2 active phase for CO_2 methanation compared to the straight channels design. Furthermore, this trend is maintained in the three different cell densities studied. However, in the monolithic catalysts with the lowest cell density (160 cpsi) a greater difference in CO_2 conversion

is identified. These results are directly related to the limitations of gas diffusion into the porous carbon structure, where part of the Ni/CeO$_2$ active phase is supported.

In other words, monoliths with lower cell density have smaller channel surface area and a larger volume occupied by the carbon structure compared to monoliths with higher cell density. That is, by supporting 800 ± 5 mg of active phase in a carbon monolith with high cell density (e.g., 420 cpsi), the active phase is more accessible to reactants because this cell configuration has a larger channel surface area, which can also be interpreted to mean that these monoliths have a smaller volume occupied by the porous carbon structure. In contrast, in carbon monoliths of lower cell density (160 cpsi), the volume occupied by the porous carbon structure is larger, so that the active phase supported within the carbon lattice is less accessible. In general, both the channel design and cell density of a monolith play an important role in the catalytic performance of the Ni/CeO$_2$ active phase in the CO$_2$ methanation reaction.

5.4. Conclusions

The advantages of combining 3D printing with the preparation of carbon xerogels have been confirmed in this work. This procedure offers the possibility to prepare different configurations of monolithic reactors, in which it is possible to modify not only their design but also their cell density. Designs that generate certain turbulence in the reaction gases path contribute to improve the interaction between these and the active phase, since it favors their diffusion within the porous carbon structure. In addition, it has been seen that increasing the cell density favors the catalytic performance of the catalyst for any design because the channels surface area where the active phase is supported increases, thus facilitating the accessibility of the reactants to the Ni/CeO$_2$ particles. However, it is necessary to find a balance between mechanical properties and catalytic performance. As seen in this work, increasing the cell density of a monolithic catalyst improves its catalytic performance, however, its mechanical properties are negatively affected. Therefore, in each catalytic reaction the configuration of the monolithic supports could be adjusted for optimal performance in its application on an industrial scale.

5.5. References

[1] Jacquemin, M., Beuls, A., Ruiz, P. (2010). Catalytic production of methane from CO2 and H2 at low temperature: Insight on the reaction mechanism, *Catalysis Today, 157*, 462–466. https://doi.org/10.1016/J.CATTOD.2010.06.016.

[2] De Piano, G., Gamboa, J.J.A., Condó, A.M., Bengió, S., Gennari, F.C. (2022). Bimetallic Ni-Fe catalysts for methanation of CO2: Effect of the support nature and reducibility, *Applied Catalysis A General, 634*, 118540. https://doi.org/10.1016/J.APCATA.2022.118540.

[3] Gómez, L., Martínez, I., Navarro, M. V., García, T., & Murillo, R. (2022). Sorption-enhanced CO and CO2 methanation (SEM) for the production of high purity methane. *Chemical Engineering Journal, 440*, 135842. https://doi.org/10.1016/J.CEJ.2022.135842.

[4] Alarcón, A., Guilera, J., Díaz, J. A., & Andreu, T. (2019). Optimization of nickel and ceria catalyst content for synthetic natural gas production through CO2 methanation. *Fuel Processing Technology, 193*, 114–122. https://doi.org/10.1016/J.FUPROC.2019.05.008.

[5] Aldana, P. A. U., Ocampo, F., Kobl, K., Louis, B., Thibault-Starzyk, F., Daturi, M., Bazin, P., Thomas, S., & Roger, A. C. (2013). Catalytic CO2 valorization into CH4 on Ni-based ceria-zirconia. Reaction mechanism by operando IR spectroscopy. *Catalysis Today*, *215*, 201–207. https://doi.org/https://doi.org/10.1016/j.cattod.2013.02.019.

[6] Sehested, J., Dahl, S., Jacobsen, J., & Rostrup-Nielsen, J. R. (2005). Methanation of CO over Nickel: Mechanism and Kinetics at High H2/CO Ratios †. *J. Phys. Chem. B, 109*(6), 2432-2438. https://doi.org/10.1021/jp040239s.

[7] Muroyama, H., Tsuda, Y., Asakoshi, T., Masitah, H., Okanishi, T., Matsui, T., & Eguchi, K. (2016). Carbon dioxide methanation over Ni catalysts supported on various metal oxides. *Journal of Catalysis, 343*, 178-184. https://doi.org/10.1016/j.jcat.2016.07.018.

[8]   Frontera, P., Macario, A., Ferraro, M., Antonucci, P., Louis, B., & Wang, Q. (2017). Supported Catalysts for CO2 Methanation: A Review. *Catalysts, 7*(2), 59. https://doi.org/10.3390/CATAL7020059.

[9]   Vita, A., Italiano, C., Pino, L., Frontera, P., Ferraro, M., & Antonucci, V. (2018). Activity and stability of powder and monolith-coated Ni/GDC catalysts for CO2 methanation. *Applied Catalysis B, 226*, 384–395. https://doi.org/10.1016/J.APCATB.2017.12.078.

[10] Freccero, R., Spennati, E., Garbarino, G., & Riani, P. (2024). Intermetallic based materials for Sabatier reaction: Surface understanding, performance assessment and comparison with commercial catalyst. *Applied Catalysis B, 343*, 123532. https://doi.org/10.1016/j.apcatb.2023.123532.

[11] Shen, W., Zhang, Y., Zhao, L., Ye, Y., & Tursun, Y. (2021). Micro-scale simulation and intensification of complex Sabatier reaction system in cylindrical catalyst bed. *Fuel, 287*, 119399. https://doi.org/10.1016/j.fuel.2020.119399.

[12] Sripada, S., & Kastner, J. R. (2023). Continuous catalytic esterification using a solid acid activated carbon monolith: Comparison of granular and monolith forms with a commercial catalyst. *Chemical Engineering Journal, 476*, 146586. https://doi.org/10.1016/J.CEJ.2023.146586.

[13] Heck, R. M., Gulati, S., & Farrauto, R. J. (2001). The application of monoliths for gas phase catalytic reactions. *Chemical Engineering Journal, 82*, 149–156. https://doi.org/10.1016/S1385-8947(00)00365-X.

[14] Giroux, T., Hwang, S., Liu, Y., Ruettinger, W., & Shore, L. (2005). Monolithic structures as alternatives to particulate catalysts for the reforming of hydrocarbons for hydrogen generation. *Applied Catalysis B, 56*, 95–110. https://doi.org/10.1016/J.APCATB.2004.07.013.

[15] Chava, R., Bhaskar, A. V. D., Roy, B., & Appari, S. (2023). Reforming of model biogas using Ni/CeO2/γ-Al2O3 monolith catalyst. *Materials Today Proceedings, 72*, 134–139. https://doi.org/10.1016/J.MATPR.2022.06.234.

[16] Pereira, V. G. F., Rodrigues, C. P., & Toniolo, F. S. (2023). Ni/Al2O3 supported on cordierite monoliths for methane steam reforming: Influence of catalyst coating methodology. *Catalysis Communications, 183*, 106759. https://doi.org/10.1016/J.CATCOM.2023.106759.

[17] Ricca, A., Palma, V., Martino, M., & Meloni, E. (2017). Innovative catalyst design for methane steam reforming intensification. *Fuel, 198*, 175–182. https://doi.org/10.1016/J.FUEL.2016.11.006.

[18] Acuña-Bedoya, J. D., Rangel-Sequeda, J. F., Loredo-Cancino, M., Maya-Treviño, M. D. L., Domínguez-Jaimes, L. P., & Hernández-López, J. M. (2022). Integration of the adsorption and electro-oxidation process using 3D printed activated carbon monoliths for the degradation of pharmaceutical compounds. *J. Environ. Chem. Eng., 10*, 108203. https://doi.org/10.1016/J.JECE.2022.108203.

[19] Osorio–Zabala, M. A., Baquero, E. A., & Daza, C. (2024). Dry reforming of methane using cordierite monoliths with immobilized Ni–Ce catalysts. *International Journal of Hydrogen Energy, 60*, 1157–1169. https://doi.org/10.1016/J.IJHYDENE.2024.02.267.

[20] Li, Y., Zhang, Q., Chai, R., Zhao, G., Cao, F., Liu, Y., & Lu, Y. (2016). Metal-foam-structured Ni–Al2O3 catalysts: Wet chemical etching preparation and syngas methanation performance. *Applied Catalysis A: General, 510*, 216–226. https://doi.org/10.1016/J.APCATA.2015.11.034.

[21] Li, Y., Zhang, Q., Chai, R., Zhao, G., Liu, Y., Lu, Y., & Cao, F. (2015). Ni-Al2O3/Ni-foam catalyst with enhanced heat transfer for hydrogenation of CO2 to methane. *AIChE Journal, 61*, 4323–4331. https://doi.org/10.1002/AIC.14935.

[22] Navarro, J. C., Centeno, M. A., Laguna, O. H., & Odriozola, J. A. (2020). Ru–Ni/MgAl2O4 structured catalyst for CO2 methanation. *Renewable Energy, 161*, 120–132. https://doi.org/10.1016/J.RENENE.2020.07.055.

[23] Fukuhara, C., Hayakawa, K., Suzuki, Y., Kawasaki, W., & Watanabe, R. (2017). A novel nickel-based structured catalyst for CO2 methanation: A honeycomb-type Ni/CeO2 catalyst to transform greenhouse gas into useful resources. *Appl. Catal. A: Gen., 532*, 12–18. https://doi.org/10.1016/J.APCATA.2016.11.036.

[24] Ström, H., Sasic, S., & Andersson, B. (2011). Effects of the turbulent-to-laminar transition in monolithic reactors for automotive pollution control. *Ind. Eng. Chem. Res., 50*(7), 3194–3205. https://doi.org/10.1021/IE102291T.

[25] Cornejo, I., Cornejo, G., Nikrityuk, P., & Hayes, R. E. (2019). Entry length convective heat transfer in a monolith: The effect of upstream turbulence. *International Journal of Thermal Sciences, 138*, 235–246. https://doi.org/10.1016/J.IJTHERMALSCI.2018.12.044.

[26] Kutin, J., & Bajsić, I. (2014). Fluid-dynamic loading of pipes conveying fluid with a laminar mean-flow velocity profile. *Journal of Fluids and Structures, 50*, 171–183. https://doi.org/10.1016/J.JFLUIDSTRUCTS.2014.05.014.

[27] Parra-Marfil, A., Ocampo-Pérez, R., Aguilar-Madera, C.G., Carrasco-Marín, F., Pérez-Cadenas, A.F., Bueno-López, A., & Bailón-García, E. (2024). Modeling and experimental analysis of CO2 methanation reaction using Ni/CeO2 monolithic catalyst. *Environmental Science and Pollution Research, 1–18*. https://doi.org/10.1007/S11356-024-33327-5.

[28] Balakrishnan, G., Raghavan, C. M., Ghosh, C., Divakar, R., Mohandas, E., Song, J. Il, Bae, S. I., & Kim, G. (2013). X-ray diffraction, Raman and photoluminescence studies of nanocrystalline cerium oxide thin films. *Ceramics International, 39*(7), 8327-8333. https://doi.org/10.1016/j.ceramint.2013.03.103.

[29] Hay, P. J., Martin, R. L., Uddin, J., & Scuseria, G. E. (2006). Theoretical study of CeO2 and Ce2O3 using a screened hybrid density functional. *The Journal of Chemical Physics, 125*(3), 034712. https://doi.org/10.1063/1.2206184.

[30] Weck, P. F., Cochrane, K. R., Root, S., Lane, J. M. D., Shulenburger, L., Carpenter, J. H., Sjostrom, T., Mattsson, T. R., & Vogler, T. J. (2018). Shock compression of strongly correlated oxides: A liquid-regime equation of state for cerium (IV) oxide. *Physical Review B, 97*(12), 125106. https://doi.org/10.1103/PhysRevB.97.125106.

[31] Olajire, A. A., & Mohammed, A. A. (2019). Green synthesis of nickel oxide nanoparticles and studies of their photocatalytic activity in degradation of polyethylene films. *Advanced Powder Technology, 31*, 211-218. https://doi.org/10.1016/j.apt.2019.10.012.

[32] Lee, M., & Delgado, H. (2017). A Raman Study of CeO2 Nanomaterials with Different Morphologies. [Master's Thesis, Friedrich-Alexander University Erlangen-Nürnberg].

[33] Schmitt, R., Nenning, A., Kraynis, O., Korobko, R., Frenkel, A. I., Lubomirsky, I., Haile, S. M., & Rupp, J. L. M. (2020). A review of defect structure and chemistry in ceria and its solid solutions. *Chemical Society Reviews, 49*(2), 554. https://doi.org/10.1039/c9cs00588a.

[34] Serafin, J., & Llorca, J. (2023). Nanoshaped Cerium Oxide with Nickel as a Non-Noble Metal Catalyst for CO2 Thermochemical Reactions. *Molecules, 28*(7). https://doi.org/10.3390/molecules28072926.

[35] Muduli, S., & Sahoo, T. R. (2022). Green synthesis and characterization of CeO2 and Ni-doped CeO2 nanoparticles and its dielectric properties. *Materials Today: Proceedings, 74*, 697-702. https://doi.org/10.1016/j.matpr.2022.10.278.

[36] Li, R. J., Zhang, J. P., Shi, J., Li, K. Z., Liu, H. L., & Zhu, X. (2022). Regulation of metal-support interface of Ni/CeO2 catalyst and the performance of low

temperature chemical looping dry reforming of methane. *J. Fuel Chem. Technol., 50*(10), 1458–1470. https://doi.org/10.1016/S1872-5813(22)60032-X.

[37] Li, Y., Wei, Z., Gao, F., Kovarik, L., Baylon, R. A. L., Peden, C. H. F., & Wang, Y. (2015). Effect of oxygen defects on the catalytic performance of VOx/CeO2 catalysts for oxidative dehydrogenation of methanol. *ACS Catalysis, 5*(5), 3006-3012. https://doi.org/10.1021/cs502084g.

[38] Lin, S., Li, Z., & Li, M. (2022). Tailoring metal-support interactions via tuning CeO2 particle size for enhancing CO2 methanation activity over Ni/CeO2 catalysts. *Fuel, 333*, 126369. https://doi.org/10.1016/j.fuel.2022.126369.

[39] Li, Y., Li, H., Li, K., Wang, R., Zhang, R., & Liu, R. (2023). Roles of oxygen vacancies in CeO2 nanostructures for catalytic aerobic cyclohexane oxidation. *ACS Applied Nano Materials, 6*(2), 14214–14227. https://doi.org/10.1021/acsanm.3c02147.

[40] Li, Z., Deng, L., Kinloch, I. A., & Young, R. J. (2023). Raman spectroscopy of carbon materials and their composites: Graphene, nanotubes and fibres. *Prog. Mater. Sci., 135*, 101089. https://doi.org/10.1016/J.PMATSCI.2023.101089.

[41] Couzi, M., Bruneel, J. L., Talaga, D., & Bokobza, L. (2016). A multi wavelength Raman scattering study of defective graphitic carbon materials: The first order Raman spectra revisited. *Carbon, 107*, 388–394. https://doi.org/10.1016/J.CARBON.2016.06.017.

[42] Chaparro-Garnica, C.Y., Jordá-Faus, P., Bailón-García, E., Ocampo-Pérez, R., Aguilar-Madera, C.G., Davó-Quiñonero, A., Lozano-Castelló, D., & Bueno-López, A. (2020). Customizable heterogeneous catalysts: Nonchanneled advanced monolithic supports manufactured by 3D-printing for improved active phase coating performance. *ACS Applied Materials & Interfaces, 12*(45), 54573–54584. https://doi.org/10.1021/acsami.0c14703.

6

AUTO-PRESSURIZED MULTI-STAGE TESLA-VALVE TYPE MICROREACTORS IN CARBON MONOLITHS OBTAINED THROUGH 3D PRINTING: IMPACT OF DESIGN ON FLUID DYNAMICS AND CATALYTIC ACTIVITY
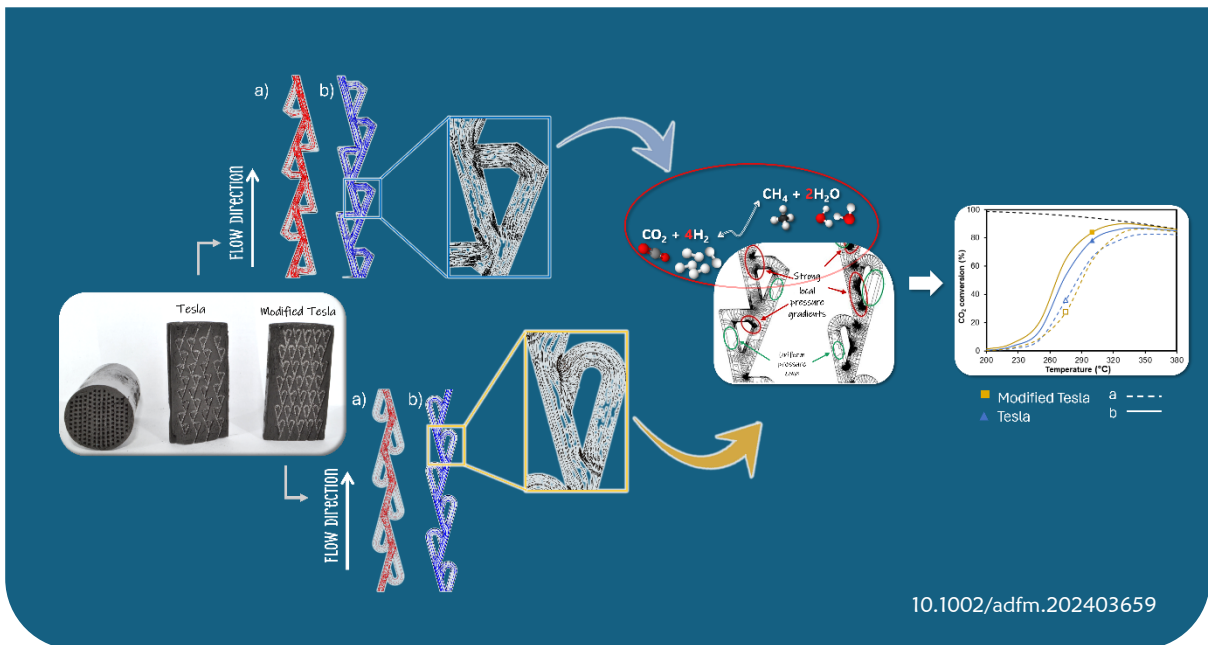
Auto-Pressurized Multi-Stage Tesla-Valve Type Microreactors in Carbon Monoliths Obtained Through 3D Printing: Impact of Design on Fluid Dynamics and Catalytic Activity

Adriana Parra-Marfil, Carlos Gilberto Aguilar-Madera, Agustín Francisco Pérez-Cadenas, Francisco Carrasco-Marín, Saúl Omar Gutiérrez-Reina, Agustín Bueno-López, Raúl Ocampo-Pérez, and Esther Bailón-García*

The present research exploits an innovative methodology for producing auto-pressurized carbon microreactors with a precise and controlled structure analyzing the influence of their design on the fluid dynamics and their catalytic performance. Carbon monoliths with Tesla-valve shape channels (Tesla, T, and modified Tesla, Tm) are synthesized through the combination of 3D printing and sol–gel process and further probed as Ni/CeO2 supports on CO2 methanation. The experimental results and mathematical modeling corroborated the improved performance obtained through the complex design compared to a conventional one. In addition to chaotic fluid flow induced by the deviation in flow direction, which improves the reagents-active phase interaction, local pressure increases due to convergence of flows may enhance the Sabatier reaction according to Le Châtelier's principle. Conversely to straight channels, T and Tm are not affected by flow rate and presented chemical control. Tesla-valve with curved angle (Tm) improved the mass transfer, achieving higher conversion and ≈30% reaction rate increase regarding right angle (T). Thus, this auto-pressurized multi-stage Tesla-valve monolith opens the gate to design specific and advanced functional materials for multitude chemical reactions where not only the reactant-active phase contact can be maximized but also the reaction conditions can be controlled to maximize the reaction kinetics.

1. Introduction

CO_2 atmospheric levels, which account for ≈79% of greenhouse gas emissions, are steadily increasing due to human activities, mainly energy consumption.[1] This growth in emissions severely impacts the climate change, thus generating a crucial necessity to find and implement solutions to this problem. Among the major strategies considered so far, the use of carbon capture and sequestration technologies, and the energy transition from fossil fuel to more sustainable energy sources can be mentioned.[2,3] In this context, the valorization of CO_2 through its transformation into high-value fuels may not only help to mitigate environmental damage, but also to reduce the existing dependence on fossil fuels.[1,4–6] This valorization can be developed via its hydrogenation to methane (1), also called as CO_2 methanation reaction or Sabatier reaction.[7,8] The product obtained is chemically similar to natural

A. Parra-Marfil, A. F. Pérez-Cadenas, F. Carrasco-Marín, E. Bailón-García
Materiales Polifuncionales Basados en Carbono (UGR-Carbon)
Departamento Química Inorgánica – Unidad de Excelencia Química
Aplicada a Biomedicina y Medioambiente – Universidad de Granada
(UEQ-UGR)
Granada ES 18071, Spain
E-mail: estherbg@ugr.es

A. Parra-Marfil, S. O. Gutiérrez-Reina, R. Ocampo-Pérez
Centro de Investigación y Estudios de Posgrado (CIEP), Facultad de
Ciencias Químicas
Universidad Autónoma de San Luis Potosí (FCQ-UASLP)
San Luis Potosí MX 78260, México

C. G. Aguilar-Madera
Facultad de Ciencias de la Tierra
Universidad Autónoma de Nuevo León (UANL)
Carretera a Cerro Prieto Km. 8 Ex Hacienda de Guadalupe, Linares MX
67700, México

A. Bueno-López
Departamento de Química Inorgánica
Universidad de Alicante (UA)
Alicante ES 03080, Spain

6.1. Introduction

CO$_2$ atmospheric levels, which account for around 79 % of greenhouse gas emissions, are steadily increasing due to human activities, mainly energy consumption [1]. This growth in emissions severely impacts the climate change, thus generating a crucial necessity to find and implement solutions to this problem. Among the major strategies considered so far, the use of carbon capture and sequestration technologies, and the energy transition from fossil fuel to more sustainable energy sources can be mentioned [2,3]. In this context, the valorization of CO$_2$ through its transformation into high-value fuels may not only help to mitigate environmental damage, but also to reduce the existing dependence on fossil fuels [1,4–6]. This valorization can be developed via its hydrogenation to methane (1), also called as CO$_2$ methanation reaction or Sabatier reaction [7,8]. The product obtained is chemically similar to natural gas, therefore can be straightly introduced into the natural gas infrastructure [9].

$$CO_2 + 4H_2 \leftrightarrow CH_4 + 2H_2O, \triangle H_{298\,K} = -165 \text{ kJ mol}^{-1} \text{ [10–12]} \tag{1}$$
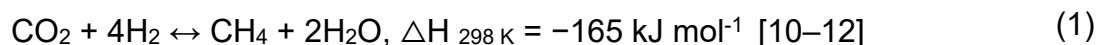
Although the CO$_2$ methanation reaction is thermodynamically suitable at low temperatures, it is also kinetically limited owing to the chemical stability of the C=O bond of CO$_2$ [1,13–15]. Hence, the development of selective, efficient, and stable catalysts that favor its dissociation is necessary for enhancing the reaction rate of CO$_2$ methanation at low temperatures. In that respect, several studies have been conducted on the production of supported catalysts usually composed of active metals, either noble (Rh, Ru, Pd, etc.) or non-noble (Co, Fe, Ni, Cu, etc.), which provide active sites for activation and dissociation of CO$_2$ and H$_2$ [4,11,16–27]. Within the catalysts developed to date, Ni-based ones are the most studied and applied owing to the great activity and methane yields provided by Ni, presenting a considerably better cost-effectiveness ratio compared to noble metals [15,28–31]. Furthermore, the large amount of surface oxygen vacancies of CeO$_2$ facilitates the activation and dissociation of CO$_2$ and metal-support interaction, therefore, Ni/CeO$_2$ catalysts enhance low temperature performance of CO$_2$ methanation [32–35].

On the other side, CO_2 methanation is a reversible and extremely exothermic reaction, thus resulting in temperature increase and hot spot formation [36]. This temperature increase may lead to carbon deposition and sintering, that is, catalyst deactivation. Therefore, besides the ability to transform the CO_2, catalyst configuration must help to handle and release the excessive heat generated from the exothermic reaction. This implies a defiance both in the temperature resistance and heat transfer properties.

Macro structured supports such as monoliths and micro-channel reactors have been studied and applied to overcome the problems commonly found in packed-bed reactors, mainly high pressure drop and heat and mass transfer limitations [37,38]. The better mass transfer between reagents flow and catalyst surface favors the reaction rate, while the heat transfer helps to prevent hot spots formation within the catalyst, as well as to avert approaching the chemical equilibrium disfavored at high temperatures that limits the methane yield [38,39]. Moreover, these structures can provide attractive advantages for their use in industrial scale, like high surface-to-volume ratios, no attrition, and easy separation process [40].

Some authors have reported that conforming the Ni-based active phase for methanation into honeycomb monoliths increases its stability and activity due to the transport properties provided by this type of structures [41,42]. Ni/GDC (gadolinium-doped-ceria) was in situ deposited by solution combustion synthesis (SCS) on cordierite monoliths by Vita et al.[43] to use them as CO_2 methanation catalysts. The structured materials exhibited high methane productivity per unit weight of catalyst at 400 °C requiring low catalytic loading and allowing the treatment of large flow rates (space velocity GHSV = 10,000-50,000 h^{-1}). Agueniou et al.[44] printed stainless steel honeycomb monoliths by selective laser sintering and washcoated them with Ni/CeO$_2$-ZrO$_2$ for the dry reforming of methane. Within the range of 750-900 °C the catalysts presented good activity with conversions around up to 95 %. Additionally, the activation time generally required is avoided due to the improvement in heat transfer assistance. Structured NiFe-loaded ceramic catalysts exhibited good catalytic activity in CO_2

methanation, reaching up to 70 % CO_2 conversion at 300 °C [45]. NiFe catalyst, originated from in situ grown layered double hydroxides, was precipitated on the exterior surface of cordierite monoliths previously coated with alumina or silica to increase its surface area. Catalyst coated with alumina exhibited greater CO_2 conversions than those with silica. This was associated to the deposition of NiFe into the channel wall, which in the case of silica washcoat loaded further inside compared to alumina one, thus resulting less accessible to the reagents flow due to the laminar flow imposed by the straight channel design.

Nonetheless, conventional straight channels force laminar flow creating radial diffusion limitations [46–48], so non-straight channels which can generate turbulence, nonlinear streamlines, and local mixing of solutes within them due to tortuous paths would be desired to increase the active phase efficiency. Although 3D printing technology has recently surged as an alternative to overcome the limitations imposed by conventional synthesis methods, such as extrusion, pressing, or corrugating foil, to produce only straight channels, it has been barely studied for producing complex monolithic catalysts [47–53]. In this context, the monolithic catalysts studied so far in CO_2 methanation have been mainly produced with conventional shape from ceramic or metal raw materials, which implies some disadvantages such as the difficulty to incorporate the active phase with a homogeneous coat. In the previous chapter, pure and integral carbon monoliths with specifically and rigorously designed geometry and porous texture were synthesized by combining the sol-gel polymerization of resorcinol and formaldehyde and the 3D printing technology. The turbulent path created by the tortuous channels that split and join successively along the monolith, favors the active phase-gas contact and, even, the gas diffusion inside the macroporosity of the carbon skeleton improving the catalytic performance of the active phase with respect to the conventional honeycomb design. Thus, it was clearly demonstrated that 3D printing opens new design possibilities that outperform conventional catalysts.

In this chapter, in addition to the control of the fluid dynamics, auto-pressurized microreactors could be created favoring the CO_2 methanation reaction by controlling

the channel morphology. Thus, the aim is on creating a monolithic structure with a Tesla-valve type channels configuration for improving fluid flow and create auto-pressurized microreactors along the channel, while also attaining the textural properties and chemical stability of carbon. Considering this, two monoliths of different types of Tesla-valve channels are produced and washcoated with Ni/CeO$_2$ to evaluate their performance as catalysts in the Sabatier reaction. Besides, a proper mathematical model to analyze the fluid dynamics, and to predict the velocity fluid profiles inside the channels of the catalytic structure is developed.

6.2. Experimental

6.2.1. Catalyst preparation

6.2.1.1. Active phase synthesis

A Ni/CeO$_2$ active phase has been prepared and used in this study. This active phase has been extensively tested and has been selected for the current study of the novel catalyst supports because has high activity, selectivity, and stability [54].

CeO$_2$ was synthesized through the thermal decomposition of cerium nitrate hexahydrate (Ce(NO$_3$)$_3$·6H$_2$O, ≥99.5% Alfa Aesar) via calcination at 500 °C in a muffle for 4 h. Subsequently, the CeO$_2$ was impregnated with an ethanolic solution of nickel (II) nitrate hexahydrate (Ni(NO$_3$)$_2$·6H$_2$O, ≥97% Sigma-Aldrich) considering a 10 wt% of Ni and, finally, a calcination process at 600 °C for 5 h was followed for decomposing the nickel salt and obtain the Ni/CeO$_2$ active phase.

6.2.1.2. Carbon supports obtained based on 3D printing.

Two monolithic carbon catalysts were produced with the advanced designs based on the Tesla-valve, Tesla (T) and modified Tesla (Tm), shown in **Figure 6.1**. Tesla-valve type channel is proposed to favor the turbulence and mass and heat transfer within the catalyst, and the impact of changing between right and curved angles in the valve (T and Tm, respectively) is evaluated in the CO$_2$ methanation performance. In order to synthesize this complex carbon structures, non-attainable through conventional methods, a methodology combining 3D printing and sol-gel process is conducted. The designs, which served as negative of the desired channels, were obtained with Cubify

Invent software, and then used in an Ultimaker^{2+} 3D printer to print polymeric templates. A conventional honeycomb carbon monolith with straight channels (C) was also obtained and used as reference.
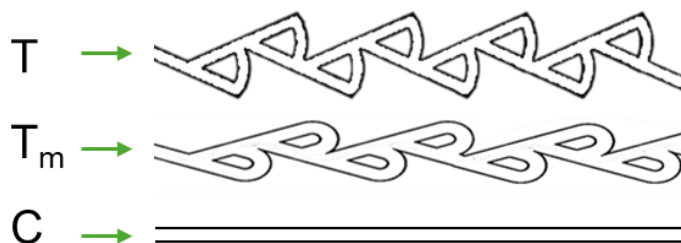
Figure 6.1. Structure design of channels: Tesla-valve type (T), modified Tesla-vale (Tm) and conventional honeycomb (C) monoliths.

After the template was printed, a carbon precursor solution was prepared consisting of resorcinol (R), formaldehyde (F), and water (W) with R/F and R/W molar ratios of 1/2 and 1/15, correspondingly. Afterward, the templates were introduced in glass tubes (~2.7 cm internal diameter) and later filled with the R/F/W solution and sealed. Then, a controlled polymerization process was conducted as follows: 1 day at room temperature, 1 day at 50 °C, and 5 days at 80 °C. Once completed, the organic monoliths obtained were demolded and immersed in acetone for 3 days to exchange the water within the structure, aiding the drying process and minimizing pore damage. Finally, the dried organic monoliths were carbonized at 850 °C for 2 h with a heating rate of 1.5 °C min^{-1}. The resulting monoliths presented an approximate 20 % shrinkage, with final dimensions of ~ 2.15 cm diameter and 3.5 cm length. the total volume of the monoliths is 12.7 mL, of which about 2.5 mL correspond to the channels' volume.

6.2.1.3. *Active phase loading*

The previously prepared Ni/CeO$_2$ active phase was loaded onto the carbon monoliths through dip-coating. Carbon monoliths were immersed in an ethanolic suspension containing Ni/CeO$_2$ at 10 wt%. Subsequently, the monoliths were horizontally rotated during 24 hours at room temperature to ensure a uniform distribution, and then they were dried overnight at 80 °C. Any excess of active phase

not firmly attached to the monolith surface, which could potentially block the channels, was removed using compressed air. The loading of Ni/CeO_2 was confirmed by observing the weight difference of the dried monoliths after each impregnation. This process was repeated until a loading of 800 ± 5 mg per monolith was achieved.

6.2.2. Catalyst characterization

To obtain data on the surface area of the carbon structure, adsorption isotherms (N_2 at -196 °C and CO_2 at 0 °C) were acquired by means of a Quantachrome Autosorb-6B instrument. Before the gas adsorption assessments, the samples underwent a degassing process at 110 °C for 8 h. Besides, Hg-porosimetry was also utilized to study the textural properties. The samples were previously degassed at 50 °C for 12 hours, and the analysis was effectuated through a Poremaster 60 GT (Quantachrome) equipment from an initial pressure of 7 KPa up to 390,000 KPa. The contact angle and surface tension used for pore size calculations were θ = 140 ° and γ = 480 dyne/cm, respectively.

The surface chemistry of the CeO_2 support and the active phase Ni/CeO_2 was analyzed through X-ray photoelectron spectroscopy (XPS). A K-ALPHA Thermo Scientific device with an X-ray source Al-Kα radiation at 1486.6 eV was used. Furthermore, the crystalline structure of the catalyst and the effect of loading onto a carbon monolith, were examined through X-ray diffraction (XRD) and Raman spectroscopy. A Bruker D8 DISCOVER X-Ray diffractometer with CuKα-ray radiation (λ =1.5418 Å) was used to obtain the XRD patterns within the 2θ range of 10–90° at 1° min^{-1}. Raman analysis was performed using a Jasco NRS-5100 dispersive micro-Raman microscope equipped with a Green Diode (532 nm, 30 mW, Elforlight G4-30; Nd:YAG).

Scanning electron microscopy (SEM) was employed to investigate the distribution of the active phase on the channels and carbon matrix of monolithic structures using a Zeiss SUPRA40VP Variable Pressure Scanning Electron Microscope (VP-FESEM) equipped with an EDX detector X-max 50. Additionally, thermal and mechanical properties were also determined. The thermal stability of the

catalysts in oxidizing atmosphere was assessed by thermogravimetric analysis (TGA). Bare and coated monoliths were analyzed using a SDT 2960 DSC-TGA equipment, heating at 10 °C per min up to 900 °C under air flow. Mechanical properties were evaluated by means of compression tests and compared with a commercial cordierite honeycomb monolith. The monolithic samples were cut into 1.5 cm high cylinders, and the bases were sanded for smooth surfaces. Tests were conducted using a Shimadzu AGS-J 10 kN instrument with a constant approach speed of 1 mm min^{-1} and the compression test direction was top to bottom.

6.2.3. Catalytic tests

The catalysts performance and the impact of geometric modification were studied in the CO_2 methanation reaction. The experimental setup comprised placing a monolith in a quartz cylindrical reactor within a temperature-controlled furnace (see *Figure 4.2*). To collect the produced water, a cold trap was integrated at the reactor's outlet, and the outflow (CO_2 and CH_4 gases) was analyzed using infrared gas sensors (Edinburgh Instruments LTD 034/00700). Before each experiment, the monolith under evaluation was subjected to treatment in a reducing atmosphere (10 % H_2/Ar) at 500 °C for 1.5 h. Subsequently, the system was allowed to cool to 150 °C, and the inlet flow was switched to the reaction gas mixture (10 % CO_2 and 40 % H_2 balanced in Ar) with total flows varying from 100 to 500 mL min^{-1}. The temperature was incremented in 25 °C steps, with each temperature held for 20 min, reaching up to 450 °C. CO_2 conversion and selectivity to CH_4 were calculated to evaluate the catalytic performance.

6.2.4. Mathematical model

The experimental data was introduced into a mathematical model which incorporates mass and momentum balances for the gas mixture of CO_2 methanation. The mathematical model incorporates four partial differential equations governing the momentum balance, the turbulent kinetic energy balance, the rate of dissipation of turbulent kinetic energy, and the gas-phase mass balance. The $\kappa - \epsilon$ mathematical model for momentum balance was applied, which is able to simulate turbulence within the monolith.

The momentum balance is given by:

$$\rho \frac{\partial \boldsymbol{u}}{\partial t} + \rho(\boldsymbol{u} \cdot \nabla)\boldsymbol{u} = -\nabla p + \nabla \cdot \mathbf{K} \tag{2}$$

With,

$$\mathbf{K} = (\mu + \mu_T)[\nabla \boldsymbol{u} + (\nabla \boldsymbol{u})^T] \tag{3}$$

Here μ_T is the turbulent viscosity which is computed as follows:

$$\mu_T = \rho C_\mu \frac{\kappa^2}{\epsilon} \tag{4}$$

The turbulent kinetic energy κ obeys the following partial differential equation:

$$\rho \frac{\partial \kappa}{\partial t} + \rho(\boldsymbol{u} \cdot \nabla)\kappa = \nabla \cdot \left[\left(\mu + \mu_T \frac{\mu_T}{\sigma_\kappa} \right) \nabla \kappa \right] + P_\kappa - \rho \epsilon \tag{5}$$

While the rate of dissipation of turbulent kinetic energy is given by:

$$\rho \frac{\partial \epsilon}{\partial t} + \rho(\boldsymbol{u} \cdot \nabla)\epsilon = \nabla \cdot \left[\left(\mu + \mu_T \frac{\mu_T}{\sigma_\epsilon} \right) \nabla \epsilon \right] + C_{\epsilon 1} \frac{\epsilon}{\kappa} P_\kappa - C_{\epsilon 2} \rho \frac{\epsilon^2}{\kappa} \tag{6}$$

The term associated to the rate of deformation is defined as:

$$P_\kappa = \mu_T \{\nabla \boldsymbol{u} : [\nabla \boldsymbol{u} + (\nabla \boldsymbol{u})^T]\} \tag{7}$$

In addition, $\boldsymbol{\rho}$ represents the fluid mass density, $\boldsymbol{u}$ is the vector of velocity, t is the time, p is the pressure, and $\boldsymbol{\mu}$ is the fluid viscosity. The gas-phase mass balance is given by the continuity equation written as:

$$\frac{\partial \rho}{\partial t} + \nabla \cdot (\rho \boldsymbol{u}) = 0 \tag{8}$$

The initial values of the pressure and velocity used to solve numerically the model are considered as:

$$\text{At} \quad t = 0 \, \text{min} \quad \boldsymbol{u} = \boldsymbol{0} \, \text{m/s}, \quad p = 1 \, \text{atm} \tag{9}$$

Further, boundary conditions were stated at the inlet and outlet of the monolith. For the inlet boundary, the velocity is determined as:

$$-\boldsymbol{n} \cdot \boldsymbol{u} = u^{in} \tag{10}$$

Where $\boldsymbol{n}$ is the unit normal vector pointing outward the inlet boundary. The inlet velocity u^{in} is computed through the flow area and volumetric flow rate as follows:

$$u^{in} = \frac{Q}{A} \tag{11}$$

Whereas, at the outlet boundary the pressure is fixed:

$$p = 1 \text{ atm} \tag{12}$$

The nonslip and impenetrability conditions are enforced for the velocity vector at the monolith surface, $u = 0$.

6.3. Results and discussion

6.3.1. Characterization of active phase

The crystal structure of Ni/CeO$_2$ active phase, both powdered and loaded onto the carbon monoliths, was analyzed by X-ray diffraction with the findings presented in **Figure 6.2**. Characteristic peaks corresponding to the fluorite face-centered cubic (FCC) crystalline structure of ceria (JCPDS 034-0394) at 28.5, 33.1, 47.6, and 56.5°, representing the (111), (200), (220), and (311) planes [54–56], were presented in the X-ray diffractograms of all samples (**Figure 6.2**). In the case of the Ni/CeO$_2$ diffractogram, small peaks at 37.2, 43.2, and 63° were observed attributed to the (111), (200), and (220) crystallographic planes of the FCC structure of NiO (JCPDS 047-1049) [58].
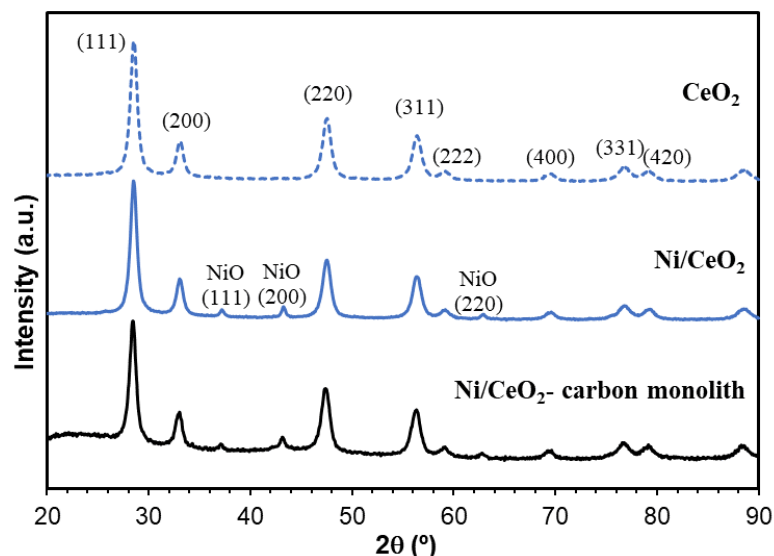
Figure 6.2. X-ray diffractograms of powdered CeO$_2$ and Ni/CeO$_2$, and Ni/CeO$_2$-coated carbon monolith.

The CeO_2 lattice parameter was estimated based on the XRD data, obtaining 0.5411 nm, consistent with that stated in JCPDS 00-034-0394. Note that CeO_2 peaks are slightly displaced in Ni/CeO_2 active phase, which is also manifested in the increase of the lattice parameter of CeO_2 (0.5420 and 0.5429 for unsupported and supported Ni/CeO_2, respectively). This change in the lattice parameter suggests that some nickel cations were introduced into the crystal lattice. Crystal sizes for CeO_2 and Ni/CeO_2 were determined using the Scherrer equation. The incorporation of nickel did not lead to a considerable change in the average size of the ceria crystals, as results were comparable for both pure CeO_2 (10.5 nm) and Ni/CeO_2 active phase (11.0 nm). Furthermore, it is important to highlight that the diffractogram of the Ni/CeO_2-coated monolith did not exhibit any notable change compared to the powdered active phase. This suggests that the coating process and the interaction between carbon structure and Ni/CeO_2 do not alter its crystalline characteristics.
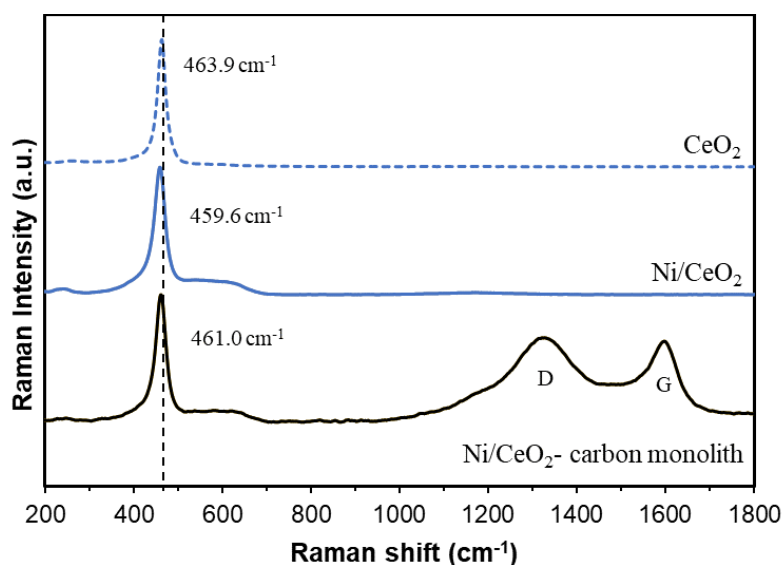
Figure 6.3. Raman spectra of powdered CeO_2 and Ni/CeO_2, and Ni/CeO_2-coated carbon monolith.

Figure 6.3 shows the Raman spectra of bare ceria and the Ni/CeO_2 active phase both unsupported and supported on carbon monolith. The bare ceria presented a single band centered at 463.9 cm^{-1}, corresponding to the F_{2g} vibrational mode of the

crystalline fluorite-type structure of ceria [57]. This intense peak is associated with symmetric $Ce-O_8$ stretching vibrations [58,59]. Owing to the presence of nickel and its interaction with ceria, the F_{2g} peak shifted to 459.5 cm^{-1} in the spectra of Ni/CeO_2 active phase confirming the insertion of Ni cations onto the ceria lattice observed by XRD. Further, a small shoulder emerges between 500 and 660 cm^{-1}, which is assigned to oxygen vacancies located at interfacial sites between Ni and CeO_2. In the Ni/CeO_2-coated carbon monolith, two new bands are observed at 1332 and 1599 cm^{-1} attributed to the D and G band of carbon, respectively. Note that both XRD and Raman data confirm that differences in ceria-related peaks are not observed between unsupported and supported on carbon monolith Ni/CeO_2 active phase, suggesting that the chemical nature of Ni/CeO_2 active phase is not alter by the coating process and anchoring on the carbon monolith surface. Therefore, the different catalytic performance of monoliths with different design should be ascribed to differences in the fluid dynamic behavior of the monolith and not to differences on the catalytic active phase.

The surface chemistry of the CeO_2 support and Ni/CeO_2 active phase was analyzed by XPS. Ce_{3d}, O_{1s} and Ni_{2p} XPS spectral regions are shown in ***Figure 6.4.*** 5 doublets are required to deconvolve the Ce_{3d} region (***Figure 6.4a***). The peaks pairs at 882.0-900.3 eV, 888.2-907.0 eV, 898.0-916.3 are attributed to Ce^{4+} whereas the peaks at 880.3-898.6 eV and 884.0-902.3 eV are assigned to Ce^{3+}. The proportion of Ce^{3+} detected by XPS must be related with the reducibility of the surface [62]. Note that the reducibility of the surface is improved by the addition of Ni, mainly if this Ni is incorporated during the synthesis due to the higher dispersion and Ce-Ni contact in this case. Consequently, it is expected that the amount of Ce^{3+} detected by XPS increases in Ni/CeO_2 active phase regarding CeO_2 support. The surface Ce^{3+} content obtained by XPS was 18.9 and 22.5 % for CeO_2 and Ni/CeO_2, respectively, due to the improved surface reducibility, which confirms the successful synthesis of Ni/CeO_2. This effect must be also observed in the O_{1s} region. The O_{1s} region requires two peaks for deconvolution (see ***Figure 6.4b***): one peak centered at 529.0 eV, associated with surface lattice oxygen (O_{latt}), and another peak centered at 531.0 eV, attributed to

adsorbed oxygen species (O_{ads}). Typically, O_{ads} species are present at oxygen vacancies, so a higher concentration of O_{ads} species suggests a greater population of oxygen vacancies. Therefore, the ratio of surface O_{ads} to O_{latt} can serve as an indicator of surface reducibility. The O_{ads}/O_{latt} ratio was 0.22 and 0.32 for CeO_2 and Ni/CeO_2, respectively indicating that Ni improves the surface ceria reducibility. Finally, the $Ni_{2p3/2}$ region of active phase was depicted in ***Figure 6.4c***. In this spectral region, a primary band is observed within the 851–859 eV range, accompanied by a satellite structure at higher binding energies (859–866 eV). To deconvolute the $Ni_{2p3/2}$ region, three peaks are necessary, occurring around 853.2, 855.0, and 857.2 eV. These peaks correspond to surface Ni^{2+} species within the NiO structure (surface NiO species), Ni^{2+} species closely associated with the ceria surface (NiO-Ce species), and Ni^{3+} or $Ni(OH)_2$ species, respectively [62, 63].
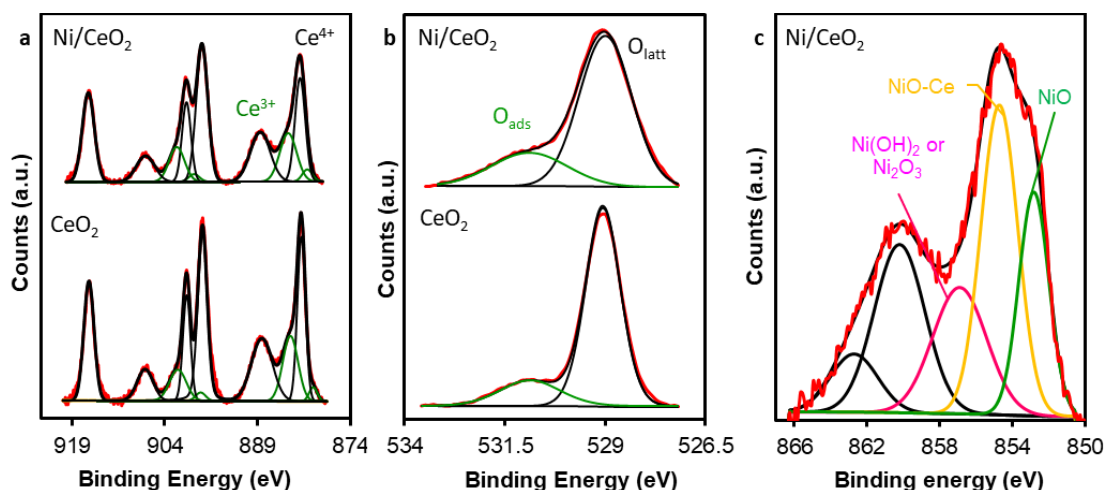
Figure 6.4. XPS results: a) Ce_{3d}, b) O_{1s} and c) $Ni_{2p3/2}$ regions.

6.3.2. Characterization of carbon supports

Carbon monoliths with three different channel designs were synthesized combining the 3D printing of polymeric templates and the RF sol-gel polymerization. A monolith without template was also synthesized to analyze the influence of the polymeric template on the textural properties of the carbon monoliths. The textural properties were analyzed by N_2 and CO_2 adsorption at -196 ºC and 0 ºC, respectively,

and Hg-porosimetry. Data were collected in *Figure 6.5* and *Table 6.1*. A type I isotherm, characteristic of microporous materials, was obtained for the carbon monolith synthesized without template. A slightly N_2 uptake is observed at intermediate relative pressures manifesting the presence of some mesoporosity. CO_2 adsorption offers insights into the narrow microporosity, specifically micropores with a diameter less than 0.7 nm. The assessment of total microporosity is reliant on the N_2 isotherm, but only in the absence of diffusion restrictions [60]. Note that V_{CO2} is greater than V_{N2} (*Table 6.1*), indicating the prevalence of narrow micropores and thus certain N_2 diffusional restrictions into the microporosity induced by such narrow microporosity.
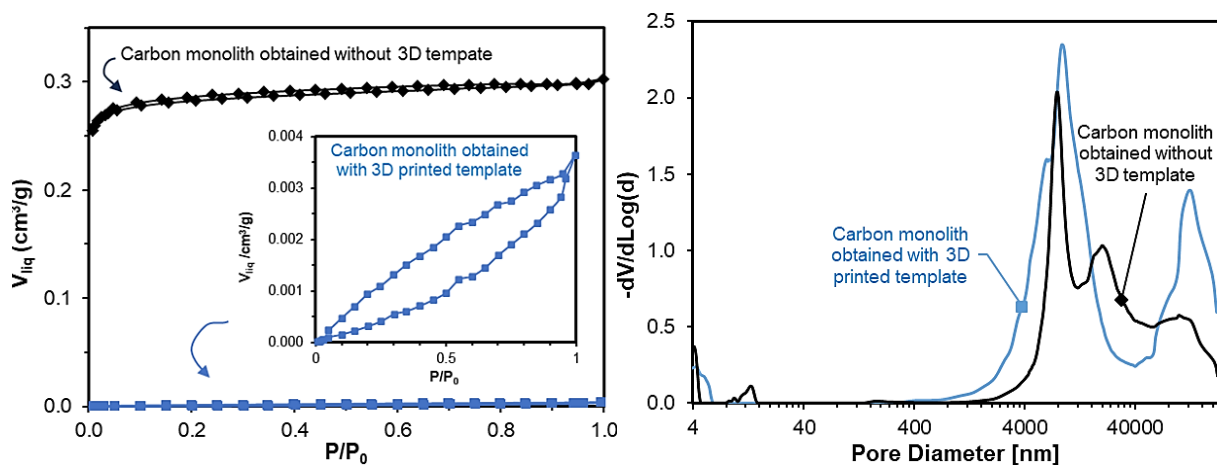
Figure 6.5. a) N_2 adsorption−desorption isotherms at −196 °C of a reference carbon monolith (without template) and a carbon monolith prepared using a 3D printed template, and b) Pore size distributions determined by mercury intrusion porosimetry.

The use of the template provokes a huge decrease of the N_2 adsorption of the carbon monolith. A Type II N_2-adsorption isotherm (*Figure 6.5a, inlet*) was obtained for the monolith with template, characteristic of non-porous or macroporous adsorbents. A practically total blockage of microporosity is observed, whereas the narrow microporosity even increases with the use of template (V_{CO2}, *Table 6.1*). Thus, this wider porosity blockage could be ascribed to the effect of the polymeric template. During the final carbonization, the thermofusible polymer occupying the channels melts at low temperatures and fills the wider porosity (macro and mesoporosity) that was

designed in the organic gel, leaving the channel with the desired geometry open. As the temperature increases, the organic RF matrix, along with the polymeric material, undergoes carbonization, obtaining the carbon monolith and removing the template. During this carbonization process, similar to what occurs in carbon molecular sieves prepared from an activated carbon by pitch pyrolysis [65], part of the gases evolved during the polymer heat treatment, after cracking, are deposited in the porosity entrance, blocking partially the porosity existing in the carbon matrix creating a high number of ultra micropores characteristic of molecular sieves.

Table 6.1. Textural characterization of carbon monoliths.

Sample	N$_2$ adsorption			CO$_2$ adsorption		Hg-porosimetry	
	S_{BET}	V_{N2}	L_0	V_{CO2}	L_0	V_{meso}	V_{macro}
	(m^2/g)	(cm^3/g)	(nm)	(cm^3/g)	(nm)	(cm^3/g)	(cm^3/g)
Monolith without template	639	0.29	0.67	0.31	0.61	0.04	0.90
Monolith with template	2	0	-	0.34	0.79	0.04	1.23

Hg-porosimetry (**Figure 6.5b** and **Table 6.1**) gives information about the wider porosity (mesopores and macropores). Note that highly opened macropores are mainly observed in both samples with a very low amount of mesopores (V$_{meso}$, **Table 6.1**). Three peaks centered at 8, 21, and 100 mm are observed in the Pore Size Distribution (PSD) of the carbon monolith obtained without template which are ascribed to the interparticle spaces leaved by the carbon gels clusters and some monolith cracks, respectively. However, the monolith obtained with the 3D printed template presents peaks centered at 6, 9 and 128 mm attributed to the filling of interparticle void of the carbon matrix and the channels, respectively. It is important to highlight that the peak ascribed to the carbon matrix voids becomes wider and shifts to lower pore diameter (**Figure 6.5b**). This carbon matrix porosity narrowing could be ascribed to the deposition of carbon residues from the template.
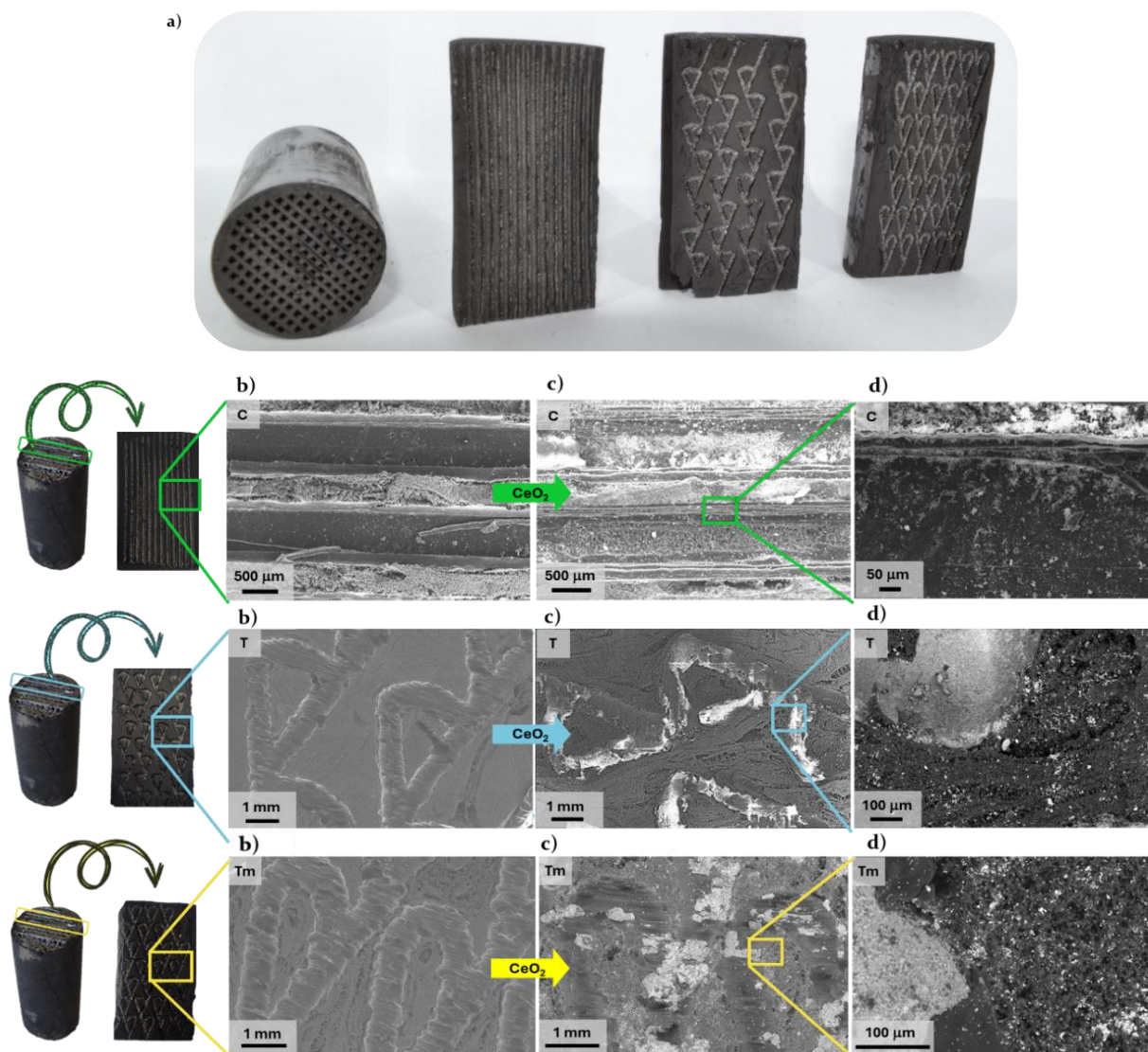
Figure 6.6. Images and SEM micrographs of C, T, and Tm carbon monoliths: a) structure of the monolith; b) channel morphology, c) Ni/CeO$_2$-impregnated monolith and d) magnification of the channel/wall interface showing the Ni/CeO$_2$ active phase distribution on the carbon matrix and the channel.

This wide macroporosity, the channel morphology, and the Ni/CeO$_2$ distribution on the carbon surface were analyzed by SEM. Images are collected in **Figure 6.6**. A perfect replica of the channel template was obtained for the three channel designs. Note that even the layer-by-layer architecture of the fused deposition 3D-printed template is reproduced (**Figure 6.6b**). After the impregnation of the active phase

(*Figure 6.6c*), the Ni/CeO_2 is distributed both along the channels and the wall carbon matrix. The magnification of the channel/wall interface (*Figure 6.6d*) shows that a huge part of the active phase is homogeneously distributed along the carbon matrix independently of the monolith design. This enhanced distribution along the carbon matrix is favored by the highly opened macroporosity of the carbon gels. SEM images of the carbon matrix (*Figure 6.7*) manifests a sponge-like structure with pore of several mm as it was also pointed out by Hg-porosimetry. This opened macroporosity favors the diffusion of the ethanolic Ni/CeO_2 suspension and is wider enough to host particles of several tens of nm of the Ni/CeO_2 active phase.
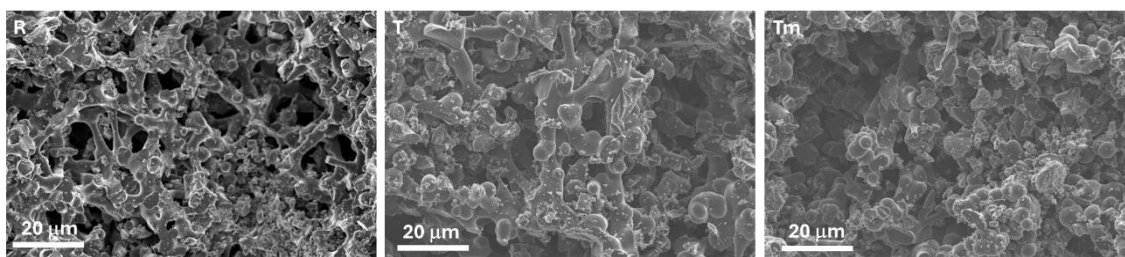
Figure 6.7. SEM images of carbon matrix in monolith without template (R) and with Tesla (T) and Tesla modified (Tm) templates.

The thermal stability of the bare and Ni/CeO_2-impregnated 3D-printed monoliths was analyzed by TGA using the T (Tesla-valve type) design (*Figure 6.8*). Both the impregnated and bare carbon monoliths are stable up to 500 ºC under oxidizing atmosphere. At higher temperatures, the monoliths start to burn being completely burned at a temperature of around 630 ºC and 620 ºC for the bare and impregnated monoliths, respectively. The presence of Ni/CeO_2, a well-known active phase for oxidizing reactions, favors the carbon phase burning off but the stability is still high to be used in reactions in which temperatures lower than 500 ºC in oxidizing atmosphere are required. In the case of CO_2 methanation, the maximum temperature used is 450 ºC under He atmosphere, so the stability of the carbon matrix is guaranteed.
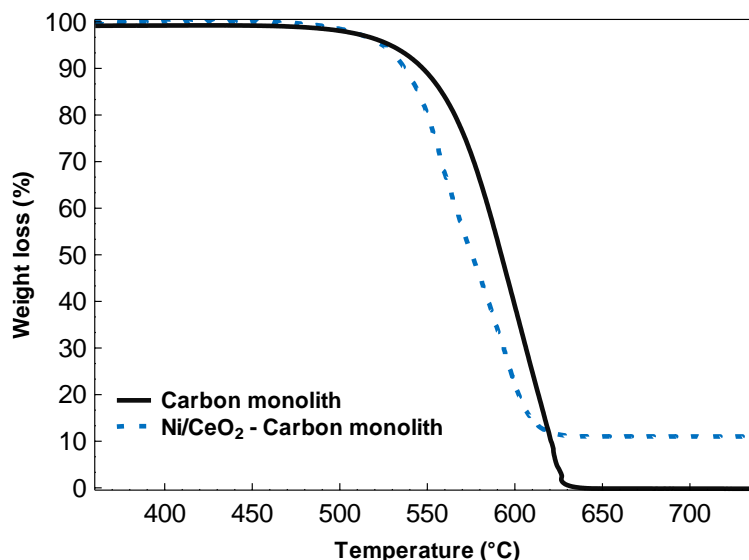
Figure 6.8. Thermogravimetric analysis in air of carbon monolith (T) and Ni/CeO₂-loaded carbon monolith (T).
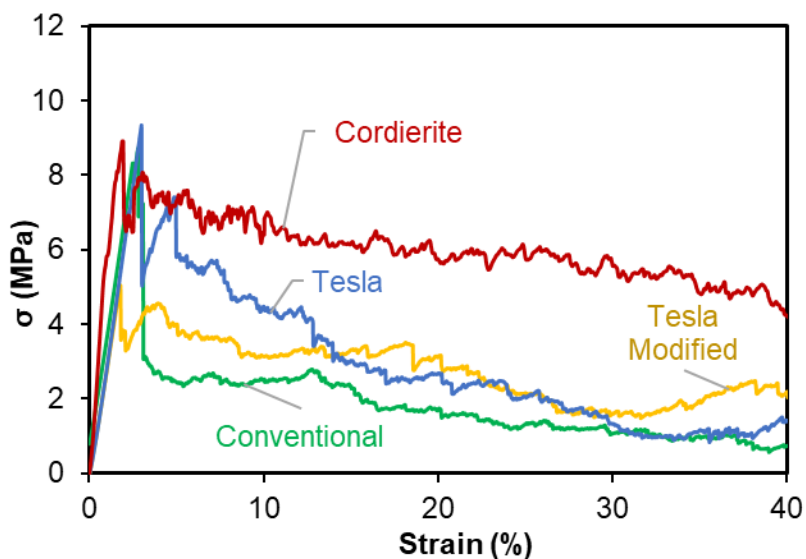
Figure 6.9. Comparison of the stress-strain curves obtained from carbon monoliths with tesla design (T), the modified tesla design (Tm), conventional design (C), and a reference commercial cordierite monolith of conventional honeycomb design.

The mechanical properties of the monoliths were also studied by means of compression tests and compared with a commercial cordierite honeycomb monolith. From the stress-strain curves (***Figure 6.9***), it is observed that the design does not highly affect the mechanical properties of the carbon monolith. At the beginning of the

compression test, a linear relationship between strength and deformation indicates an elastic deformation. Once achieved the maximum stress resistance (σ_{max}), stress reduction is not as pronounced as occur in polymeric materials, indicating that the damage in both ceramic and carbon monoliths results from the gradual crushing of layers at the extremities. Note that the Tesla-valve type carbon monolith shows similar mechanical properties than the cordierite one, being the yield points 9.34 and 9.0 MPa (**Table 6.2**), respectively. Therefore, carbon monoliths are stronger enough to be used as monolithic supports in industrial applications where cordierite monoliths are usually used.

Table 6.2. Maximum compressive stress (σ_{max}) and Young's modulus (E) of the monoliths.

Sample	$\sigma_{máx}$ MPa	E Pa
T	9.34	3.20
Tm	*5.04*	*2.93*
C	9.15	3.10
Cordierite	*9.0*	*1.90*

6.3.3. Catalytic results

The catalytic performance of the Ni/CeO$_2$-impregnated carbon monoliths was studied in the methanation of CO$_2$. To allow the comparison of the catalytic performance of carbon monoliths with different channel designs, a similar Ni/CeO$_2$ load was supported on all carbon monoliths (800 ± 5 mg). The variation of the CO$_2$ conversion and CH$_4$ selectivity with temperature for carbon monoliths prepared with different channels architectures is plotted in **Figure 6.10** for flow rates of 100 (continuous lines) and 500 mL min^{-1} (dashed lines). In all cases, as expected for Ni/CeO$_2$ active phase, the CH$_4$ selectivity is always higher than 80 % (**Figure 6.10b**). However, note that the channel architecture influences the catalytic activity of the active phase (**Figure 6.10a**). The turbulence created by the Tesla-valve type channel configurations (T and Tm) enhances the reactants-active phase contact regarding the

straight channeled design (C) improving mass and heat transfer within the catalyst and so, the catalytic performance.
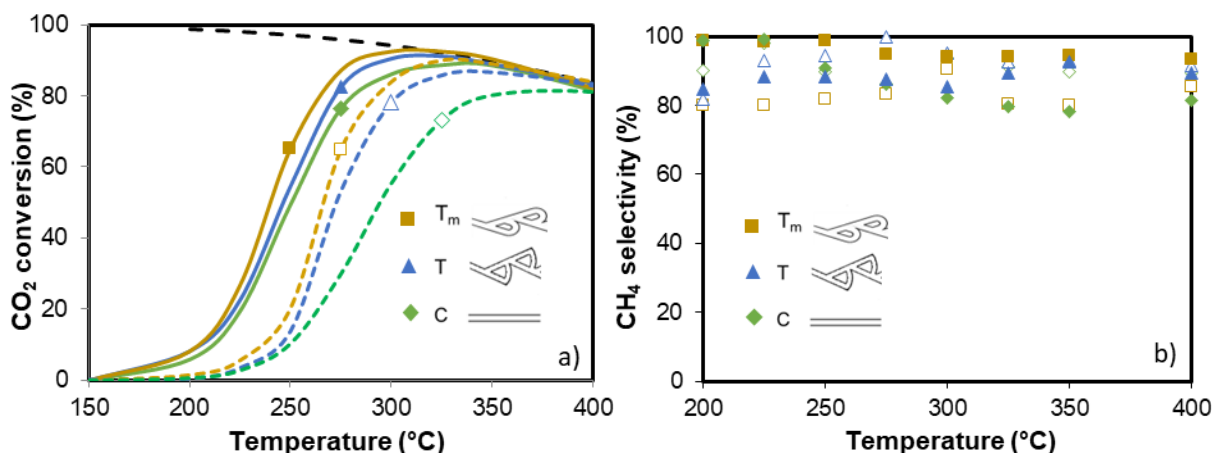
Figure 6.10. a) Conversion of CO_2 and b) selectivity to CH_4 of the Ni/CeO_2 active phase supported on carbon monoliths prepared with different channel architecture. Gas flow of 100 mL min^{-1} (continuous line) and 500 mL min^{-1} (dashed line).

Tesla-valve structure has exceptional one-directional flow characteristics, either in forward or reverse flow direction, which selection under the same inlet pressure may affect the performance of the valve [66,67]. Several studies have shown that, due to its complex design, the reverse flow direction, or blocking direction, in the Tesla-valve causes the fluid to follow highly chaotic trajectories, prompted by the flow direction swerving [68]. This chaotic flow favors turbulence, leading to improved mixing, a higher interaction between the fluid and the structure, as well as an enhanced mass and heat transfer [67-69]. Furthermore, as the fluid bifurcates and later converges, the flow impingement at Tesla-valve junctions results in increased velocity and a certain amount of pressure drop [61–63]. However, local increases in pressure may also occur due to the obstruction and convergence of flows. In line with Le Châtelier's principle [73-75], and considering the characteristics of Sabatier reaction, these pressure points may boost the CH_4 production. The change of the Tesla-valve angle from right (T) to curved angle (Tm) also improves the catalytic performance due to a better fluid dynamic of

gases in Tm which allows a better mass and heat transfer as will be analyzed in the next section.
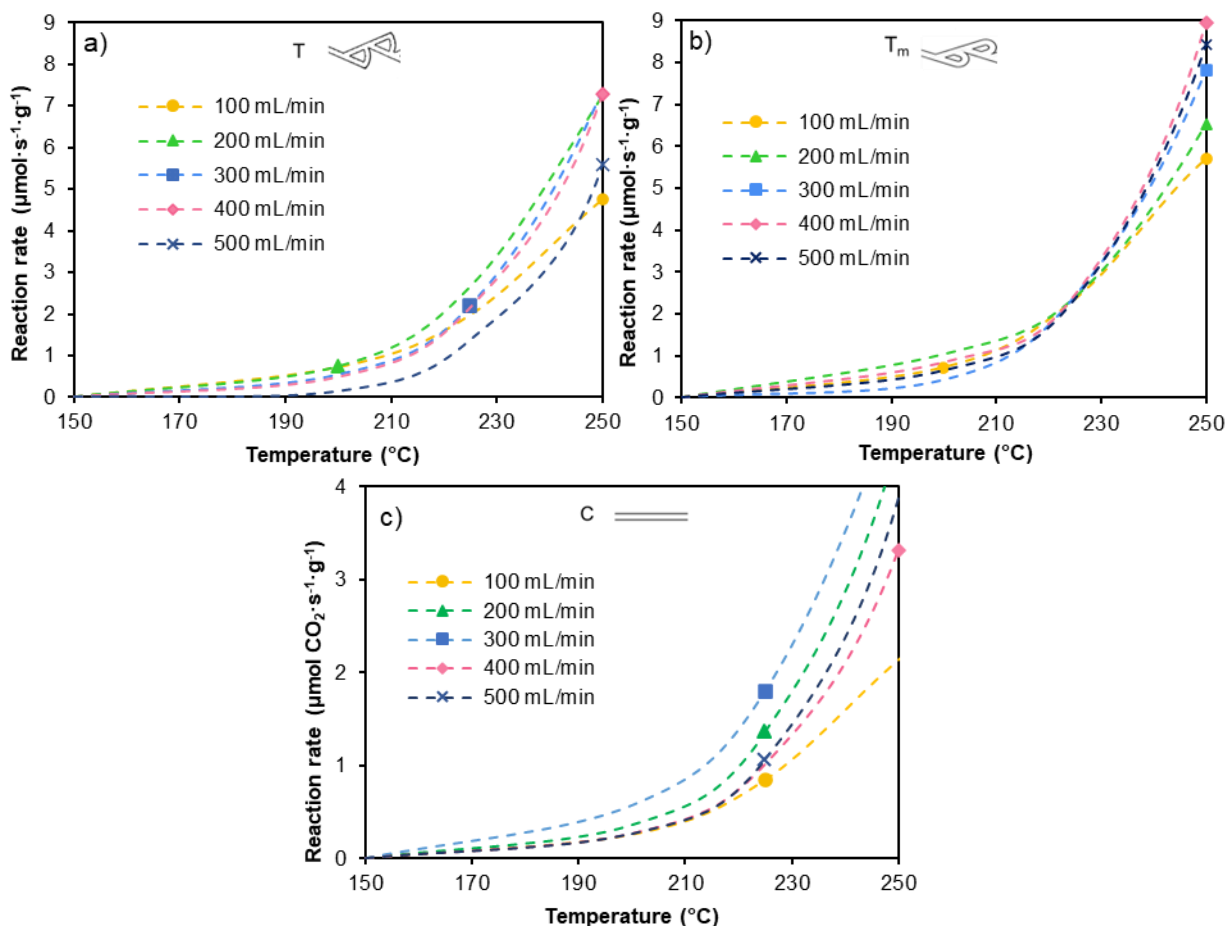
Figure 6.11. Reaction rate normalized by weight of Ni/CeO$_2$ supported on carbon monolithic catalysts: a) Tesla design; b) modified Tesla design and c) conventional design.

It is important to highlight that this catalytic activity enhancement is more severe at high gas flow. This fact could be ascribed to the gas flow through both the carbon matrix and the channels which is affected by the gas flow rate. As it was pointed out in the monolith characterization section, the carbon matrix is composed by highly opened macroporosity (several ten of micras) where the active phase is also deposited. Thus, the gas could flow through both this opened porosity and/or the channels. However, the pathway followed by the gases depends on the flow rate. At low flow rates, gas

easily traverses both the channels and the broad porosity of the carbon skeleton in all monoliths, mitigating the impact of channel design in the catalytic activity. However, with an increase in flow rate a predominant portion of the gas is compelled to flow through the channels, resulting in a more severe impact of the channel architecture.

In order to analyze in more detail the effect of mass flow on the reaction rate, catalytic tests at different flow rates were performed and the reaction rate normalized by weight of Ni/CeO$_2$ is plotted in **Figure 6.11** for the three studied designs. A heterogeneous catalytic reaction can work under two regimens: diffusional control in which the reaction rate is controlled by the diffusion of reagents and products between the fluid bulk and the catalyst surface, or under chemical control in which the reaction rate is controlled by the kinetics of the chemical reaction. Under diffusional control, high volumetric flows augment the swift delivery of reactants and simultaneous removal of products thereby favoring the chemical reaction rate, so it relies on gas flow and, consequently, on the design of the monolith. On the other hand, in the chemical control of the reaction rate, the effectiveness of the catalyst's active phase is pivotal. **Figure 6.11c** shows that the reaction rate in C monolith increases by increasing the flow from 100 to 300 mL min^{-1}, indicating that the monolith with conventional straight channel design consistently operates under diffusional control. Note that at flows higher than 300 mL min^{-1}, the reaction rate declines with further increases in flow. This decline is attributed, as mentioned earlier, to the forced flow through straight channels, resulting in the loss of accessible active phase for catalytic reactions. In contrast, in monoliths with Tesla-valve type design (T and Tm), the reaction rate is not highly affected by the flow rate, denoting that they work under chemical control, at least up to 240 °C. It is important to highlight that again the modified Tesla-valve design (Tm) presents a better performance than that of the Tesla-valve (T). The Tm monolith works under chemical control at all the flows tested and the reaction rate is almost 30 % higher than for the T monolith. This suggests that the presence of the tortuous Tesla-valve channels, mainly in Tm monolith, enhances the availability of active sites for

facilitating chemical reactions. This effect is supported by the streamlines of fluid computed by numerical simulations in the following section.

However, the Tesla-valve channel architecture has a special configuration so that the fluid flows in different way in one direction or the other of the monolith (***Figure 6.12***). In the blocked direction (***Figure 6.12a***), part of the fluid seems "to rotate" (red) and interferes with the forward flow (black) in each stage. However, this does not occur in the opposite direction (***Figure 6.12b***) where the gas flows unobstructed. Thus, in the blocked direction local increases in pressure may arise due to the obstruction and convergence of flows, whereas it does not happen in the opposite direction. To analyze the benefits of the creation of these multistage auto-pressurized local microreactors on the catalytic performance, the Tm and T monoliths were tested in both directions at a flow of 500 mL min^{-1} to enhance a preferential flow through the channel rather than through the carbon matrix. The CO_2 conversion and the reaction rate are included in ***Figure 6.13***.
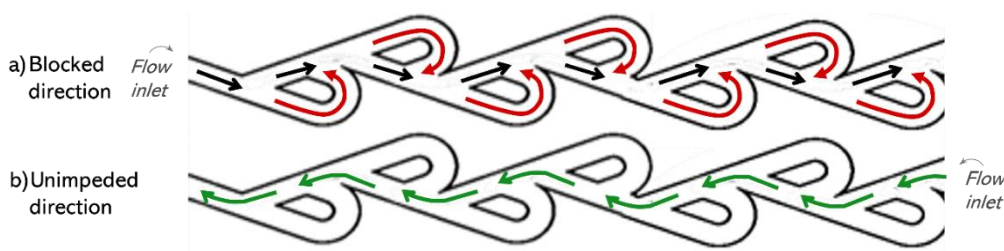
Figure 6.12. Principle of operation of a Tesla valve. a) blocked direction and b) unimpeded direction.

In both Tesla-valve monoliths, the catalytic performance is enhanced in the blocked direction due to the fluid back-mixing and the local multistage auto-pressurized microreactors created by this mixing which, according to Le Chatelier's principle, shifts the equilibrium to the CH_4 production. Note also, that the catalytic performance (CO_2 conversion and reaction rate) is, as commented above, improved in the Tm monolith regarding the T one due to the modification of the fluid dynamic caused by the change of the Tesla-valve angle. But this improvement, as expected, is observed in the blocked direction but not in the unimpeded direction. In the latter, the gas does not pass through

226

the Tesla bifurcation so, the flow path is the same in both Tesla monoliths showing a similar catalytic performance. Therefore, the improvement of curved angle is only observed in the blocked direction, where the flow bifurcates and converges through the Tesla-valve stages.
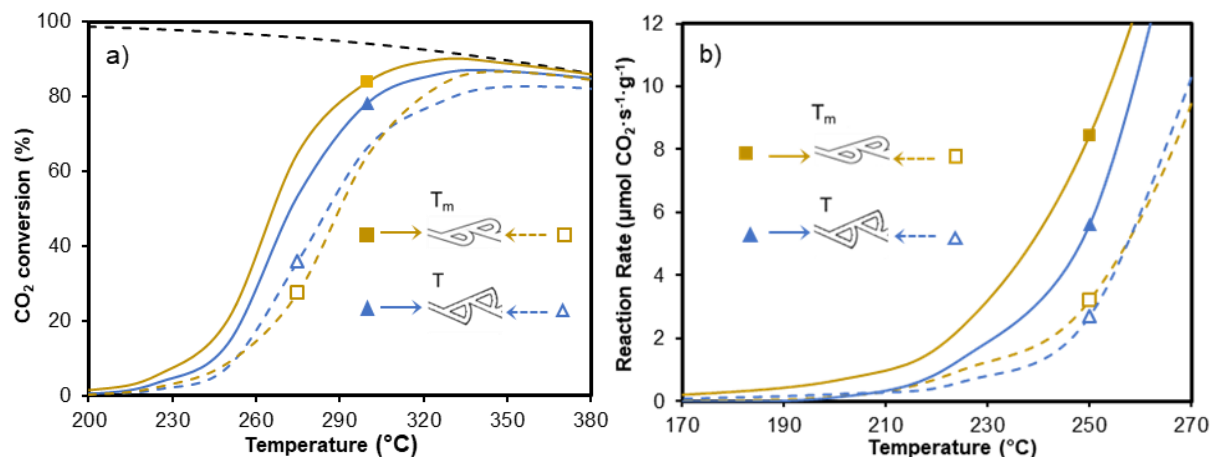
Figure 6.13. Comparison of catalytic performance of Tesla (T) and modified Tesla (Tm) design monoliths in the blocked direction (continuous line) and unimpeded direction (dashed line). a) CO_2 conversion and b) reaction rate normalized by weight of Ni/CeO_2 supported. Inlet volumetric flow of 500 mL min^{-1}.

6.3.4. Fluid dynamics study

The mathematical model presented in Section 5.2.4 was numerically solved to compute the gas velocity and pressure inside the channels of the Tesla monoliths. With this objective, the software Comsol Multiphysics was used, which is based on the finite element method to convert the system of partial differential equations in a set of unknown primary variables in multiple subdomains discretizing the channels of the Tesla monoliths. Due to the repeatability of the channels that make up the Tesla monoliths, it is enough to solve the governing equations in a unique channel, by using the appropriate volumetric gas flow for just one channel. **Figure 6.14** presents the CAD design of the Tesla monoliths in the environment of the software Comsol Multiphysics.
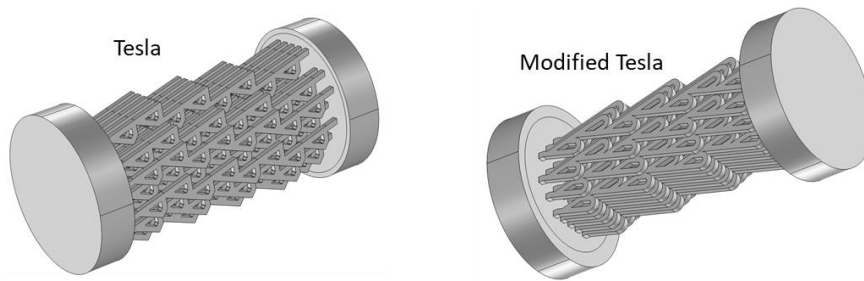
Figure 6.14. CAD design of the Tesla and modified Tesla monoliths in the Comsol Multiphysics environment.
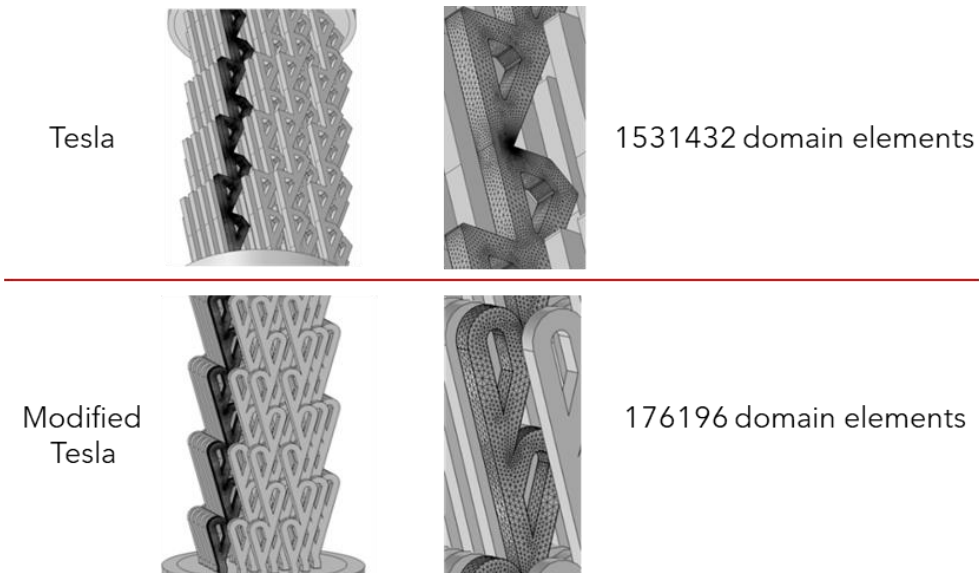
Figure 6.15. Discretization of the Tesla monoliths into multiple tetrahedra and pyramids as grid mesh subdomains.

Once the geometry is available in Comsol, it is discretized into multiple subdomains (tetrahedra and pyramids) composing the grid mesh where primary unknowns (pressure, velocity in each direction, kinetic energy, and the rate of dissipation of kinetic energy) are computed by using iterative numerical methods. Comsol Multiphysics includes powerful algorithms to develop the grid mesh and solve the primary unknowns, and, in this study, the default configuration of such algorithms has been employed. Observe in *Figure 6.15* how sharp corners induce the generation of thousands of subdomains, increasing noticeably the number of subdomain elements for the case of the Tesla monolith, while for the modified Tesla monolith the existence

of round lobes needs much fewer subdomains. Despite such differences, care was taken that the computed pressure and velocity do not depend on the number of domain elements.

Figures 6.16 and *6.17* present the gas fluid velocity for the Tesla and modified Tesla monoliths, correspondingly. There are appreciable differences in the magnitude and preferential directions of the reactive gaseous mixture flowing through the catalytic monoliths. On the one hand, the modified Tesla design yields a major contrast between the velocity reached by the fluid in the central channel in comparison with the fluid velocity in the adjacent lobes (look at the contrast of the color legends). In simple words, it seems the appearance of "stagnant fluid" in the lobes surrounding the main flow channel. This effect is not observed in the Tesla monolith, where the angle of the entrance to the lobes yields a "more uniform" spatial distribution of the gas velocity through the entire monolith, of course, in comparison with the modified Tesla. This phenomenon, undoubtedly, affects the rate of providing reactants and removing products from the lobes surrounding the central channel of the monolith.
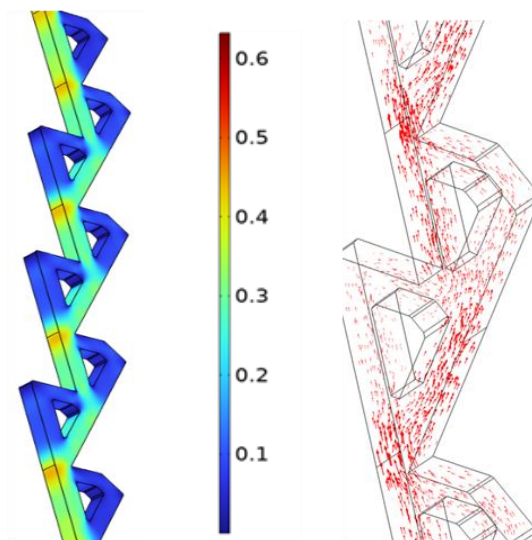
Figure 6.16. Magnitude of the fluid velocity (m s^{-1}) inside a channel of the Tesla monolith (left image) and the fluid direction (right image). Gas flow rate= 500 mL min^{-1}.
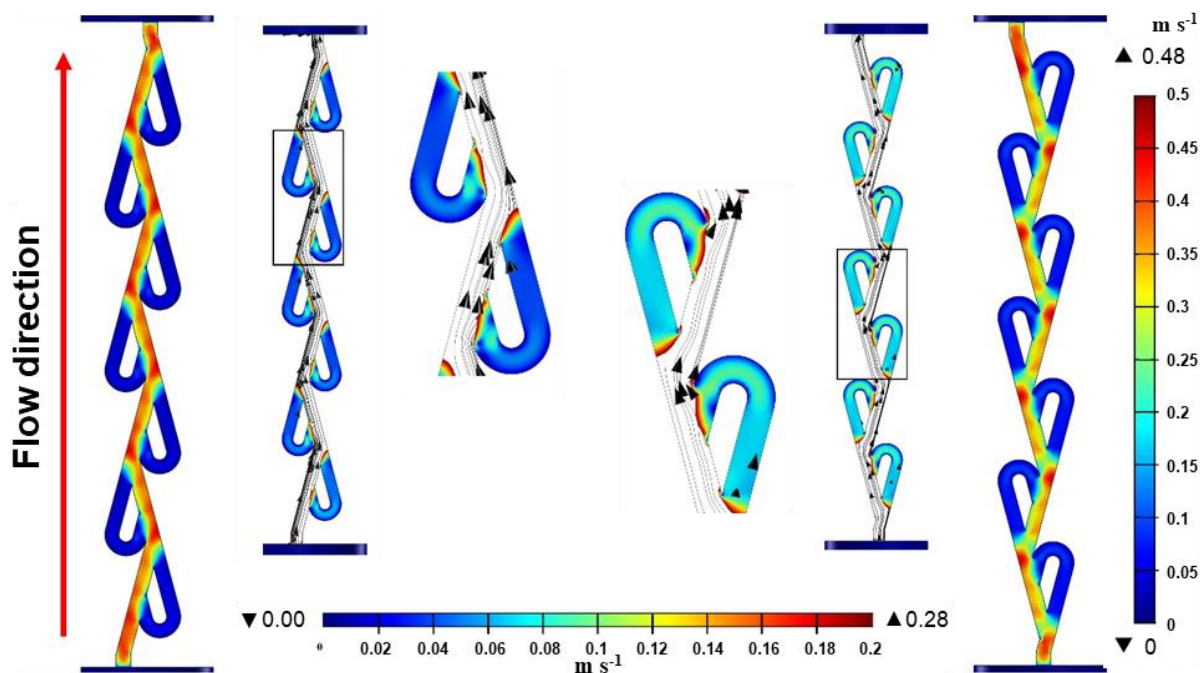
Figure 6.17. The magnitude of the fluid velocity inside one channel of the modified Tesla monolith. The black arrows show the main flow paths of the gaseous mixture. Gas flow rate = 500 mL min^{-1}.

The flow patterns were investigated in both monolith designs by varying the flow direction and volumetric flow rate. In **Figure 6.18** there are plotted streamlines corresponding to the Tesla monolith, while the analogous graphics for the modified Tesla monolith are presented in **Figure 6.19**. There are notorious differences appreciated in the flow patterns between both Tesla monoliths. The quantity of stagnant fluid is larger when the blocking phenomenon takes place, according to the explanation of **Figure 6.12**, and this phenomenon is more significant in the modified Tesla (note the quantities and length of the velocity vectors, arrows, between the central region and those in the surrounding lobes). Such a feature is not notoriously observed in the case of the Tesla monolith. The case of the monolith with angled lobes provides conditions for a major entrance of fluid with larger velocity and, furthermore, decreases slightly the fluid pressure. As observed further, this variation of pressure explains why the modified Tesla operating under blocking flow configuration yields better reaction conditions for CO_2 consumption.
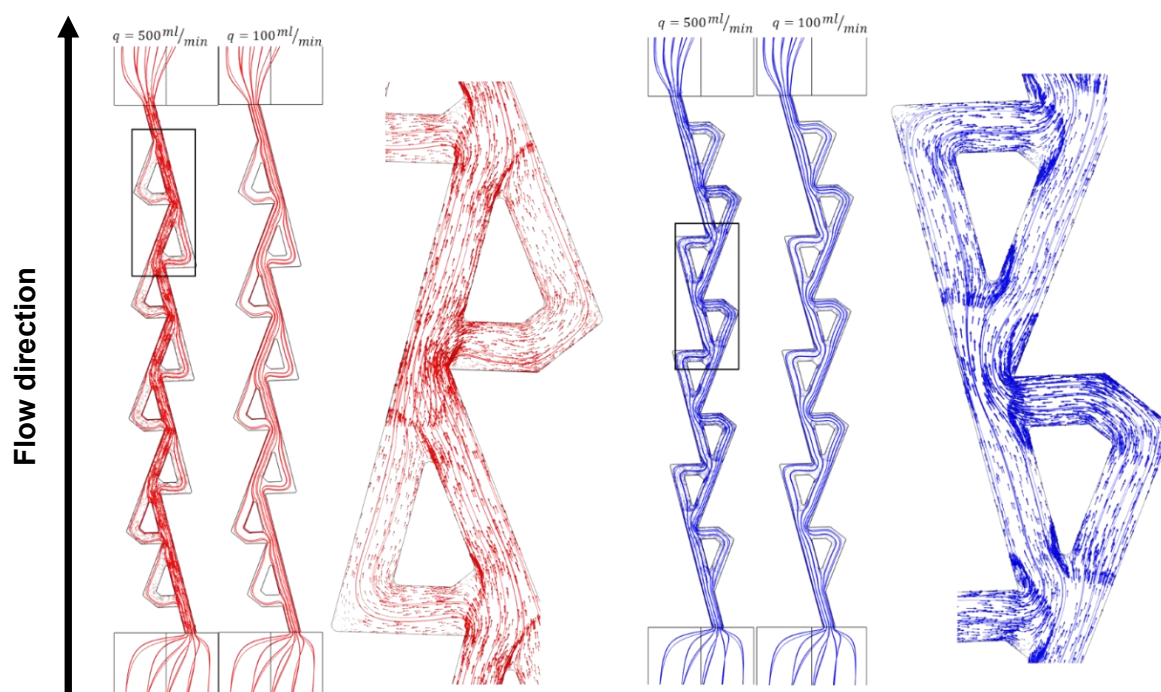
Figure 6.18. Streamlines of the reactive gaseous mixture inside one channel of the Tesla monolith, varying the gas flow rate and flow direction.

In **_Figure 6.19_** those zones where the gas performs back-mixing just when the fluid is incorporated from the lateral lobe into the central channel have been identified in green circles. Besides, observe how the back-mixing conditions are more notorious in the modified Tesla in comparison with the Tesla monolith. Eventually, as demonstrated by the experimental chemical reaction results, the existence of retro-mixing favors positively the CO_2 conversion.

Another variable that may be influencing the rate of chemical reactions is the concentration of solutes. Owing to working in gaseous state, the molar concentrations of all the chemical components depend on the local pressure and temperature. A "practically linear" variation of the fluid pressure along the monolith as observed in the results plotted in **_Figure 6.20_**. However, a thorough inspection allows us to observe slightly major pressures in the lobes of the monolith corresponding to the blocked direction configuration (see **_Figure 6.12_**), this will lead to larger solute concentrations with further improvement in the chemical reaction rates.
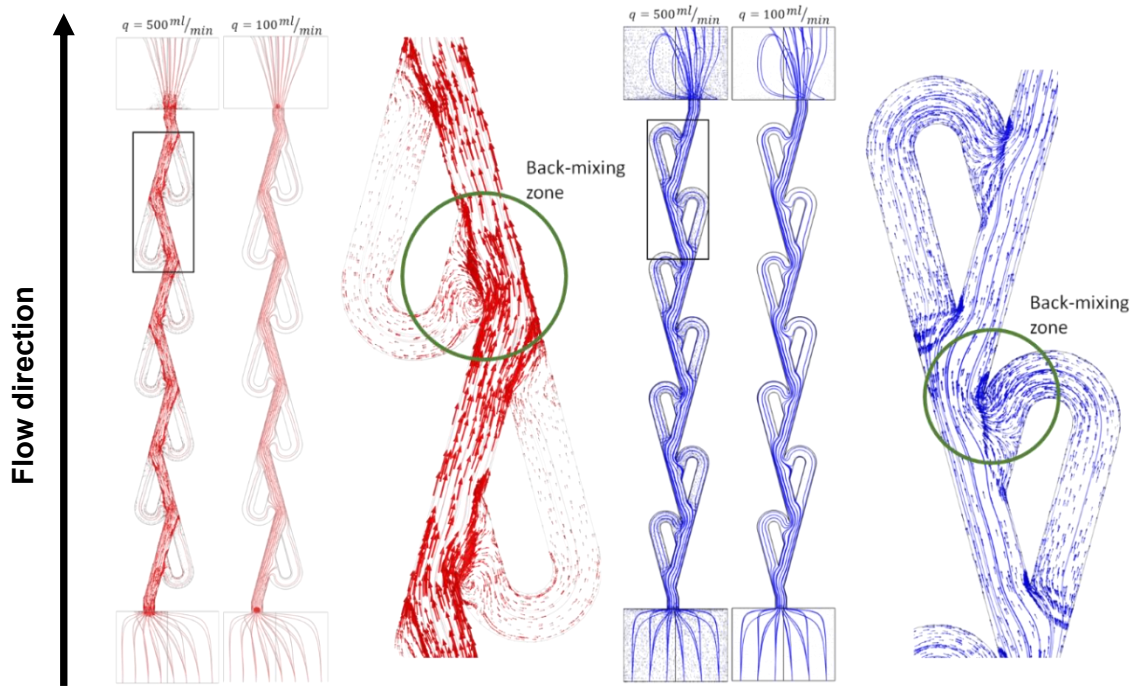
Figure 6.19. Streamlines of the reactive gaseous mixture inside one channel of the modified Tesla monolith, varying the gas flow rate and flow direction. The green circles identify the back mixing zones as depicted by arrows getting back.
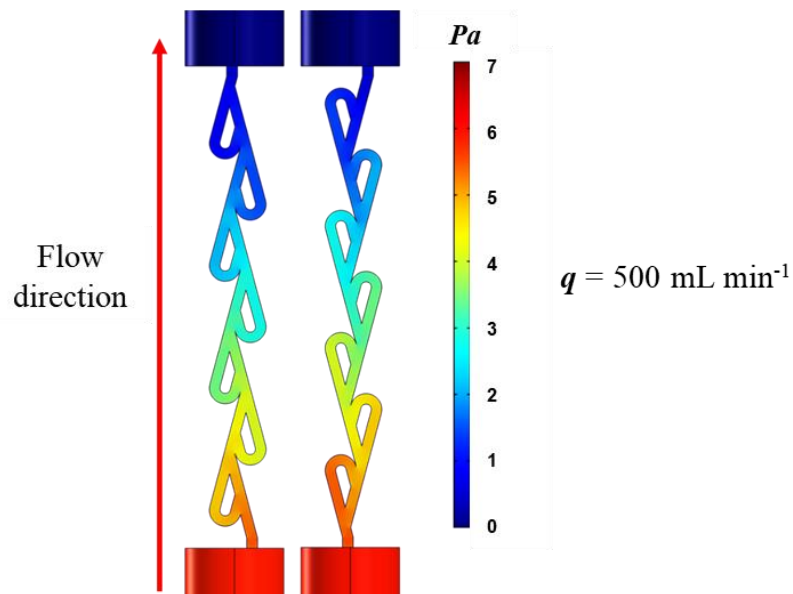
Figure 6.20. Fluid pressure profile inside the modified Tesla monolith. Here the pressure subtracted by the atmospheric pressure (gauge pressure).
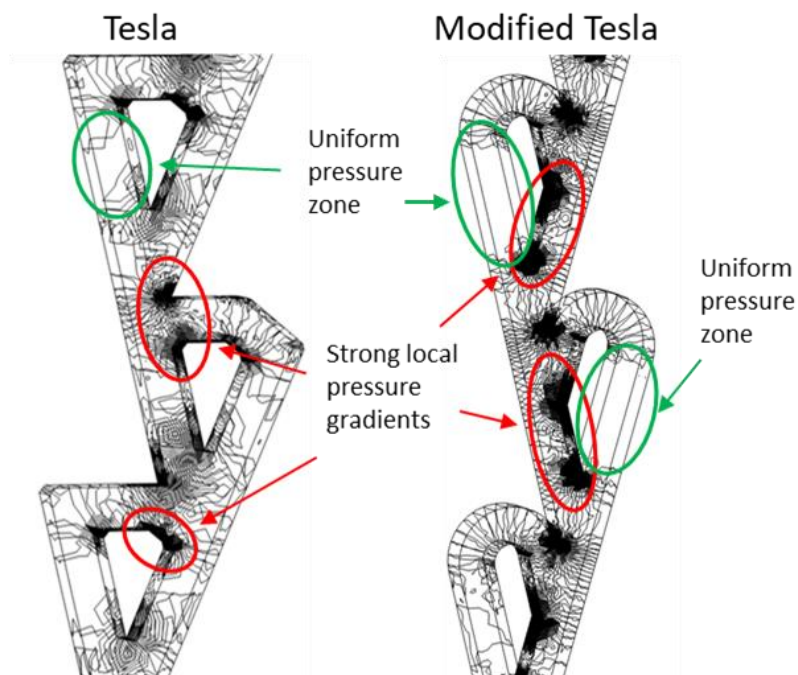
Figure 6.21. Level curves of the fluid pressure inside the Tesla monoliths.

Finally, the level curves of pressure for each monolith have been also plotted, as one alternative to highlight the local variations of the fluid pressure (***Figure 6.21*).** In this type of graphic, isolated concentrated level curves indicate the existence of strong pressure gradients in one small region. In this sense, strong local pressure gradients are observed more clearly in the modified Tesla monolith. Such pressure behavior agrees well with the generation of a "more uniform" fluid velocity in the surrounding lobes (see the green ellipses in ***Figure 6.21***). In turn, the existence of uniform pressure zones favors higher concentrations of solutes.

6.4. Conclusions

The combination of the sol-gel polymerization and 3D printing technology allows to obtain monolithic catalysts with specifically controlled channels designs which has opened the gate to obtain advanced functional materials for many industrial applications. A new concept is developed in this chapter, auto-pressurized multi-stage Tesla-valve type monolithic microreactors where not only the fluid dynamics and thus, the active phase-reactants contact is perfectly controlled and optimized but also local

reaction conditions such as pressure is controlled to enhance the reaction kinetic. For that, carbon monoliths featuring Tesla-like channel shapes (referred to as T and Tm) were created using a combination of 3D printing and the sol-gel process and compared with a conventional honeycomb monolith. These monoliths were further utilized as supports for Ni/CeO$_2$ catalysts in the methanation of CO$_2$, a significant method for both CO$_2$ utilization and environmental remediation. Furthermore, a mathematical model incorporating momentum balance was developed to analyze velocity profiles and pressure drops in the monolithic structures. Experimental data and mathematical simulations confirmed the enhanced performance achieved with the complex design compared to conventional one. The irregular flow patterns induced by changes in flow direction, along with local pressure increases resulting from flow convergence, potentially enhance the Sabatier reaction in accordance with Le Châtelier's principle.

Unlike straight channels, the T and Tm designs exhibited consistent performance regardless of flow rate and demonstrated chemical control, particularly up to temperatures of 240 °C. Additionally, the Tm configuration, featuring curved angles, improved mass transfer, leading to higher conversion rates and approximately a 30 % increase in reaction rate compared to the T configuration.

In conclusion, this auto-pressurized multi-stage Tesla-valve monolith opens up possibilities for designing specific and advanced functional materials for various chemical reactions. It not only maximizes contact between reactants and active phases but also enables control over reaction conditions to optimize reaction kinetics.

6.5. References

[1]   Modak, A., Bhanja, P., Dutta, S., Chowdhury, B., & Bhaumik, A. (2020). Catalytic reduction of CO2 into fuels and fine chemicals. *Green Chemistry, 22*(14), 4002–4033. https://doi.org/10.1039/D0GC01092H.

[2]   Wang, Y., Jeong, S., Hang, Y., & Wang, Q. (2023). Determinants of net energy-related CO2 emissions in China: A source-to-sink decomposition analysis.

Environmental Impact Assessment Review, 98, 106979. https://doi.org/10.1016/j.eiar.2022.106979.

[3] Zambrano-Monserrate, M. A. (2023). Clean energy production index and CO2 emissions in OECD countries. *Science of the Total Environment, 907*(10), 167852. https://doi.org/10.1016/j.scitotenv.2023.167852.

[4] Bacariza, M. C., Spataru, D., Karam, L., Lopes, J. M., & Henriques, C. (n.d.). Promising catalytic systems for CO2 hydrogenation into CH4: A review of recent studies. *Processes, 8*(12), 1646. https://doi.org/10.3390/pr8121646.

[5] Biswas, S., Kundu, C., Ng, W. L., Samudrala, S. P., Jarvis, T., Giddey, S., & Bhattacharya, S. (2023). CO2 valorisation to methane on highly stable iron impregnated ceria-zirconia based 3D-printed catalyst. *Journal of CO2 Utilization, 72*, 102501. https://doi.org/10.1016/j.jcou.2023.102501.

[6] Huang, W., Dai, J., & Xiong, L. (2022). Towards a sustainable energy future: Factors affecting solar-hydrogen energy production in China. *Sustain. Energy Technol. Assessments, 52*, 102059. https://doi.org/10.1016/j.seta.2022.102059.

[7] Uchida, H., & Harada, M.R. (2019). Application of Hydrogen by Use of Chemical Reactions of Hydrogen and Carbon Dioxide. In de Miranda, P.E.V. (Ed.), *Science and Engineering of Hydrogen-Based Energy Technologies: Hydrogen Production and Practical Applications in Energy Generation* (pp. 279–289). Academic Press. https://doi.org/10.1016/B978-0-12-814251-6.00013-7.

[8] Steinberger-Wilckens, R., & Sampson, B. (2019). Market, Commercialization, and Deployment—Toward Appreciating Total Owner Cost of Hydrogen Energy Technologies. In de Miranda, P.E.V. (Ed.), *Science and Engineering of Hydrogen-Based Energy Technologies: Hydrogen Production and Practical Applications in Energy Generation* (pp. 383–403). Academic Press. https://doi.org/10.1016/B978-0-12-814251-6.00008-3.

[9] Styring, P., McCord, S., & Rackley, S. (2023). Carbon dioxide utilization. In Racley, S., Andrews, G., Clery, D., et al. (Eds.) *Negative Emissions Technologies*

for Climate Change Mitigation, (pp. 391–413). Elsevier. https://doi.org/10.1016/B978-0-12-819663-2.00005-8.

[10] Gba Yarbas, T., & Ayas, N. (2023). A detailed thermodynamic analysis of CO2 hydrogenation to produce methane at low pressure. *Int. J. Hydrogen Energy, 49*, 1134-1144. https://doi.org/10.1016/j.ijhydene.2023.06.223.

[11] Di, L., Fu, Z., Dong, M., Zhu, A., Xia, G., & Zhang, X. (2023). Cold plasma-prepared Ru-based catalysts for boosting plasma-catalytic CO2 methanation. *Chem. Eng. Sci., 280*, 119056. https://doi.org/10.1016/j.ces.2023.119056.

[12] Gómez, L., Martínez, I., Navarro, V., & Murillo, R. (2023). Selection and optimisation of a zeolite/catalyst mixture for sorption-enhanced CO2 methanation (SEM) process. *Journal of CO2 Utilization, 77*, 102611. https://doi.org/10.1016/j.jcou.2023.102611.

[13] Xie, Y., Wen, J., Li, Z., Chen, J., Zhang, Q., Ning, P., Chen, Y., & Hao, J. (2023). Progress in reaction mechanisms and catalyst development of ceria-based catalysts for low-temperature CO2 methanation. *Green Chemistry, 25*, 130-152. https://doi.org/10.1039/d2gc03512j.

[14] Amez, I., Gonzalez, S., Sanchez-Martin, L., Ortega, M. F., & Llamas, B. (2021). Underground methanation, a natural way to transform carbon dioxide into methane. In *Climate Change Science: Causes, Effects and Solutions for Global Warming* (pp. 81–106). https://doi.org/10.1016/B978-0-12-823767-0.00005-7.

[15] Lin, S., Tang, R., Liu, X., Gong, L., & Li, Z. (2024). Modulating CO2 methanation activity on Ni/CeO2 catalysts by tuning ceria facet-induced metal-support interaction. International *Journal of Hydrogen Energy, 51*(4), 360–3199. https://doi.org/10.1016/j.ijhydene.2023.10.095.

[16] Li, Z., Zhao, T., Zhang, L., (2018). Promotion effect of additive Fe on Al2O3 supported Ni catalyst for CO2 methanation. *Applied Organometallic Chemistry, 32*, e4328. https://doi.org/10.1002/aoc.4328.

[17] Tsiotsias, A. I., Charisiou, N. D., Italiano, C., Ferrante, G. D., Pino, L., Vita, A., Sebastian, V., Hinder, S. J., Baker, M. A., Sharan, A., Singh, N., Polychronopoulou, K., & Goula, M. A. (2024). Ni-noble metal bimetallic catalysts for improved low temperature CO2 methanation. *Applied Surface Science, 646*, 158945. https://doi.org/10.1016/J.APSUSC.2023.158945.

[18] Mihet, M., & Lazar, M. D. (2018). Methanation of CO2 on Ni/γ-Al2O3: Influence of Pt, Pd or Rh promotion. *Catalysis Today, 306*, 294–299. https://doi.org/10.1016/J.CATTOD.2016.12.001.

[19] Chein, C. R. Y., & Wang, C.-C. (2020). Experimental Study on CO2 Methanation over Ni/Al2O3, Ru/Al2O3, and Ru-Ni/Al2O3 Catalysts. *Catalysts, 10*(10) 1112. https://doi.org/10.3390/catal10101112.

[20] Quindimil, A., De-La-Torre, U., Pereda-Ayo, B., Davó-Quiñonero, A., Bailón-García, E., Lozano-Castelló, D., González-Marcos, J. A., Bueno-López, A., & González-Velasco, J. R. (2020). Effect of metal loading on the CO2 methanation: A comparison between alumina supported Ni and Ru catalysts. *Catalysis Today, 356*, 419–432. https://doi.org/10.1016/J.CATTOD.2019.06.027.

[21] Alves, L. M. N. C., Almeida, M. P., Ayala, M., Watson, C. D., Jacobs, G., Rabelo-Neto, R. C., & Noronha, F. B. (2021). CO2 methanation over metal catalysts supported on ZrO2: Effect of the nature of the metallic phase on catalytic performance. *Chemical Engineering Science, 239*, 116604. https://doi.org/10.1016/J.CES.2021.116604.

[22] Quindimil, A., Bacariza, M. C., González-Marcos, J. A., Henriques, C., & González-Velasco, J. R. (2021). Enhancing the CO2 methanation activity of γ-Al2O3 supported mono- and bi-metallic catalysts prepared by glycerol assisted impregnation. *Applied Catalysis B: Environmental, 296*, 120322. https://doi.org/10.1016/J.APCATB.2021.120322.

[23] Wei, Y., Ji, J., Liang, F., Ma, D., Du, Y., Pang, Z., Wang, H., Li, Q., Shi, G., & Wang, Z. (2023). Adjusting active sites and metal-support interactions of ceramic-loaded

Pd/P-CeO2-Al2O3 coating to optimize CO2 methanation pathways. *Journal of Environmental Chemical Engineering, 11*(3), 110773. https://doi.org/10.1016/J.JECE.2023.110773.

[24] Mendoza-Núñez, E. M., Fierro-Gonzalez, J. C., Zepeda, T. A., & Solis-Garcia, A. (2022). Effect of platinum addition on the reaction mechanism of the CO2 methanation catalyzed by ZrO2-supported Rh. *Molecular Catalysis, 533*, 112801. https://doi.org/10.1016/J.MCAT.2022.112801.

[25] Tamimi, K., Alavi, S. M., Rezaei, M., & Akbari, E. (2021). Preparation of the Mn-Promoted NiO–Al2O3 nanocatalysts for low temperature CO2 methanation. *J. Energy Inst., 99*(1), 48–58. https://doi.org/10.1016/J.JOEI.2021.08.008.

[26] Liao, Y., He, Y., Cui, X., Liu, L., & Liu, L. (2024). Elemental Fe conditioning for the synthesis of highly selective and stable high entropy catalysts for CO2 methanation. *Fuel, 355*, 129494. https://doi.org/10.1016/J.FUEL.2023.129494.

[27] Zhang, T., Zheng, P., Gu, F., Xu, W., Chen, W., Zhu, T., Han, Y. F., Xu, G., & Zhong, Z., & Su, F. (2023). The dual-active-site tandem catalyst containing Ru single atoms and Ni nanoparticles boosts CO2 methanation. *Applied Catalysis B: Environmental, 323*, 122190. https://doi.org/10.1016/J.APCATB.2022.122190.

[28] Lee, W. J., Li, C., Prajitno, H., Yoo, J., Patel, J., Yang, Y., Lim, S. (2021). Recent trend in thermal catalytic low temperature CO2 methanation: A critical review. *Catalysis Today, 368*, 2–19. https://doi.org/10.1016/J.CATTOD.2020.02.017.

[29] Varvoutis, G., Lampropoulos, A., Oikonomou, P., Andreouli, C. D., Stathopoulos, V., Lykaki, M., Marnellos, G. E., & Konsolakis, M. (2023). Fabrication of highly active and stable Ni/CeO2-nanorods wash-coated on ceramic NZP structured catalysts for scaled-up CO2 methanation. *Journal of CO2 Utilization, 70*, 102425. https://doi.org/10.1016/J.JCOU.2023.102425.

[30] Song, M., Shi, L., Xu, X., Du, X., Chen, Y., Zhuang, W., Tao, X., Sun, L., & Xu, Y. (2022). Ni/M/SiO2 catalyst (M=La, Ce or Mg) for CO2 methanation: Importance

of the Ni active sites. *Journal of CO2 Utilization, 64*, 102150. https://doi.org/10.1016/J.JCOU.2022.102150.

[31] Safdar, M., González-Castaño, M., Penkova, A., Centeno, M. A., Odriozola, J. A., & Arellano-García, H. (2022). CO2 methanation on Ni/YMn1-xAlxO3 perovskite catalysts. *Applied Materials Today, 29*, 101577.

https://doi.org/10.1016/J.APMT.2022.101577.

[32] Gao, J., Liu, Q., Gu, F., Liu, B., Zhong, Z., & Su, F. (2015). Recent advances in methanation catalysts for the production of synthetic natural gas. *RSC Advances, 5*, 22759–22776. https://doi.org/10.1039/C4RA16114A.

[33] Nguyen, H. T. T., Kumabe, Y., Ueda, S., Kan, K., Ohtani, M., & Kobiro, K. (2019). Highly durable Ru catalysts supported on CeO2 nanocomposites for CO2 methanation. *Applied Catalysis A: General, 577*, 35–43. https://doi.org/10.1016/J.APCATA.2019.03.011.

[34] Zhang, T., Wang, W., Gu, F., Xu, W., Zhang, J., Li, Z., Zhu, T., Xu, G., Zhong, Z., & Su, F. (2022). Enhancing the low-temperature CO2 methanation over Ni/La-CeO2 catalyst: The effects of surface oxygen vacancy and basic site on the catalytic performance. *Applied Catalysis B: Environmental, 312*, 121385. https://doi.org/10.1016/J.APCATB.2022.121385.

[35] Hu, F., Jin, C., Wu, R., Li, C., Song, G., Gani, T. Z. H., Lim, K. H., Guo, W., Wang, T., Ding, S., Ye, R., Lu, Z. H., Feng, G., Zhang, R., & Kawi, S. (2023). Enhancement of hollow Ni/CeO2-Co3O4 for CO2 methanation: From CO2 adsorption and activation by synergistic effects. *Chemical Engineering Journal, 461*, 142108. https://doi.org/10.1016/J.CEJ.2023.142108.

[36] Seemann, M., & Thunman, H. (2019). Methane synthesis. In *Substitute Natural Gas from Waste: Technical Assessment and Industrial Applications of Biochemical and Thermochemical Processes* (pp. 221–243). https://doi.org/10.1016/B978-0-12-815554-7.00009-X.

[37] Chava, R., Bhaskar, A. V. D., Roy, B., & Appari, S. (2023). Reforming of model biogas using Ni/CeO2/γ-Al2O3 monolith catalyst. *Materials Today: Proceedings, 72*, 134–139. https://doi.org/10.1016/J.MATPR.2022.06.234.

[38] Chen, H. Y., Pihl, J., Toops, T. J., & Sinha Majumdar, S. (2023). Layer structured bifunctional monolith catalysts for energy-efficient conversion of CO2 to dimethyl ether. *Applied Catalysis A: General, 656*, 119140. https://doi.org/10.1016/J.APCATA.2023.119140.

[39] Majidian, N., & Soltanali, S. (2016). Comparison of Fischer-Tropsch Fixed and Monolith Bed Reactors Using Pseudo-homogeneous 2D Model. *Journal of the Japan Petroleum Institute, 59*(3), 126–139. https://doi.org/10.1627/JPI.59.126.

[40] Roy, S., Heibel, A. K., Liu, W., & Boger, T. (2004). Design of monolithic catalysts for multiphase reactions. *Chemical Engineering Science, 59*(5), 957–966. https://doi.org/10.1016/J.CES.2003.12.001.

[41] Danaci, S., Protasova, L., Lefevere, J., Bedel, L., Guilet, R., & Marty, P. (2016). Efficient CO2 methanation over Ni/Al2O3 coated structured catalysts. *Catalysis Today, 273*, 234–243. https://doi.org/10.1016/J.CATTOD.2016.04.019.

[42] Fukuhara, C., Hayakawa, K., Suzuki, Y., Kawasaki, W., & Watanabe, R. (2017). A novel nickel-based structured catalyst for CO2 methanation: A honeycomb-type Ni/CeO2 catalyst to transform greenhouse gas into useful resources. *Appl. Catal. A Gen., 532*, 12–18. https://doi.org/10.1016/J.APCATA.2016.11.036.

[43] Vita, A., Italiano, C., Pino, L., Frontera, P., Ferraro, M., & Antonucci, V. (2018). Activity and stability of powder and monolith-coated Ni/GDC catalysts for CO2 methanation. *Applied Catalysis B: Environmental, 226,* 384–395. https://doi.org/10.1016/J.APCATB.2017.12.078.

[44] Agueniou, F., Vidal, H., López, J. de D., Hernández-Garrido, J. C., Cauqui, M. A., Botana, F. J., Calvino, J. J., Galvita, V. V., & Gatica, J. M. (2021). 3D-printing of metallic honeycomb monoliths as a doorway to a new generation of catalytic

devices: The Ni-based catalysts in methane dry reforming showcase. *Catal. Commun., 148,* 106181. https://doi.org/10.1016/J.CATCOM.2020.106181.

[45] Huynh, H. L., Tucho, W. M., & Yu, Z. (2020). Structured NiFe catalysts derived from in-situ grown layered double hydroxides on ceramic monolith for CO2 methanation. *Green Energy & Environment, 5,* 423–432. https://doi.org/10.1016/J.GEE.2020.09.004.

[46] Groppi, G., Tronconi, E., & Forzatti, P. (1993). Modelling of catalytic combustors for gas turbine applications. *Catalysis Today, 17*(3), 237–249. https://doi.org/10.1016/0920-5861(93)80028-Y.

[47] Chaparro-Garnica, C. Y., Bailón-García, E., Davó-Quiñonero, A., Lozano-Castelló, D., & Bueno-López, A. (2022). Sponge-like carbon monoliths: Porosity control of 3D-printed carbon supports and its influence on the catalytic performance. *Chemical Engineering Journal, 432*, 134218. https://doi.org/10.1016/J.CEJ.2021.134218.

[48] Davó-Quiñonero, A., Sorolla-Rosario, D., Bailón-García, E., Lozano-Castelló, D., & Bueno-López, A. (2019). Improved asymmetrical honeycomb monolith catalyst prepared using a 3D printed template. *Journal of Hazardous Materials, 368*, 638–643. https://doi.org/10.1016/J.JHAZMAT.2019.01.092.

[49] González-Castaño, M., Baena-Moreno, F., Navarro de Miguel, J. C., Miah, K. U. M., Arroyo-Torralvo, F., Ossenbrink, R., Odriozola, J. A., Benzinger, W., Hensel, A., Wenka, A., & Arellano-García, H. (2022). 3D-printed structured catalysts for CO2 methanation reaction: Advancing of gyroid-based geometries. *Energy Conversion and Management, 258*, 115464. https://doi.org/10.1016/J.ENCONMAN.2022.115464.

[50] Chaparro-Garnica, C. Y., Bailón-García, E., Lozano-Castelló, D., & Bueno-López, A. (2021). Design and fabrication of integral carbon monoliths combining 3D printing and sol–gel polymerization: Effects of the channel morphology on the

CO-PROX reaction. *Catalysis Science & Technology, 11*, 6490–6497. https://doi.org/10.1039/D1CY01104A.

[51] Wei, Q., Li, H., Liu, G., He, Y., Wang, Y., Tan, Y. E., Wang, D., Peng, X., Yang, G., & Tsubaki, N. (2020). Metal 3D printing technology for functional integration of catalytic system. *Nature Communications, 11*, 4098. https://doi.org/10.1038/s41467-020-17941-8.

[52] Lefevere, J., Mullens, S., & Meynen, V. (2018). The impact of formulation and 3D-printing on the catalytic properties of ZSM-5 zeolite. *Chemical Engineering Journal, 349*, 260–268. https://doi.org/10.1016/J.CEJ.2018.05.058.

[53] Chaparro-Garnica, C. Y., Davó-Quiñonero, A., Bailón-García, E., Lozano-Castelló, D., & Bueno-López, A. (2019). Design of Monolithic Supports by 3D Printing for Its Application in the Preferential Oxidation of CO (CO-PrOx). *ACS Applied Materials & Interfaces, 11*(39), 36763–36773. https://doi.org/10.1021/acsami.9b12731.

[54] Cárdenas-Arenas, A., Soriano Cortés, H., Bailón-García, E., Davó-Quiñonero, A., Lozano-Castelló, D., & Bueno-López, A. (2021). Active, selective and stable NiO-CeO2 nanoparticles for CO2 methanation. *Fuel Processing Technology, 212*, 106637. https://doi.org/10.1016/j.fuproc.2020.106637.

[55] You, S., Xing, S., & Jiang, C. (2023). The influence of CeO2 particle with various sizes on the microstructure and properties of electrodeposited Ni-CeO2 composite coatings. *Materials Characterization, 205*, 113327. https://doi.org/10.1016/J.MATCHAR.2023.113327.

[56] Ma, J., Xu, N., Luo, Y., Liu, Q., & Pu, Y. (2023). Defect generation and morphology transformation mechanism of CeO2 particles prepared by molten salt method. *Ceram. Int., 49*, 4929–4943. https://doi.org/10.1016/J.CERAMINT.2022.10.007.

[57] Liu, K. Q., Wu, C. B., & Kang, W. Q. (2024). Preparation of CeO2-PVA composite film based on in-situ generation of nano CeO2 particles. *Optical Materials, 148*, 114840. https://doi.org/10.1016/J.OPTMAT.2024.114840.

[58] Lang, F., Sun, D., Liu, J., Wang, H., & Yan, H. (2016). Improved size-tunable synthesis of monodisperse NiO nanoparticles. *Materials Letters, 181*, 328–330. https://doi.org/10.1016/J.MATLET.2016.06.056.

[59] Serafin, J., & Llorca, J. (2023). Nanoshaped Cerium Oxide with Nickel as a Non-Noble Metal Catalyst for CO2 Thermochemical Reactions. *Molecules, 28*(7), 2926. https://doi.org/10.3390/molecules28072926.

[60] Loridant, S. (2021). Raman spectroscopy as a powerful tool to characterize ceria-based catalysts. *Catalysis Today, 373*, 98–111. https://doi.org/10.1016/J.CATTOD.2020.03.044.

[61] Kainbayev, N., Sriubas, M., Virbukas, D., Rutkuniene, Z., Bockute, K., Bolegenova, S., & Laukaitis, G. (2020). Raman Study of Nanocrystalline-Doped Ceria Oxide Thin Films. *Coatings, 10*(5), 432. https://doi.org/10.3390/COATINGS10050432.

[62] Sellers-Antón, B., Bailón-García, E., Cárdenas-Arenas, A., Davó-Quiñonero, A., Lozano-Castelló, D., & Bueno-López, A. (2020). Enhancement of the Generation and Transfer of Active Oxygen in Ni/CeO2 Catalysts for Soot Combustion by Controlling the Ni–Ceria Contact and the Three-Dimensional Structure. *Environ. Sci. Technol., 54*(4), 2439−2447. https://doi.org/10.1021/acs.est.9b07682.

[63] Cárdenas-Arenas, A., Quindimil, A., Davó-Quiñonero, A., Bailón-García, E., Lozano-Castelló, D., De-La-Torre, U., Pereda-Ayo, B., González-Marcos, J. A., González-Velasco, J. R., & Bueno-López, A. (2020). Design of active sites in Ni/CeO2 catalysts for the methanation of CO2: tailoring the Ni-CeO2 contact. *Applied Materials Today, 19,* 100591. https://doi.org/10.1016/j.apmt.2020.100591

[64] Bailón-García, E., Carrasco-Marín, F., Pérez-Cadenas, A. F., & Maldonado-Hódar, F. J. (2016). Influence of the Pt-particle size on the performance of carbon supported catalysts used in the hydrogenation of citral. *Catalysis Communications, 82*, 36-40. https://doi.org/10.1016/j.catcom.2016.04.014.

[65] Miura, K., Hayashi, J., & Hashimoto, K. (1991). Production of molecular sieving carbon through carbonization of coal modified by organic additives. *Carbon, 29*(4-5), 653–660. https://doi.org/10.1016/0008-6223(91)90133-4

[66] Guo, H., Tian, S., Wang, L., Xiao, C., & Yang, S. (2024). Numerical study of Tesla valve flow field on proton exchange membrane fuel cell performance. *International Journal of Hydrogen Energy, 50*, 1573–1583. https://doi.org/10.1016/J.IJHYDENE.2023.11.108.

[67] Qian, J. Y., Chen, M. R., Gao, Z. X., & Jin, Z. J. (2019). Mach number and energy loss analysis inside multi-stage Tesla valves for hydrogen decompression. *Energy, 179*, 647–654. https://doi.org/10.1016/J.ENERGY.2019.05.064.

[68] Bao, Y., & Wang, H. (2022). Numerical study on flow and heat transfer characteristics of a novel Tesla valve with improved evaluation method. *International Journal of Heat and Mass Transfer, 187*, 122540. https://doi.org/10.1016/J.IJHEATMASSTRANSFER.2022.122540.

[69] Monika, K., Chakraborty, C., Roy, S., Sujith, R., & Datta, S. P. (2021). A numerical analysis on multi-stage Tesla valve based cold plate for cooling of pouch type Li-ion batteries. *International Journal of Heat and Mass Transfer, 177*, 121560. https://doi.org/10.1016/J.IJHEATMASSTRANSFER.2021.121560.

[70] Gamboa, A. R., Morris, C. J., & Forster, F. K. (2004). Improvements in fixed-valve micropump performance through shape optimization of valves. *Journal of Fluids Engineering, 127*(2), 339–346. https://doi.org/10.1115/1.1891151.

[71] Thompson, S. M., Paudel, B. J., Jamal, T., & Walters, D. K. (2014). Numerical investigation of multistaged Tesla valves. *Journal of Fluids Engineering, 136*(8), 081102. https://doi.org/10.1115/1.4026620.

[72] Porwal, P. R., Thompson, S. M., Walters, D. K., & Jamal, T. (2018). Heat transfer and fluid flow characteristics in multistaged Tesla valves. *Numerical Heat Transfer, Part A: Applications, 73*(4), 347–365.

https://doi.org/10.1080/10407782.2018.1447199.

[73] Martinez-Monteagudo, S. I., & Rathnakumar, K. (2021). High-Pressure Processing: Fundamentals, Misconceptions, and Advances. In Knoerzer, K., & Muthukumarappan, K. (Eds), *Innovative Food Processing Technologies: A Comprehensive Review* (pp. 19–38). Elsevier. https://doi.org/10.1016/B978-0-08-100596-5.22949-1.

[74] Sehrawat, R., Kaur, B. P., Nema, P. K., & Tewari, S. (2021). Microbial inactivation by high pressure processing: principle, mechanism and factors responsible. *Food Science and Biotechnology, 30*(1), 19–35. https://doi.org/10.1007/S10068-020-00831-6/TABLES/3.

[75]   Hu, H., & Balasubramaniam, V. M. (2024). High-Pressure Processing. In Smithers, G.W. (Ed), *Encyclopedia of Food Safety* (pp. 531–551). Academic Press. https://doi.org/10.1016/B978-0-12-822521-9.00103-9.

7

REMOVAL OF METFORMIN FROM WATER BY AOPs WITH SULFATE RADICALS: EVALUATION OF DEGRADATION, MINERALIZATION, TOXICITY AND DEGRADATION MECHANISM
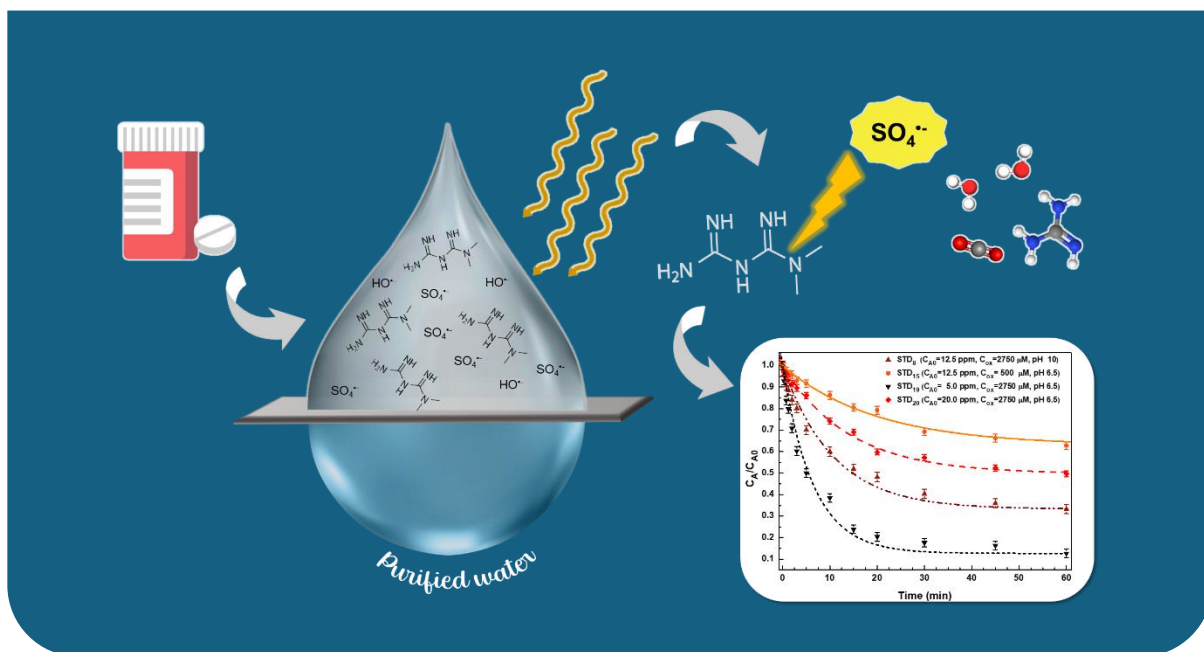
7.1. Introduction

Metformin is one of the main drugs used in the treatment of type 2 diabetes since it helps in glucose control without the risk of hypoglycemia or weight gain. In addition, it is a low-cost compound that can reduce the risk of cardiovascular events and death, but it is also used in the treatment of some other endocrine disorders, such as polycystic ovary syndrome [1, 2]. Due to the increase in cases of obesity and diabetes since 2000 [3], there has been a rise in its consumption. Once administered, less than half of this pharmaceutical is metabolized in the body and about 52% is excreted through urine [2, 4], resulting in its presence in wastewater treatment plant influent at concentrations up to 100 µg L^{-1} [5, 6]. Moreover, it has also been detected in a maximum concentration of 160 ng L^{-1} in drinking water [7]. Conventional wastewater treatment cannot completely remove metformin due to its physicochemical properties such as high solubility, low octanol-water partition coefficient (Kow), low biodegradation rate, and high mobility in aqueous solutions [2]. Furthermore, metformin can be transformed into guanylurea and methyl biguanide during biological treatment [8] or carcinogenic disinfectant byproducts during chlorine disinfection in wastewater treatment plants [9, 10].

The existence of this type of compounds in the ecosystem has detrimental effects on living beings and the environment, including oxidative stress, mutagenesis, carcinogenesis, reproductive toxicity, drug resistance, and allergic reactions [2, 11-14]. Therefore, there has been an increasing interest in applying methods for the elimination of metformin from contaminated waters using different conventional processes, such as phytoremediation [7], biodegradation [15, 16], ozonation [13], chlorination [9], and adsorption [15, 17, 18]. For instance, metformin removal using the *Typha latifolia* plant was investigated by Cui and Schröder [19], and the results demonstrated that the degradation process follows a first-order kinetics behavior with a removal efficiency between 74 and 81 % after one month of treatment. Piai et al. [20] studied the biodegradation of metformin with biologically active granular activated carbon. The results evidenced that after 33 days of treatment a removal percentage of 90 % was obtained regardless of the initial concentration of metformin. Mahmoud et

al. [2] synthesized biochar modified with NaOH from artichoke leaves at 350 °C to remove metformin from water obtaining a maximum adsorption capacity of 36.5 mg g^{-1} at 288 K and pH 6 in 150 min. In this sense, although conventional technologies can partially remove metformin from water, the associated treatment times remain long, and the adsorption capacities are low. Therefore, the development of new technologies or the optimization of current ones is a priority to reduce the presence of this pollutant.

An alternative to conventional systems is Advanced Oxidation Processes (AOPs). These processes involve the in-situ generation and use of transitory species with a high oxidizing power to generate deep changes within the chemical structure of pollutants [21, 22]. Among the AOP technologies employed for the degradation of organic contaminants, the Fenton process and the UV-based merged with oxidants such as H_2O_2, O_3, Cl_2 and NH_2Cl can be mentioned [23-25]. In this regard, the UV/H_2O_2 system has been the most widely applied system to degrade pollutants from water due to the high quantum yield of H_2O_2 [2, 25-27]. Recently, the sulfate radical based AOP is gaining attention due to its ability to replace the conventionally used UV/H_2O_2 system [28, 29]. The use of sulfate radicals compared to hydroxyl radicals for the degradation of some organic compounds has been shown to have higher degradation and mineralization rates [30-32], faster degradation kinetics [33, 34], and lower toxicity of the degradation byproducts [35, 36]. These results have been associated to different characteristics of sulfate radical such as its selectivity and slower recombination in comparison to hydroxyl radicals ($kSO_4^{-\bullet} = 4{\times}10^8$ M^{-1}s^{-1} vs $kOH^{\bullet} = 5.5{\times}10^9$ M^{-1}s^{-1} [35]). Whereas HO· is a non-selective free radical with <u>redox potential</u> ranging from 1.7 to 2.8 V, the $SO_4{\cdot}^{-}$ radical is high selective and has redox potentials of 2.5–3.1 V [27-29]. Moreover, compared to hydroxyl radicals, sulfate radicals possess various advantages including a higher stability and therefore a longer half-life (~40 µs for $SO_4^{\bullet-}$ regarding to 20 ns for HO$^{\bullet}$), higher solubility in aqueous solution, and its applicability in a wider range of pH values (2-8) [29, 37]. Additionally, the low molar absorption coefficient of H_2O_2 at 254 nm limits the efficient generation of HO· and excessive amounts of H_2O_2 are needed resulting in additional steps to remove any unreacted H_2O_2 [38], whereas the larger radical quantum yield for UV-254 nm/$S_2O_8^{2-}$ (1.8 vs 1.0 of UV-254

250

nm/H_2O_2, [35]) leads to low oxidant requirement [39, 40]. The application of AOPs for metformin degradation has been limited mainly to the use of Fenton processes [41-43] and photocatalysis [44, 45].

On the other hand, attaining an appropriate model to describe a phenomenon is essential for analyzing and designing any operation system. Response surface methodology (RSM) is a statistical method, which helps to unearth maximal information by performing minimal experimentation, therefore, saving time, cost, and efforts [46, 47]. It also provides a more appropriate model for optimization than the one-factor-at-a-time methodology since it considers multifactorial experiments in a holistic manner to identify an accurate factor-response relationship [48]. So far, there are no published studies in the literature related to degradation of metformin through the UV/$S_2O_8^{2-}$ system, even though it has been shown that UV radiation has a low efficiency for metformin degradation [49]. Therefore, in this chapter it is aimed to gain insights in the photodegradation kinetics, mechanisms, and toxicity of metformin for its potential risk assessment, as well as to take advantage of the Response Surface Methodology to analyze and evaluate the main effects of operational conditions (pH, temperature, metformin initial concentration, and concentration of oxidant) and their simultaneous interactions on the degradation process. In addition, the photodegradation byproducts will be identified along with their toxicity, which is crucial for comprehensive ecological risk evaluation. Finally, based on the percentage of mineralization obtained, the degradation mechanism will be proposed.

7.2. Materials and Methods

7.2.1. Chemicals

Metformin ($C_4H_{11}N_5 \cdot xHCl$) with purity ≥ 97% was supplied by Sigma-Aldrich. ***Table 7.1*** shows some of its physicochemical properties highlighting its high solubility in water and, consequently, its low octanol/water partition coefficient. The species distribution diagram of metformin was constructed from the pK_a values. ***Figure 7.1*** exhibits that metformin has a strong basic character at pH values up to 8, since its protonation for both amino groups is complete; thus, it is found as a double charged cation. On the

other hand, single and double charged cations are in equilibrium at a pH range between 9 and 10.3, while the neutral molecule is superiorly presented only at a very high pH.

The oxidant employed was $K_2S_2O_8$ with purity of 100% and supplied by Fermont. Acetonitrile and methanol were analytical-reagent grade and purchased from Sigma Aldrich. All chemicals were used as received without additional purification, and solutions were prepared with deionized water.
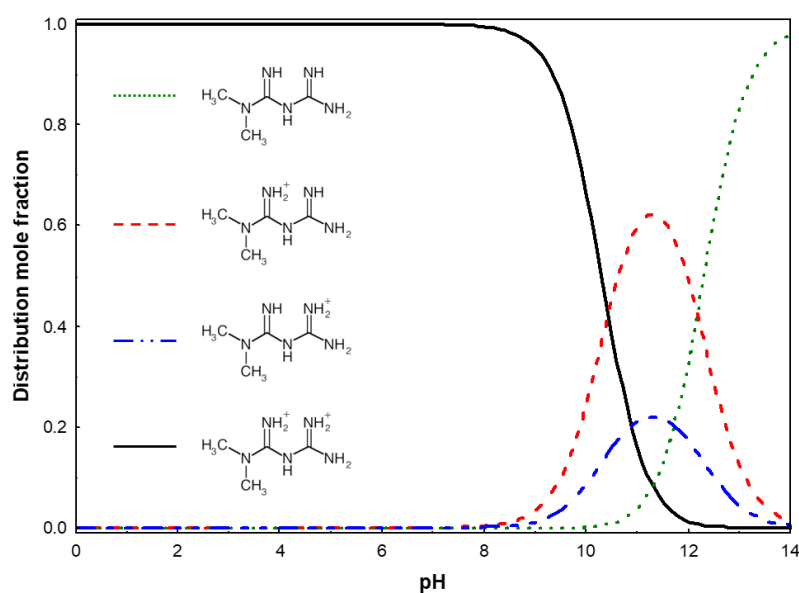
Figure 7.1. Species distribution diagram of metformin in water.

Table 7.1. Physicochemical properties of metformin.

Compound	Molecular formula	Molecular weight	pKa	log Kow[*]	Water solubility[*] (mg mL^{-1})
Metformin	$C_4H_{11}N_5$	129.17	**pK$_{a1}$=10.3** **pK$_{a2}$=12.3**	-2.64	200

*Obtained at 25 °C [50-52].

7.2.2. Analytical procedures

Metformin concentration in aqueous solution was determined by High-Performance Liquid Chromatography (HPLC) using a liquid chromatograph Waters e2695 equipped with a PDA-2998 ultraviolet-visible detector. A C_8 chromatographic column (5 μm particle size and 4.6 × 200 mm) was employed for the HPLC analysis. The mobile phase used consisted of 50% of Milli-Q water acidified with a 1 M H_3PO_4 solution up to pH 2.5, 30% of acetonitrile, and 20% methanol in isocratic mode at a flow of 0.5 mL min^{-1}. The detector wavelength was set at 230 nm, and the injection volume was 20 μL proving a retention time of 3.6 min.

Degradation byproducts were identified by using a High-Performance Liquid Chromatography-Electrospray Ionization Mass Spectrometry technique (HPLC-EIS-MS). The HPLC-EIS-MS was carried out by using an Agilent 610 Series Quad LC/MS system and a C_8 column of 4.6×150 mm with a particle size of 5 μm. The chromatography and mass spectrometry were performed following the Cahill et al. [53] methodology.

Total Organic Carbon (TOC) present in the system was determined for each sample at initial (TOC_0) and final (TOC_f) time using a Shimadzu V-CSH analyzer with ASI-V. The mineralization percentage (%TOC) was obtained by the following equation:

$$\%TOC = \frac{TOC_0 - TOC_f}{TOC_0} \times 100 \%$$ (1)

Degradation byproducts toxicity was determined based on the effects of the samples on cell biomass of *Chlamydomonas reinhardtii* culture (CC-125). Cell numbers were determined in a hemocytometer chamber under a light microscope. Toxicity is expressed as inhibition percentage after 120 hours of exposure with reference to a control of the initial concentration of algae cells of 4.58×10^6 cells mL^{-1}:

$$\text{Inhibitory rate } (\%) = \left(1 - \frac{N}{N_0}\right) \times 100 \%$$ (2)

where N is the cells concentration of the samples (cells mL^{-1}) and N_0 is the cells concentration of the control (cells mL^{-1}).

7.2.3. Experimental response surface design

A Box–Behnken-type response surface design [46] was used to analyze the effect of the operating conditions on the degradation percentage and the kinetics rate constant, using the Design Expert software (Version 7.0.0). The degradation experiments were performed varying: (i) the temperature (T) from 15 to 45 °C; (ii) the solution pH (pH) from 3 to 10; (iii) the initial concentration of $K_2S_2O_8$ (C_{ox}) from 500 to 5000 μM; and (iv) the initial concentration of metformin (C_{A0}) from 5 to 20 mg L^{-1}. **Table 7.2** shows the resulting experimental design, which consisted of 27 experiments. The experiments were labeled STDx, where x corresponds to the numbers shown in **Table 7.2**.

Table 7.2. Experimental design for metformin degradation.

STD	C_{A0}	C_{ox}	T	pH	(%D)	k_{app}	Inhibition rate
	mg L^{-1}	μM	°C		%	min^{-1}	%
1	5	500	30	6.5	49.8	0.122	43.7
2	20	500	30	6.5	26.1	0.050	15.2
3	5	5000	30	6.5	84.2	0.094	10.0
4	20	5000	30	6.5	62.0	0.082	10.6
5	12.5	2750	15	3	52.9	0.122	15.8
6	12.5	2750	45	3	60.3	0.085	37.4
7	12.5	2750	15	10	59.2	0.094	25.4
8	12.5	2750	45	10	66.8	0.044	18.4
9	5	2750	30	3	63.2	0.172	36.8
10	20	2750	30	3	44.6	0.083	25.3
11	5	2750	30	10	75.0	0.116	19.4
12	20	2750	30	10	53.3	0.051	56.7
13	12.5	500	15	6.5	37.9	0.093	17.3
14	12.5	5000	15	6.5	67.1	0.219	-2.5
15	12.5	500	45	6.5	37.2	0.087	-3.1
16	12.5	5000	45	6.5	75.2	0.224	2.0
17	5	2750	15	6.5	86.4	0.090	0.2
18	20	2750	15	6.5	43.8	0.155	4.4
19	5	2750	45	6.5	87.3	0.084	22.3
20	20	2750	45	6.5	50.3	0.030	5.6
21	12.5	500	30	3	35.4	0.328	7.6
22	12.5	5000	30	3	68.2	0.071	1.2
23	12.5	500	30	10	34.4	0.238	8.1
24	12.5	5000	30	10	75.0	0.108	10.0
25	12.5	2750	30	6.5	60.9	0.051	1.2
26	12.5	2750	30	6.5	62.0	0.076	-2.3
27	12.5	2750	30	6.5	54.1	0.076	2.4

The experimental data were interpreted using a second-order polynomial regression model according to the following equation [46] Equation (3):

$$Y = \beta_0 + \beta_1 \cdot C_{A0} + \beta_2 \cdot C_{ox} + \beta_3 \cdot T + \beta_4 \cdot pH + \beta_5 \cdot C_{A0} \cdot C_{ox} + \beta_6 \cdot C_{A0} \cdot T +$$
$$\beta_7 \cdot C_{A0} \cdot pH + \beta_8 \cdot C_{ox} \cdot T + \beta_9 \cdot C_{ox} * pH + \beta_{10} \cdot T \cdot pH + \beta_{11} \cdot C_{A0}^2 + \beta_{12} \cdot C_{ox}^2 + \qquad (3)$$
$$\beta_{13} \cdot T^2 + \beta_{14} \cdot pH^2$$

where β_{0-14} are the regression coefficients, and Y represents the analyzed response, which consists of the degradation percentage (%D), and the pseudo first-order kinetic constant (k_{app}).

7.2.4. Photolysis reactor and experimental procedure

Metformin degradation experiments were conducted in a photoreactor formed by concentric tubes: a stainless-steel outer tube (inner diameter of 13 cm × height of 18 cm) and quartz inner tube (i.d. of 5.5 cm × height of 45 cm). The inner tube contained a low-pressure Hg lamp (Heraeus Noblelight model TNN 15/32, nominal power 15 W at $\lambda = 254$ nm). The annular space of the photoreactor contained a sample holder with a capacity for six quartz reaction tubes (i.d. of 1.6 cm × height of 20 cm). The system was kept at constant temperature using a Frigiterm ultrathermostat, whereas continuous agitation was supplied at the reaction tubes by a magnetic agitation system.

The experimental data were obtained by the following procedure: In 50 mL volumetric flasks, solutions of known initial concentrations of metformin were prepared according to the experimental design showed in **Table 7.2**. Subsequently, the solutions were poured into quartz tubes, which in turn were introduced into the photoreactor. The thermostat was turned on and the operating temperature of the system was adjusted according to the experimental design. Once the system reached the operating temperature, the corresponding aliquot of a 0.1 M solution of $K_2S_2O_8$ was added to obtain the desired initial concentration of oxidant. Afterwards, the lamp and timer were turned on to start the degradation kinetic. The concentration of metformin within the photoreactor was monitored by withdrawing 0.2 mL aliquots at intervals of: 0.25, 0.75, 1.25, 2, 3, 5, 10, 15, 20, 30, 45, and 60 min.

The dimensionless concentration of metformin was plotted against time to obtain the concentration decay curve. The experimental data were fitted to a pseudo-first order kinetic model, represented by the following equation (Equation 4):

$$\frac{dC_A}{dt}=k_{app}(C_A-C_{Af})$$ (4)

where,

C_A = Concentration of metformin at time t, mg L^{-1}

C_{Af} = Final concentration of metformin after 60 min, mg L^{-1}

k_{app} = Apparent reaction rate constant, min^{-1}

t = Time, min

To estimate the percentage of metformin degradation (%D) the following equation was used (Equation 5):

$$\%D=\frac{C_{A0}-C_{Af}}{C_{A0}}\times100\ \%$$ (5)

7.3. Results and discussions

7.3.1. Metformin degradation

Based on the studies reported in the literature, it has been found that the photolysis of metformin under UV light is ineffective. For instance, Quintão et al. [49] obtained low degradation (9.2 %) and mineralization (0.72 %) efficiencies for the photolysis of metformin (10 mg L^{-1}) by UV-C radiation (25.7 W) in 30 min. Similarly, Carbuloni et al. [54] studied the photolysis of metformin solution (10 mg L^{-1}) using a 125 W Hg lamp at 25 °C and pH 5.4, achieving a degradation percentage close to 20%. Finally, Wols et al. [55] analyzed the photodegradation of metformin with low and medium pressure lamps, obtaining that metformin is not degraded in both cases. These works have demonstrated that direct photolysis through UV radiation is inadequate for treating water contaminated with metformin. Therefore, the use of radical generating species is a requirement for the efficient degradation of metformin.

Figures **7.2a-b** show, as an example, the experimental dimensionless concentration decay curves of metformin at different pH, initial concentration, and initial oxidant concentration, at 15 °C and 45 °C in the presence of UV radiation, while the **Table 7.2** summarizes the %D obtained after 60 minutes of treatment. Experiments with UV radiation alone (not showed) demonstrated a null metformin degradation. In general, the degradation time varied from 25 to 60 minutes, while the %D ranged from 26.1 to 87.3 % depending on the operating conditions used. As shown in **Table 7.2**, the lowest %D was obtained with the highest initial metformin concentration and the lowest oxidant concentration, achieving 26.1 % in 60 minutes (Exp. STD_2). It can be seen in **Figures 7.2a-b** that, for both temperatures, the lowest %D was obtained using an oxidant concentration of 500 μM with a metformin concentration of 12.5 mg L^{-1} at pH 6.5 ($STD_{13,15}$). By increasing the concentration of $K_2S_2O_8$ up to 2750 μM ($STD_{7,8}$) it is possible to observe a 1.6-1.8-fold increase in %D, being slightly higher at 45 °C. On the other side, rising the initial metformin concentration almost double ($STD_{18,20}$) results in a reduction of approximately 16% of the %D regardless of the temperature used. Besides, when going from basic to acidic pH, the photodegradation was slightly diminished (less than 7 %D), as can be observed in **Figure 7.2a** ($STD_{7,5}$). Furthermore, the most efficient metformin degradation, around 3.34-fold greater and in practically half of the time, was attained when the lowest initial concentration of metformin and higher temperature were employed (**Figure 7.2b**, STD_{19}). The high %D of metformin obtained is attributed to the presence of $SO_4^{•-}$ ($E_0 = 2.6$ V) in the medium due to photoactivation of $S_2O_8^{2-}$ according to the following reaction (Equation 6).

$$S_2O_8{}^{2-} + h\upsilon \rightarrow 2SO_4^{\cdot-} \tag{6}$$

Additionally, sulfate radicals may lead to the presence of other radical species in the medium ($HO^{\cdot}$, $HO_2^{\cdot}$) via the following reactions (Equations 7 to 17).

$$SO_4^{\cdot-} + RH_2 \rightarrow H^+ + SO_4^{2-} + RH^{\cdot} \tag{7}$$

$$RH^{\cdot} + S_2O_8{}^{2-} \rightarrow SO_4^{\cdot-} + R + H^+ + SO_4^{2-} \tag{8}$$

$$SO_4^{\cdot-} + RH \rightarrow R^{\cdot} + H^+ + SO_4^{2-} \tag{9}$$

$$2R^{\cdot} \rightarrow RR \text{ (dimer)} \tag{10}$$

$$SO_4^{\cdot-} + H_2O \rightarrow HSO_4^- + HO^{\cdot\cdot} \tag{11}$$

$$HSO_4^- \rightarrow H^+ + SO_4^{2-} \tag{12}$$

$$HO^{\cdot} + S_2O_8^{2-} \rightarrow HSO_4^- + SO_4^{\cdot-} + \frac{1}{2}O_2 \tag{13}$$

$$2HO^{\cdot} \rightarrow H_2O_2 \tag{14}$$

$$HO^{\cdot} + H_2O_2 \rightarrow H_2O + HO_2^{\cdot} \tag{15}$$

$$2\ HO_2^{\cdot} \rightarrow H_2O_2 + O_2 \tag{16}$$

$$S_2O_8^{2-} + H_2O_2 \rightarrow 2H^+ + 2SO_4^{2-} + O_2 \tag{17}$$
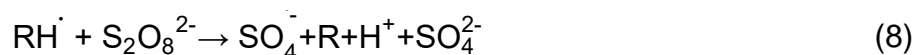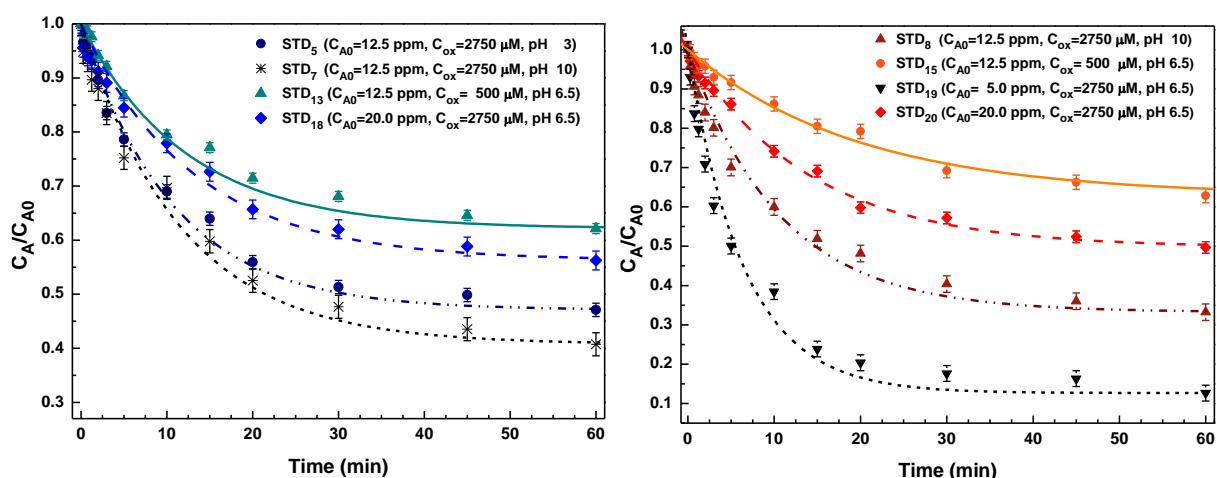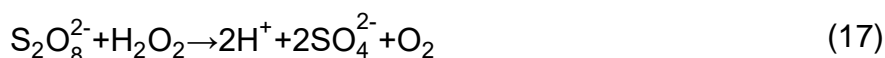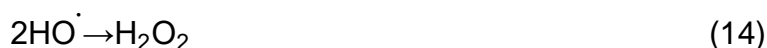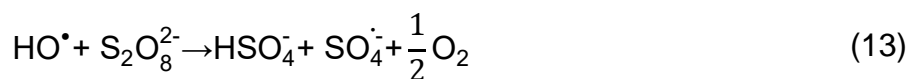
(**a**)   (**b**)

Figure 7.2. Photodegradation of metformin by $UV/S_2O_8^{2-}$ system using different operating conditions: a) T= 15 °C; and b) T= 45 °C.

The values of %D were fitted to the quadratic model given by Equation (3). ANOVA (see Table 3) was performed to assess the relevance of the model and its coefficients using a confidence interval of 95%. The p-value was used to indicate the significance of each factor, where a value of $p < 0.05$ indicates that the factor is statistically important. According to Box-Cox analysis, the base 10 Log transformation ($y' = \log_{10}(y + w)$) where $w = 0$, for %D resulted appropriate. **Table 7.3** shows that the significant factors were C_{A0}, C_{ox}, T (it was considered since its p-value was in the limit), pH, $C_{A0}*C_{ox}$, and C_{ox}^2. The p-value of the model was minor at 0.0001; thus, the

quadratic model can be used to describe the variation of the experimental response. In addition, the initial concentrations of metformin and oxidant were found to be the most important factors, with p-values minor to 0.0001. The final expression of the model, excluding insignificant terms and respecting the hierarchy, is described by the following equation (Equation 18):

$$Log_{10} (\%D) = 1.660 - 0.020*C_{A0} + 1.173e^{-4}*C_{ox} + 1.198e^{-3}*T \qquad (18)$$
$$+ 6.509e^{-3}*pH + 2.186e^{-6}*C_{A0}C_{ox} - 1.430e^{-8}*C_{ox}^2$$

Table 7.3. Analysis of variance (ANOVA) for the percentage of degradation (%D).

Source	Sum of squares	df	Mean Square	F Value	p-value Prob > F	
Model	0.444	6	0.07	78.36	< 0.0001	Significant
C_{A0}- Initial metformin concentration (mgL^{-1})	0.130	1	0.13	137.11	< 0.0001	
C_{ox}- Oxidant concentration (µM)	0.264	1	0.26	279.67	< 0.0001	
T-Temperature (°C)	0.004	1	0.00	4.10	0.0564	
pH	0.006	1	0.01	6.59	0.0184	
$C_{A0}*C_{ox}$	0.005	1	0.01	5.76	0.0263	
C_{ox}^2	0.035	1	0.03	36.95	< 0.0001	
Residual	0.019	20	0.00			
Lack of Fit	0.017	18	0.00	0.90	0.6479	Not significant
Pure Error	0.002	2	0.00			

Cor Total	0.463	26		
Std. Dev.	0.031	R^2	0.9592
Mean	1.75	Adjusted R^2	0.9470
C.V. %	1.76	Predicted R^2	0.9325
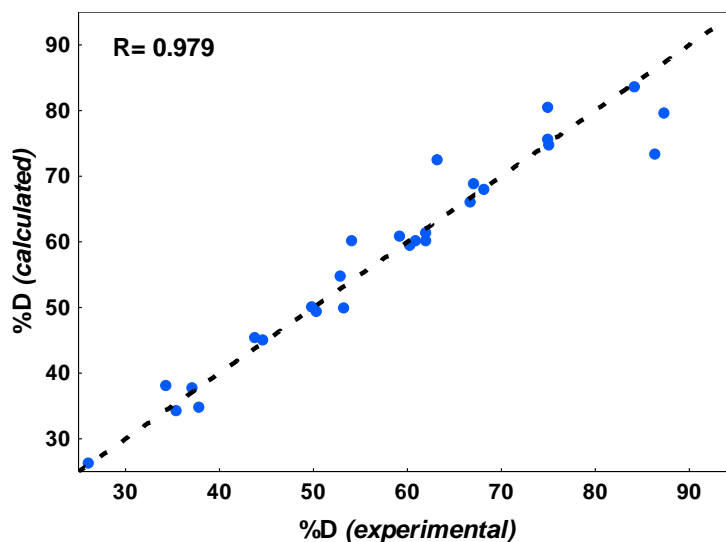
Figure 7.3. Predicted %D values by Eq. (18) against experimental %D data.

Figure 7.3 shows the predicted values of %D versus the experimental data; the points fall on a straight line, indicating that the estimations were in good agreement with the experimental values. Equation (18) shows that C_{A0} has a negative coefficient; thus, an increase in the initial concentration of metformin will reduce the degradation percentage obtained. Conversely, the terms C_{ox}, T, and pH have positive coefficients, indicating that as the concentration of oxidant, the temperature, or the pH of operation augment, the degradation percentage will rise. This agrees with the study realized by Aseman and Sayyaf [56], who reported that increasing the initial metformin concentration from 15 to 80 mg L^{-1} resulted in a 18.04% reduction of removal efficiency in the heterogeneous iron catalytic degradation of metformin. That fact was ascribed to the formation of more intermediates that competed against metformin molecules. In relation to the oxidant concentration, an increase in its dosage improves the

effectiveness of the system, since UV absorption by $K_2S_2O_8$ is greater at higher concentration, favoring the generation of radicals, mainly $SO_4^{\bullet-}$. Nevertheless, the negative coefficient of the quadratic term C_{ox}^2 suggests that the response will exhibit a maximum within the range studied, from which higher concentrations will not produce an increase in metformin degradation. This is attributed to the excessively generated $SO_4^{\bullet-}$ radicals that, at high concentrations of $K_2S_2O_8$, can recombine in accordance with Eqs. (19) and (20) [33]. Furthermore, as presented in Equation (11), $HO^{\bullet}$ radicals are also generated in this system, and at high concentrations, they can be inhibited or recombined, in agreement with Eqs. (13-16, 21 and 22) [57, 58].

$$SO_4^{\bullet-} + SO_4^{\bullet-} \rightarrow S_2O_8^{2-} \qquad\qquad k = 4.0 \times 10^8 \ M^{-1}s^{-1} \qquad (19)$$

$$SO_4^{\bullet-} + S_2O_8^{2-} \rightarrow SO_4^{2-} + S_2O_8^{\bullet-} \qquad\qquad k = 6.1 \times 10^9 \ M^{-1}s^{-1} \qquad (20)$$

$$SO_4^{\bullet-} + HO^{\bullet} \rightarrow HSO_4^{-} + \frac{1}{2}O_2 \qquad\qquad k = (0.1\text{-}1.0) \times 10^{10} \ M^{-1}s^{-1} \quad (21)$$

$$SO_4^{\bullet-} + HO^{\bullet} \rightarrow HSO_5^{-} \qquad\qquad k = 1.0 \times 10^{10} \ M^{-1}s^{-1} \qquad (22)$$

(a) (b)
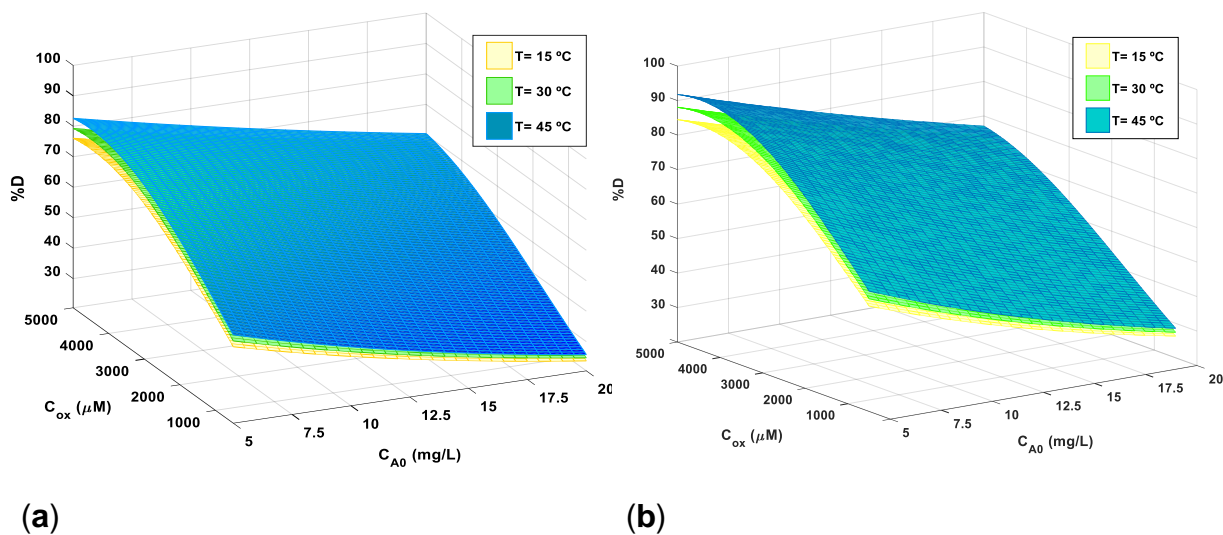
Figure 7.4. Response surface for the percentage of degradation (%D): a) pH 3; b) pH 10. Oxidant concentration (C_{ox}) vs initial metformin concentration (C_{A0}). Temperature 15, 30, and 45 °C.

Figure 7.4 shows the interaction between C_{A0} and C_{ox} and its effect on %D at different temperatures (15, 30, and 45 °C) and pH (3 and 10). It can be observed that the highest values of %D are acquired for the lowest initial concentration of metformin and higher amount of oxidant, since this condition allows a good ratio between radicals generated and metformin molecules to be attacked $[SO_4^{\bullet-}]/[Met]_0$. However, as mentioned above, it is possible to observe that the maximum for the oxidant concentration is reached near to 5000 µM. On the other side, in the UV/$K_2S_2O_8$ system $S_2O_8^{2-}$ can be activated by applying heat (see Eq. 6). Therefore, a slight effect of temperature is observed in **Figures 7.4a-b** since the rise of 30 °C led to an improvement close to 7 %D by the additional activation of $S_2O_8^{2-}$. A reduction of about 9 %D is also observed when going from pH 10 to pH 3 (**Figures 7.4a** and **7.4b**, correspondingly). The above is ascribed to several factors:

i) The acidification of the medium that leads to the presence of chloride ions with an inhibiting character. According to Eq. (23), chloride ions can react with $SO_4^{\bullet-}$ radicals [59] thus inhibiting them and decreasing their concentration for metformin degradation.

$$SO_4^{\bullet-}+Cl^-\rightarrow SO_4^{2-}+Cl^{\bullet} \; ; \qquad k= 3.2 \times 10^8 \text{ M}^{-1}\text{s}^{-1} \qquad (23)$$
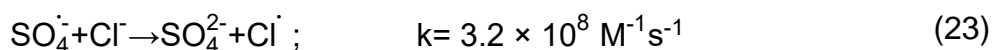
ii) Acidic inorganic products, such as H_2SO_5, H_2SO_4, $HS_2O_8^-$, and HSO_4 —that have a lower oxidation potential than $SO_4^{\bullet-}$ and $HO^{\bullet}$ radicals— are favorably produced at low pH; and,

iii) As shown in **Figure 7.1**, pH values up to 8 favor double protonation of amino groups of metformin molecule, leading to a decrease in electron density at hydrogen atoms, thus becoming the bonds more resistant.

The dimensionless concentration decay curves were fitted using the pseudo-first order kinetic model represented by Equation (4). The k_{app} values were estimated by a nonlinear least-squares method through the Rosenbrock–Newton algorithm using the Statistica software and are summarized in **Table 7.2**. k_{app} values ranged from 0.030

to 0.328 min^{-1}, and they present a decrease as the initial concentration of metformin increases. This relation could be attributed to the increment of metformin molecules to be attacked by radicals as the ratio of radical concentration to metformin concentration reduces. Regarding some metformin degradation apparent rate constants reported in the literature using different oxidation processes, the k_{app} = 0.084 min^{-1}, attained with the conditions leading to the highest %D, resulted greater in most cases as presented in *Table 7.4*. For instance, the works realized by Prashanth, Priyanka and Remya [60], and Carbuloni et al. [54] for photocatalytic degradation of metformin led to k_{app} values up to 16 folds lower. However, Dolatabadi and Ahmadzadeh [61] achieved a k_{app} about 5 times higher using an electro-Fenton system with H_2O_2 and a current density of 6 mA cm^{-2}.

Table 7.4. Comparison of metformin degradation apparent rate constants reported in the literature using different oxidation processes.

Process	Degradation (%)	Pseudo-1st order (min^{-1})	Conditions	References
AOP using sulfate radicals	87.3	0.0840	C_0 = 5 mg L^{-1} C_{ox} = 2750 mM T = 45 °C pH = 6.5 Mercury lamp 15 W	Present work
Solar photocatalytic by TiO_2 synthesized using Calotropis gigantea leaf extract	96.7	0.0140	C_0 = 9.7 mg L^{-1} Catalyst dosage= 0.7 gL^{-1} pH = 9.7	[60]
AOP using electro-Fenton	98.6	0.4224	C_0 = 10 mg L^{-1} Current density 6 mAcm^{-2} H_2O_2 dosage 250 mL L^{-1}	[61]
Photolysis under UV radiation	28.0	0.0050	C_0 = 10 mg L^{-1} T = 25 °C Mercury lamp 125-W Catalyst dosage= 0.5 gL^{-1}	[54]
Photodegradation using TiO_2 under UV radiation	52.5	0.0082	C_0 = 10 mg L^{-1} T = 25 °C Mercury lamp 125-W Catalyst dosage= 0.5 gL^{-1}	[54]

	Sum of squares	df	Mean Square	F Value	p-value Prob > F	

Photodegradation using 5% ZrO_2-TiO_2 under UV radiation	51.3	0.0099	C_0 = 10 mg L^{-1} T = 25 °C Mercury lamp 125-W Catalyst dosage= 0.5 gL^{-1}	[54]
Photodegradation using 5% TiO_2-ZrO_2 under UV radiation	37.0	0.0055	C_0 = 10 mg L^{-1} T = 25 °C Mercury lamp 125-W Catalyst dosage= 0.5 gL^{-1}	[54]
Photodegradation using ZrO_2 under UV radiation	50.6	0.0071	C_0 = 10 mg L^{-1} T = 25 °C Mercury lamp 125-W Catalyst dosage= 0.5 gL^{-1}	[54]

Table 7.5 presents the ANOVA (α = 0.05) results for the quadratic model obtained for predicting the values of k_{app}. According to Box-Cox analysis, the inverse square root transformation ($y' = (y+w)^{-1/2}$) where w = 0, for k_{app} resulted appropriate. In the case of the reaction rate, the pH resulted significant along with C_{ox}, C_{A0}, T*pH, and T^2. Additionally, the C_{ox} turned out to be the most important term, and the lack of fit was insignificant, confirming that the reaction rate is sensitive to changes in these factors and that the obtained quadratic model can be used to depict the variation of the experimental response.

Table 7.5. Analysis of variance (ANOVA) for the kinetic rate constant (k_{app}).

Source	Sum of squares	df	Mean Square	F Value	p-value Prob > F	
Model	17.61	7	2.52	13.48	< 0.0001	Significant
C_{A0}- Initial metformin concentration (mgL^{-1})	1.49	1	1.49	8.00	0.0107	
C_{ox}- Oxidant concentration (µM)	12.76	1	12.76	68.32	< 0.0001	
T-Temperature (°C)	0.16	1	0.16	0.88	0.3593	
pH	0.91	1	0.91	4.86	0.0399	
T*pH	0.60	1	0.60	3.20	0.0398	

C_{ox}^2	0.48	1	0.48	2.59	0.0435	
T^2	0.88	1	0.88	4.72	0.0426	
Residual	3.55	19	0.19			
Lack of Fit	3.53	17	0.21	19.44	0.0570	Not significant
Pure Error	0.021	2	0.011			
Cor Total	21.16	26				
Std. Dev.	0.43		R^2		0.832	
Mean	3.33		Adjusted R^2		0.771	
C.V. %	12.98		Predicted R^2		0.616	

The refined regression model for the transformed response $k_{app}^{-1/2}$, acquired respecting the hierarchy, is given by the following equation (Equation 24):

$$k_{app}^{-1/2} \, (min^{-1})^{-1/2} = 4.128 + 0.047*C_{A0} - 7.568e^{-4}*C_{ox} + 0.043*T - 0.142*pH + 7.356e^{-3}*T*pH + 5.430e^{-8}*C_{ox}^2 - 1.650e^{-3}*T^2 \tag{24}$$

Figure 7.5 presents the relation between the experimental values of the rate constant k_{app} and the predicted ones obtained by means of the Eq. (24), with a R coefficient greater than 0.9; it confirms that the model acquired appropriately interprets the experimental data. The positive coefficient of C_{A0} in Equation (24) indicates that an increase in this factor leads to an increase in $k_{app}^{-1/2}$, that is, a reduction in the rate constant k_{app}. Although, an effect related to the variation of temperature by its own is not significant (p-value > 0.05), this term was considered in the model due to hierarchy.
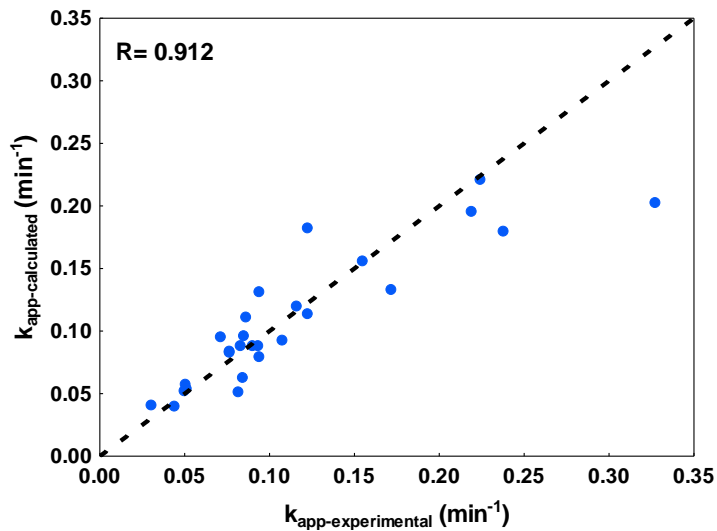
Figure 7.5. Predicted values of the rate constant (k_{app}) by Equation (24) against experimental k_{app} data.
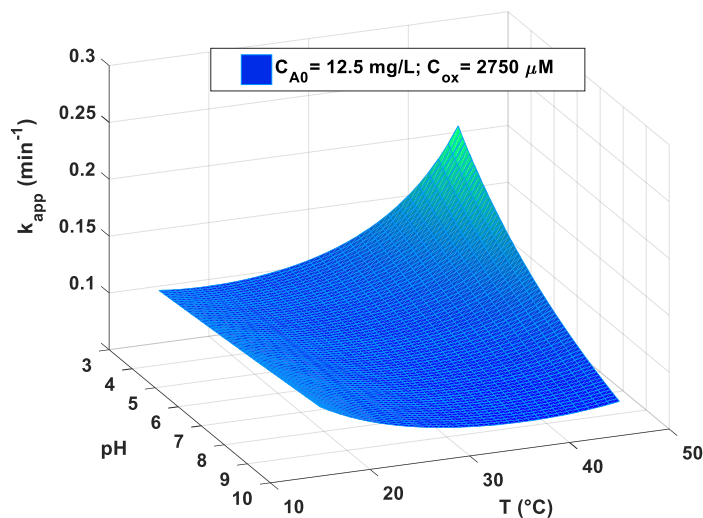
Figure 7.6. Response surface for the kinetic rate constant (k_{app}): Temperature (T) vs medium pH (pH). C_{A0}= 12.5 mgL^{-1} and C_{ox}= 2750 μM.

Nevertheless, within the range analyzed, there is a synergy effect between temperature and pH (***Figure 7.6***). With acidic pH, a grow in temperature from 30 to 45 °C decreases around 20% the $k_{app}^{-1/2}$ value, that is, the rate constant increases (approx. 65%). When the degradation medium is near to neutral pH, changes in the temperature process led to variations smaller than 15%, and a 30 °C increment is required to get a slight improvement in the reaction rate. On the other hand, in basic

medium a temperature rise results in a reaction rate reduction due to the favoring of recombination and inhibition reactions, as shown in Eqs. (21) and (22). Besides, the energy required for thermal persulfate activation under acidic environment is lower than in neutral or alkaline medium (about 29 and 39% less, respectively, Kiejza et al. [62]) leading to an increase in reaction rate.

7.3.2. Metformin mineralization

The aim of the advanced oxidation processes is to achieve the mineralization of the pollutant treated, this is, its complete degradation to its mineral components (carbon dioxide and water) [63]. However, the complete destruction of a chemical compound to get all the carbon converted to CO_2 is not easily achieved, and contrarily some of the mass of the chemical may be decomposed in smaller byproducts containing carbon. Thus, even though a compound can be degraded, to some extent depending on the operational conditions, there is not a direct relationship between degradation and mineralization, and the pollutant would not be necessarily complete converted to CO_2 [64-66]. Consequently, some other organic molecules could remain in the solution treated. In this sense, total organic carbon (TOC) is a practical and reliable parameter useful as an indicator of the organic content in a water sample [67, 68] which helps us to estimate the amount of the compound degraded that has been mineralized. ***Figure 7.7*** shows the %TOC after 60 min of treatment for all experiments. This figure shows that the %TOC varies drastically with the operating conditions of the system. Similar than %D and k, an attempt was made to incorporate the %TOC as a response in the experimental design, however due to the nature of the data it was not possible to obtain a statistically reliable model. On average the mineralization percentages are lower than 40% for the most of experiments. The highest %TOC was obtained for STD 16 which was carried out at 45 °C, C_{A0}=12.5 mgL^{-1}, pH = 6.5 and C_{ox} = 5000 μM. The low values of %TOC indicate the presence of chemically stable degradation byproducts. According to Kumar and Brumme [69], the mineralization process varies according to the number of the carbon atoms of the alkyl group and the N atom position using microbial degradation of alkylated ureas. Moreover, a shorter

267

mineralization process was observed when the two alkyl groups were on different N atoms, as opposed to when they were on the same N atom.
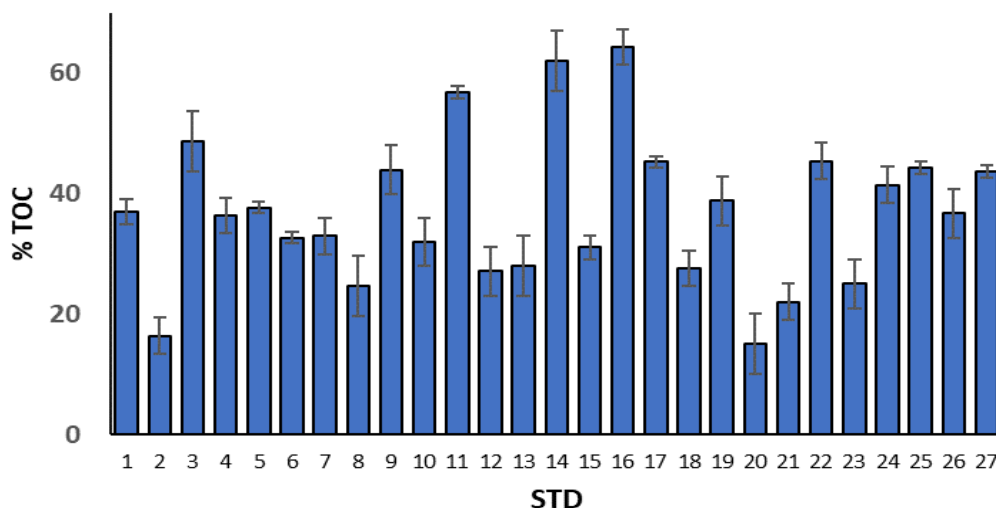
Figure 7.7. Responses of the percentage of mineralization (% TOC) at different experimental conditions.

7.3.3. Degradation byproducts and toxicity

Metformin was rapidly degraded by sulfate radicals, and six principal degradation byproducts were detected from the metformin degradation solutions. After five minutes of degradation, five products were observed: N-cyanoguanidine m/z= 85; N,N-dimethylurea m/z= 89; N,N-dimethyl-cyanamide m/z= 71 N,N-dimethyl-formamide m/z= 74; and glycolonitrile m/z= 58. After twenty minutes of degradation, the guanidine m/z= 60 was observed as well. All these degradation products have been also observed by Luo et al. [70] using acidic, basic, and oxidative conditions, and by Badran et al. [71] under oxy-cracking process.

The general mechanism of metformin degradation is described in ***Figure 7.8***, where three degradation pathways are suggested according to the HPLC-MS analysis results. The proposed pathway *a* (***Figure 7.9***) is a double dealkylation at N_{12}. Sulfate radicals ($SO_4^{\bullet-}$) oxidize the methyl groups followed by the elimination of formaldehyde by hydrolysis reaction. Lin et al. [72], suggested that the N_{12} y N_{10} atoms would be the

primary site attacked by radicals. However, the biguadine intermediate was not observed.
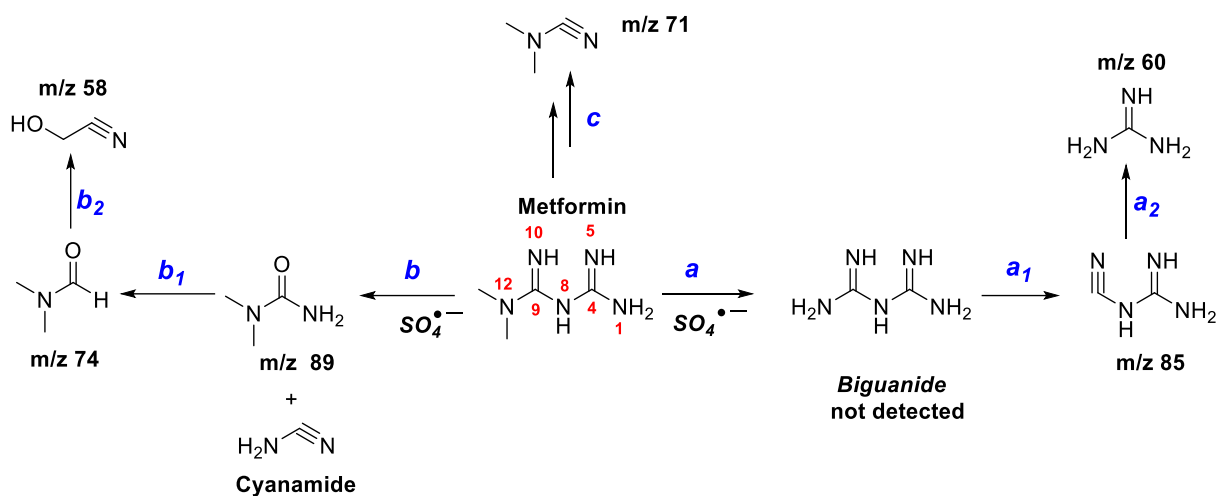
Figure 7.8. General mechanism of metformin degradation.
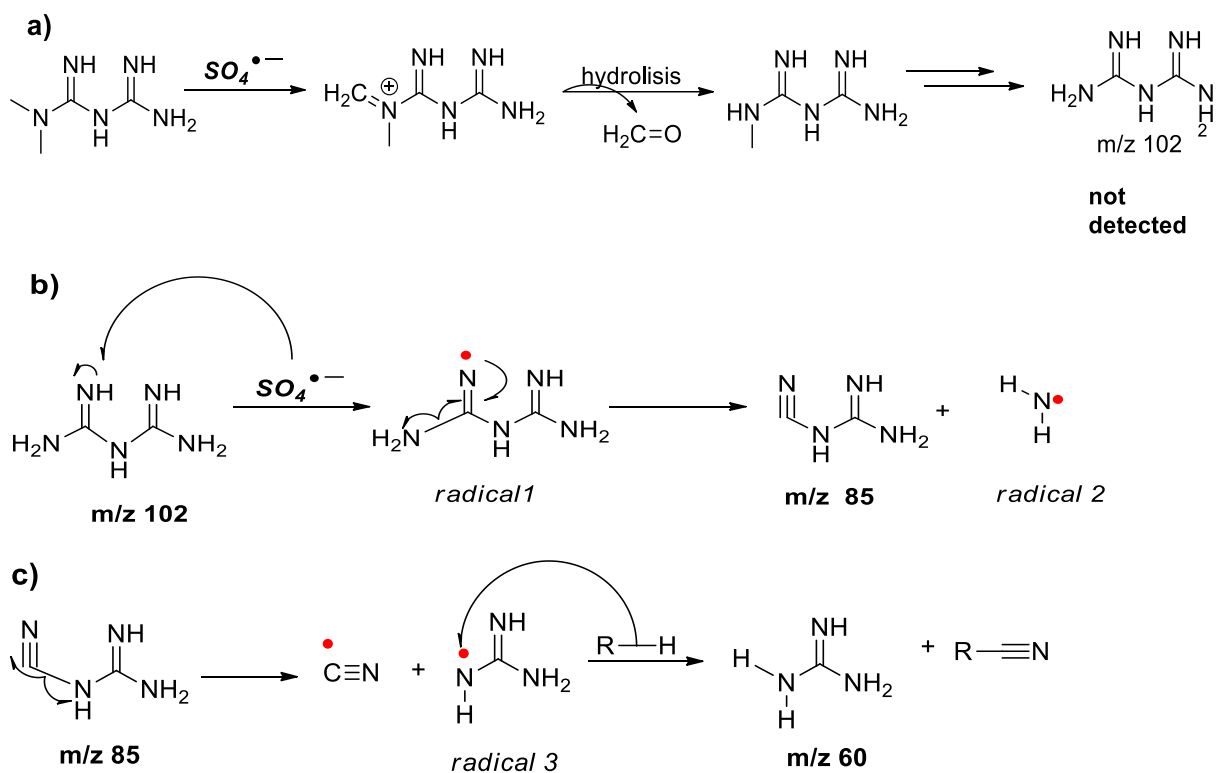
Figure 7.9. Proposed pathway *a* for metformin degradation: a) General pathway *a*, b) pathway *a1*, and c) pathway *a2*.

Pathway *a1*: The H-abstraction by $SO_4^{\bullet-}$ on biguadine intermediate leads to N-cyanoguanidine m/z 85 and amino radical (radical 2) which can be converted to ammonia.

Pathway *a2*: The N-cyanoguanidine leads to the guanidine intermediate m/z 60 by the radical 3 formation due to the C-N homolytic bond cleavage. Luo et al. [70], suggested that the detected peaks of m/z 85.0508 and m/z 60.0557 might be equivalent to protonated ion by losing dimethylamide and guanidyl from $[M^+H]^+$ ion of metformin.

The proposed pathway b (***Figure 7.10***) is the H-abstraction on the N_5 atom which leads to the radical 4. The 8-4 N-C bond homolytic cleavage leads to cyanamide and the radical 5 that, under hydrolysis reaction, leads to N,N-dimethyl-urea m/z 89.
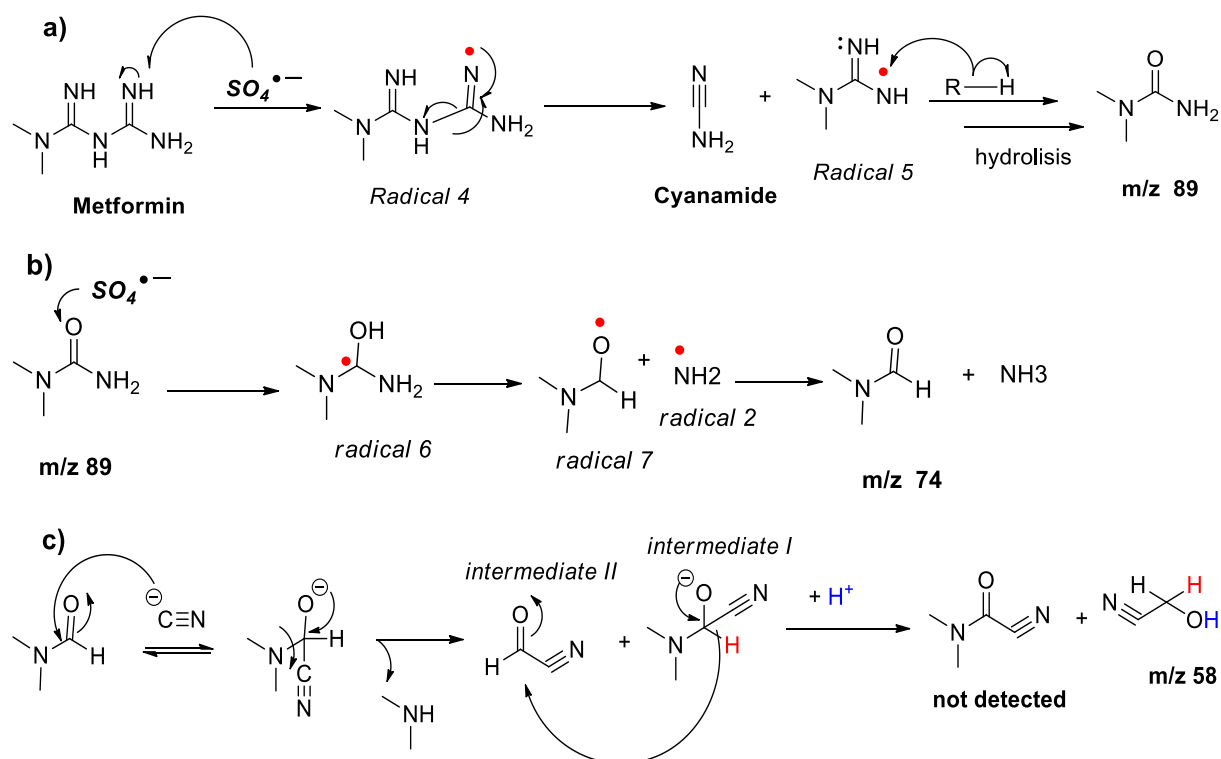

Figure 7.10. Proposed pathway *b* for metformin degradation: a) General pathway *b*, b) pathway *b1*, and c) pathway *b2*.

Pathway *b1*: Badran et al. [71] report that the H-abstraction on N,N-dimethyl-urea would lead to the formation of radical 6. This is followed by isomerization to form radical 7 and radical 2, that finally lead to dimethyl-formamide m/z 74 and ammonia.

Pathway *b2*: Through Canizzaro reaction the dimethylformamide would lead to the formation of glycolonitrile intermediate m/z 58. Two successive nucleophilic additions: cyanide ion to give the intermediate I, followed the addition of a hydride ion of intermediate I to the second aldehyde molecule (intermediate II). The presence of the negative charge on the intermediate I help to lose the hydride ion.

On the other side, *Chlamydomonas reinhardtii* cultures were used to determine the toxicity of the degradation byproducts generated at different experimental conditions. ***Figure 7.11*** depicts the inhibitory rate percentage of initial metformin solutions (untreated) and the solutions after 60 min of treatment, as well as the degradation percentage (% D) resulting in each experiment. It is observed that in most cases inhibitory rate of the by-products decreased (up to 33 %) or remained close to that of the initial metformin solution. Interestingly, for experiments $STD_{14, 15, 22, \& 26}$ a certain growth stimulation or hormesis effect (< 10 %) was observed. From growth inhibition tests, some authors have also observed that at low concentrations of different compounds there is a hormesis effect of cell biomass. For instance, Hurtado et al. [73] reported the growth increase (< 20%) of microalga *Chlamydomonas reinhardtii* upon exposure to superparamagnetic iron oxide nanoparticles (SPION) at concentrations lower than 5 mg L^{-1}. Similarly, the presence of chlortetracycline and oxytetracycline (CTC+OTC) in concentrations below 3 mg L^{-1} resulted in a hormesis effect (≈ 15 %) on the growth of *Spirulina platensis* [74]. The hormesis phenomenon refers to a biphasic organism dose-response to a chemical, which consists of a low dose stimulatory or beneficial effect and a high dose inhibitory or toxic effect [73, 75]. On the other hand, hormesis is considered an evolutionary mechanism since it is an adaptive response of cells and organisms to a moderate and intermittent stress or imbalance to prevent their extinction [76-78].
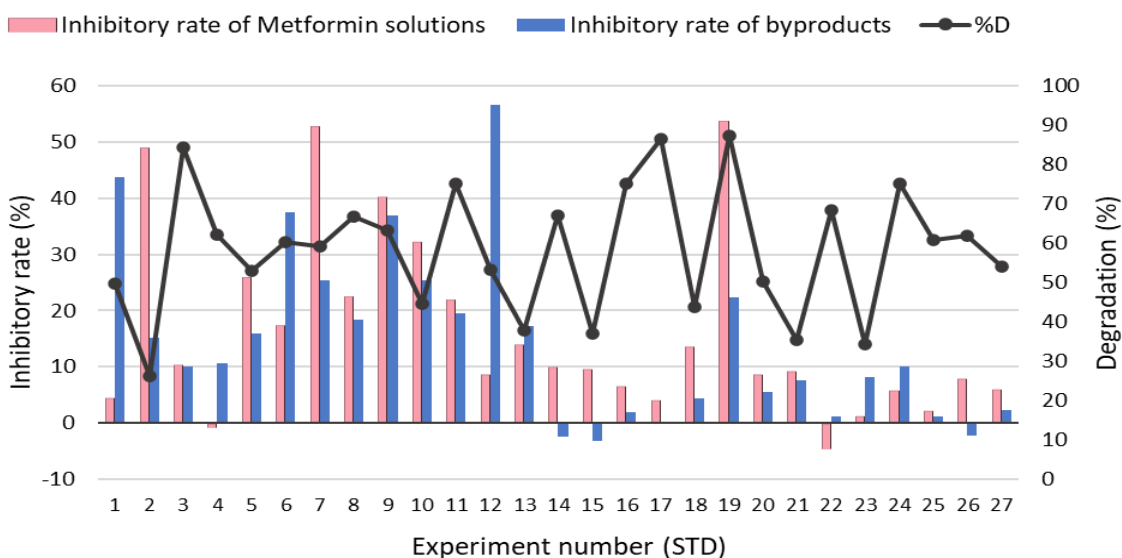
Figure 7.11. Growth inhibition rate (%) of *Chlamydomonas reinhardtii* cultures exposed to initial metformin solutions (pink bars) and byproducts (blue bars) of each experiment.

Nevertheless, by-products of the STD_{12} experiment presented the highest inhibitory rate increase, around 50 %. This could be attributed to the relatively low degradation percentage achieved during this experiment (53 %). STD_{12} operational conditions could lead to the presence of intermediates and transitory species with higher toxicity, such as H_2O_2, which generation is favored at basic pH and elevated temperatures according to Eqs. (14–16). In addition, byproducts of $STD_{2,7,19}$ experiments showed the highest inhibitory rate difference when compared with their respective initial metformin solutions. Interestingly, inhibitory rate of STD_{19} by-products, which showed 87.3 % metformin degradation, was halved when compared with its untreated solution. A similar result can be caused by STD_7 byproducts, although in this case %D was 59.2 %. Concentration of the different byproducts obtained could vary according to the operational conditions used in each experiment. However, at this point there is no clear tendency between C_{A0}, C_{ox}, T, and pH variations and inhibition rate.

7.4. Conclusions

In this work, the effectiveness of AOPs using sulfate radicals (UV/$S_2O_8^{2-}$ system) in the degradation of metformin was studied to determine the relevance and effects of operating conditions. Metformin degradation experiments were performed in a photoreactor equipped with a low-pressure Hg lamp, and $K_2S_2O_8$ was used as oxidant. A response surface experimental design considering the initial metformin concentration (C_{A0}), oxidant concentration (C_{ox}), temperature (T), and pH, as input variables was followed. The metformin degradation and mineralization percentages (%D and %TOC, respectively), as well as the apparent rate constant (k_{app}), were correlated with the factors analyzed.

The degradation percentages obtained ranged from 26.1 to 87.3 % depending on the operating conditions used. Moreover, the high %D results achieved are attributed to the presence of $SO_4^{\bullet-}$ radicals by photoactivation of $S_2O_8^{2-}$, as well as due to the slow rate of recombination of these radicals and the high selectivity of $SO_4^{\bullet-}$ radical in its reaction with metformin. According to the ANOVA, three of the factors studied — C_{A0}, C_{ox}, and T — resulted significant in the %D and %TOC obtained, being both concentrations the most important factors. Contrary to C_{A0}, the increase in C_{ox} and T has a positive effect on %D and %TOC responses. C_{ox} rise favors the generation of radicals, hence, a good ratio of radicals/metformin molecules to be attacked. However, there is a maximum concentration of oxidant around 5000 μM, in which radicals produced can be inhibited or recombined leading to a degradation reduction.

On the other hand, acidic pH affects the process because of the presence of both, chloride ions inhibiting $SO_4^{\bullet-}$ radicals, and acidic inorganic products with a low oxidation potential, as well as due to the double protonation of metformin molecules. The positive effect of temperature is more significant in acidic pH, while in a basic medium, a temperature elevation diminishes the effectiveness of the process due to recombination and inhibition reactions.

Furthermore, the HPLC-EIS-MS analysis detected six principal degradation byproducts: N-cyanoguanidine, N,N-dimethyl-Urea, N,N-dimethyl-cyanamide, N,N-dimethyl-formamide, glicolonitrilo, and guanidine. Additionally, three degradation

pathways were suggested according to the HPLC-MS analysis results. Finally, most of the remaining degradation solutions presented a decrease, up to 33%, in the inhibitory rate.

7.5. References

[1] Lalau, J., Al-Salameh, A., Hadjadj, S., Goronflot, T., Wiernsperger, N., Pichelin, M., Allix, I., Amadou, C., Bourron, O., Duriez, T., Gautier, J., et al. (2020). Metformin use is associated with a reduced risk of mortality in patients with diabetes hospitalised for COVID-19. *Diabetes & Metabolism, 47*(5), 101216. https://doi.org/10.1016/j.diabet.2020.101216.

[2] Mahmoud, M. E., El-Ghanam, A. M., Saad, S. R., & Mohamed, R. H. A. (2020). Promoted removal of metformin hydrochloride anti-diabetic drug from water by fabricated and modified nanobiochar from artichoke leaves. *Sustainable Chemistry and Pharmacy, 18*, 100336. https://doi.org/10.1016/j.scp.2020.100336.

[3] Cusioli, L. F., Quesada, H. B., de Brito Portela Castro, A. L., Gomes, R. G., & Bergamasco, R. (2020). Development of a new low-cost adsorbent functionalized with iron nanoparticles for removal of metformin from contaminated water. *Chemosphere, 247*, 125852. https://doi.org/10.1016/j.chemosphere.2020.125852.

[4] Kinaan, M., Ding, H., & Triggle, C. R. (2015). Metformin: An old drug for the treatment of diabetes but a new drug for the protection of the endothelium. *Medical Principles and Practice, 24*(5), 401–415. https://doi.org/10.1159/000381643.

[5] Kumar, R., Akbarinejad, A., Jasemizad, T., Fucina, R., Travas-Sejdic, J., & Padhye, L. P. (2021). The removal of metformin and other selected PPCPs from water by poly(3,4-ethylenedioxythiophene) photocatalyst. *Science of The Total Environment, 751*, 142302. https://doi.org/10.1016/j.scitotenv.2020.142302.

[6] Quesada, H. B., Baptista, A. T. A., Cusioli, L. F., Seibert, D., de Oliveira Bezerra, C., & Bergamasco, R. (2019). Surface water pollution by pharmaceuticals and an alternative of removal by low-cost adsorbents: A review. *Chemosphere, 222*, 766–780. https://doi.org/10.1016/j.chemosphere.2019.02.009.

[7] Briones, R. M., Sarmah, A. K., & Padhye, L. P. (2016). A global perspective on the use, occurrence, fate and effects of anti-diabetic drug metformin in natural and engineered ecosystems. *Environmental Pollution, 219*, 1007–1020. https://doi.org/10.1016/j.envpol.2016.07.040.

[8] Straub, J. O., Caldwell, D. J., Davidson, T., D'Aco, V., Kappler, K., Robinson, P. F., Simon-Hettich, B., & Tell, J. (2019). Environmental risk assessment of metformin and its transformation product guanylurea. I. Environmental fate. *Chemosphere, 216*, 844–854. https://doi.org/10.1016/j.chemosphere.2018.10.036.

[9] Armbruster, D., Happel, O., Scheurer, M., Harms, K., Schmidt, T. C., & Brauch, H. (2015). Emerging nitrogenous disinfection byproducts: Transformation of the antidiabetic drug metformin during chlorine disinfection of water. *Water Research, 79*, 104–118. https://doi.org/10.1016/j.watres.2015.04.020.

[10] Zhang, R., He, Y., Yao, L., Chen, J., Zhu, S., Rao, X., Tang, P., You, J., Hua, G., Zhang, L., Ju, F., & Wu, L. (2021). Metformin chlorination byproducts in drinking water exhibit marked toxicities of a potential health concern. *Environment International, 146*, 106244. https://doi.org/10.1016/j.envint.2020.106244.

[11] Niemuth, N. J., & Klaper, R. D. (2015). Emerging wastewater contaminant metformin causes intersex and reduced fecundity in fish. *Chemosphere, 135*, 38–45. https://doi.org/10.1016/j.chemosphere.2015.03.060.

[12] Klaper, R. D., & Niemuth, N. J. (2016). On the unexpected reproductive impacts of metformin: A need for support and new directions for the evaluation of the

impacts of pharmaceuticals in the environment. *Chemosphere, 165*, 570–574. https://doi.org/10.1016/j.chemosphere.2016.08.048.

[13] Elizalde-Velázquez, G. A., & Gómez-Oliván, L. M. (2020). Occurrence, toxic effects and removal of metformin in the aquatic environments in the world: Recent trends and perspectives. *Science of The Total Environment, 702*, 134924. https://doi.org/10.1016/j.scitotenv.2019.134924.

[14] Lee, J. W., Shin, Y., Kim, H., Kim, H., Kim, J., Min, S., Kim, P., Yu, S. D., & Park, K. (2019). Metformin-induced endocrine disruption and oxidative stress of Oryzias latipes on two-generational condition. *Journal of Hazardous Materials, 367*, 171–181. https://doi.org/10.1016/j.jhazmat.2018.12.084.

[15] Mrozik, W., & Stefańska, J. (2014). Adsorption and biodegradation of antidiabetic pharmaceuticals in soils. *Chemosphere, 95*, 281–288. https://doi.org/10.1016/j.chemosphere.2013.09.012.

[16] Poursat, B. A. J., van Spanning, R. J. M., Braster, M., Helmus, R., de Voogt, P., & Parsons, J. R. (2019). Biodegradation of metformin and its transformation product, guanylurea, by natural and exposed microbial communities. *Ecotoxicology and Environmental Safety, 182*, 109414. https://doi.org/10.1016/j.ecoenv.2019-109414.

[17] Khan, S., Dai, X., Ali, T., Mahmood, S., Haq, M. u., Riaz, M. S., & Hu, Y. (2022). Recent advances on photo-thermo-catalysis for carbon dioxide methanation. *International Journal of Hydrogen Energy, 48*(64), 24756-24787. https://doi.org/10.1016/j.ijhydene.2022.09.224.

[18] Hethnawi, A., Alnajjar, M., Manasrah, A. D., Hassan, A., Vitale, G., Jeong, R., & Nassar, N. N. (2020). Metformin removal from water using fixed-bed column of silica-alumina composite. *Colloids and Surfaces A: Physicochemical and Engineering Aspects, 597*, 124814. https://doi.org/10.1016/j.colsurfa.2020.124814

[19] Cui, H., & Schröder, P. (2016). Uptake, translocation and possible biodegradation of the antidiabetic agent metformin by hydroponically grown Typha latifolia. *J. Hazard. Mater., 308*, 355–361. https://doi.org/10.1016/j.jhazmat.2016.01.054.

[20] Piai, L., Blokland, M., van der Wal, A., & Langenhoff, A. (2020). Biodegradation and adsorption of micropollutants by biological activated carbon from a drinking water production plant. *Journal of Hazardous Materials, 388*, 122028. https://doi.org/10.1016/j.jhazmat.2020.122028.

[21] Mazivila, S. J., Ricardo, I. A., Leitão, J. M. M., & Esteves da Silva, J. C. G. (2019). A review on advanced oxidation processes: From classical to new perspectives coupled to two- and multi-way calibration strategies to monitor degradation of contaminants in environmental samples. *Trends in Environmental Analytical Chemistry, 24*, e00072. https://doi.org/10.1016/j.teac.2019.e00072.

[22] Domènech, X., Jardim, W., & Litter, M. (2004). Procesos avanzados de oxidación para la eliminación de contaminantes. Colección Documentos

[23] Priyadarshini, M., Das, I., Ghangrekar, M. M., & Blaney, L. (2022). Advanced oxidation processes: Performance, advantages, and scale-up of emerging technologies. *Journal of Environmental Management, 316*, 115295. https://doi.org/10.1016/j.jenvman.2022.115295.

[24] Ye, T., Zhang, T., Tian, F., & Xu, B. (2021). The fate and transformation of iodine species in UV irradiation and UV-based advanced oxidation processes. Water Research, 206, 117755. https://doi.org/10.1016/j.watres.2021.117755.

[25] Yao, Z., Wang, M., Jia, R., Zhao, Q., Liu, L., & Sun, S. (2023). Comparison of UV-based advanced oxidation processes for the removal of different fractions of NOM from drinking water. *Journal of Environmental Sciences, 126*, 387–395. https://doi.org/10.1016/j.jes.2022.03.040.

[26] Meng, T., Sun, W., Su, X., & Sun, P. (2021). The optimal dose of oxidants in UV-based advanced oxidation processes with respect to primary radical concentrations. *Water Research, 206*, 117738. https://doi.org/10.1016/j.watres.2021.117738.

[27] Lu, Z., Ling, Y., Sun, W., Liu, C., Mao, T., Ao, X., & Huang, T. (2022). Antibiotics degradation by UV/chlor(am)ine advanced oxidation processes: A comprehensive review. *Environmental Pollution, 308*, 119673. https://doi.org/10.1016/j.envpol.2022.119673.

[28] Ike, I. A., Linden, K. G., Orbell, J. D., & Duke, M. (2018). Critical review of the science and sustainability of persulphate advanced oxidation processes. *Chemical Engineering Journal, 338,* 651–669. https://doi.org/10.1016/j.cej.2018.01.034.

[29] Scaria, J., & Nidheesh, P. V. (2022). Comparison of hydroxyl-radical-based advanced oxidation processes with sulfate radical-based advanced oxidation processes. *Current Opinion in Chemical Engineering, 36*, 100830. https://doi.org/10.1016/j.coche.2022.100830.

[30] Amor, C., Fernandes, J. R., Lucas, M. S., & Peres, J. A. (2021). Hydroxyl and sulfate radical advanced oxidation processes: Application to an agro-industrial wastewater. *Environmental Technology & Innovation, 21*, 101183. https://doi.org/10.1016/j.eti.2020.101183.

[31] Olmez-Hanci, T., & Arslan-Alaton, I. (2013). Comparison of sulfate and hydroxyl radical based advanced oxidation of phenol. *Chemical Engineering Journal, 224*, 10–16. https://doi.org/10.1016/j.cej.2012.11.007.

[32] Fernandes, A., Makoś, P., Khan, J. A., & Boczkaj, G. (2019). Pilot scale degradation study of 16 selected volatile organic compounds by hydroxyl and sulfate radical based advanced oxidation processes. *Journal of Cleaner Production, 208*, 54–64. https://doi.org/10.1016/j.jclepro.2018.10.081.

[33] Ocampo-Pérez, R., Sánchez-Polo, M., Rivera-Utrilla, J., & Leyva-Ramos, R. (2010). Degradation of antineoplastic cytarabine in aqueous phase by advanced oxidation processes based on ultraviolet radiation. *Chemical Engineering Journal, 165*, 581–588. https://doi.org/10.1016/j.cej.2010.09.076.

[34] Khan, J. A., He, X., Shah, N. S., Khan, H. M., Hapeshi, E., Fatta-Kassinos, D., & Dionysiou, D. D. (2014). Kinetic and mechanism investigation on the photochemical degradation of atrazine with activated H2O2, S2O82− and HSO5−. *Chem. Eng. J., 252*, 393–403. https://doi.org/10.1016/j.cej.2014.04.104.

[35] Ocampo-Pérez, R., Rivera-Utrilla, J., Mota, A. J., Sánchez-Polo, M., & Leyva-Ramos, R. (2016). Effect of radical peroxide promoters on the photodegradation of cytarabine antineoplastic in water. *Chemical Engineering Journal, 284*, 995–1002. https://doi.org/10.1016/j.cej.2015.08.162.

[36] Torres-Luna, J. R., Ocampo-Pérez, R., Sánchez-Polo, M., Rivera Utrilla, J., Velo-Gala, I., & Bernal-Jacome, L. A. (2013). Role of HO and SO4- radicals on the photodegradation of remazol red in aqueous solution. *Chemical Engineering Journal, 223*, 155–163. https://doi.org/10.1016/j.cej.2013.02.127.

[37] Domingues, E., Silva, M. J., Vaz, T., Gomes, J., & Martins, R. C. (2022). Sulfate radical based advanced oxidation processes for agro-industrial effluents treatment: A comparative review with Fenton's peroxidation. Science of The Total Environment, 832, 155029. https://doi.org/10.1016/j.scitotenv.2022.155029.

[38] Molnar Jazić, J., Đurkić, T., Bašić, B., Watson, M., Apostolović, T., Tubić, A., & Agbaba, J. (2020). Degradation of a chloroacetanilide herbicide in natural waters using UV activated hydrogen peroxide, persulfate and peroxymonosulfate processes. *Environmental Science: Water Research & Technology, 6*, 2800–2815. https://doi.org/10.1039/D0EW00358A.

[39] Fernandes, A., Makoś, P., & Boczkaj, G. (2018). Treatment of bitumen post oxidative effluents by sulfate radicals based advanced oxidation processes (S-AOPs) under alkaline pH conditions. *Journal of Cleaner Production, 195*, 374–384. https://doi.org/10.1016/j.jclepro.2018.05.207.

[40] Urán-Duque, L., Saldarriaga-Molina, J., & Rubio-Clemente, A. (2021). Advanced Oxidation Processes Based on Sulfate Radicals for Wastewater Treatment: Research Trends. *Water, 13*(17), 2445. https://doi.org/10.3390/w13172445.

[41] Orata, E. D., De Leon, P. D. P., & Doma, B. T. (2019). Degradation of metformin in water using electro-Fenton process. *IOP Conf. Ser.: Earth Environ. Sci., 344*(1), 012007. https://doi.org/10.1088/1755-1315/344/1/012007.

[42] Khan, N. A., Khan, A. H., Tiwari, P., Zubair, M., & Naushad, M. (2021). New insights into the integrated application of Fenton-based oxidation processes for the treatment of pharmaceutical wastewater. *Journal of Water Process Engineering, 44*, 102440. https://doi.org/10.1016/j.jwpe.2021.102440.

[43] Neamţu, M., Grandjean, D., Sienkiewicz, A., Le Faucheur, S., Slaveykova, V., Colmenares, J. J. V., ... de Alencastro, L. F. (2014). Degradation of eight relevant micropollutants in different water matrices by neutral photo-Fenton process under UV254 and simulated solar light irradiation – A comparative study. *Appl. Catal. B Environ., 158-159*, 30–37. https://doi.org/10.1016/j.apcatb.2014.04.001.

[44] Chinnaiyan, P., Thampi, S. G., Bharath Krishnaa, A. C., Sasi, M., & Tejashwi, L. (2019). Optimisation of system parameters for the removal of Metformin in a photocatalytic reactor employing TiO2. *IOP Conf. Ser.: Mater. Sci. Eng., 561*(1), 012087. https://doi.org/10.1088/1757-899x/561/1/012087.

[45] Balakrishnan, A., Sillanpää, M., Jacob, M. M., & Vo, D. N. (2022). Metformin as an emerging concern in wastewater: Occurrence, analysis and treatment methods. *Environ. Res., 213,* 113613. https://doi.org/10.1016/j.envres.2022.113613.

[46] Montgomery, D. C. (2019). *Design and Analysis of Experiments*. Wiley.

[47] Karimshoushtari, M., & Novara, C. (2020). Design of experiments for nonlinear system identification: A set membership approach. *Automatica, 119*, 109036. https://doi.org/10.1016/j.automatica.2020.109036.

[48] Beg, S., & Rahman, M. (2021). Chapter 11 - Design of experiments application for analytical method development. In S. Beg, M. S. Hasnain, M. Rahman, & W. H. Almalki (Eds.), *Handbook of Analytical Quality by Design* (pp. 191–197). Academic Press

[49] Quintão, F. J. O., Freitas, J. R. L., Machado, C. de F., Aquino, S. F., Silva, S. de Q., & Afonso, R. J. de C. F. (2016). Characterization of metformin by-products under photolysis, photocatalysis, ozonation and chlorination by high-performance liquid chromatography coupled to high-resolution mass spectrometry. *Rapid Communications in Mass Spectrometry, 30*(19), 2360–2368. https://doi.org/10.1002/rcm.7724.

[50] Scheurer, M., Sacher, F., & Brauch, H. (2009). Occurrence of the antidiabetic drug metformin in sewage and surface waters in Germany. *Journal of Environmental Monitoring, 11*(9), 1608–1613. https://doi.org/10.1039/B909311G.

[51] Chhetri, H. P., Thapa, P., & Van Schepdael, A. (2014). Simple HPLC-UV method for the quantification of metformin in human plasma with one step protein precipitation. *Saudi Pharmaceutical Journal, 22*(5), 483–487. https://doi.org/10.1016/j.jsps.2013.12.011.

[52] National Center for Biotechnology Information. (2022). *PubChem Compound Summary for CID 4091, Metformin*. Retrieved September 2, 2022, from https://pubchem.ncbi.nlm.nih.gov/compound/Metformin.

[53] Cahill, J. D., Furlong, E. T., Burkhardt, M. R., Kolpin, D., & Anderson, L. G. (2004). Determination of pharmaceutical compounds in surface- and ground-water samples by solid-phase extraction and high-performance liquid chromatography-electrospray ionization mass spectrometry. *Journal of Chromatography A, 1041*(1–2), 171–180. https://doi.org/10.1016/j.chroma.2004.04.005.

[54] Carbuloni, C. F., Savoia, J. E., Santos, J. S. P., Pereira, C. A. A., Marques, R. G., Ribeiro, V. A. S., & Ferrari, A. M. (2020). Degradation of metformin in water by TiO2–ZrO2 photocatalysis. *Journal of Environmental Management, 262*, 110347. https://doi.org/10.1016/j.jenvman.2020.110347.

[55] Wols, B. A., Hofman-Caris, C. H. M., Harmsen, D. J. H., & Beerendonk, E. F. (2013). Degradation of 40 selected pharmaceuticals by UV/H2O2. *Water Research, 47*(18), 5876–5888. https://doi.org/10.1016/j.watres.2013.07.008.

[56] Aseman-Bashiz, E., & Sayyaf, H. (2020). Metformin degradation in aqueous solutions by electro-activation of persulfate and hydrogen peroxide using natural and synthetic ferrous ion sources. *Journal of Molecular Liquids, 300*, 112285. https://doi.org/10.1016/j.molliq.2019.112285.

[57] Hermosillo-Arellano, E., Ocampo-Perez, R., Sanchez-Polo, A. M., Sanchez-Polo, M., Flores-Vélez, L. M., & Mendoza-Mendoza, E. (2019). Role of the radical promoter systems on the degradation of an antipeleptic drug using HO and SO4-species. *Journal of Water Process Engineering, 27*, 162–170. https://doi.org/10.1016/j.jwpe.2018.12.002.

[58] Sánchez-Polo, M., Abdel daiem, M. M., Ocampo-Pérez, R., Rivera-Utrilla, J., & Mota, A. J. (2013). Comparative study of the photodegradation of bisphenol A by HO, SO4− and CO3−/HCO3 radicals in aqueous phase. *Science of The Total Environment, 463-464*, 423–431. https://doi.org/10.1016/j.scitotenv.2013.06.012.

[59] Yu, X., Bao, Z., & Barker, J. R. (2004). Free Radical Reactions Involving Cl•, Cl2-•, and SO4-• in the 248 nm Photolysis of Aqueous Solutions Containing S2O82- and Cl-. *The Journal of Physical Chemistry A, 108*(14), 295–308. https://doi.org/10.1021/jp036211i.

[60] Prashanth, V., Priyanka, K., & Remya, N. (2021). Solar photocatalytic degradation of metformin by TiO(2) synthesized using Calotropis gigantea leaf extract. *Water Sci. Technol., 83*(5), 1072–1084. https://doi.org/10.2166/wst.2021.040.

[61] Dolatabadi, M., & Ahmadzadeh, S. (2019). A rapid and efficient removal approach for degradation of metformin in pharmaceutical wastewater using electro-Fenton process; optimization by response surface methodology. *Water Science and Technology, 80*(4), 685–694. https://doi.org/10.2166/wst.2019.312.

[62] Kiejza, D., Kotowska, U., Polińska, W., & Karpińska, J. (2021). Peracids - New oxidants in advanced oxidation processes: The use of peracetic acid, peroxymonosulfate, and persulfate salts in the removal of organic micropollutants of emerging concern − A review. *Science of The Total Environment, 790*, 148195. https://doi.org/10.1016/j.scitotenv.2021.148195.

[63] Knapp, J. S., & Bromley-Challoner, K. C. A. (2003). Recalcitrant organic compounds. In D. Mara & N. Horan (Eds.), *Handbook of Water and Wastewater Microbiology* (pp. 559–595). Academic Press.

[64] He, S., Liu, T., Kang, C., Xue, H., Sun, S., & Yu, S. (2021). Photodegradation of dissolved organic matter of chicken manure: Property changes and effects on Zn2+/Cu2+ binding property. *Chemosphere, 276*, 130054. https://doi.org/10.1016/j.chemosphere.2021.130054.

[65] Mmelesi, O. K., Patala, R., Nkambule, T. T. I., Mamba, B. B., Kefeni, K. K., & Kuvarega, A. T. (2022). Effect of Zn doping on physico-chemical properties of cobalt ferrite for the photodegradation of amoxicillin and deactivation of E. coli.

Colloids and Surfaces A: Physicochemical and Engineering Aspects, 649, 129462. https://doi.org/10.1016/j.colsurfa.2022.129462.

[66] Choi, J., & Chung, J. (2020). Photodegradation of low molecular weight organic compounds by 185-nm UV light in ultrapure water production system. *J. Water Process Eng., 37*, 101437. https://doi.org/10.1016/j.jwpe.2020.101437.

[67] Sillanpää, M., Matilainen, A., & Lahtinen, T. (2015). Characterization of NOM. In M. Sillanpää (Ed.), *Natural Organic Matter in Water* (pp. 17–53). Butterworth-Heinemann.

[68] Albert, D. E. (2015). Methods for Verifying Medical Device Cleanliness. In R. Kohli & K. L. Mittal (Eds.), *Developments in Surface Contamination and Cleaning* (pp. 109–128). William Andrew Publishing.

[69] Praveen-Kumar, & Brumme, R. (1995). Alkylated ureas: mineralization and evaluation as N sources. *Fertilizer Research, 41*(2), 117–124. https://doi.org/10.1007/BF00750753.

[70] Luo, M., Zheng, L., Wang, S., Zhu, J., Tang, Z., & Gao, P. (2021). Characterization of four major degradation products in metformin by 2D LC-QTOF/MS/MS. *Journal of Pharmaceutical and Biomedical Analysis, 192*, 113662. https://doi.org/10.1016/j.jpba.2020.113662.

[71] Badran, I., Manasrah, A. D., & Nassar, N. N. (2019). A combined experimental and density functional theory study of metformin oxy-cracking for pharmaceutical wastewater treatment. *RSC Advances, 9*(23), 13403–13413. https://doi.org/10.1039/C9RA01641D.

[72] Lin, W., Zhang, X., Li, P., Tan, Y., & Ren, Y. (2020). Ultraviolet photolysis of metformin: mechanisms of environmental factors, identification of intermediates,

and density functional theory calculations. *Environmental Science and Pollution Research, 27*(17), 17043–17053. https://doi.org/10.1007/s11356-020-08255-9.

[73] Hurtado-Gallego, J., Pulido-Reyes, G., González-Pleiter, M., Salas, G., Leganés, F., Rosal, R., & Fernández-Piñas, F. (2020). Toxicity of superparamagnetic iron oxide nanoparticles to the microalga Chlamydomonas reinhardtii. *Chemosphere, 238,* 124562. https://doi.org/10.1016/j.chemosphere.2019.124562.

[74] Zhou, T., Cao, L., Zhang, Q., Liu, Y., Xiang, S., Liu, T., & Ruan, R. (2021). Effect of chlortetracycline on the growth and intracellular components of Spirulina platensis and its biodegradation pathway. *Journal of Hazardous Materials, 413*, 125310. https://doi.org/10.1016/j.jhazmat.2021.125310.

[75] Mattson, M. P. (2008). Hormesis defined. *Ageing Research Reviews, 7*(1), 1–7. https://doi.org/10.1016/j.arr.2007.08.007.

[76 Jacob, R. S., de Souza Santos, L. V., d'Auriol, M., Lebron, Y. A. R., Moreira, V. R., & Lange, L. C. (2020). Diazepam, metformin, omeprazole and simvastatin: a full discussion of individual and mixture acute toxicity. *Ecotoxicology, 29*(8), 1062–1071. https://doi.org/10.1007/s10646-020-02239-8.

[77] Calabrese, E. J., & Baldwin, L. A. (2001). Hormesis: U-shaped dose responses and their centrality in toxicology. *Trends in Pharmacological Sciences, 22*(6), 285–291. https://doi.org/10.1016/S0165-6147(00)01719-3.

[78] Calabrese, E. J. (2008). Hormesis: Why it is important to toxicology and toxicologists. Environmental Toxicology and Chemistry, 27(7), 1451–1474. https://doi.org/10.1897/07-541.

8

GENERAL CONCLUSIONS

8. General conclusions

In this Doctoral Thesis, an evaluation of monolithic structures used as catalytic supports for high flow rates treatment was carried out, focusing on the significance of their shape and configuration on catalytic performance. The monoliths used for the analyses were coated with Ni/CeO_2, a catalytically active phase for the relevant environmental reaction under study: CO_2 methanation.

In the first case, from the study of the significance of cell density and the effect of straight channels on CO_2 conversion using conventional cordierite monoliths, it has been possible to conclude the following:

❖ The lower impact of diffusional control observed in the intermediate (CoI) and high cell (CoH) densities, about 200 mL min^{-1} lower than CoL, is attributed to better distribution and accessibility of the Ni/CeO_2 owing to a greater exposed surface area. In this sense, the importance of the exposed surface area lies in the low porosity of the cordierite material. This low porosity constrained the diffusion of the ethanolic suspension of the active phase through the walls during impregnation, concentering it on the channels' surface, except for the high cell density monolith, which presented slightly bigger pore volume, thus allowing some introduction into the channels' walls.

❖ The formulated mathematical model confirmed that, as expected from friction forces, the velocity profile developed within the straight channels consists of a steady radial profile, for which the maximum velocity is encounter at the center of the channel. This, in turn, affects the contact between the fluid and the Ni/CeO_2 attached to the surface.

❖ CO_2 conversion obtained using the intermediate cell density catalyst was less affected by increases in the gas hourly space velocity compared to the low cell density monolith. This was ascribed to the larger surface-to-volume ratio leading to improved dispersion and availability of the active phase, thus facilitating better interaction with the reaction mixture despite the radial velocity profile. Nonetheless, although the high cell density monolith has a bigger surface-to-

volume ratio, the introduction of active phase into the walls affects its ease of access, principally at high flow rates when diffusion through the ceramic matrix is weakened.

❖ In general, cell density is an important factor in catalytic activity through the distribution and accessibility of the catalytic compound. However, the results of this study suggest it is interesting to generate non-linear channels that avoid or reduce this type of radial velocity profile to improve the reactive-active phase interaction. New forms could improve fluid circulation within the catalysts, even favoring diffusion through the structure and therefore taking advantage of the active phases dispersed in the matrix of the monolithic support.

Considering the above, from the study of the development of complex intricate structures through combining 3D printing and sol-gel process, the following conclusions have been obtained:

❖ Whereas traditional synthesis methods restrict monolithic structure geometry to parallel straight channels, leading to transfer limitations, the proposed methodology has proven its feasibility for achieving diverse unconventional, sophisticated, and complex monolithic designs. The exact replica of the polymeric channels' templates was observed even at microscale. However, it is important to consider in the design the shrinking observed after thermal treatment.

❖ Textural characterization of carbon monoliths confirmed macroporosity, which favored homogeneous dispersion of the active phase on the channel surface and within the carbon matrix. Besides, chemical characterization evidenced that the properties of the active phase remained unchanged after loading onto carbon, hence proving that catalytic activity was affected only by the design of the monoliths.

❖ Complex designs promote turbulence within the catalysts. Contrary to conventional straight channels that force laminar flow of the fluid with radial diffusion limitations, the turbulence generated in advanced designs further leads to better mass transfer, enhanced reactant-active sites interaction, thus increasing reaction rate, conversion, and selectivity.

❖ The modification of cell geometry from conventional straight to crisscrossed channels allows the catalysts to achieve chemical control, at least up to 230 °C. Conversely to straight channel catalysts, the reaction rate is not affected by the treated flow rate.

❖ The improved catalytic performance of the crisscrossed channels was observed regardless of the cell density used. Nevertheless, the lowest cell density exhibited the largest difference in CO_2 conversion between both designs. This difference is attributed to diffusion limitations that constrain the accessibility of some of the active phase that is supported on the porous carbon structure of straight channels monoliths.

From the study of designing and analyzing auto-pressurized multi-stage Tesla-valve type microreactors as the monolithic channels of the catalyst, the following conclusions have been drawn:

❖ Both experimental and computational results have validated that the new concept of auto-pressurized multi-stage Tesla-valve type microreactors exhibits superior efficacy over conventional straight channels. The non-uniform flow dynamics induced by directional changes, coupled with localized pressure points from flow convergence at the intersections of the Tesla-valve stages, potentially favor methane production through the Sabatier reaction, in line with Le Châtelier's principle.

❖ In contrast to straight channels, both Tesla-valve type configurations (right angle T, and curved angle Tm) demonstrated consistent performance despite flow rate increases and showcased chemical control, primarily up to 240 °C. This has been attributed to the enhanced interaction between the fluid and catalyst due to the chaotic trajectory caused. In this sense, the curved angle augments even more the mass transfer, resulting in heightened conversion rates and approximately a 30% growth in reaction rate regarding the configuration with a right angle.

❖ The auto-pressurized multi-stage Tesla-valve monolith corroborates the opportunities offered by the methodology proposed in this Thesis for tailoring

advanced functional materials. The versatility of the technique, along with its precision, allows to enhance the reactant-active phase interaction even with a small change, and affords control over reaction conditions to fine-tune reactions kinetics.

As an additional work, a significant environmental issue associated with water remediation has been addressed through advanced oxidation processes (AOPs). From the study of metformin degradation by AOPs using sulfate radicals, the following has been concluded:

❖ The metformin degradation results (%D), varying from 26 to 87 %, were ascribed to the presence of highly selective $SO_4^{\bullet-}$ radicals formed by the photoactivation of $S_2O_8^{2-}$, and, to a lesser extent, $HO^{\bullet}$ radicals.

❖ According to the analysis of variance (ANOVA), temperature (T), but mainly the initial concentration of metformin (C_{A0}), and oxidant concentration (C_{ox}) have a significant effect on metformin degradation (%D) and mineralization (%TOC) percentages. While the increase in C_{ox} leads to a higher production of $SO_4^{\bullet-}$ radicals, a lower C_{A0} results in a greater ratio between radicals and metformin molecules to be degraded, improving the process. Nonetheless, the positive effect of increasing C_{ox} presents a maximum (around 5000 µM) since an overdose of oxidant, in turn, causes an excess of radicals that can recombine and be inhibited. Besides, the slight effect observed when augmenting the temperature by 30 °C is associated with an additional heat activation of $S_2O_8^{2-}$.

❖ The reduction in metformin degradation when treating in an acidic medium is attributed to three principal factors: chloride ions that inhibit the $SO_4^{\bullet-}$ radicals, production of acidic inorganic compounds with a lower oxidation potential regarding $SO_4^{\bullet-}$ and $HO^{\bullet}$, and the generation of more resistant bonds due to double protonation of amino groups of metformin molecules favored at low pHs.

❖ Regarding the apparent reaction rate constant (k_{app}), C_{ox} resulted in the most significant factor, whereas the temperature effect depended on the pH medium. For acidic pH, an increase in temperature causes an important k_{app} rise; however,

in basic medium higher temperatures favor recombination and inhibition reactions, affecting the k_{app}.

❖ Six principal degradation byproducts were detected by HPLC-EIS-MS analysis: N-cyanoguanidine, N,N-dimethyl-Urea, N,N-dimethyl-cyanamide, N,N-dimethyl-formamide, glycolonitrile, and guanidine, and these results served to suggest three degradation pathways.

❖ Although it was not possible to establish a relationship between inhibition rate and operational conditions, the toxicity analyses demonstrated most of the remanent degradation solutions showed a decrease in the inhibitory rate (up to 33 %). The increase in inhibitory rates of experiments with low degradation percentages was associated with the existence of intermediates and transitory species with higher toxicity than metformin. However, in some cases, a slight growth of cell biomass was observed as a hormesis effect of the low amounts of the degradation byproducts.

ADRIANA PARRA MARFIL

Julio 2024